University of Bath

UNIVERSITY OF BATH

PHD

Molecular Photocrystallography

A Study of Metastable and Transient Species by Non-Ambient Crystallographic Techniques

Hatcher, Lauren

Award date:
2014

Awarding institution:
University of Bath

Link to publication

Molecular Photocrystallography:

A Study of Metastable and Transient Species by Non-Ambient Crystallographic Techniques

Lauren Elizabeth Hatcher

A thesis submitted for the degree of Doctor of Philosophy
University of Bath
Department of Chemistry

January 2014

Table of Contents

List of Figures and Tables

Acknowledgements

I would like to thank Professor Paul Raithby for his support, guidance and direction throughout my PhD and for his continued supply of enthusiasm and ideas, from which the project has grown. I am also grateful to him for providing me with numerous opportunities to participate at national and international conferences, allowing me to develop my presentational skills and exhibit my work to the wider crystallographic community.

This work also owes much to the work of previous members of the Raithby research group and in particular I would like to thank Dr Mark Warren for his hard work and enthusiasm, both during his time at Bath and in his current postdoctoral role on Beamline I19 at Diamond Light Source. I am also appreciative of all members of the Raithby and Wilson groups, both past and present, who have been involved in the project, without whose hard work and collaborative effort during both laboratory and synchrotron experiments these studies would not have been possible.

I am grateful for the allocation of synchrotron beamtime at both the Advanced Light Source (ALS) in Berkeley, CA, USA and Diamond Light Source, Didcot, UK. At the ALS, I must particularly acknowledge contributions from Dr Simon Teat and Dr Christine Beavers during our visits to them on Beamline 11.3.1, where much of the steady-state data for this report was collected. At Diamond I am grateful to Dr David Allan and the rest of the team on Beamline I19, where the time-resolved photocrystallographic experiments reported here-in were developed.

Finally I would like to thank the University of Bath for funding my PhD research *via* a 3.5 year DTA studentship and providing me with the opportunity to work in such a vibrant and exciting research environment.

Abstract

This thesis describes the synthesis and crystallisation of a selection of known and novel transition-metal – nitrite complexes and their detailed study using non-ambient X-ray diffraction techniques. These coordination compounds are specifically investigated for their ability to undergo nitro – nitrito linkage isomerisation in the single-crystal, with conversion between isomers achieved on either thermal- or photoactivation. The lifetime of the excited-state isomer is strongly dependent on the experimental temperature and, as such, this thesis is also concerned with time-resolved crystallographic methods. This work relies primarily on the technique of photocrystallography, a growing area of crystallographic research that has enjoyed considerable interest in recent decades.

Chapter 1 reviews the seminal progress made in both time-resolved and photocrystallographic research, made possible by dramatic technological advances in the field in recent decades.

Chapter 2 outlines the goals of this research project, aiming to obtain a more detailed understanding of the factors that influence the solid-state nitro – nitrito isomerisation.

Chapter 3 describes the X-ray methods used in these studies, introducing both fundamental crystallographic principles and detailing the experimental procedures that are undertaken.

Chapters 4 and 5 record steady-state photocrystallographic studies conducted for a series of complexes containing bulky, chelating ancillary ligands accompanying a monodentate nitrite group expected to be capable of nitro – nitrito isomerism. The response of these systems to both thermal- and photoactivation is investigated *via* single-crystal diffraction methods. The analysis focusses on the potential steric and electronic influences from the surrounding crystalline environment, which may have an impact on the progress of the solid-state reaction.

Chapter 6 introduces photocrystallographic kinetic methods to investigate the progress of nitro – nitrito conversion in real time. These studies are the first of their kind to be conducted on nitrite linkage isomer species and some novel methodology is introduced.

Finally, Chapter 7 discusses pseudo-steady-state and trial time-resolved experiments conducted using the new time-resolved diffraction set-up on Beamline I19 at the Diamond Light Source. These early results indicate the power of time-resolved methods for elucidating key information on the nitro – nitrito conversion process and show promise for future experiments.

Abbreviations

ADP	anisotropic displacement parameter
ALS	Advanced Light Source
CCD	charge-coupled device
CSD	Cambridge Structural Database
DSC	Differential Scanning Calorimetry
ES	excited state
EXAFS	Extended X-ray Absorption Fine Structure
GS	ground state
IR	infrared
JMAK	Johnson, Mehl, Avrami and Kolmogorov
LED	light-emitting diode
LFSE	ligand field stabilisation energy
LIESST	Light-Induced Spin-State Trapping
MLCT	metal-to-ligand charge transfer
MS	metastable state
MX	macromolecular crystallography
QM/MM	Quantum Mechanical / Molecular Mechanics
TM	transition-metal
TR	time-resolved
UV	ultraviolet
XAFS	X-ray Absorption Fine Structure
X-FEL	X-ray Free Electron Laser
XRPD	X-ray Powder Diffraction

Chapter 1.

An Introduction to Photocrystallography and its Applications

Chapter 1. An Introduction to Photocrystallography and its Applications

1.1.   Photocrystallography

Although widely acknowledged as one of the most reliable methods of structural determination, until recently single-crystal X-ray diffraction has been thought limited to providing information that is both space-averaged over all molecules in the crystal and time-averaged over the full duration of the experiment. As such, it is somewhat counterintuitive that the technique can be used to study solid-state reactions, in which structural changes occur that disrupt the ordered crystalline array necessary to obtain diffraction, and happen over a short timescale. Recent decades have seen a significant reduction in the time needed to collect and process X-ray data, thanks to dramatic advances in the technologies that underpin the method, and the improvements have facilitated the development of a broad new range of single-crystal experiments. It is now possible to study a wide spectrum of solid-state phenomena, including single-crystal-to-single-crystal reactions induced by different excitation stimuli including temperature, pressure and light.

Extensive study of photoinduced changes in crystals was first conducted by Schmidt *et al.* in 1964, who concluded that solid-state photochemical reactions are controlled by topochemical factors. Their Topochemical Postulate proposes that restrictions imposed by the crystal lattice ensure that the reaction will follow a minimum energy pathway, undergoing the least amount of atomic movement possible in order to preserve the crystalline environment.[1-3] Although Schmidt was limited by the technological restrictions of the time, allowing the investigation of only ground state (GS) species *via* crystallography, recent advances have since allowed the study of photoinduced products by X-ray techniques and since the 1990s the phrase photocrystallography has been developed to describe this diverse new research area.[4]

1.2. Time-Resolved Crystallography

The study of dynamic changes in a sample as they occur requires that both the experiment and the process to be studied are brought onto a common timescale; either by slowing the reaction down to match the progress of the experiment, or by speeding up the experiment to match the rate of the dynamic process. These ideas form the basis for time-resolved (TR) experimentation and such techniques are routinely applied in several spectroscopic disciplines, including Mössbauer,[5] X-ray Absorption Fine Structure (XAFS),[6, 7] infrared (IR) and absorption spectroscopy.[8, 9] While spectroscopic methods provide valuable insight, in most cases detailed structural information can only be inferred from these data, at best. As such, the development of TR crystallography is required to conclusively determine the full, three-dimensional structures of transient species.[10]

1.2.1. Advances in Technique and Instrumentation

Advancements in four key technological areas have facilitated the rapid development of TR crystallography, allowing the "fourth dimension of time" to be incorporated into the X-ray experiment.[11] Firstly, the dramatic and continuing improvement in computing power provides the basis for many other advances in the field, allowing several time-consuming elements of the crystallographic method to be automated and ultimately reducing the time required to collect, process and solve X-ray data. Secondly, developments in cryogenic technologies have led to the widespread availability of *in-situ* cooling apparatus, making low temperature X-ray data collection a routine process. Most laboratory diffractometers are now equipped with cryogenic devices supplying liquid nitrogen to cool the crystal as low as 90 K, while temperatures approaching 4 K can be accessed using open-flow helium devices. In addition to the associated advantages of reduced dynamic disorder, higher resolution data, smaller thermal parameters and reduced radiation damage,[12] low temperature X-ray data is invaluable in TR studies where reliable control of the experiment conditions can be crucial to control the lifetime of the transient species under study. In addition, the development of third generation synchrotron facilities around the globe has led to the increased availability of high intensity X-ray sources.[13] Higher X-ray flux can both dramatically reduce the time needed to conduct an experiment and also allow the study of much smaller crystals, both of which are beneficial in photocrystallographic and TR diffraction studies. Additionally, the advent of X-ray Free Electron Laser (X-FEL) sources and their very recent availability to research groups is providing access to even higher X-ray intensities, with flux levels greater than 700 MGy routinely achieved at such facilities.[14] Finally, recent decades have also seen significant advances in X-ray detector science. The introduction of charge-coupled device (CCD) area detectors in the mid-1990s further reduced X-ray experiment times,[15] allowing the

whole of reciprocal space to be accessed in a period of hours or less. Most recently the commercialisation of pixel detectors with ultrafast read-out times continues to revolutionise the field allowing, in combination with high energy synchrotron or X-FEL radiation, the collection of full X-ray datasets in a single image.[14, 16] By achieving shorter and shorter time resolution studies are beginning to approach the timescale of a chemical reaction, making it increasingly feasible to use diffraction methods to record "molecular movies" following a reaction in real time.[17-19]

1.2.2. Types of TR Crystallographic Experiment

The type of TR crystallographic experiment conducted is necessarily dictated by the lifetime of the species under study and, as such, can be broadly categorised by this variable.[20] (i) Metastable state (MS) species are studied *via* "steady-state" methods (§ 3.2.2) and have lifetimes on a minute scale and longer. Most systems can be made to exist infinitely under certain experimental conditions, allowing their study by standard, single-crystal X-ray methods. (ii) Excited state (ES) species existing for periods between minutes and milliseconds can be studied by "pseudo-steady-state" methods (§ 3.2.3), in which the crystal is continuously pumped at the excitation wavelength for the duration of the experiment. After an initial period, under continued illumination the excitation and decay processes reach an equilibrium or steady-state, allowing a standard, single-crystal X-ray dataset to be obtained. (iii) Species with lifetimes in the millisecond to microsecond range are studied *via* "pump-probe", or "stroboscopic" methods, using synchrotron radiation. Both the excitation "pump" and X-ray "probe" sources are pulsed and synchronised to match the species' lifetime, with the X-ray pulse achieved by the use of a mechanical "chopper".[21] (iv) Picosecond-lived species are again studied by "pump-probe" methods, but in this case the probe pulse is generated by the naturally temporal nature of the synchrotron[13] and the excitation source must be timed to coincide with the synchrotron repetition rate. (v) Finally, the study of femtosecond species is now possible using single shot experiments, as X-FEL facilities increasingly become operational[22] (§ 1.4.3).

1.3. Metastable Species and Steady-State Methods

In the context of solid-state photochemical reactions, a metastable system is an ES species that can be made to exist for long periods, by careful control of the experimental conditions. In photocrystallographic studies this is usually achieved by photoactivation at low temperatures, with the temperature controlled using *in-situ* cryogenic cooling apparatus, and the process is reversible on warming. Figure 1.1 gives a schematic energy diagram for this situation, where the system is trapped into a local minimum to generate the MS. When the MS lifetime can be extended beyond the length of a single-crystal experiment it is possible to study the species using conventional X-ray methods and, as the system is held steadily in its MS for the duration, this is known as the "steady-state" crystallographic method (§ 3.2.2).
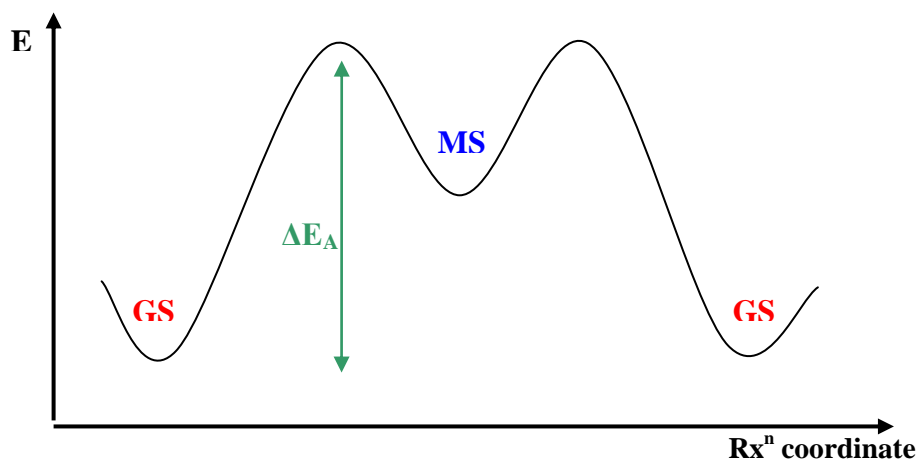
Figure 1.1: Schematic energy diagram for reversible photoactivation in a metastable species; GS = ground state, MS = metastable state, ΔE_A = activation energy

1.3.1. Single-Crystal-to-Single-Crystal Reactions

To study a system by single-crystal photocrystallography, the solid-state process occurring must meet certain criteria. As outlined by Schmidt *et al.*,[1] restrictions imposed by the crystal lattice mean that only topotactic reactions involving small atomic rearrangements can occur without compromising crystallinity. At the same time, the structural change must be large enough for a difference to be observed in the resultant X-ray data. This paradox necessarily limits the type of process that can be investigated, but nevertheless a variety of irreversible[2, 23, 24] and reversible[25] systems have been successfully investigated. For the photocrystallographic study of MS species, however, reversible photoreactions are exclusively required. Suitable processes have included spin-crossover systems that show Light-Induced Excited Spin-State Trapping (LIESST) behaviour,[26-30] photoinduced metal – metal bond changes[21, 31] and solid-state linkage isomerism.

1.3.2. Linkage Isomerism

The phenomenon by which an ambidentate ligand can bind to a metal *via* more than one different donor atom was first explained in by Jörgensen in 1894.[32] The molecules formed are structurally distinct despite sharing an identical chemical composition, and are known as linkage isomers. Though different linkage isomers of the same system can be prepared directly by varying reaction conditions,[33] conversion between isomers can also be induced on activation by some external stimulus (Figure 1.2). When the isomerising ligand is small and the required rearrangements are modest, the process can occur in the solid-state and often leads to the production of a MS at low temperature. Examples of ligands known to display solid-state linkage isomerism include NO,[34, 35] NO_2,[36-38] N_2,[39] SO_2,[40] and DMSO.[41] These solid-state processes are suitable candidates for photocrystallographic investigation, as the atomic rearrangement is both large enough to produce a change in the diffraction pattern but also moderate enough that crystallinity is often maintained.
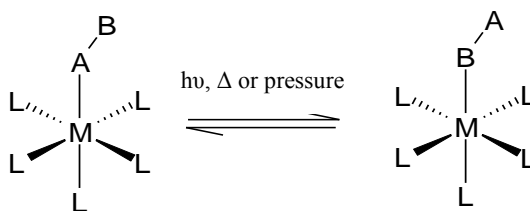
Figure 1.2: Linkage isomerism, M = metal, AB = arbitrary isomerisable ligand, L = spectator ligands

Nitrosyl Linkage Isomers

Nitric oxide is important in many biological and biochemical processes and in particular transition-metal (TM) – nitrosyl complexes have attracted attention for their ability to release NO on excitation,[42] a property that suggests their potential as NO delivery systems for medical applications. As such, greater understanding of TM – nitrosyl complexes and their behaviour on excitation is desirable, an area to which photocrystallographic research has contributed greatly.

The first observations of photoinduced metastable species in a TM – nitrosyl complex were made using Mössbauer spectroscopy on the iron(II) system sodium nitroprusside (SNP).[5] This and subsequent investigations[43, 44] struggled to provide a conclusive explanation for the nature of the two photoinduced states, MS_1 and MS_2, with theories involving charge transfer models still failing to explain the surprising stability of MS_1 and MS_2 at low temperature.[45] An improved explanation was provided in a photocrystallographic study by Coppens *et al.* in 1997, which identified that the changes were actually the result of linkage isomerism in the nitrosyl ligand (Figure 1.3).[34] A single-crystal of SNP was irradiated with 488 nm laser light at 50 K, causing 37% of the crystal to be converted from a (η^1-NO) GS to a (η^1-ON) metastable species, MS_1. The authors determined that linkage isomerisation had been induced by studying the anisotropic displacement parameters

(ADPs) for the nitrosyl group. They found that the ADPs for nitrogen and oxygen in the photoactivated data were more physically acceptable when their positions were exchanged, showing the isonitrosyl arrangement had been induced. Subsequent irradiation at $\lambda = 1064$ nm induced 10% conversion to the second ES, MS_2. The observation of new peaks in the photodifference map showed that MS_2 is also the result of linkage isomerisation, this time to a side-on bound (η^2-NO) isomer. Later spectroscopic and theoretical studies have corroborated these results and led to general acceptance of this explanation for the two metastable species.[46]
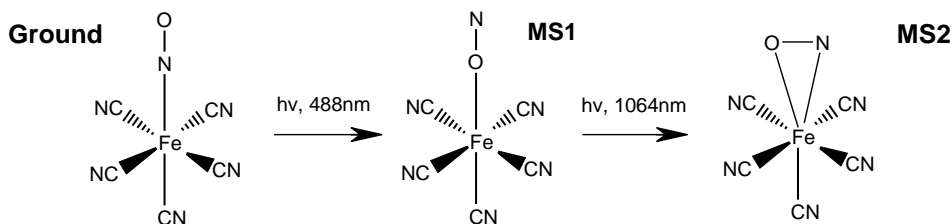
Figure 1.3: GS, MS_1 and MS_2 states of sodium nitroprusside (SNP)[47]

Coinciding with spectroscopic studies of SNP, photoinduced changes in the complex [Ni(NO)(η^1-Cp)] (Cp = cyclopentadienyl, $C_5H_5^-$) were also observed by Crichton and Rest using IR spectroscopy.[48] Later Extended X-ray Absorption Fine Structure (EXAFS) experiments suggested that excitation caused bending in the Ni–N–O moiety, reducing the initially linear Ni–N–O angle to between 133 and 160°.[49] It took photocrystallographic work with the related Cp* complex (Cp* = $C_5Me_5^-$) in 1998 to determine that the changes were actually the result of linkage isomerism.[50] The use of the methylated Cp* analogue was required to give crystals, as the Cp complex is a liquid at room temperature. 47% conversion to a (η^2-NO) isomer, MS_2, was achieved on excitation at $\lambda = 458$ nm and 25 K. The crystallographic data indicated a fully side-on bound arrangement was induced alongside a Ni–N–O angle of 92°, considerably smaller than that observed previously by EXAFS. Parallel DFT studies confirmed that MS_2 represents a minimum on the potential energy surface and also suggested the existence of an MS_1 isomer. Photocrystallographic evidence for MS_1 in this system has not been reported, although in 2000 Guida *et al.* observed bands typical of this isomer by low temperature IR spectroscopy.[51]

Several other metal – nitrosyl complexes have been investigated in photocrystallographic experiments by the Coppens group including some ruthenium and heme systems, which are described in greater detail in their own review.[35] Most recently, Cormary *et al.* have reported a study of a series of ruthenium – nitrosyl cations, investigating the influence of different counter-anions on the nitrosyl – isonitrosyl isomerisation process *via* photocrystallographic methods.[52]

Mixed Linkage Isomers: NO / NO$_2$

By including two ambientate ligands in the same complex the potential for further interesting linkage isomerism behaviour is created and, in 2005, the complex [Ru(bpy)$_2$(NO)(NO$_2$)](PF$_6$) (bpy = 2,2'-bipyridine) provided such an example for the Coppens group.[53] Exposure to Ar$^+$ laser light induced oxygen transfer between ligands, causing a direct swop of the NO and NO$_2$ sites. The authors determined that the mechanism for oxygen transfer was facilitated by linkage isomerism in both ligands, by the use of steady-state photocrystallographic methods. At 90 K, a double isomerisation was identified, with the nitrite ligand undergoing nitro – nitrito conversion and a nitrosyl – isonitrosyl conversion also occurring to yield a MS at this temperature. The authors propose that oxygen transfer proceeds *via* the atomic rearrangements and DFT calculations provide further evidence to support their existence, confirming the species to be local minima on the potential energy surface.

Sulfur Dioxide Linkage Isomers

Linkage isomerism in the sulfur dioxide group was not known until seminal IR spectroscopic studies conducted by Johnson and Dew.[54] Their work in 1979 reports the first observation of SO$_2$ photoisomerism, in a solution sample of *trans*-[Ru(NH$_3$)$_4$Cl(SO$_2$)]Cl. Irradiation with 365 nm light at 195 K induced changes in the GS v(SO$_2$) bands, from which the authors inferred that a change in bonding mode had been induced, producing an (η^2-O,SO) isomer (Figure 1.4(iii)). This ES has subsequently been assigned the label MS$_2$ in analogy with the side-on bound nitrosyl species. Further irradiation at lower temperatures produced new features, indicating another isomerisation, but the authors could not infer any further structural details from these data. Photocrystallographic evidence for MS$_2$ was obtained much later, when the single-crystal X-ray structure for the photoactivated (η^2-O,SO) isomer was obtained *via* steady-state studies with the same complex in 2002.[55]
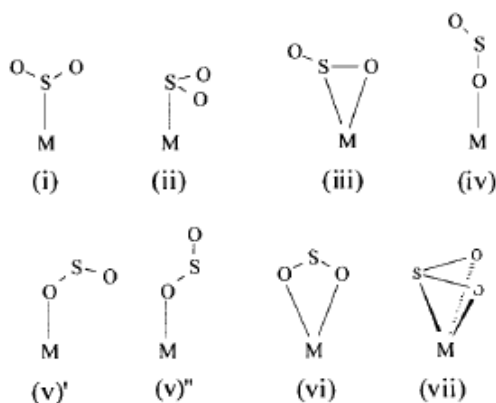
Figure 1.4: Possible coordination modes for the sulfur dioxide ligand[55]

In this initial publication crystallographic results were complimented by IR and Differential Scanning Calorimetry (DSC) experiments and, subsequently, similar investigations were also reported for a number of related ruthenium – nitrosyl species.[56] Although expected from the earlier spectroscopic investigations, crystallographic evidence for other linkage isomer modes of sulfur dioxide were not observed until a photocrystallographic study conducted by Bowes *et al.* in 2006.[40] A bent (η^1-OSO) arrangement (Figure 1.4(v)) was determined at 36% occupancy in the single-crystal, on photoactivation of the complex $[Ru(NH_3)_4(H_2O)(SO_2)][MeC_6H_4SO_3]_2$ at 13 K. This MS species was assigned the label MS_1, being comparable to the η^1-ON nitrosyl isomer. More recent photocrystallographic experiments involving sulfur dioxide isomers have continued to focus on ruthenium compounds and, despite the relatively low level of conversion observed in these species and the associated challenges, work investigating the effect of the surrounding crystalline environment on photoisomerisation[57, 58] and kinetic studies following the progress of MS decay in the crystal[59] have been reported. In another recent study, a nanomechanical change is reported to occur as a result of photoinduced (η^1-SO_2) to (η^1-OSO) conversion in the single-crystal. Linkage isomerism is thought to induce a transduction effect, leading to rotational movement further along the molecule.[60] Here, as the reaction is induced with natural light, it is suggested that the reaction could be useful in clean energy applications.

Nitro – Nitrito Linkage Isomers

Amongst some of the earliest investigations into the phenomenon of linkage isomerism, work by Jörgensen was the first to report the ambidentate nature of the nitrite group.[32] In identifying the nitro and nitrito isomers of $[Co(NH_3)_5(NO_2)]Cl_2$, Jörgensen paved the way for extensive study of such systems. Theoretically, the nitrite group may adopt up to nine different coordination modes,[61] although the most common of these are the nitro-(η^1-NO_2), *endo-* and *exo*-nitrito-(η^1-ONO) and nitrito-(η^2-O,ON) isomeric arrangements (Figures 1.5(i), (ii), (iii), (iv) respectively).
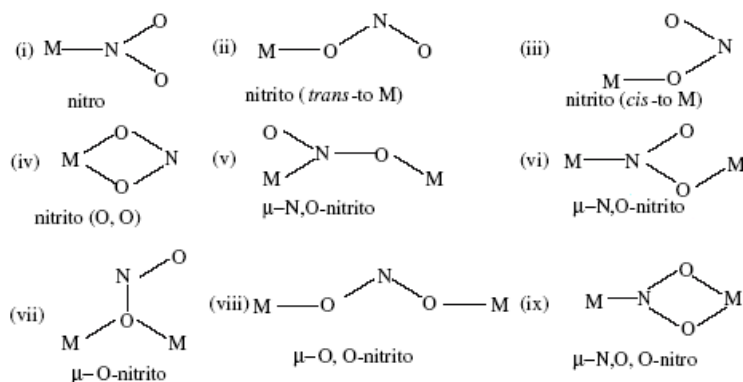
Figure 1.5: Possible binding modes for the nitrite ligand in a TM complex[61]

Photochemical Nitro – Nitrito Isomerism

Photoinduced nitro – nitrito conversion in a TM complex was first studied extensively by Adell *et al.* in 1944.[33] They determined that while the cation $[Co(NH_3)_5(NO_2)]^{2+}$ can be selectively prepared as either nitro-(η^1-NO_2) and nitrito-(η^1-ONO) isomers in solution, conversion between GS nitro-(η^1-NO_2) and ES nitrito-(η^1-ONO) forms can be photoinduced by irradiating the solution with ultraviolet (UV) light. This cobalt species has proved popular as a model system for studying the photochemical reaction, with a number of later studies also utilising this complex. Seminal work by Grenthe and Nordin investigated the mechanisms of both the photochemical nitro – nitrito and thermal nitrito – nitro back-reaction in the cation, using X-ray powder diffraction (XRPD).[38] The authors followed each reaction in real time by collecting a series of powder diffraction patterns at regular intervals. Successive patterns show a progressive shift in the relative peak positions, reflecting changes in unit cell dimensions as each reaction progresses (Figure 1.6), and from these data the authors proposed a two-step mechanism for the thermal isomerisation process. However, it is important to remember that, due to technological limitations at the time of this study, analysis of the XRPD data is mostly qualitative. Later studies into both the photochemical[62] and the thermal[63] processes using IR spectroscopy have since reported further kinetic information.
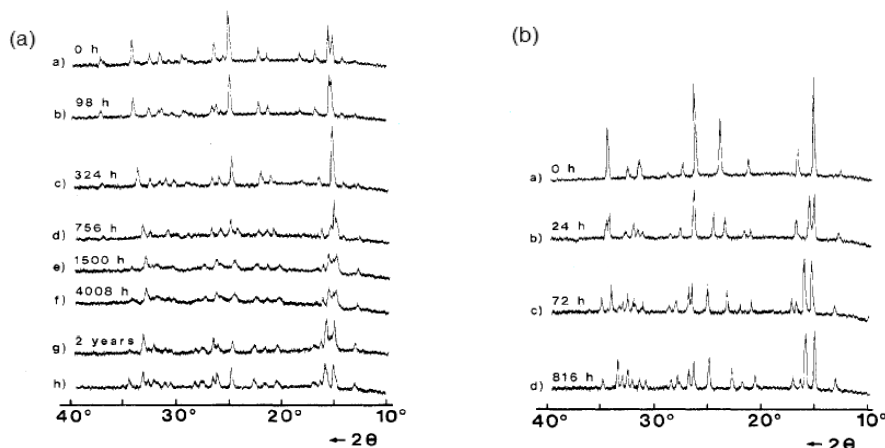
Figure 1.6: XRPD data for **(a)** thermal nitrito – nitro isomerisation and **(b)** photochemical nitro – nitrito isomerisation in the $[Co(NO_3)_5(NO_2)]^{2+}$ cation[37, 38]

A key limiting factor on the progress of photocrystallographic studies with linkage isomer species has been the relatively low level of photoactivation that can be promoted in the single-crystal. Before 2009, the maximum conversion level had not been reported to exceed 50%,[35] a problem that has implications for the potential applications of these species. High conversion rates that can be reliably controlled and repeated are ultimately desirable, in order for these long-lived photoexcited states to find application in any potential real-world technology.

As a result of investigations aimed at improving photoconversion levels, Warren *et al.* reported the first example of fully-reversible 100% nitro – nitrito conversion in the nickel – nitrite system [Ni(dppe)(NO$_2$)Cl] (dppe = 1,2-*bis*-(diphenylphosphino)ethane).[36] In choosing the complex to be investigated, the authors made use of the ideas outlined by the Topochemical Postulate and aimed to reduce steric strain in the crystal lattice by incorporating the dppe ancillary ligand. It was proposed that the crystal packing would be dominated by this bulky di-phosphine group, which is photoinert and so should remain unchanged on excitation. This should then allow isomerisation to occur in the smaller nitrite ligand with minimal change in the overall structure. Irradiation of the GS nitro-(η^1-NO$_2$) isomer with 400 nm light produced a MS, which was then studied using steady-state photocrystallographic methods. After just 20 min of irradiation a partially converted structure was determined with an already surprising 70% conversion to an *endo*-nitrito-(η^1-ONO) arrangement. Further irradiation was sufficient to complete the photoreaction, with a 100% *endo*-nitrito isomer determined after a total of 90 min UV irradiation (Figure 1.7). The reverse nitrito – nitro process occurs on warming the crystal above its MS limit, showing that conversion is fully-reversible and the whole process occurs without the loss of single-crystal integrity. Two related systems, [Ni(dppe)(NO$_2$)$_2$] and [Ni(dcpe)(NO$_2$)$_2$] (dcpe = 1,2-*bis*-(dicyclohexylphosphino)ethane) have also been shown to undergo reversible 100% conversion to a metastable nitrito-(η^1-ONO) form following irradiation with UV light.[64]
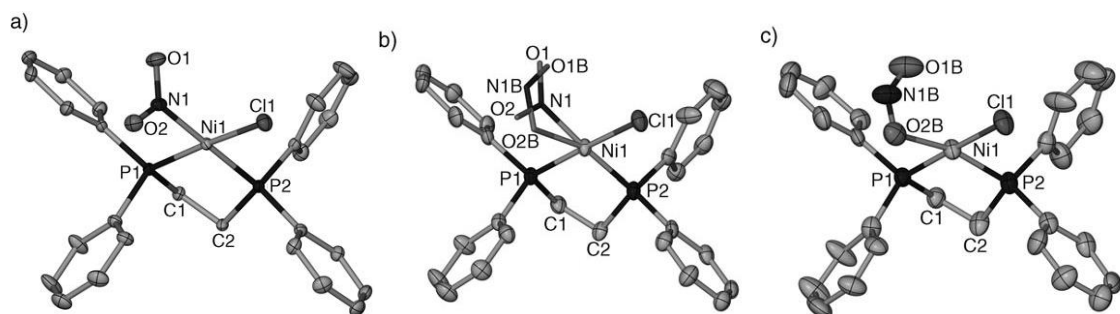
Figure 1.7: Single-crystal X-ray structures of [Ni(dppe)(NO$_2$)]Cl, **(a)** GS, **(b)** mixed isomer MS arrangement after 20 min irradiation, **(c)** 100% *endo*-nitrito MS arrangement after 90 min irradiation[36]

Subsequent studies have investigated nitro – nitrito conversion in a selection of other TM – nitrite complexes containing phosphine ancillary ligands, including palladium(II) and platinum(II) species,[65, 66] but none of these systems are reported to undergo full conversion between isomers. As such, further work is required to fully understand the requirements to repeatedly induce high levels of reversible photoconversion that can be fully controlled, before the rational design of useful linkage isomer compounds can be efficiently targeted.

Thermal Nitro – Nitrito Isomerism

Nitro – nitrito conversion can also be induced using heat as the external stimulus and studies of the thermal reaction have mainly focussed on *trans*-oriented nickel – nitrite species of the general formula $[NiL_2(NO_2)_2]$, where **L** are *N*-substituted ethylenediamine auxiliary ligands. Initial solution-state spectroscopic studies were performed by Goodgame and Hitchman in the mid-1960s, from which they suggested that the preference for a particular nitrite isomer is dictated by the steric requirements of the amine ancillary ligand.[67, 68] Using a combination of IR and electronic spectroscopic data the authors determined that red solutions containing nitro-(η^1-NO$_2$) isomers were obtained using more compact amines, while blue solutions of nitrito-(η^1-ONO) complexes were obtained with bulkier ethylenediamine co-ligands.

Later work by Laskar *et al.* in 2001 investigated thermal isomerisation in the single-crystal, using a $[NiL_2(NO_2)_2]$ system where **L** = *N,N'*-dipropylethylenediamine, a bulky amine group (Figure 1.8).[69] Brown crystals obtained from the fresh reaction mixture were found to exclusively contain the nitro-(η^1-NO$_2$) isomer, however, on aging the sample at room temperature a colour change was observed, producing green-blue single-crystals after a few days. A subsequent X-ray dataset confirmed that a single-crystal-to-single-crystal reaction had occurred, leaving one nitrito-(η^2-O,ON) ligand while the second nitrite had been released. The fact that conversion was achieved at room temperature is indicative that nitrito-(η^2-O,ON) is the more thermodynamically stable isomer, again suggesting that bulkier ancillary ligands promote nitrito coordination. The argument for steric control of the isomerisation reaction remains a popular hypothesis to explain nitro – nitrito behaviour and is echoed in the latter photochemical results discussed previously.[36] In their thermal study Laskar *et al.* state that conversion to the side-on bound nitrito isomer is accelerated with temperature, however they do not include any high-temperature crystallographic data in support of this. It was also observed that the brown nitro-(η^1-NO$_2$) isomer could be preserved when the crystals were stored below 10 °C, further suggesting thermodynamic control.
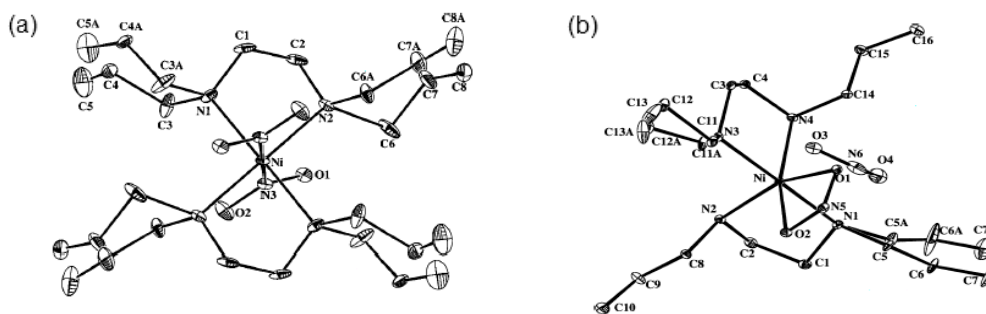
Figure 1.8: Linkage isomers of $[Ni(N,N'$-dipropylethylenediamine$)(NO_2)_2]$; (a) GS, (b) thermal ES[69]

The omission of crystallographic results obtained above room temperature in this work reflects the associated difficulty in obtaining good quality diffraction data at elevated temperature. The larger ADPs and increased levels of dynamic disorder due to greater thermal motion at higher temperatures make it more difficult to detect the small changes involved in single-crystal-to-single-crystal reactions. In addition, decomposition processes occur much faster in the crystal at elevated temperatures[12] and so it is often difficult to maintain single-crystal integrity on heating. Similar issues were also evident during studies of thermally induced nitro – nitrito isomerisation in $[Ni\{C_6H_4(NH_2)_2\}_2(NO_2)_2]$ by Sabbini and Das.[70] Single-crystals could not be obtained for the high temperature isomer, preventing crystallographic analysis and here instead the process is studied *via* a combination of IR and electronic spectroscopy. Considering these difficulties, full single-crystal structures obtained at elevated temperatures are desirable for future studies of thermal nitro – nitrito conversion.

1.3.3. Generation of Metastable State Species: Electronic and Mechanistic Studies

For ES species to be produced on the absorption of light by a complex, conversion must be initiated, in some way, by an optical electronic excitation. Investigation into the electronic structure of ML_5NO complexes has been conduced extensively by Woike *et al.*, from which they have proposed a schematic profile for the generation of nitrosyl linkage isomer species MS_1 and MS_2.[71]
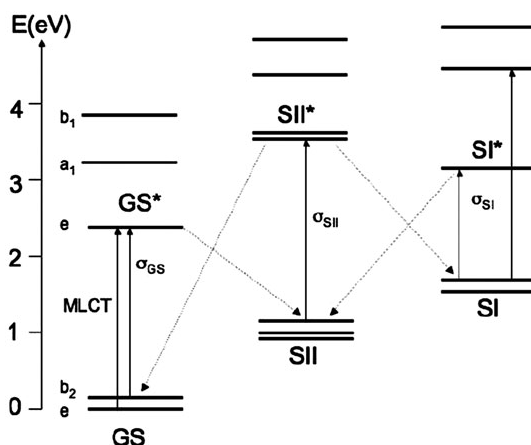
Figure 1.9: Schematic diagram outlining the general pathway to formation of metastable linkage isomer species in metal – nitrosyl species of compositon ML_5NO[71]

The proposed pathway (Figure 1.9) indicates that conversion is mainly facilitated by metal-to-ligand-charge-transfer (MLCT), induced by absorption of photons in the correct spectral range. The authors suggest that two key conditions must be fulfilled before photoisomerisation can occur. Firstly, optical excitation should induce an electronic transition between two orbitals such that the nature of the metal – nitrosyl bond is altered, *e.g.* a MLCT $d \rightarrow \pi^*(NO)$ transition.
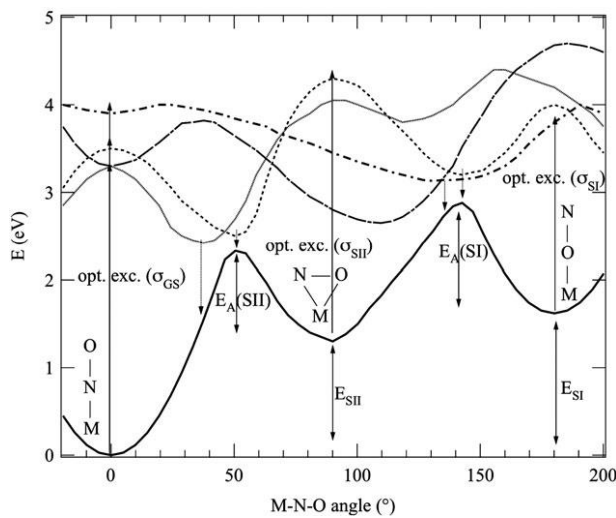
Figure 1.10: Schematic representation of potential energy surfaces calculated with respecting to changing M–N–O angle, for ground and photoexcited states of ML_5NO complexes[71]

Their second condition relates to the relative positions of maxima and minima in the potential energy surfaces for GS and MS species, which have been calculated along a reaction coordinate defined by the changing M–N–O angle (Figure 1.10). For the production of a metastable isomer, the potential ES must have a minimum point that directly overlaps a maximum point (or "saddle point") on the GS surface. Two such points are evident in Figure 1.10, corresponding to the generation of MS_1 and MS_2. The authors also discuss the importance of relative electronic populations in each state and their absorption cross sections at the excitation wavelength. For a MS to be observed these values must be such that the rate at which the electronic state is occupied exceeds the rate of depopulation, under the photoactivation conditions. This latter point provides a possible explanation for why different excitation levels can be observed for metastable linkage isomer species, as the balance between population and depopulation of an electronic state can differ between complexes. Woike *et al.* also comment that they expect the general scheme to be transferrable to other isomerisable ligands, including nitrite species, considering that extensive study has suggested that analogous excitation processes occur in all such linkage isomer systems.

Most recently, Woike *et al.* report experimental data from fs-resolved TR IR spectroscopic studies, from which mechanistic information for the initial GS to MS_2 photoconversion process is inferred.[72] The study is conducted at room temperature using single-crystals of SNP, which, the authors highlight, removes any ambiguity that might be caused by the solvent response to photoactivation. Additionally, competitive processes leading to the photorelease of NO, known to occur in SNP on room temperature excitation in solution,[73] are less prevalent in the solid-state. By following the changes in $\upsilon(NO)$ with fs time-resolution and combining these data with theoretical studies, the structural rearrangements on initial photoactivation are observed and structural information for the Fe–N–O angle is inferred by comparing the energies of ES species to those known for GS, MS_1 and MS_2 minima under steady-state conditions. On illumination an immediate response occurs, close to the limit of the experiment resolution at *ca.* 340 fs, that is attributed to the excitation from the GS to an initial higher energy state ES*. Fast relaxation of ES* then occurs on the order of 300 fs, which is assigned to the depopulation of this state towards higher vibrational modes associated with either MS_2 or GS arrangements. The authors infer that it is during this second step that an NO rotation of ~ 90º occurs, towards the geometry for MS_2. Finally, a slower decay process is then observed on a timescale of a few ps, which is attributed to the relaxation of these vibrational states towards the local minima for either MS_2 or GS isomers. These experimental data compare well to the general scheme for the photogeneration of the MS_2 species in Figures 1.9 and 1.10, helping Woike *et al.* to corroborate their previous results.

1.4.   Photocrystallographic Studies of Transient ES Species

The investigation of transient photoactivated species in single-crystals has required the development of more sophisticated X-ray diffraction methods, generating short, ultrafast X-ray pulses that may be synchronised with the output from high repetition laser sources. As the development of diffraction technologies continues and the availability of high-intensity X-rays at centralised facilities increases, the achievable resolution for TR crystallographic studies is further reduced. Previous photocrystallographic research involving transient species spans both the macromolecular and small molecule disciplines, providing a diverse range of systems for study.

1.4.1. Pump-Probe Experiments

The earliest breakthroughs in TR diffraction were made for macromolecular crystallography (MX), where fast data collection and processing procedures are developed and conducted more routinely than for small molecule methods, driven in-part by the increased likelihood of radiation damage for biological samples.[74] MX experiments make use of the Laue diffraction method, in which the crystal is retained in a single orientation while it is subject to a continuum of X-ray wavelengths from a polychromatic beam.[75] Laue methods have the advantage that far more reflections can be collected in a single image than for monochromatic data, which is beneficial to reduce the time needed for data collection. However there are other associated issues, in particular the need to deconvolute these data to determine the X-ray wavelength corresponding to each diffraction spot in the image, which dramatically complicate the data processing procedure.

The first study of a protein single-crystal at nanosecond resolution was reported by Moffat *et al.* in 1996, through the investigation of the photolysis in carbon monoxy-myoglobin (MbCO).[76] The photoactivity of the carbon monoxide complex of myoglobin is well known and the authors were able to determine structural information that complemented the wealth of ultrafast spectroscopic data already determined for the complex.[77, 78] The diffraction study was conducted using a pump-probe strategy: after a 630 nm pump pulse of laser light with a pulse width of 7.5 nm, the crystal was then probed by a synchrotron X-ray pulse after a specified time delay. The authors varied the pump-probe delay to investigate the system at six different time points between 4 ns and 1.9 μs. For data collected at the shortest delay times, between 4 ns and 1 μs, examination of photodifference maps showed regions of negative electron density at the position of CO. These confirm that the laser pulse causes photodissociation of the ligand, which then appears to migrate away from its binding position. An area of positive electron density was also located below the heme centre over this very short timeframe, indicating that the Fe atom relaxes out of the heme

plane following photolysis. Data collected at longer time delays showed these features had disappeared, suggesting later recombination of the CO ligand and re-relaxation of the system back into the MbCO arrangement, with the whole process complete within a few milliseconds. Many questions remained as to the mechanisms involved in the process and, in particular, the position of the CO ligand once dissociated from the heme centre was not clear from this initial study. Further clarification on these points was provided by a later publication.[79] By collecting further data in the 1 ns – 1 μs range and with a dramatic improvement in the signal-to-noise ratio, in 2001 the authors could confirm the presence of transient docking sites in the heme pocket for the dissociated CO ligand, helping to confirm the pathway for photolysis. In addition, kinetic data for the recombination process was determined and the motion in the rest of the myoglobin molecule was also resolved from the background noise, allowing determination of the minor structural changes resulting from relaxation of the protein. Finally, due to the wider range of probe-pulse time delays investigated, the authors were able to construct a "molecular movie" of the whole photodissociation process. These early results demonstrate the potential power of TR X-ray techniques to elucidate both mechanistic information and the three-dimensional structures of intermediates, in real time as the process occurs. The challenge of determining small structural changes from lower resolution diffraction data, and the requirement for processes to be reversible, means that finding systems suitable for TR Laue studies is difficult. While the field of TR structural biology is more established than its chemical counterpart, the number of TR studies using Laue diffraction reported is still relatively few.[74]

While the progress of TR crystallography in small molecule samples has been comparatively slower than for MX methods, TR diffraction studies using monochromatic radiation are becoming increasingly prevalent. Early work by Techert *et al.* describes the use of TR XRPD to study photoinduced changes in *N,N*-dimethylaminobenzonitrile (DMABN).[10] Pump-probe experiments proved effective to monitor relaxation in the molecule on excitation at $\lambda = 267$ nm. As relaxation happens over a few picoseconds, the synchrotron beam was divided into suitable probe pulses using a mechanical chopper and synchronised with the output from a Ti:sapphire laser for delays between –200 and 1400 ps. This set-up allowed intensity changes in selected Bragg peaks to be followed with time and refinement of these data using Rietveld methods revealed the transient structural rearrangements involved in the relaxation pathway. Although XRPD does not provide full, three-dimensional information, these experiments mark some of the earliest investigations of molecular species in the picosecond timeframe, using diffraction methods at atomic resolution.

The development of the TR method for small molecule single-crystal samples has again been pioneered by the Coppens group and has mainly focussed on the study of photoinduced triplet ES generated by pulsed laser sources. The first reported study investigates the structural distortions in the $[Pt_2(pop)_4]^{4-}$ anion (pop = pyrophosphate, $[H_2P_2O_5]^{2-}$) caused by the production of a triplet ES at $\lambda = 355$ nm. Earlier spectroscopic[80] and EXAFS[6] results had indicated that a shortening of the Pt – Pt bond was expected on excitation, with a contraction as large as 0.52 Å predicted by EXAFS. In 2002, Coppens *et al.* conducted stroboscopic photocrystallographic studies on a crystal of $(TEA)_3H[Pt_2(pop)_4]$ (TEA = tetraethylammonium) at 17 K.[21] After collection of a GS structure, a monochromatic synchrotron beam was chopped into 33 μs-width pulses at 5100 Hz and synchronised with the laser to allow the collection of four ES datasets. Data were collected using a "light-on / light-off" strategy in which the ES and GS images for the same frame are collected in succession, aiming to minimise any systematic errors that might occur due to long-term changes in the crystal on repeated exposure to the radiation. Refinement using the "response ratio" method[81, 82] indicated that only a small excitation of *ca.* 2% was achieved in the single-crystal and, due to this low conversion level, only the coordinates of the Pt atoms could be refined freely for the ES. The lighter atoms were subject to a rigid-body refinement using the GS as a reference. Despite this, the authors determine a Pt – Pt shortening of 0.28 Å along with a small, *ca.* 3° rotation of the Pt – Pt vector, in agreement with the spectroscopic results (Figure 1.11).
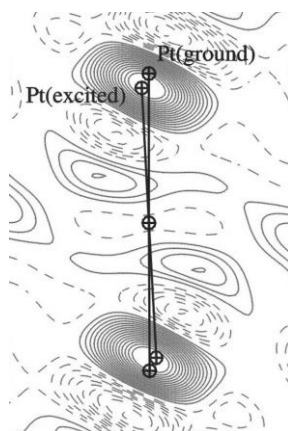
Figure 1.11: Photodifference map displaying the reduction in Pt – Pt bond distance in $[Pt_2(pop)_4]^{4-}$ on photoactivation at $\lambda = 355$ nm[21]

The Coppens group later report an even more pronounced change in metal – metal bond length for a di-rhodium species $[Rh_2(dimen)_4]^{2+}$ (dimen = 1,8-diisocyanomenthane).[31] In spectroscopic studies, Miskowski *et al.*[83] had observed photoinduced changes in the cation, which were explained as the result of excitation to a long-lived triplet ES with an expected lifetime of 11.3 μs in the single-crystal. In light of these early results, Coppens *et al.* investigated the rhodium species *via* similar pump-probe techniques to those used for the $[Pt_2(pop)_4]^{4-}$ system. At 23 K a 2.5% ES

population was refined following irradiation at $\lambda = 335$ nm. Again, the low conversion level only allowed for free refinement of the heavy atoms, with the rest of the structure subject to a rigid-body refinement. Nevertheless, the authors were able to report a Rh – Rh shortening of 0.86 Å, the largest structural change observed in an atomic resolution TR crystallography study by a considerable margin. The molecule is also observed to rotate by *ca.* 13°. Although parallel DFT calculations support the experimental result, these predict an even larger reduction than that observed experimentally and a concomitant change in Rh – Rh bond order, suggesting that steric influences from the surrounding crystalline lattice act to moderate the structural response.

Other TR studies using monochromatic X-ray sources have been reported by the Coppens group, including work with the trimeric Cu complex $\{[3,5\text{-}(CF_3)_2\text{pyrazolate}]Cu\}_3$. This photoactivated species is unusual among these metal – metal systems as excitation occurs intermolecularly between two adjacent copper trimers, rather than the intramolecular processes seen for the di-platinum and di-rhodium compounds. Excitation using 355 nm laser light induces the formation of excimer pairs of Cu units at 17 K, with a lifetime in the millisecond range.[84] A later study in 2009 reports that significant distortions are induced in the $[Cu(dmp)(dppe)]^+$ cation (dmp = 2,9-dimethyl-1,10-phenanthroline) on photoactivation, though here the changes are thought to result from charge transfer between dmp and dppe ligands.[85] The cation is observed to "flatten-out" on excitation, alongside an average Cu – P bond length increase of 0.028 Å, and these structural changes are determined from an ES population of 7 – 10 %. Coppens *et al.* have additionally studied the potential advantages of embedding photoactive Cu complexes as a guest species in supramolecular structures, investigating the changes that occur on irradiation of these systems by TR crystallography.[86] By incorporation into an inert host framework the photoactive species is appreciably diluted, with the aim that photoconversion will proceed to a higher level without the loss of crystallinity. The approach also provides an effective way to vary the surrounding environment, allowing detailed investigation of the effect this can have on photoactivation. A study conducted in 2006 investigates variation in the photoactive properties of $[Cu(dmp)_2]^+$ on embedding the cation in various anionic frameworks. It is found that the emission lifetime of the Cu species changes depending on the nature of the host framework, emphasising the important effect the surrounding environment can have on photochemical properties.[87] Compared to MS species, transient processes require faster relaxation mechanisms by which the ES can decay and, as such, it is perhaps unsurprising that the lifetime of these species is found to be so strongly dependent on the nature of the surrounding crystalline array.

1.4.2. Atomic Resolution Laue Diffraction Studies

A key issue for monochromatic TR diffraction studies is the limited X-ray intensity available, even from a synchrotron beam. Limited flux from the ultra-short monochromatic pulses used in stroboscopic experiments means that many pump-probe cycles are required to obtain sufficient X-ray intensity on the image. The sample is thus exposed to many laser pulses, causing temperature increases that can lead to increased radiation damage.[88] In 2011, the Coppens group conducted a TR study applying atomic resolution Laue diffraction to a molecular species, aiming to improve on these limitations.[22] The continuum of wavelengths used for Laue methods means that photons of a wider energy range are incident on the crystal, making more efficient use of the X-ray beam. Exposure times can also be reduced, allowing shorter time-resolution than for monochromatic studies. Laue data also contains many more reflections per frame, removing the need for repeated exposures and resulting in fewer laser pulses and less radiation damage.[88] Despite these advantages, the inaccuracies that commonly plague Laue diffraction must still be addressed, including observed changes in the spot size and shape and the λ-dependence of the data that cause additional issues during data processing.[75] In their single-pulse Laue study of Rh – Rh bond changes in $[Rh_2(\mu\text{-PNP})_2(PNP)_2]BPh_4$, (PNP $=$ *N,N*-bis-(dimethoxyphosphanyl)methanamine) Coppens *et al.* side-step some of these inaccuracies by employing their "RATIO" method.[82]
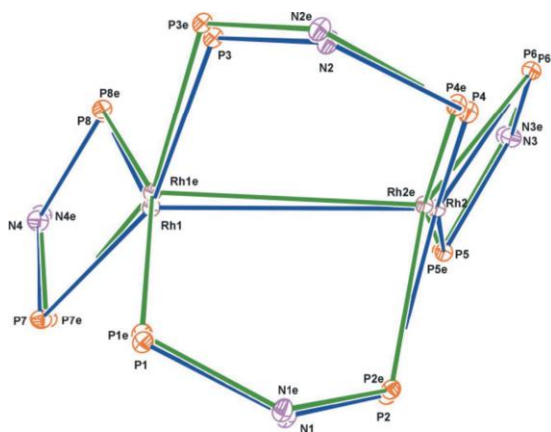
Figure 1.12: Shortening of the Rh – Rh bond on photoactivation at $\lambda = 337$ nm in $[Rh_2(\mu\text{-PNP})_2(PNP)_2]BPh_4$ and resulting rotation of the molecule[22]

The experiment was conducted at 225 K to reduce the crystal strain caused by cryo-cooling, and a crystal was subjected to a 35 ps pump pulse followed by a single 100 ps X-ray probe pulse after a delay time of 100 ps. Excitation at $\lambda = 337$ nm generates a triplet ES in the di-rhodium system,[89] which reportedly manifests itself in a Rh – Rh shortening of 0.154 Å and rotation of the molecule by *ca.* 2.5º (Figure 1.12). Calculations suggest the surrounding lattice has a constraining effect on the molecule, with gas-phase DFT predicting a much greater change while Quantum Mechanical / Molecular-Mechanics (QM/MM) calculations, taking into account a "shell" of nearest neighbour

molecules to the central cation in the form of an MM force field, give a result that quantitatively agrees with the experimental value. The shortening in $[Rh_2(\mu\text{-}PNP)_2(PNP)_2]^+$ is much less than that observed for the $[Rh_2(dimen)_4]^{2+}$ cation[31], although the authors report that experimental standard deviations for the Laue data are much improved compared to those for the previous monochromatic study. A smaller temperature increase is also found for the single-pulse experiment, indicating reduced errors and improved data quality for the TR Laue technique. This result highlights the benefits of greater flux for TR crystallographic studies and explains the current drive in producing ever-brighter X-ray sources.

1.4.3. Free-Electron Laser Experiments

As researchers aim to achieve diffraction on shorter and shorter timescales, from smaller samples and in increasingly complex experiments, it becomes necessary to have X-ray facilities capable of producing ever higher X-ray intensities. With a number of fourth generation X-FEL sources now coming on-line, access to flux levels of MGy and higher is now becoming a reality. A key problem when using such high X-ray intensities is the concomitant radiation damage: in some cases the beam can obliterate the crystal before sufficient diffraction can be measured.[90] A pioneering study by Chapman *et al.* in 2011 aimed to bypass these issues by using X-FEL radiation to "outrun" the radiation damage.[14] Previous simulations had indicated the chance for femtosecond-resolved images to be obtained before even the fastest decay processes can progress.[91] In an experiment conducted at the Linac Coherent Light Source,[92] diffraction was recorded from a liquid water jet stream of protein nanocrystals sprayed into the X-FEL beam.[93] Using this "diffract-and-destroy" approach, the authors could combine the single images from *ca.* 1500 individual nanocrystals to reconstruct the diffraction pattern of the known protein. These results compared well to synchrotron data collected on the same system, providing proof-of-concept for the X-FEL method. Since this time, X-FEL studies are becoming more prevalent with not only biological examples[94] but also studies involving inorganic species reported.[95] While such progress is exciting, X-FEL experiments still present a number of practical issues which need to be addressed by effective experimental or software corrections, with examples including sample delivery,[96] the mass production of uniform nanocrystals for analysis, evaluation and recombination of single-shot images from thousands of separate nanocrystals and the X-ray dose reproducibility between successive pulses.[97] As technologies continue to progress these issues are successively addressed and, as smaller sample sizes and ever-shorter timescales are reportedly achieved, it is expected TR methods will continue to be an important and expanding area of crystallographic research.

Chapter 2.

Aims and Objectives

Chapter 2. Aims and Objectives

The current work aims to better understand the photoactivated nitro – nitrito linkage isomerisation process that occurs in the single-crystal, aiding the rational design of new systems to undergo photoactivation at a maximum level that is both controllable and reproducible. It is hoped that the chemical and photophysical processes that influence the progress of this solid-state reaction can be identified by photocrystallographic studies of a selection of TM – nitrite complexes, containing both amine and phosphine ancillary ligands. In particular, the analysis is focussed on four key areas, namely; (i) the effect of steric influences from the crystalline lattice, (ii) electronic influences from the constituent elements and functional groups incorporated, (iii) kinetic factors that might influence both the rate of conversion and the progress of isomerisation throughout the crystal, and (iv) the light absorption properties of the sample.

For (i), the importance of steric effects induced by the surrounding crystalline array have been highlighted both in early work by Schmidt and Cohen[1-3] and in subsequent studies.[36, 52, 87, 98] In an initial attempt to alleviate the strain induced on excitation as a result of the atomic rearrangements, the TM – nitrite systems under study have been optimised by considering some simple crystal engineering principles. Continuing from previous results in the research group,[36] bulky, chelating ancillary ligands have been incorporated into the photoactive species, with the aim that these large, photoinert fragments will forcibly dictate the crystal packing arrangement. With the majority of the crystal system dominated by these photoinert species, it is hoped that conversion will occur to maximal levels in the comparatively smaller nitrite ligand without compromising single-crystal integrity. This approach builds on previous work by Ohashi *et al.* who investigated the effect of the "reaction cavity" on the progress of solid-state photoreactions. The reaction cavity concept was first outlined by Cohen as an extension to the Topochemical Postulate[99] and aims to provide a better description of the role played by immediate neighbouring moieties during solid-state conversion. The reaction cavity, or cage, is defined as the region which encapsulates the photoactive part of the system and any necessary atomic rearrangements are assumed to occur within the cavity. The cavity walls are not confined to be rigid, but any atomic movements are expected to exert pressure, leading to distortion of the cavity region. Thus, it is expected that high levels of photoactivation will most likely be achieved in systems whose reaction cavity undergoes the least change on excitation. Ohashi *et al.* have used the concept to rationalise the progress of racemisation in single-crystals of cobaltoxime compounds.[98, 100] In the current project, the reaction cavity comprises the region surrounding the photoisomerisable ligand. The choice of chelating ancillary ligands and / or counterion species has therefore also been made with the aim of

maximising the available reaction cavity, in the hope of facilitating higher photoconversion levels. In addition, it is important to consider not only the static crystalline environment that exists over an averaged timescale, but additionally the localised changes that might be induced for short periods at the point of photoactivation. It has been suggested that, at an individual point in time and space where rearrangement takes place, localised instabilities in the lattice may occur that can accommodate much larger atomic displacements than might be expected when only the static crystal is considered.[101, 102] As such, the possible dynamic behaviour of the lattice should also be taken into account when assessing the influence of steric factors on the linkage isomerisation reaction.

In investigating (ii), both charged and neutral photoactive species will be considered and the nature of the central metal atom will also be varied. Any trend in isomerisation behaviour will be analysed in reference to electronic trends expected for the species under study. In addition, the likely electronic influence of ancillary ligands on the nitro and nitrito isomers will be considered.

For (iii), while ultra-fast TR spectroscopic studies[72, 103] and computational methods[71] have been used to infer some mechanistic information for the linkage isomerisation process in nitrosyl complexes, no *in-situ* experiments following nitro – nitrito photoconversion in the single-crystal are reported in the literature. As such, novel laboratory-based experiments are developed in the current project, aiming to follow the photoreaction as it occurs. This data will then be used to infer details of the mechanism by which nitro – nitrito conversion proceeds in the single-crystal.

Finally for (iv), previous work has shown that the light absorption properties of the sample strongly influence the maximum achievable level of photoconversion in the solid-state. The optical properties of both the GS and MS arrangements,[71] and also the degree to which the excitation source can penetrate throughout the crystal, will have a marked effect on photoconversion levels. In the current work, solid-state UV/visible spectra will be collected for all species under study, and these data will be used to suggest the wavelength of radiation most likely to induce high levels of photoactivation. Additionally, the smallest possible crystal size allowed by the experimental set-up will be selected for photocrystallographic studies, helping to achieve the maximum possible penetration depth of the excitation light through the sample.[104] As a result, much of the X-ray data collected for this project is obtained using high intensity synchrotron radiation.

Chapter 3.

The X-ray Crystallographic Method

Chapter 3. The X-ray Crystallographic Method

3.1.   Fundamental Principles of Crystallography

3.1.1.   Bragg's Law

The first Nobel Prize in Physics was awarded in 1901 to Wilhelm Röntgen for his observation of "a new kind of rays" in 1895.[105] For more than 15 years after their discovery the nature of these "X-rays" was the subject of debate as to whether they consisted of waves or particles. Laue was first to correctly suggest that, should X-rays display wave-like properties, diffraction should be observed when they were passed through a crystal.[106]

A crystal is a solid consisting of a regular array of atoms, molecules or ions, extending in three dimensions to give an ordered structure. The order gives rise to sets of planes through the crystal, known as Miller planes,[107] each identified by three indices *hkl*. Incident X-rays are diffracted from the electron clouds of atoms in the crystal and, as the spacing d_{hkl} between planes is of the same order as the X-ray wavelength, the planes act as a diffraction grating to produce a regular pattern.
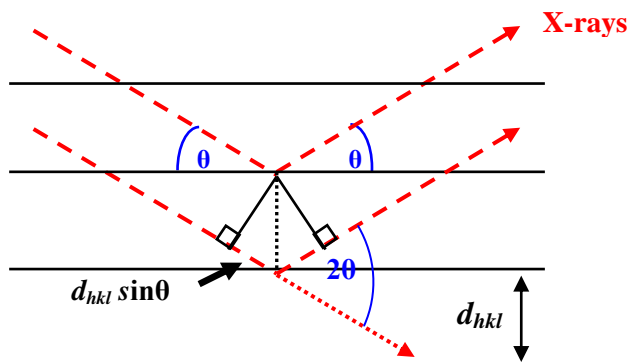
Figure 3.1: Bragg reflection of X-rays from a set of Miller planes (*hkl*) separated by a distance d_{hkl}

Although Laue received the Nobel Prize in 1914, his analysis did not fully account for the pattern seen. Later experiments by William Henry Bragg and theoretical work by his son William Lawrence led the proposal of Bragg's Law (Figure 3.1, Equation 3.1),[108, 109] which underpins modern X-ray crystallography. The Bragg's shared the Nobel Prize in 1915 for their contribution.

$$n\lambda = 2d_{hkl}\sin\theta \qquad\qquad \text{Equation 3.1}$$

3.1.2. The Diffraction Pattern and Reciprocal Space
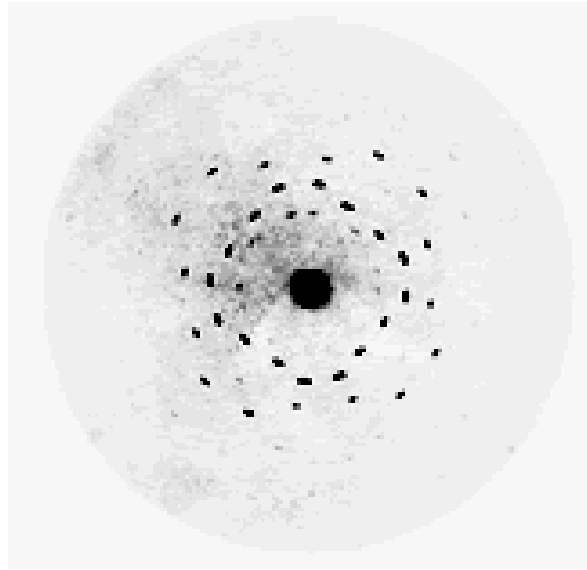
Figure 3.2: Image of the diffraction of X-rays from a crystal of ZnS, obtained in experiments by Max von Laue, Paul Knipping and Walter Friedrich[106] and reproduced by W.L Bragg[110]

The diffraction of X-rays from the periodic crystal array produces a pattern of bright spots, or Bragg reflections (Figure 3.2), at positions where multiple rays interfere constructively so that the diffraction condition in Equation 3.1 is met. The crystal, or in fact the electron density distribution of its constituent atoms, is related to its diffraction pattern by Fourier transformation. As such, the "direct lattice" of the crystal in direct space is inversely proportional to the "reciprocal lattice" of the diffraction pattern. This relationship is evident from the rearrangement of Equation 3.1 to show that d_{hkl} is inversely proportional to sin θ. Reciprocal space has dimensions of $1/d_{hkl}$ and units of Å^{-1}, with its coordinates represented as (h, k, l) or the Miller indices of the reflection. The Fourier relation between reciprocal and direct space is well understood and routinely applied to reconstruct the electron density distribution in a crystal from its diffraction pattern (§ 3.1.7).[15, 111]

3.1.3. The Unit Cell

The positions of spots in the diffraction pattern give information on the dimensions of the unit cell (Figure 3.3). As the crystal consists of a regular array of atoms or molecules, it can be described in terms of its translational symmetry. When each identical environment is replaced by a point, an infinite lattice is generated. These lattice points can be joined to give the smallest repeat unit of highest symmetry, or unit cell, which generates the full lattice when translated in three dimensions.
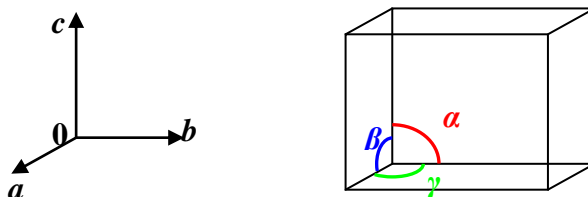
Figure 3.3: The unit cell, representing the smallest repeating unit of highest symmetry in a crystal lattice

The unit cell is defined by its three vector lengths (*a, b, c*) and three angles (*α, β, γ*). When no rotation or reflection symmetry is present the conventional unit cell is chosen so that the three lengths are as short as possible, and angles are as close to 90° as may be achieved. The presence of rotation or reflection symmetry introduces restrictions on the choice of unit cell, requiring exceptions to these two conventions. Overall, the unit cell is chosen to best represent the full symmetry of the structure, adopting the smallest and most regular shape and will always include at least one asymmetric unit. The asymmetric unit is the most basic motif from which the rest of the structure is generated and contains no internal symmetry. When all symmetry operations of the space group (see § 3.1.4) are applied to the asymmetric unit the full unit cell is produced.[15, 111]

All of the possible ways of joining lattice points to generate the unit cell give rise to four lattice types (Figure 3.4), differentiated by the number of lattice points contained within the chosen cell. In addition there are seven unit cell types, known as the seven Crystal Systems. The combination of these lattice types and Crystal Systems yields 14 unique Bravais Lattices (Table 3.1) and for any crystal structure the unit cell determined will belong to one of these 14 Bravais Lattices.[15]
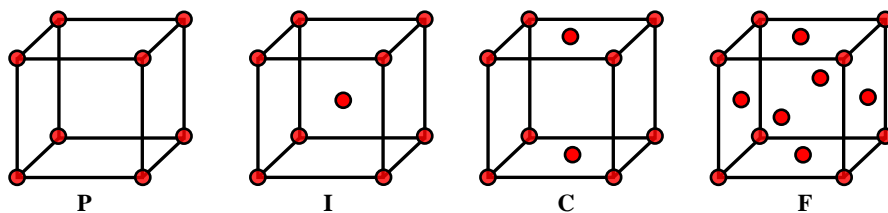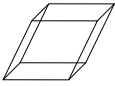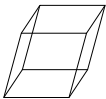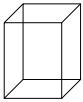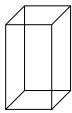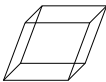
Figure 3.4: The four lattice types: **P** = primitive, **I** = body-centred, **C** = centred, **F** = face-centred

Crystal System		Axes	Angle	Symmetry	Lattice Types
Triclinic		$a \neq b \neq c$	$\alpha \neq \beta \neq \gamma \neq 90°$	None	P
Monoclinic		$a \neq b \neq c$	$\alpha = \gamma = 90°,$ $\beta \neq 90°$	2 and / or m along one axis	P, C
Orthorhombic		$a \neq b \neq c$	$\alpha = \beta = \gamma = 90°$	2 and / or m along all axes	P, I, C, F
Tetragonal		$a = b \neq c$	$\alpha = \beta = \gamma = 90°$	4 along one axis	P, I
Hexagonal		$a = b \neq c$	$\alpha = \beta = 90°,$ $\gamma = 120°$	6 along one axis	P
Trigonal		$a = b \neq c$ $(a = b = c)$	$\alpha = \beta = 90°,$ $\gamma = 120°$ $(\alpha = \beta = \gamma \neq 90°)$	3 along one axis	P, (R)
Cubic		$a = b = c$	$\alpha = \beta = \gamma = 90°$	3 in all four directions	P, I, F

3.1.4 Symmetry Elements and Space Groups

Individual asymmetric units are the initial building-blocks of the full crystal array and are related to one another by the combination of a set of symmetry operations to generate the unit cell. Crystallographic symmetry elements fall into one of two categories: non-translational or translational components. There are four different non-translational symmetry elements (Figure 3.5(a)): (i) rotation about an axis (symbol = order of rotation); (ii) inversion about a point (symbol = ○); (iii) reflection in a mirror plane (symbol = m) and (iv) rotary-inversion about an axis (symbol = order of rotation plus "bar"). In addition, there are two translational operations (Figure 3.5(b)): (i) screw axes, which comprise of a combination of a rotation followed by a translation along the direction of the rotation axis; and (ii) glide planes, comprising of a translation followed by reflection in a mirror plane parallel to the direction of the translation.

(a)

(i)

$1 = 360°$ $2 = 180°$ $4 = 90°$

(ii) (iii) (iv)

$\overline{2} = 180°$ rotary-inversion

(b)

(i) (ii)

1/2 1/2

2_1 **axis**
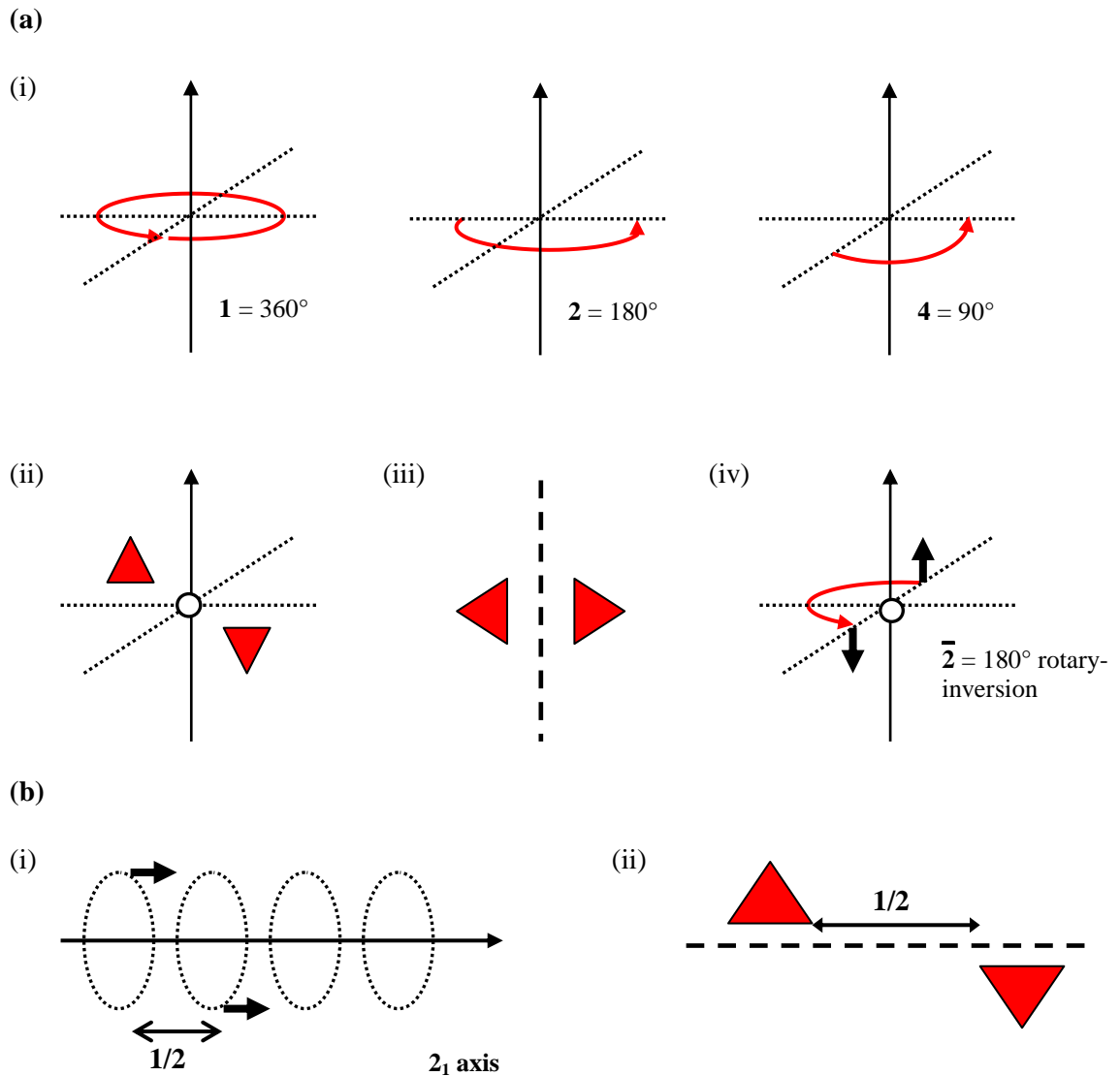
Figure 3.5: (a) Non-translational symmetry elements (i) rotation, (ii) inversion, (iii) reflection, (iv) rotary-inversion; **(b)** translational symmetry elements (i) screw-axis, (ii) glide plane

Excepting the triclinic system that imposes no restrictions, each of the Crystal Systems requires some essential symmetry that is imposed by the conditions on its unit cell dimensions (Table 3.1).

There are a limited number of ways in which these symmetry operations may be combined sensibly and the combination of the six symmetry elements with the 14 Bravais Lattice types produces a total of 230 different possible combinations. These sets are known as Space Groups and thus the Space Group symmetry describes all of the operations necessary to generate the next asymmetric unit from the first in the unit cell.[112]

3.1.5. X-ray Scattering Factors

Bragg's Law (Equation 3.1) does not provide information about reflection intensities I_{hkl}. The amount an X-ray is scattered from an atom is determined by quantum mechanics and is dependent on the number of electrons in that atom. As such the atomic scattering factor f_j, describing the ability of a neutral atom to scatter X-rays, is characteristic for each element. Scattering curves (Figure 3.6) describe the change in X-ray scattering factors as a function of diffraction angle, and show that f_j decreases strongly with increasing 2θ. This trend is the result of diffraction effects within the material itself. As the X-ray wavelength is of an order comparable to the size of the diffracting atom, interference occurs between beams scattered from different parts of that atom. According to Bragg's Law, diffracted X-rays leaving the crystal at higher 2θ angles have a longer path difference $d_{hkl}\sin\theta$ (Figure 3.1). This leads to larger phase shifts between the different beams and greater destructive interference, causing intensity to fall-off more quickly with increasing 2θ.[15]
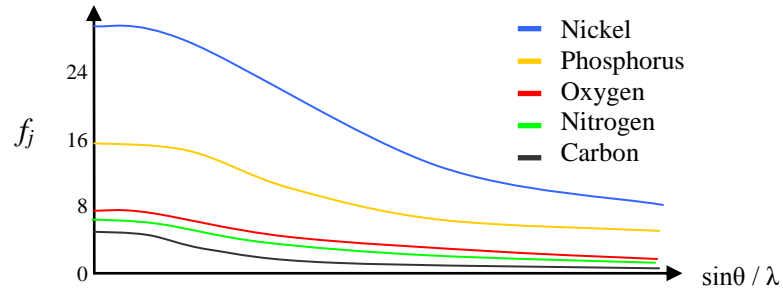
Figure 3.6: X-ray scattering factors f_j for selected elements

3.1.6. Structure Factors

While the scattering from individual atoms is weak, combined diffraction from a crystalline array of identical molecules gives a stronger signal that can be detected. The contribution of individual scattering factors f_j to the intensity of a refection is represented by the structure factor F_{hkl},

$$F_{hkl} = \sum_{j=1}^{N} f_j \exp[2\pi(hx_j + ky_j + lz_j)]$$

Equation 3.2

where F_{hkl} are complex numbers such that

$$F_{hkl} = |F_{hkl}| \exp(i\phi_{hkl})$$

Equation 3.3

Each F_{hkl} represents one set of Miller planes therefore, by Equation 3.2, every reflection contains information on the whole structure and a complete diffraction pattern is needed for a successful solution. Amplitudes $|F_{hkl}|$ are determined from experimental intensities by the relation $|F_{hkl}|^2 \propto I_{hkl}$ and the electron density image is reconstructed by reverse Fourier transform (Equation 3.4).[15]

$$\rho_{xyz} = \frac{1}{V} \sum_{hkl} \left[|F_{hkl}| \exp[i\phi(hkl)] \exp[-2\pi i(hx + ky + lz)] \right]$$

Equation 3.4

3.1.7.   The Phase Problem and Structure Solution

With knowledge of both the unit cell and structure factor amplitudes $|F_{hkl}|$ obtained from the experiment, one further piece of information is still required before Equation 3.4 can be solved. The phases φ_{hkl} of the reflections cannot be recovered from the data, leaving the crystallographer with an incomplete set of information. This dilemma is known as the phase problem and various methods have been developed and are implemented routinely to determine these missing phases.

Patterson Synthesis

Patterson methods make use of the complex nature of structure factors F_{hkl} to determine phases. Each F_{hkl} in Equation 3.4 is replaced by the product of that value with its complex conjugate F^*_{hkl}

$$F_{hkl} \cdot F^*_{hkl} = \left|F_{hkl}\right|^2 \qquad\qquad \text{Equation 3.5}$$

removing the phase dependence in Equation 3.4. The reverse Fourier transform now yields a real number and the result is Patterson map rather than an electron density map, whose maxima relate not to the positions of individual atoms but to vectors between atom pairs (Equation 3.6).

$$P_{uvw} = \frac{1}{V} \sum_{hkl} \left[\left|F_{hkl}\right|^2 \cos[2\pi(hu + kv + lw)]\right] \qquad\qquad \text{Equation 3.6}$$

All Patterson maps show inversion symmetry, regardless of the crystal symmetry, as Equation 3.6 dictates that two equal and opposite vectors are defined for each atom pair. Patterson synthesis also includes "self-vectors", *i.e.* a peak is created for the vector of every atom with itself that necessarily has a value of zero. These all occur at the origin and so the largest peak in a Patterson map occurs at (0, 0, 0). As vector peak size is proportional to the product of the atomic numbers Z for the two atoms, the next largest maxima correspond to vectors between the heaviest atoms and their positions are located first. Patterson methods are therefore most often applied to structures in which some heavier elements are expected. Once these are located the structure is refined, allowing the lighter atoms positions to be determined. Patterson methods are also effective to solve structures known to consist mainly of rigid fragments, *e.g.* fused ring systems. Such moieties create characteristic vector patterns in the map and so are identified more easily.[15]

Direct Methods

While Patterson synthesis requires some prior knowledge of the structure, other common solution techniques, known as direct methods, aim to determine phases without any information on the expected crystal composition. Direct methods make use of known physical properties of electron density and these are applied as mathematical constraints on the electron density function ρ_{xyz} and hence, by Equation 3.4, on the phases φ_{hkl} to be determined. Among the most important of these

properties is the fact that the electron density peaks seen are always discrete. This leads to the assumption that the crystal contains discrete atoms, removing the need to consider atom shapes and allowing the calculation of normalised structure factors E_{hkl}. A second important physical property of electron density is that it can never be negative, allowing the constraint $\rho_{xyz} \geq 0$ to be applied. Carrying this condition through to the normalised E_{hkl} allows the derivation of Karle-Hauptman inequalities, which essentially can restrict the allowed values for φ_{hkl} in terms of the $|E_{hkl}|$ values obtained from experimental intensities. Both these inequality relationships and a further assumption that the distribution of atoms should be random throughout the structure suggest a probabilistic approach to the phase problem and allow phase relationships to be created. These identify sets of three structure factors, *e.g.* $E(h)$, $E(k)$ and $E(h-k)$, whose related phases $\varphi(h)$, $\varphi(k)$ and $\varphi(h-k)$ should satisfy the probability that

$$\phi(h) \approx \phi(h-k) + \phi(k)$$

Equation 3.7

It can be shown that these relationships have a higher probability of being satisfied when large $|E_{hkl}|$ are used. Once identified, these sets of strong reflections are recorded for use later in the phasing process. An additional requirement is that the value of $\int \rho^3_{xyz} \, dV$ is always maximised, and the consideration of this constraint leads to the derivation of the tangent formula

$$\tan(\phi(h)) \approx \frac{\sum_k |E(k)E(h-k)| \sin(\phi(k) + \phi(h-k))}{\sum_k |E(k)E(h-k)| \cos(\phi(k) + \phi(h-k))}$$

Equation 3.8

An alternative approach was suggested by Sayre in 1952 and relies on an assumption that, in many crystals and particularly organic compounds, the constituent atoms are essentially similar. The analysis is then based on a hypothetical situation in which all of the atoms are equal and isotropic and the electron density is squared.[113] It can be shown that both methods lead to a derivation of the tangent formula, which is then used as the basis for an iterative process by which the correct phases are identified. Although the reflections whose phases are to be determined can be chosen in reference to the formulae discussed previously, initial phases must be approximated and are often assigned random starting values. As the iterative process is conducted figures of merit are calculated from the phase sets output at each stage, which indicate the quality of the solution. The best phases determined at the end of process are then inserted into Equation 3.4 to allow the creation of electron density maps from which the crystal structure may be solved.[15]

Other solution methods, for example Charge Flipping,[114] make use of continued improvements in computing power and have become popular alternatives to these more established methods.

3.1.8. Structure Refinement

The output from the structure solution is a reconstruction of the average electron density, which is a continuous function ρ_{xyz}. Most structure solution programs will, if given some prior knowledge of the expected crystal composition, output an approximate trial structure in which some atomic positions have been assigned. However, this structure is often incomplete. Although the term "crystal structure" is often used here, this trial structure is in reality a parameterised model, constructed to best represent the calculated electron density. The use of a model is convenient, as it allows the consideration of discrete atoms rather than continuous electron density. The refinement process, then, is the method by which the parameters of the trial model are optimised to achieve the best possible fit between the observed and calculated diffraction patterns.

The "refinable parameters" in the model are values that can be adjusted to improve the fit, with the most important of these including: positional coordinates of the atoms *xyz*; isotopic and anisotropic displacement parameters U_{ij}; site occupancy factors for the atoms; and the overall scale factor, which acts to bring the observed and calculated intensities of the reflections onto a common scale.

Refinement by Least Squares Fitting

Crystallographic refinements of molecular species are commonly conducted using "least squares" methods. These involve minimisation of the function

$$M = \sum_n w(Y_0 - Y_C)^2$$

Equation 3.9

where Y_0 = the strength of an observed reflection (either in terms of F_0, F_0^2 or I), Y_C = the calculated value of that reflection based on the current model (either in terms of F_C or F_C^2) and w = a weight, assigned to reflect the importance of that reflection on the overall sum. The sum is then taken over all measured reflections in the experiment *n*. Minimising the value of M should lead to optimal values of the parameters and their standard deviations σ, for that structural model.

In considering the values for Y_0, it is possible to refine the model against either F_0, F_0^2 or I experimental values, and each approach has both its merits and weaknesses.[15] While there is still much debate over which is more advantageous, the use of F_0^2 values is marginally more common.

In terms of the weights *w*, it can be shown for an ideal situation that the most suitable parameters are obtained when *w* is inversely proportional to the variance on the observed value, where the variance is defined as σ^2.[15] However, practically it is difficult to be certain of the errors in the

observed X-ray data and, as such, crystallographic weights are generally chosen to ensure there is no appreciable trend in the value of *M*, which could signify systematic errors.

As the refinement procedure aims towards determining optimal parameter values, it can be useful to either increase or decrease the number of refinable parameters in order to improve the fit, particularly when dealing with poorer quality data. This can be achieved by the use of restraints and constraints, which impose mathematical conditions on parts of the model leading to a change in the number of parameters that need to be freely refined. A restraint is a non-rigid condition that generally arises from considering some prior knowledge of a chemical or physical property, which is required by the expected structure. An example of such a condition might be to restrict the value of one or several bond lengths or angles, to be similar to a value usually observed in similar types of compound. As such, restraints are treated in the refinement as if they were an extra experimental observation, meaning their inclusion increases the number of parameters that must be freely refined. By contrast, a constraint is a rigid requirement on the model that might arise from consideration of the chemical or physical requirements of the known structure, for example the atomic positions of hydrogen atoms in a model are often constrained relative to the position of the carbon atom to which they are attached (known as a "riding model"). Constraints can also be generated as a result of the space group symmetry, for example an atom situated on a special position will necessarily require restrictions on its xyz coordinates, U_{ij} values and site occupancy factor. Constraints are therefore implemented in the refinement as exact mathematical relationships and, as such, act to reduce the number of parameters to be freely refined.

In addition to the parameters highlighted above, other values may also be varied during refinement and, for disordered structures, these include free variables. In some structures there may be positional disorder indicating that, on average over the whole crystal, there are two or more possible sites where an atom has been observed. The electron density distribution will reflect this disorder and, as such, both positions must be modelled effectively. The occupancy factor for the disordered atom will be < 1 at each position, with the sum of the occupancies at all of the disorder sites totalling to unity. The relative occupancies of the sites can be determined during refinement. The fractional site occupancy for the disordered atom is assigned a free variable, beginning as a random value between 0 and 1, which is then refined to fit the available electron density at each disordered position. As such, the introduction of free variables again adds to the number of parameters that must be freely refined.

The Resultant R-Factor

As is implicit from the above discussion, least squares refinement is an iterative process that should proceed towards convergence as the fit between the experimental and calculated diffraction patterns improves. During refinement, residual values are determined that can be used to assess how well the model fits to the observed data. The "conventional R-factor" is calculated during each cycle of refinement and is defined as

$$R = \frac{\sum |F_0 - F_C|}{\sum |F_0|}$$
Equation 3.10

and provides a assessment of the agreement between the current calculated structure factor values and those obtained experimentally. The final R-factor, obtained from the very last cycle of refinement, is therefore commonly used to assess the quality of the structural model proposed. Other residual factors are additionally quoted during refinement, and among these the weighted R-factor wR, defined as

$$wR = \sqrt{\frac{\sum |w||Y_0 - Y_C|^2}{\sum |wY_0^2|}}$$
Equation 3.11

is frequently used to monitor how well a refinement is progressing. Although R-factors are often treated as a measure of the suitability of a particular model, this should be done with care. The values of these residual factors are strongly dependent on the reflections made available for refinement and, as such, their values can be adjusted quite easily by selectively omitting some reflections, in particular those which show poor agreement between F_0 and F_C.

The Final Structure?

As the refinement converges on a final model, there are a few key values that are commonly used as indicators of a "good structure". As previously discussed, the resultant R-factor is most often reviewed and, for the crystal structures of small, molecular species, a value of $R < 0.05$ is typically considered acceptable. The σ values on the refined parameters of the model are also considered, with small values suggesting a good fit between the model and experimental data. Additionally, a Fourier electron density difference map can be constructed between the modelled and experimental density. Positive peaks in this map indicate the presence of residual, unmodelled electron density and, usually, when the highest residual peaks are smaller than those expected for a hydrogen atom the model is considered to be a good representation of the calculated electron density. Finally, there must be good completeness of the data collected, that is, the diffraction data must cover at least the unique region of reciprocal space required to model the structure.

3.2.   Experimental Outlines

3.2.1.   Single Crystal X-ray Diffraction

The typical set-up for a single crystal X-ray diffraction experiment, using a four-circle laboratory diffractometer equipped with a CCD area detector, is shown in Figure 3.7.
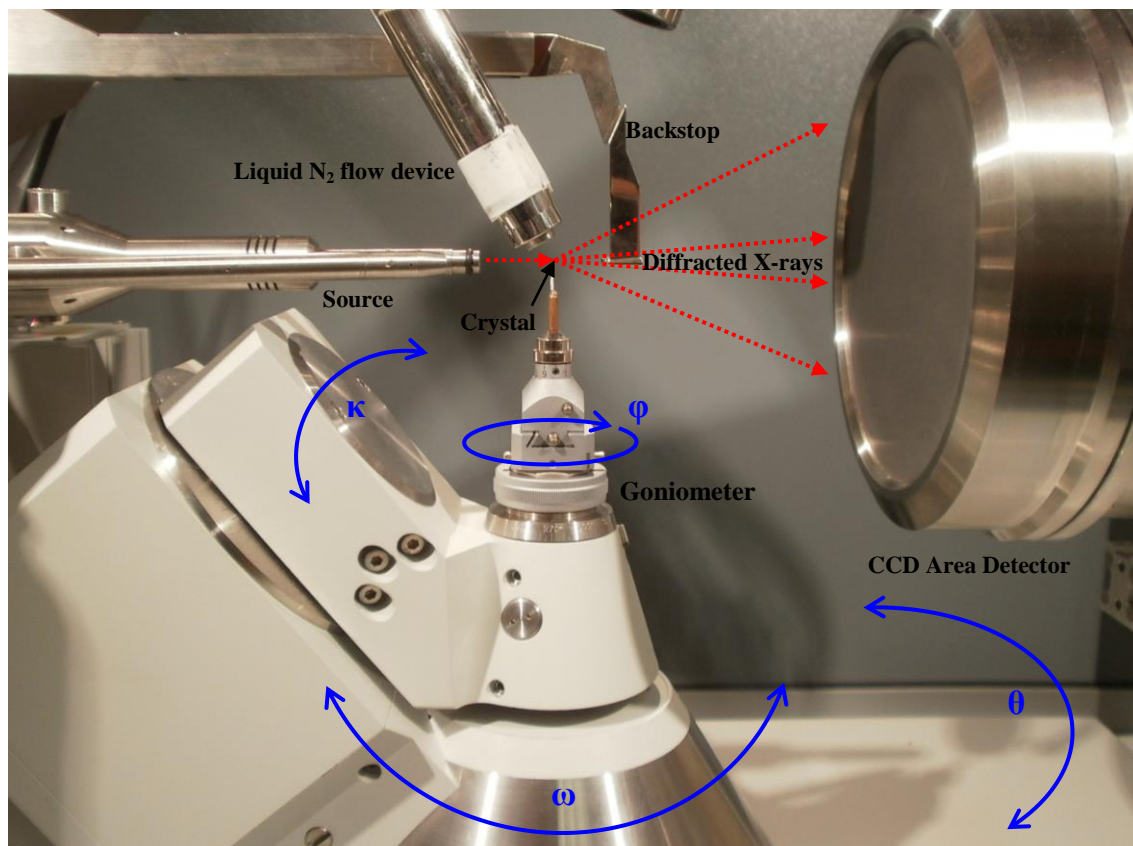
Figure 3.7: Typical laboratory experimental set-up for a single crystal X-ray diffraction experiment

A single crystal is chosen by polarised light microscopy and mounted in paratone oil on a glass fibre attached to the goniometer head. The goniometer is rotated about three axes (ω, κ, φ) in the experiment to ensure that every unique reflection is collected, so the crystal is first carefully centred to ensure that it does not precess out of X-ray beam at any of the positions adopted during data collection. The crystal position is also aligned with a liquid nitrogen flow device, allowing the sample temperature to be controlled throughout the experiment. Laboratory data collections are routinely run at low temperature,[12] with typical values between 150 and 100 K. The wavelength and therefore energy of the X-rays is dependent on the source and, for the sealed-tube systems most commonly found in laboratory set-ups, monochromatic X-ray sources typically include either a copper target (Cu K$_\alpha$, λ = 1.54184 Å) or molybdenum (Mo K$_\alpha$, λ = 0.71073 Å). The most suitable wavelength is chosen by considering both the experiment and the type of sample

to be studied. Typically, X-rays generated from the source first travel through a monochromator crystal, to select the appropriate single wavelength, before being passed along a collimator to ensure they remain tightly focussed until they are incident on the crystal. When the X-rays reach the crystal, some beams are diffracted and these are collected by the CCD area detector. Those X-rays that pass directly through the sample without diffraction are absorbed by the backstop. The detector moves about its own rotation axis (θ) to different collection positions during the experiment. In a typical CCD detector the incoming X-ray first passes through a protective beryllium layer and interacts with a phosphor, converting it into a light signal that is then relayed to the CCD chip, usually *via* a fibre optic taper. The taper reduces the light image to be the same size as the CCD chip, which is a small array of light-sensitive pixels. Once the pattern of light is recorded on the CCD, the chip must then be read-out, *i.e.* charges stored in the single pixels must be sequentially transferred to the controller and the analogue CCD response converted to a digital signal. Read-out typically occurs at the corners of the chip and must be achieved one pixel at a time to preserve the information. When a digital signal is obtained the data can then be relayed to the controlling PC to be processed.

The diffraction images are recreated in the software and are first searched using a peak hunting module to establish the location of all the Bragg reflections. The peaks are next indexed, a process by which the Miller indices relating to each reflection are determined and a list generated from which the unit cell can be determined. An integration process is then initiated, during which the total pixel counts associated with each reflection are totalled to give the recorded intensity, I_{hkl}. Structure Factor (F_{hkl}) calculation, phasing and refinement may then be carried out as described in detail in § 3.1, allowing Equation 3.4 to be satisfied and the structure to be solved.

In the current project, laboratory single-crystal X-ray experiments were conducted using an Agilent Technologies[115] Gemini A Ultra Diffractometer equipped with an Atlas CCD area detector. The sample temperature was controlled using an Oxford Instruments CryojetXL liquid nitrogen flow device. Data collection, indexing and integration procedures were carried out using the Agilent Technologies software CrysAlis Pro.[116] Experiments conducted on Beamline 11.3.1 at the Advanced Light Source, Berkeley,[117] were conducted using a Bruker AXS[118] D8 diffractometer equipped with an Apex II CCD area detector. The sample temperature was controlled using an Oxford Cryosystems[119] Cryostream Plus and data collection, indexing and integration procedures completed using Bruker software Apex II.

3.2.2. Steady-State Photocrystallographic Methods

Steady-state photocrystallographic methods are routinely used in the current project to study metastable photoactivated species. Figure 3.8 shows a schematic representation of the timing sequence for sample excitation, X-ray exposure and light irradiation in a steady-state experiment.
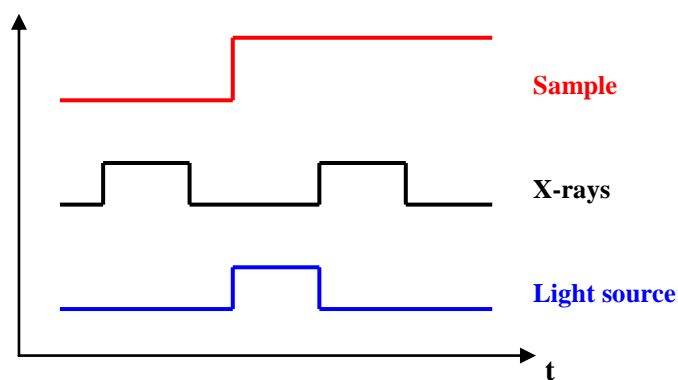
Figure 3.8: Schematic outline of the timing sequence for steady-state photocrystallographic studies

In the current project, a typical steady-state diffraction experiment is conducted as follows.

(i) A high quality GS dataset is first obtained, at low temperature and in the absence of any light, to act as a reference to any photoactivated data later collected.

(ii) The same crystal is then irradiated *in-situ* on the diffractometer for a specified time period, while the crystal is held at 100 K, to induce a photoactivated MS.

(iii) As the MS should be long lived when thermally trapped at low temperature, the irradiation is then switched off and a second identical X-ray dataset obtained in the absence of further light.

(iv) The GS structure model is then imported into the photoactivated data and a Fourier electron density difference map, or "photodifference map", is generated. This map is then examined for any significant residual electron density in the region of the isomerising ligand, corresponding to the production of an MS arrangement.

(v) Once the MS is identified, the sample is irradiated further and repeat datasets collected to determine whether further excitation can be induced. This process is continued until no further change is observed, indicating that a photostationary state has been achieved.

(vi) The crystal is then held at 100 K in the dark for a further period, after which time a repeat dataset is obtained to confirm that the species is truly metastable.

(vii) Finally, variable temperature parametric studies are conducted to determine the temperature range over which the ES is metastable. In these experiments the crystal is slowly warmed in stages and identical datasets collected at regular intervals to determine the nitro – nitrito ratio.

While many studies use laser light to induce a MS in the single crystal,[34, 120] all of the metastable species investigated in the current report are activated using light-emitting diodes (LEDs). LEDs provide a low-cost alternative to lasers and, for single crystal samples, the lower intensity light is also beneficial as it is less likely to cause significant radiation damage. Lower intensity LED light is also unlikely to induce non-linear processes, such as two-photon excitation, that can lead to ambiguity. LEDs allow more flexibility and control over illumination as both the number of LEDs and dominant wavelength are easily varied. LED wavelengths of 500 nm (1500 mcd, 3.5 V, 20 mA), 470 nm (700 mcd, 3.0 V, 30 mA) and 400 nm (350 mcd, 3.8 V, 30 mA) are used in the current project.
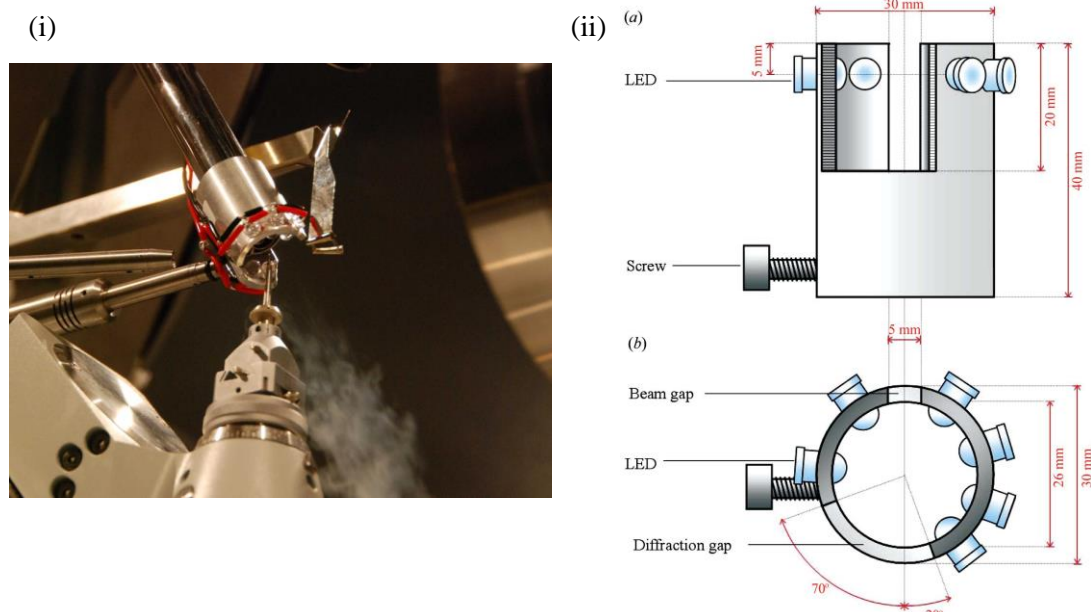
Figure 3.9: LED ring for single crystal photocrystallographic experiments: **(i)** mounted on the neck of the nitrogen flow device, **(ii)** schematic of the LED ring design, (a) side view, (b) aerial view[121]

Uniform irradiation of the crystal is important to ensure that maximum excitation is reached and in the current project this is achieved with specifically designed equipment. A LED ring array (Figure 3.9) is mounted on the neck of the nitrogen flow device and positions six LEDs *ca.* 1 cm from the sample in a uniform circle.[121] This arrangement provides uniform illumination over 270°, which is an advantage over laser excitation as laser light is highly focussed and so necessarily delivered to a single point. The LED ring also allows continuous irradiation during an X-ray data collection, with gaps for both incident and diffracted X-ray beams incorporated into the design.

The data collected by all of the photocrystallographic techniques described here are solved using the procedures outlined in § 3.1. Photoactivated species are treated as a disorder model, allowing the linkage isomer occupancies to be refined freely using standard free variables.

3.2.3. Pseudo-Steady-State Photocrystallographic Methods

Photoactivated species with minute – millisecond lifetimes can be made to adopt a pseudo-steady-state arrangement by continuous optical pumping of the sample during data collection (Figure 3.10). To study these ES, pseudo-steady-state diffraction methods are required that achieve continuous illumination of the crystal while ensuring minimal interference with the X-ray experiment.
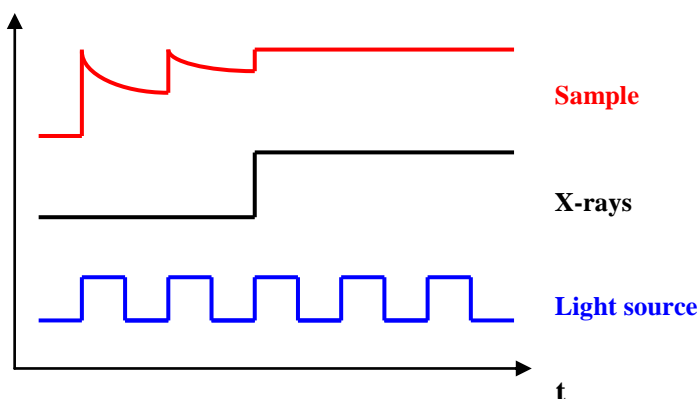
Figure 3.10: Schematic outline of the timing sequence for pseudo steady-state photocrystallographic studies

Pseudo-steady-state experiments at Diamond Light Source

For pseudo-steady-state studies conducted in Experimental Hutch 2 (EH2) on Beamline I19 at Diamond Light Source,[122] continuous illumination was achieved using a Vibrant OPO Nd:YAG laser, pumped at 355 nm and tuned to 500 nm. The pulsed system operates at 10 Hz with a pulse width of 6 – 7 ns, which is effectively a continuous source in the timeframe of these experiments. The laser was first attenuated by an aperture, producing an output of 0.5 mJ at this point, before being guided to the diffractometer *via* a fibre optic cable. The output from the fibre optic cable is then refocused at the crystal position by a lens. The sample temperature was controlled with an Oxford Cryosystems Cobra cryostream and data were collected and processed with CrysAlis Pro.

Laboratory-based pseudo-steady-state experiments

Pseudo-steady-state experiments were also conducted using the laboratory photocrystallographic set-up. As shown by Figure 3.9, continuous illumination of the crystal during data collection is facilitated by the LED ring, with minor restrictions imposed on the normal diffractometer limits. The detector position is confined to $\theta = -25°$ to eliminate any shielding on the image from the LED ring. Restrictions on the κ and ω ranges of $-55° < \kappa < 60°$ and $-60° < \omega < 10°$ respectively are additionally required to ensure that the goniometer does not collide with the LED ring casing. Despite these limitations, a hemisphere of complete data can be collected without interference.

3.2.4. Test Pump-Probe Photocrystallographic Experiments on Beamline I19

The experimental set-up for test pump-probe experiments conducted in EH2 on Beamline I19, Diamond Light Source, was similar to that described for pseudo-steady-state experiments with laser pump pulses obtained using the same Vibrant OPO laser set-up described in § 3.2.3. X-ray probe pulses were generated using a dual-wheel mechanical chopper,[123] and were synchronised to the laser pulse train. The pump-probe cycle was governed by the repetition rate of the laser, which could be operated at 10 Hz. The delay time between laser pump and X-ray probe pulses could therefore be varied in the range of 0 – 100 ms and the shortest achievable time resolution was limited to 1 ms. Cooling was again achieved using an Oxford Cryosystems Cobra cryostream and TR crystallographic data were again collected and processed using CrysAlis Pro.

Chapter 4.

Steady-State Studies of Group 10 Complexes with Tridentate Amine Ligands

Chapter 4. Steady-State Studies of Group 10 Complexes with Tridentate Amine Ligands

The literature discussed in § 1.3.3 highlights a particular interest in nickel systems of the general formula [$NiL_2(NO_2)$], where **L** are chelating phosphine or amine groups. In particular several complexes containing amine ancillary ligands display interesting linkage isomeric behaviour, both in their crystallisation preference[124] and on exposure to both light and heat.[69, 125]

A search of the Cambridge Structural Database[126] (CSD) was conducted to ascertain the scope of crystallographic studies involving such species, not limited to the topic of linkage isomerism. A simple search fragment was used containing one nickel atom surrounded by two nitrogen donors and one nitrite group (Figure 4.1), with no additional geometric conditions imposed. The search resulted in 38 hits, of which 28 were unique structures (Search 1). Of these 28 compounds all contain an octahedral nickel centre, four are cationic and the rest are neutral species. The majority of these contain bidentate amine ligands, with five tetradentate and just three tridentate species returned. With a very few exceptions,[124] most bidentate systems display *trans* geometry, commonly containing two *trans*-oriented nitro-(η^1-NO_2) ligands, and several photocrystallographic studies involving amine derivatives have focussed on systems of this type (§ 1.3.3). By contrast the tetra- and tridentate amine species display more variation in nitrite coordination mode on crystallisation, with nitro-(η^1-NO_2), *exo*-nitrito-(η^1-ONO) and nitrito-(η^2-O,ON) ligands all being observed. However, it is of note that the *endo*-nitrito-(η^1-ONO) isomer is not found to crystallise preferentially in any of these structures.
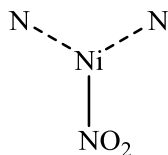
Figure 4.1: Fragment used to conduct Search 1 of the Cambridge Structural Database

In light of these observations, a systematic study of nitrite systems containing tridentate amine ancillary ligands appears appropriate, given their potential to display interesting linkage isomerism and the relatively small number of such systems investigated to date. Although the bulk of this work focuses on nickel – nitrite complexes (§ 4.2), other Group 10 elements are also included to assess the change in isomerisation behaviour on incorporating heavier transition-metal centres.

4.1.   *N,N,N'N'*-tetraethyldiethylenetriamine Complexes

4.1.1.   Complex [1]: Dinitro-(*N,N,N',N'*-tetraethyldiethylenetriamine)nickel(II)

Complex [1] was synthesised *via* the procedure outlined in § 9.2.1 and green, plate-like crystals were obtained *via* slow evaporation from a methanolic solution in the absence of light. A single-crystal was mounted with minimal light exposure and flash cooled to 100 K, before a standard single-crystal X-ray data collection was conducted as outlined in § 3.2.1.

Crystal Structure and Bonding

The nickel complex crystallises in the orthorhombic space group $P2_12_12_1$ with the metal adopting pseudo-octahedral geometry, this distortion likely due to the "bite" of the chelating amine ancillary ligand. This tridentate ligand is bound in a meridional arrangement, causing the nitrite groups to occupy sites approximately *trans* to one another. One nitrite ligand is also chelating, adopting a stable nitrito-(η^2-O,ON) configuration. The second nitrite is monodentate and is disordered, producing a "mixed" structure containing two linkage isomers. The major nitro-(η^1-NO$_2$) component is at 78% occupancy in this initial flash cooled structure, with the remaining 22% bound as *endo*-nitrito-(η^1-ONO) (Figure 4.2). Crystal data for [1] are displayed in Table 4.1.
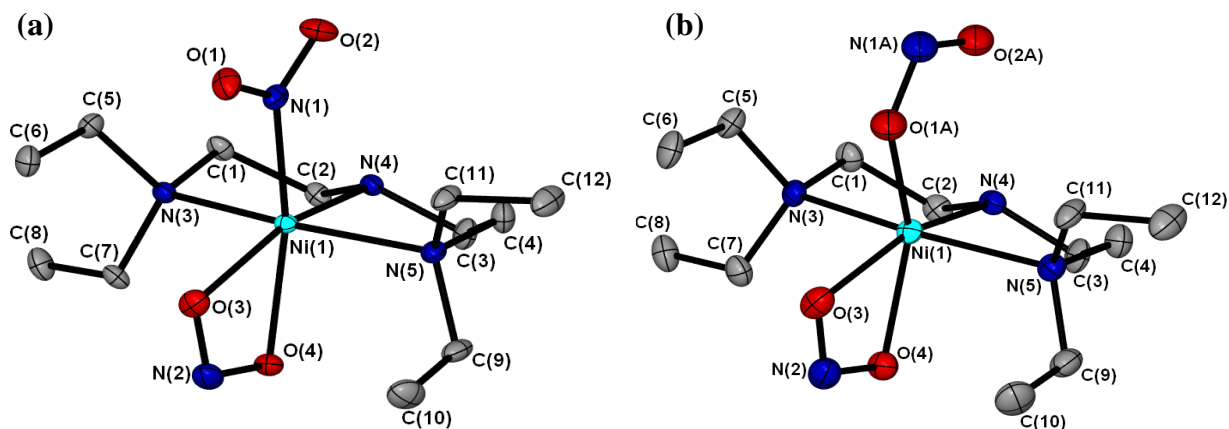
Figure 4.2: Single-crystal X-ray structure of complex [1] showing the atomic arrangement for the two linkage isomers present in the flash-cooled crystal; **(a)** nitro-(η^1-NO$_2$) = 78% occupancy, **(b)** *endo*-nitrito-(η^1-ONO) = 22% occupancy. Ellipsoids shown at 50% probability and hydrogen atoms removed for clarity
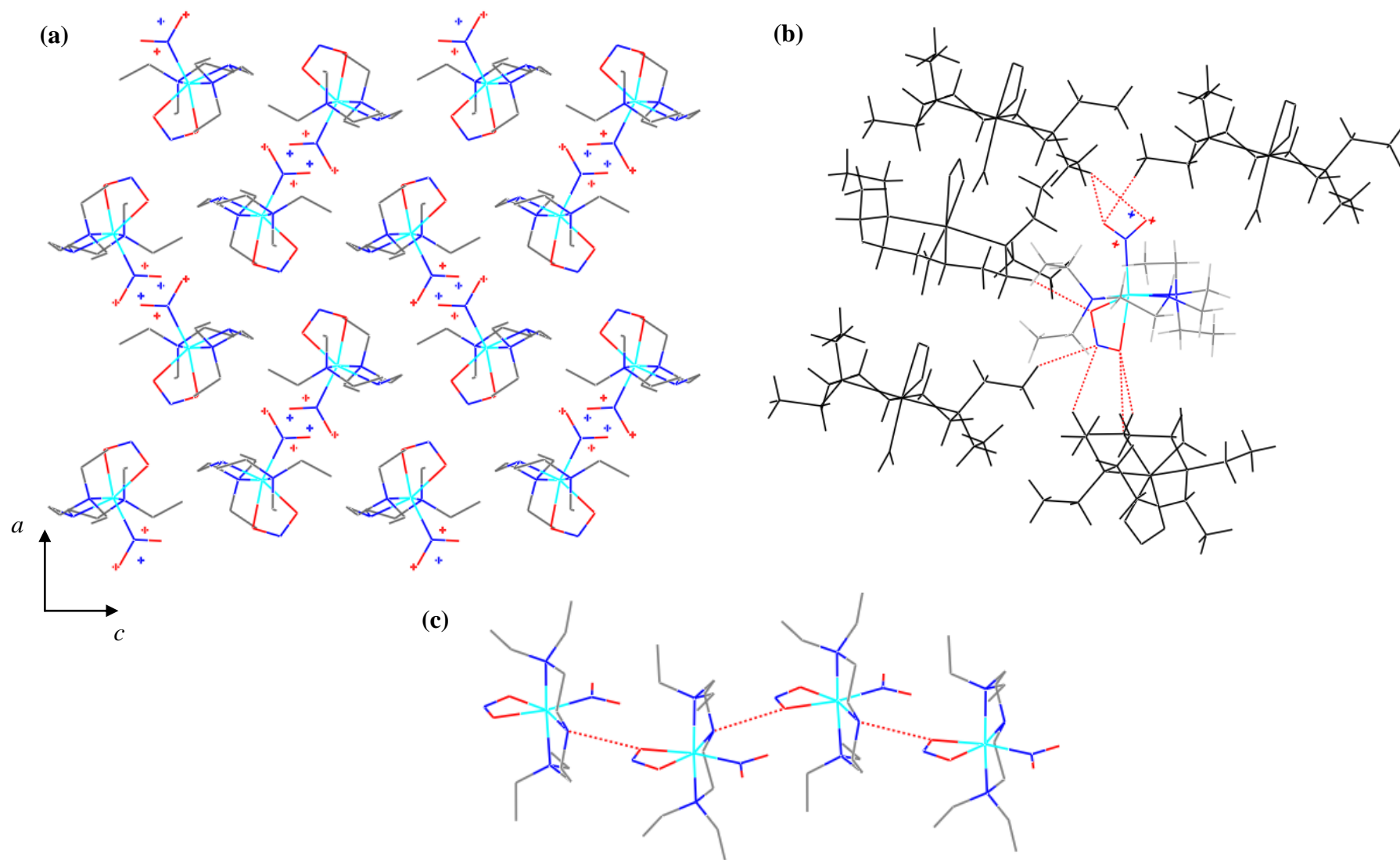
Figure 4.3: Crystal packing arrangement for the flash-cooled structure of [1]; **(a)** packing diagram, viewed along the *b*-axis, *c*-axis horizontal, **(b)** close-contacts (red dotted lines) to the nitrite ligands, **(c)** Hydrogen bonded chains (red dotted lines) extending parallel to the *a*-axis.

Figure 4.3 describes the packing arrangement for [1]. The individual molecules align in chains along the *a*-axis, linked by a discrete N(4)-H(4)…O(4) hydrogen bond (Figure 4.3(c); Table 1, Appendix 1). For this contact to be maintained, adjacent molecules are rotated with respect to one another and rows are arranged such that molecules are slightly offset, forming channels along the *c*-axis into which the nitrite groups are positioned. Despite the appearance of space within these channels in Figure 4.3(a), calculations in Mercury[127] indicate that there is no void space in the static structure, for a contact surface calculation with a probe radius of 1.2 Å and grid spacing 0.1 Å. In accordance with this observation, the nitrite groups are involved in short contacts with neighbouring species (Figure 4.3(b)), indicating the molecules are tightly packed. It should be noted, however, that these intermolecular contacts are comparatively weak and no strong hydrogen bonds are formed between the monodentate nitrite and the surrounding lattice.

Table 4.1: Single-crystal X-ray data for the flash-cooled structure of [1]

Temperature	100(2) K
Radiation source	Synchrotron
Wavelength	0.68890 Å
Empirical formula	C12 H29 N5 O4 Ni
Formula weight	366.11
Crystal size	0.07 x 0.07 x 0.01 mm^3
Crystal system	Orthorhombic
Space group	$P2_12_12_1$
Unit cell dimensions	$a = 11.409(2)$ Å $b = 11.677(2)$ Å $c = 12.891(3)$ Å
Volume	1717.5(6) Å^3
Z	4
Density (calculated)	1.416 M g m^{-3}
Absorption coeff. μ	1.154 mm^{-1}
Flack x parameter	0.028(7)
F(000)	784
R(int)	0.0665
R1 (obs. data)	0.0287
wR2 (all data)	0.0699
Reflections (indep.)	21175 (5873)

Thermal Studies

The "mixed" structure observed on flash cooling suggests that [1] has the potential to undergo nitro – nitrito linkage isomerism. Work by Laskar *et al.* has shown that a nickel complex containing a similar ethylenediamine ancillary ligand undergoes nitro – nitrito isomerism in the solid-state upon thermal excitation.[69] In light of these results, thermal studies were conducted on [1] to investigate if a change in the isomeric ratio could be induced with variable temperature.

A crystal was first mounted at 298 K, with minimal light exposure, and a series of low temperature data collections were conducted at intervals between 298 and 100 K. The crystal was held at each stage for 5 min to allow the temperature to equilibrate, before a new experiment was executed. Three repeat experiments were conducted at each temperature, with all datasets collected on the same crystal. For the first repeat the crystal was cooled between datasets, *in-situ* on the diffractometer. For the second repeat the temperature was raised, to investigate the possibility of a hysteresis. Finally, the crystal was re-cooled during the third set of experiments. Table 4.2 displays the nitro : nitrito ratio at each temperature, as determined from crystallographic data.

Table 4.2: Crystallographically determined ratios of nitro and *endo*-nitrito isomers in **[1]** as a function of temperature (100 – 298 K = repeat set 1)

Temp / K	Refined Occupancy (esd)	
	Nitro-(η^1-NO$_2$)	Nitrito-(η^1-ONO)
100	1.00*	0.00*
150	1.00*	0.00*
175	0.97(1)	0.03(1)
200	0.95(1)	0.05(1)
225	0.94(1)	0.06(1)
250	0.90(1)	0.10(1)
275	0.84(1)	0.16(1)
298	0.82(1)	0.18(1)
350	0.64(1)	0.36(1)
370	0.58(1)	0.42(1)

* No esd is reported for full occupancy or zero occupancy as these ratios were not refined

At 298 K a mixed structure was obtained, similar to that of the flash cooled structure in Figure 4.2, with a 82 : 18 ratio of nitro to nitrito isomers. This indicates that on flash cooling the system is cryo-trapped, "freezing" it in its ambient state so that a mixture of isomers is still observed. On slow cooling the nitro : nitrito ratio changed, with occupation of the minor *endo*-nitrito component decreasing with lower temperature. By 150 K, no trace of the *endo*-nitrito form could be identified, showing that a clean, 100% nitro-(η^1-NO$_2$) isomer is produced by slow cooling. Comparison of repeat datasets (Table 3, Appendix 1) reveals the isomeric ratio is consistent at each temperature, regardless of whether the crystal is cooled or heated. The thermal isomerisation in [1] therefore shows no hysteresis and the results also confirm that conversion is a fully reversible process.

In a second series of experiments a crystal was heated *in-situ* above 298 K and high temperature studies conducted. As predicted by the thermal trend at 100 – 298 K, elevated temperatures increased conversion to the *endo*-nitrito-(η^1-ONO) isomer. High temperature data collections can introduce problems such as increased radiation damage[12] and large anisotropic displacement parameters due to increased thermal motion. However, despite a small reduction in data quality, it was easily ascertained that conversion had increased to 36% at 350 K, while a maximum thermal excitation of 42% to *endo*-nitrito-(η^1-ONO) was observed at 370 K. Unfortunately, above 370 K the crystal decomposed to such an extent that single-crystal integrity was irreversibly lost.

The results suggest that the isomers are close in energy and exist in a thermodynamic equilibrium (Equation 4.1), the position of which shifts on varying the temperature. At low temperatures nitro-(η^1-NO$_2$) is favoured, indicating this is the more thermodynamically stable isomer. This correlates with the fact that [1] crystallises with this isomer as the major component at ambient temperature.

$$\text{nitro-}(\eta^1\text{-NO}_2) \rightleftharpoons \textit{endo}\text{-nitrito-}(\eta^1\text{-ONO}) \qquad \text{Equation 4.1}$$

$$\text{K}_{eq} = \frac{[\eta^1 - NO_2]}{[\eta^1 - ONO]} \qquad \text{Equation 4.2}$$

$$\Delta G = \Delta H - T\Delta S = -RT\ln(K_{eq}) \qquad \textit{where R = 8.314 J K}^{-1}\textit{ mol}^{-1} \qquad \text{Equation 4.3}$$

$$(-R)\ln(K_{eq}) = \Delta H(\frac{1}{T}) - \Delta S$$
$$y \quad = \text{m} \ x \ + \ \text{C} \qquad \text{Equation 4.4}$$

Analysis of the thermodynamic equilibrium can be made using a Van't Hoff plot, in which Equation 4.4 is applied to the data. The equilibrium constant K_{eq} is obtained by dividing the occupation of nitro-(η^1-NO$_2$) by nitrito-(η^1-ONO) (Equation 4.2). It can be shown that the equation for the Gibbs free energy ΔG (Equation 4.3) can be rearranged such that it compares to the equation of a straight line (Equation 4.4). Thus, a plot of (1/T) against (–R)ln(K_{eq}) (where R is the molar gas constant, 8.314 J K^{-1} mol^{-1}) is expected to give a straight line that can be used to calculate the standard enthalpy (ΔH = gradient) and the entropy (–ΔS = intercept) for the thermal isomerisation process. This analysis was applied to the data obtained in low temperature experiments, where the same crystal was used to collect three repeat datasets at each temperature. When nitrito-(η^1-ONO) is no longer observed the value of K_{eq}, and so also Equation 4.4, become meaningless, therefore only data between 298 K and 175 K are analysed. A plot of the results is given in Figure 4.4.

The data show good linear regression, with a R^2 value of 0.981 (3 sig. figs). The negative gradient (ΔH) indicates that the nitro-(η^1-NO_2) isomer is enthalpically favoured by 7.2 ($\pm$ 0.3) kJ mol^{-1}, while the intercept gives an entropy change (ΔS) of -11.6 ($\pm$ 1.1) J K^{-1} mol^{-1}. These values represent a relatively low energy barrier between the two isomers, which is consistent with their co-existence in the crystal at room temperature, with ΔH comparable to the ambient value of kT = 2.479 kJ mol^{-1}.
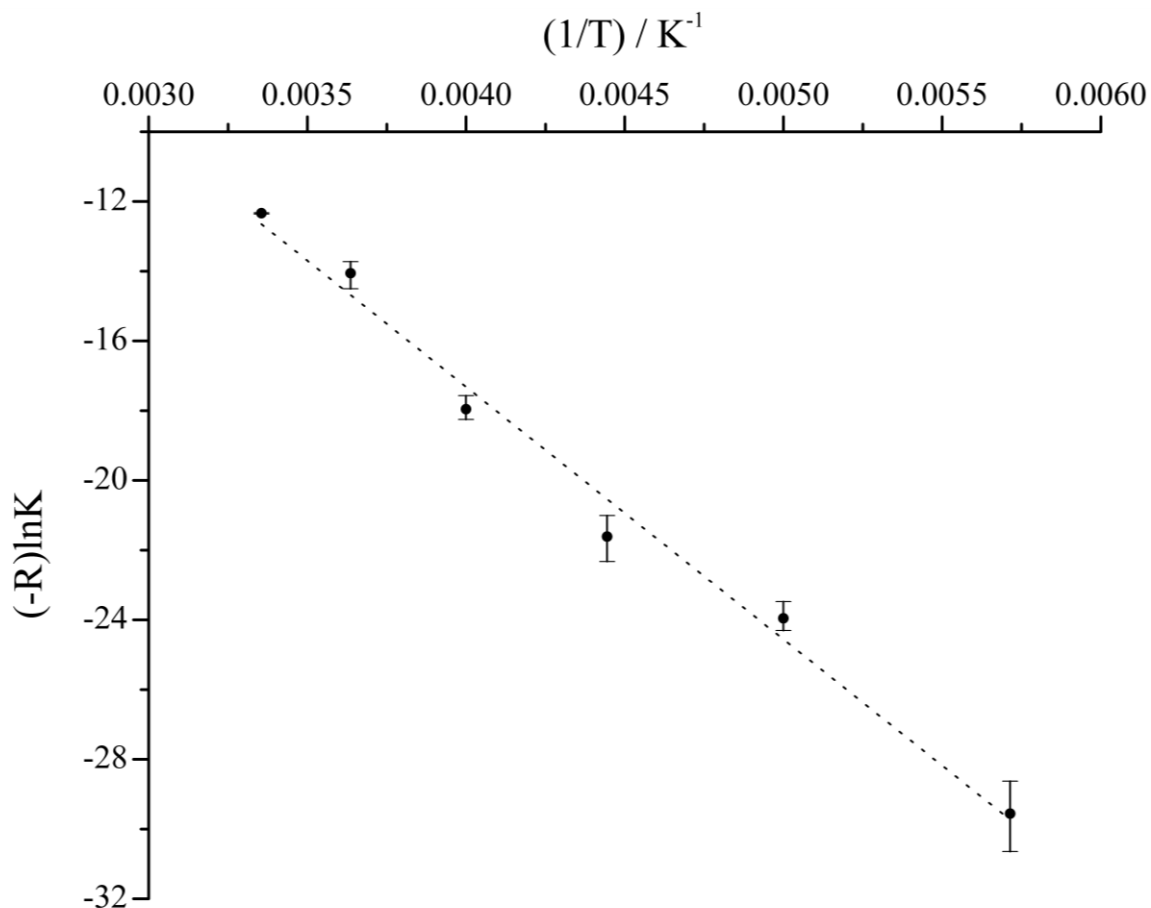
Figure 4.4: Van't Hoft plot for the thermodynamic equilibrium in complex [1]. Slope m = standard enthalpy (ΔH) = -7.2 ($\pm$ 0.3) kJ mol^{-1}, intercept C = entropy (ΔS) = -11.6 ($\pm$ 1.1) J K^{-1} mol^{-1}, R^2 = 0.981

$$k_{eq} = Ae^{-\frac{E_A}{RT}}$$

Equation 4.5

$$\ln(k_{eq}) = -E_A(\frac{1}{RT}) + \ln(A)$$

$$y \quad = \quad m \ x \ + \ C$$

Equation 4.6

Additionally, application of the Arrhenius equation (Equation 4.5) to the data allows the activation energy (E_A) of the process to be estimated. The plot of $\ln(K_{eq})$ against (1/RT) (Equation 4.6, Figure 4.5) is expected to give a straight line and the value of the slope provides an estimate of E_A.
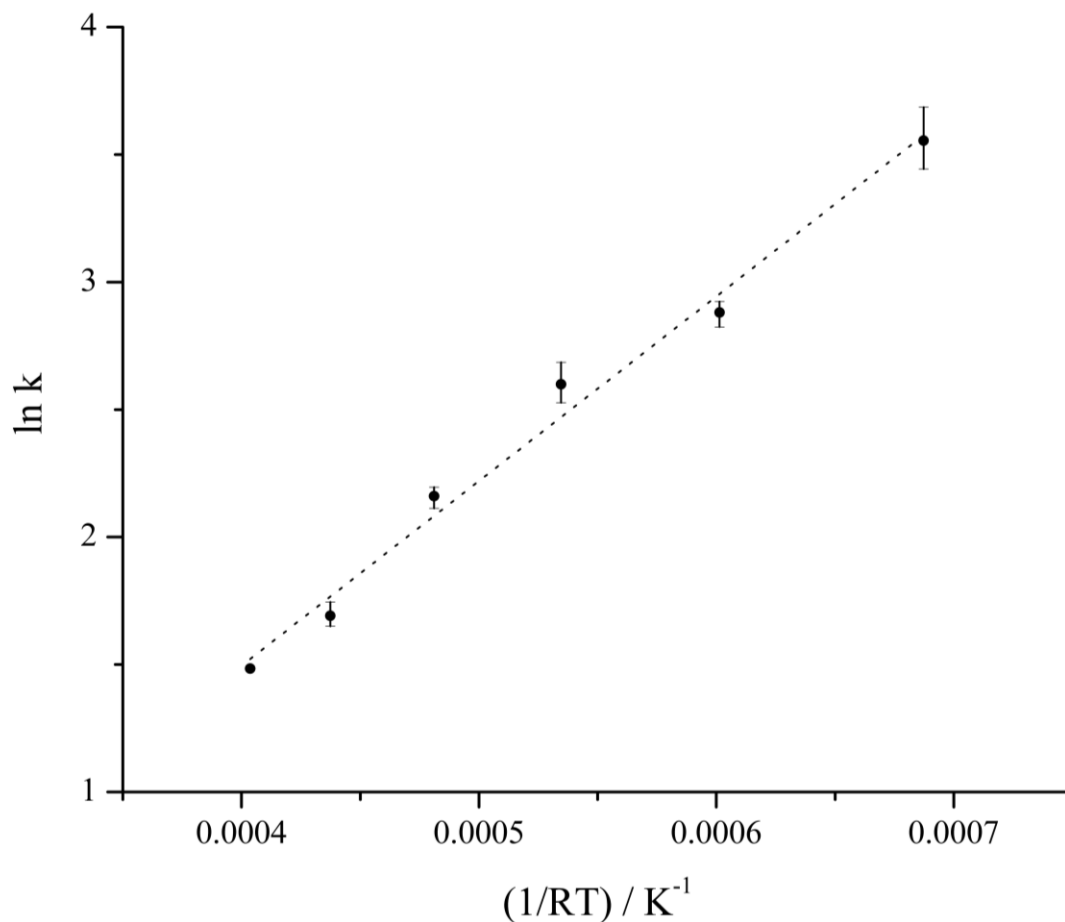
Figure 4.5: Arrhenius plot for the thermally induced isomerisation reaction in complex [1]. Activation energy $E_A = -7.2 \ (\pm 0.4)$ kJ mol^{-1}, $R^2 = 0.985$

The data again show good linear regression ($R^2 = 0.985$) and the value of $E_A = -7.2 \ (\pm 0.4)$ kJ mol^{-1} indicates an energetically favourable process. This is expected if nitro-(η^1-NO$_2$) is the more thermodynamically favourable isomer, although the small value for E_A indicates there is only a very small difference in energy between the two isomeric arrangements in this temperature range.

Crystal Packing and Sterics

Changes in the unit cell and crystal packing as a result of the isomerisation may suggest the nitro – nitrito conversion level is affected, to some degree, by steric influences in the crystal lattice.

Table 4.4 compares the unit cell parameters at all of the temperature intervals discussed above, and it can be seen that the cell volume increases with increasing temperature. The expansion is relatively isotropic, with all axes increasing with temperature. The changes are expected in line with thermal lattice expansion on heating, and so from this data it cannot be concluded that there is any dependence of the cell parameters on the level of thermally-induced nitro – nitrito conversion.

Table 4.4: Unit cell parameters and close contact distances for variable temperature data collections on [1]

| Temp / K | Experiment | Constrained unit cell | | | | Volume / Å^3 |
		a / Å	b / Å	c / Å	α, β, γ / °	
100	Flash-cool	11.409(2)	11.677(2)	12.891(3)	90	1717.5(5)
100	VT cool	11.328(5)	11.597(5)	12.828(5)	90	1685.2(12)
150	VT cool	11.337(5)	11.621(5)	12.863(5)	90	1694.7(12)
175	VT cool	11.343(5)	11.647(5)	12.887(5)	90	1702.5(12)
200	VT cool	11.358(5)	11.653(5)	12.897(5)	90	1707.0(12)
225	VT cool	11.373(5)	11.687(5)	12.927(5)	90	1718.2(12)
250	VT cool	11.390(5)	11.689(5)	12.937(5)	90	1722.4(12)
275	VT cool	11.412(5)	11.730(5)	12.972(5)	90	1736.5(13)
298	VT	11.434(5)	11.734(5)	12.972(5)	90	1740.4(13)
350	VT heat	11.466(6)	11.792(7)	13.051(7)	90	1764.6(17)
370	VT heat	11.455(5)	11.799(5)	13.058(5)	90	1764.8(12)

A more relevant comparison is made between the parameters of the flash cooled and slow cooled structures at 100 K. The slow cooled nitro-(η^1-NO$_2$) isomer has a smaller cell volume than that of the mixed, flash cooled structure with a value of $\Delta V = 32.3(5)$ Å^3, or 1.9%, and again the changes are isotropic. The difference in volume is considered significant, on application of the "3σ rule". This rule states that if two parameters differ by more than three times the standard uncertainty (σ) on their difference, they are statistically different with a 99% probability (Equation 4.7).[15]

$$\frac{V_1 - V_2}{\sqrt{\sigma_1^2 + \sigma_2^2}} \geq 3 \qquad \text{or} \qquad \frac{\Delta V}{\sigma(\Delta V)} \geq 3 \qquad\qquad \text{Equation 4.7}$$
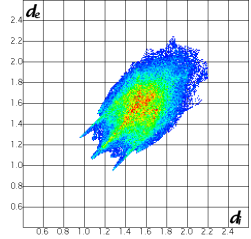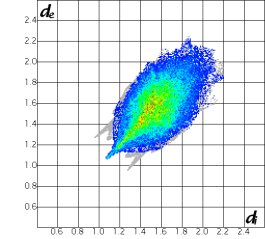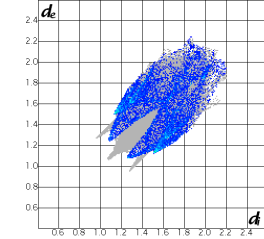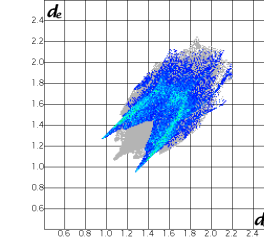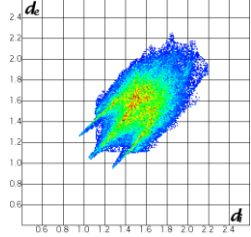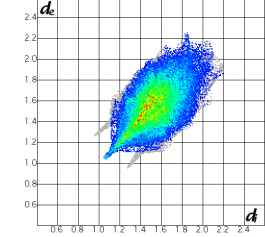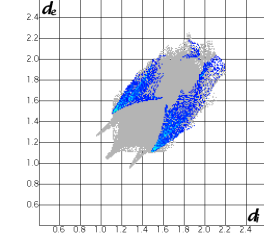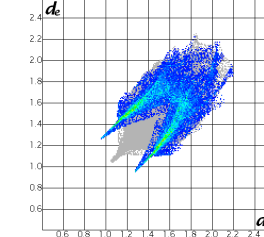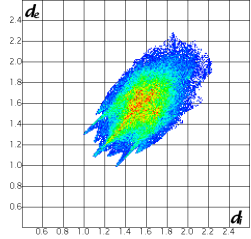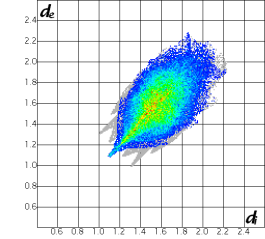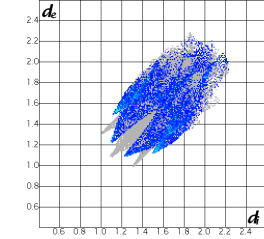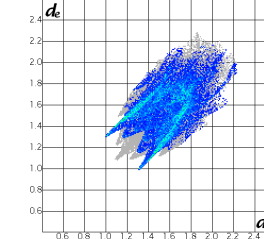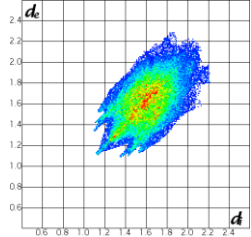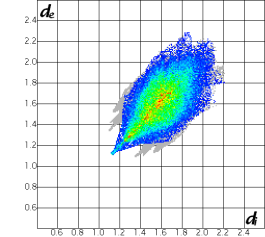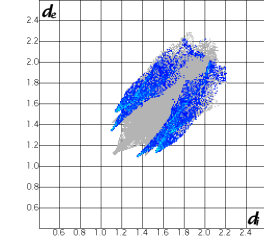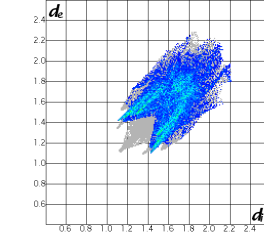
where σ_1 = s.u. on V_1, σ_2 = s.u. on V_2 and $\sigma(\Delta V)$ = s.u. on ΔV

It is possible that ΔV is simply an artifact of the different cooling methods used, as slower cooling may allow for more efficient thermal relaxation of the lattice. However, considering that significant nitro – nitrito rearrangement occurs, whilst most other variables are the same, ΔV could reasonably be attributed to the thermal isomerisation. Comparison of the packing diagrams also confirms there is little change in the overall structure with temperature, with all diagrams closely resembling Figure 4.3(a). In addition, no voids are present in the lattice at any temperature.

Intermolecular interactions are also analysed in Crystal Explorer.[128] The Hirshfeld Stockholder Partitioning theorem is used to separate the crystal into discrete molecular surfaces that are visualised in the software.[129] Many properties can be mapped onto the Hirshfeld surface, including those related to intermolecular contacts. It is also possible to produce 2-D scatterplots, in which each point compares d_i, the distance from the surface to a specified atom inside that surface, with d_e, the distance from the surface to the atom external to that surface. As such, these "Fingerprint" plots provide a graphical summary of the unique set of intermolecular interactions present. The plots allow quick visual comparison between structures and Table 4.5 shows plots describing the changes in [1] with varying temperature. Complete plots for [1] are given in Table 4, Appendix 1.

The overall shape of the Fingerprint plot changes little between temperatures, confirming that the overall structure is largely unchanged. However, on closer inspection some subtle differences are revealed. There are only three types of contacts present, N…H, O…H and H…H interactions. While both N…H and O…H contacts must involve the isomerising ligand, H…H contacts solely represent the rest of the crystal. For the 100% nitro-(η^1-NO$_2$) isomer slow cooled at 100 K, N…H contacts appear quite long and there is a small range for their distance (small, defined features). As thermal isomerisation begins, above 175 K new and more diffuse features appear at lower d_i/d_e values, representing a shortening in N…H contacts on isomerisation. The changes are consistent with rearrangement of N(1) to N(1A) and become more prevalent as nitrito occupancy increases. Similar trends are also observed for O…H contacts: sharp "spikes" dominating the low temperature structures, and so associated with the nitro-(η^1-NO$_2$) isomer, become less pronounced at higher temperatures. Instead new peaks appear and become more pronounced with temperature, indicating these are new interactions related to nitrito-(η^1-ONO). By contrast H…H contacts, representing the rest of the structure, remain constant at all temperatures. In summary, changes in N…H and O…H features confirm there are localised rearrangements resulting from the isomerisation, but suggest there is very little change in the rest of the lattice. This suggests that no large amount of steric strain is induced in the crystal upon thermal isomerisation, and is consistent with the fact that single-crystal integrity is maintained during the experiment.

Table 4.5: Fingerprint plots, generated in Crystal Explorer,[128] showing the changes in intermolecular contacts for [1] at selected temperatures. d_i = the distance from the surface to a specified atom inside that surface, d_e = the distance from the surface to the symmetry-related atom external to that surface. The colour of the point represents the amount of the Hirshfeld surface taken up by the interaction: dark-blue = low area, red = high area

Temp	Experiment	All Contacts	H…H contacts	N...H contacts	O…H contacts
100	Flash cool				
100	Slow cool				
298	VT				
370	VT heat				

Steady-State Photocrystallography

Photocrystallographic studies were also conducted to investigate the possibility of photoactivated linkage isomerism in complex [1].

A crystal was mounted at room temperature with minimal light exposure and slowly cooled *in-situ* to 100 K in the dark. A high quality X-ray dataset was then obtained to confirm the presence of the clean, 100% nitro-(η^1-NO$_2$) isomer and this was taken as the GS structure. The crystal was then irradiated *in-situ* with 400 nm LED light for a period of 1 h, using the experimental set-up and procedure for steady-state investigations described in § 3.2.2. A second data collection was conducted, which revealed that the crystal had been excited to 86% of the nitrito-(η^1-ONO) form. Further irradiation with the same crystal caused no appreciable change in the nitro : nitrito occupancy, confirming this to be the photostationary state for the system using 400 nm light. The crystal was held at 100 K for a further 1 h and a subsequent X-ray dataset showed that the ES structure remained unchanged, confirming that a MS had been induced under these conditions.
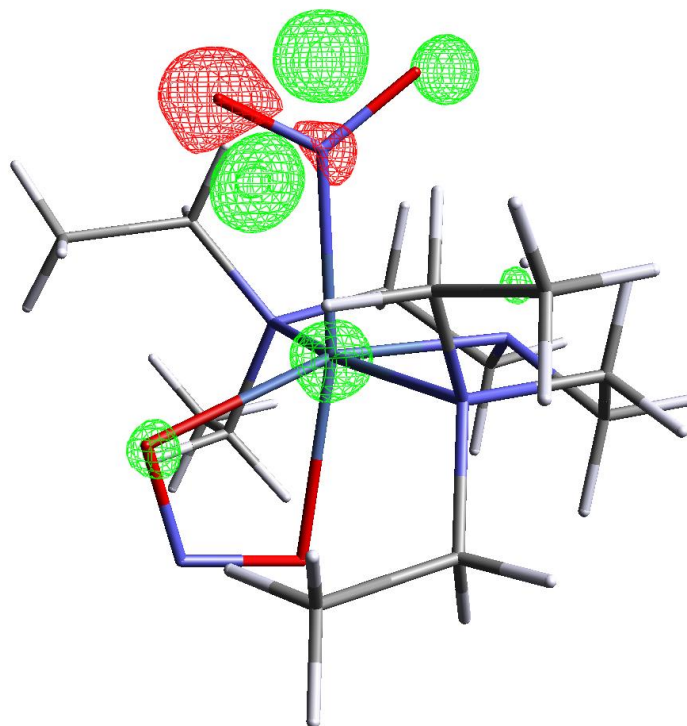
Figure 4.6: Photodifference map showing the change in Fourier electron density distribution between the GS and MS of **[1]**; red = negative contours at -1.22 eÅ^{-3}, green = positive contours at +1.22 eÅ^{-3}

The presence of the MS state is confirmed by studying the photodifference map, showing the change in Fourier electron density distribution between the photoactivated data and the GS structure (Figure 4.6). The map clearly shows the production of the MS, with regions of positive

electron density (green) present at the atomic positions of the *endo*-nitrito-(η^1-ONO) ligand. The reduction of electron density at the positions of O(1) and N(1) in the GS nitro-(η^1-NO$_2$) isomer is shown by red contours, confirming that the occupancy of this isomer decreases on excitation.

Table 4.6: Crystallographically determined ratios of nitro and *endo*-nitrito isomers in [1] as a function of exposure to 400 nm LED light in steady-state photocrystallographic studies

Irradiation time / h	Temp / K	Refined Occupancy	
		Nitro-(η^1-NO$_2$)	Nitrito-(η^1-ONO)
0	100	1.00*	0.00*
1	100	0.14(1)	0.86(1)
2	100	0.14(1)	0.86(1)
2	140	0.23(1)	0.77(1)
2	160	0.33(1)	0.67(1)
2	180	1.00*	0.00*

* No esd is reported for full occupancy or zero occupancy as these ratios were not refined

Another crystal photoactivated for 2 h with 400 nm light at 100 K was then the subject of variable temperature parametric studies, to determine the temperature range over which the system is metastable. Refined nitro : nitrito ratios for all steady-state photocrystallographic experiments with [1] are given in Table 4.6. The nitrito-(η^1-ONO) isomer still exists as the major component at 160 K. By 180 K the system returns to its GS configuration, showing that photoinduced linkage isomerism in [1] is a fully reversible process, as was found for the analogous thermal process.

Photoactivation with Different Wavelengths

As this project aims both to achieve reproducibly high levels of photoisomerisation and to better understand the underlying processes that influence isomerisation, it is of interest to investigate why conversion in [1] does not proceed to 100% using 400 nm light. As noted in Chapter 2, the light absorption properties of the sample have been shown to have an effect on the progress of the photoreaction and problems, including the degree to which the excitation light can penetrate through the crystal, are known to limit the overall level of conversion achievable.[71, 104] To investigate the degree to which the optical properties of [1] affect the level of achievable photoactivation, test experiments were conducted using a selection of different LED wavelengths.
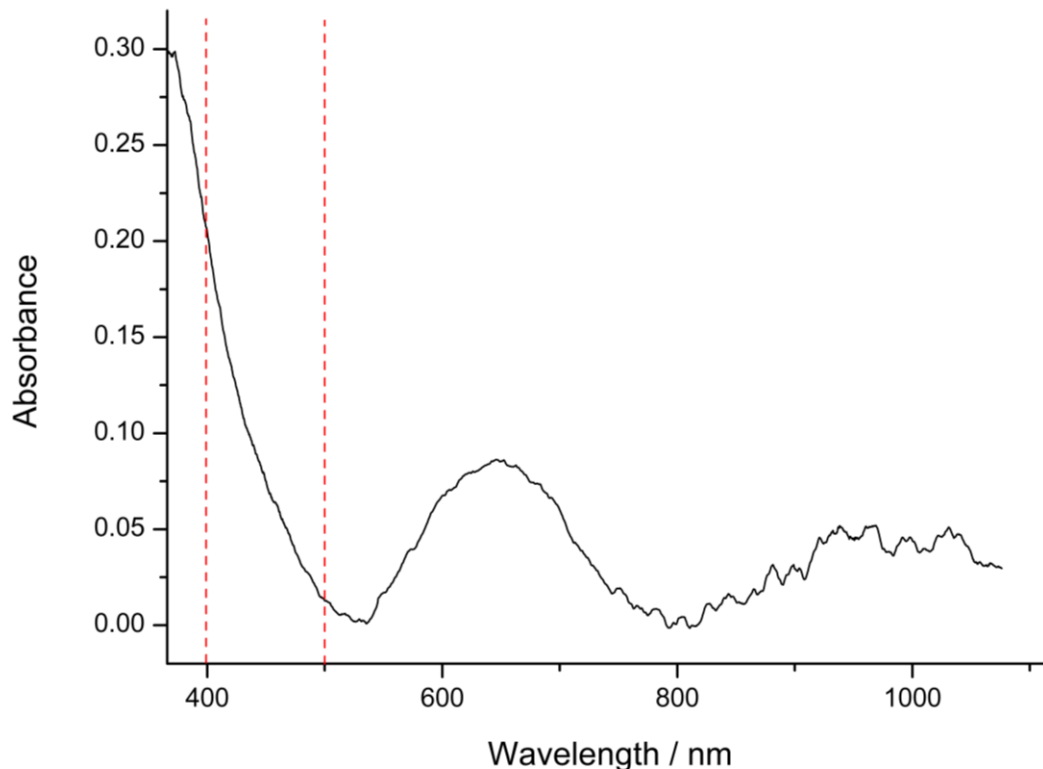
Figure 4.7: Solid-state UV/visible spectrum from a single-crystal sample of [1]

To guide wavelength selection, a solid-state UV/vis spectrum was collected for [1] (Figure 4.7), at room temperature on a single-crystal cut into a 0.6 x 0.6 x 0.04 mm plate. This is comparable to crystals used for photocrystallographic work. The peak at 646 nm is characteristic of nickel-based d-d transitions. The stronger absorption beginning at 535 nm and extending into the UV region is characteristic of MLCT. Calculations in the literature indicate that MLCT transitions are involved in linkage isomerism processes in similar first row transition-metal complexes,[71] and so the spectrum indicates that wavelengths in this region are most likely to induce isomerism in [1]. Test experiments were therefore conducted with wavelengths between 365 and 500 nm. Research by Enkelmann *et al.* has discussed the wavelength dependence of solid-state photodimerisation reactions, and the authors suggest that wavelengths near the absorption peak are not beneficial to induce maximum photoconversion.[23, 130] Such wavelengths are, necessarily, strongly absorbed and do not penetrate fully throughout the crystal, causing incomplete conversion at the centre. Additionally, strong absorption may also promote crystal decay. To minimise such problems, whilst still inducing excitation, a wavelength in the tail of the band is suggested. In agreement, test experiments with 500 nm light induced the most promising conversion levels in [1] and so a new, steady-state photocrystallographic study was conducted at this wavelength.

A crystal of [1] was subject to 2 h irradiation with 500 nm LED light at 100 K, before a single-crystal X-ray dataset was collected. This data revealed a 100% *endo*-nitrito-(η^1-ONO) isomer, showing that irradiation with 500 nm LED light induces complete nitro – nitrito conversion in [1]. The result is highly reproducible and the *endo*-nitrito isomer remains when crystal is held at 100 K, confirming it is metastable at this temperature. The diffraction data for the GS and MS are of comparable quality, indicating there is little crystal decay upon photoactivation. The molecular structure of the 500 nm MS state is identical to that described in Figure 4.2(b), and crystal data for GS, 400 nm and 500 nm MS structures are given in Table 4.7.

Table 4.7: Single-crystal X-ray data for ground state (GS) and metastable state (MS) structures of [1] in steady-state photocrystallographic experiments, following irradiation with 400 nm and 500 nm LED light

	GS	400 nm MS	500 nm MS
Photoconversion	0%	86%	100%
Temperature	100(2) K	100(2) K	100(2) K
Radiation source	Mo K$_\alpha$	Mo K$_\alpha$	Mo K$_\alpha$
Wavelength	0.71073 Å	0.71073 Å	0.71073 Å
Empirical formula	C12 H29 N5 Ni1 O4	C12 H29 N5 Ni1 O4	C12 H29 N5 Ni1 O4
Formula weight	366.11	366.11	366.11
Crystal size	0.40 x 0.20 x 0.10 mm^3	0.40 x 0.20 x 0.10 mm^3	0.30 x 0.3 x 0.10 mm^3
Crystal system	Orthorhombic	Orthorhombic	Orthorhombic
Space group	$P2_12_12_1$	$P2_12_12_1$	$P2_12_12_1$
Unit cell dimensions	$a = 11.315(5)$ Å $b = 11.601(5)$ Å $c = 12.830(5)$ Å	$a = 11.493(5)$ Å $b = 11.656(5)$ Å $c = 12.830(5)$ Å	$a = 11.517(5)$ Å $b = 11.658(5)$ Å $c = 12.799(5)$Å
Volume	1684.1(12) Å^3	1715.8(12) Å^3	1718.5(12) Å^3
Z	4	4	4
Density (calculated)	1.444 M g m^{-3}	1.417 M g m^{-3}	1.415 M g m^{-3}
Absorption coeff. μ	1.177 mm^{-1}	1.155 mm^{-1}	1.153 mm^{-1}
Flack x parameter	-0.015(8)	-0.005(14)	0.008(13)
F(000)	784	784	784
R(int)	0.0210	0.0372	0.0353
R1 (obs. data)	0.0225	0.0363	0.0362
wR2 (all data)	0.0521	0.0828	0.0806
Reflections (indep.)	3969	3976	4706

Variable temperature parametric studies were also conducted on this crystal and the results show a similar trend to that seen for the 400 nm MS state, with the system decaying back to the majority nitro-(η^1-NO$_2$) GS arrangement by 160 K. This comparable behaviour indicates that the same MS is induced on excitation at either wavelength. Table 4.8 gives the nitro : nitrito ratios determined from the crystallographic data for all 500 nm photocrystallographic experiments.

Table 4.8: Crystallographically determined ratios of nitro and *endo*-nitrito isomers in [1] as a function exposure to 500 nm LED light in steady state photocrystallographic studies

Irradiation time / h	Temp / K	Refined Occupancy	
		Nitro-(η^1-NO$_2$)	Nitrito-(η^1-ONO)
0	100	1.00*	0.00*
2	100	0.00*	1.00*
2	140	0.00*	1.00*
2	150	0.14(1)	0.86(1)
2	160	0.85(1)	0.15(1)
2	170	1.00*	1.00*
2	180	1.00*	0.00*

* No esd is reported for full occupancy or zero occupancy as these ratios were not refined

Crystal Packing and Sterics

As observed for the thermal process, the packing arrangement is largely unchanged upon photoactivation; the crystal retains the same, orthorhombic $P2_12_12_1$ space group and the structure of the 500 nm MS state closely resembles that in Figure 4.3(a), excepting the change in nitrite coordination. Table 4.7 shows a change in volume between GS and 500 nm MS unit cells, with an increase of $\Delta V = 34.4(17)$ Å^3, or 2.04%, of the GS volume on excitation. This difference is significant on applying the 3σ rule, with a value of $\Delta V / \sigma(\Delta V) = 20.2$. In addition, as found for the thermally-induced isomerisation, the increase in cell volume occurs in a relatively isotropic manner. Despite this increase in cell volume, as for the GS no voids are calculated to be present in the photoactivated structure, when the same probe sphere of radius 1.2 Å and 0.1 Å grid spacing are applied in Mercury. This would suggest that there is little free space in the static structure both before and after photoactivation, however physically it is expected that there must be some flexibility in the lattice as the atoms of the nitrite group must move to achieve isomerisation.

Crystal Explorer fingerprint plots again show little change in the intermolecular interactions on photoactivation, excepting those involving the nitrite atoms (Table 4.9). H…H plots are largely unchanged after photoactivation and are also similar to those calculated for thermal studies with [1]. N…H interactions shorten on excitation, as is expected when N(1) is rearranged to N(1A). The O…H plots show fewer changes, although there are less points in the MS plot indicating that the number of O…H contacts reduces on photoactivation. In summary, the fingerprint plots are in agreement with the rest of the structural analysis, reflecting only localised changes involving the nitrite group and showing no more dramatic structural rearrangement as a result of isomerisation.

Table 4.9: Fingerprint plots generated in Crystal Explorer showing changes in intermolecular contacts in [1] following exposure to 500 nm LED light

	GS	500 nm MS
All Contacts		
H…H contacts		
N...H contacts		
O…H contacts		
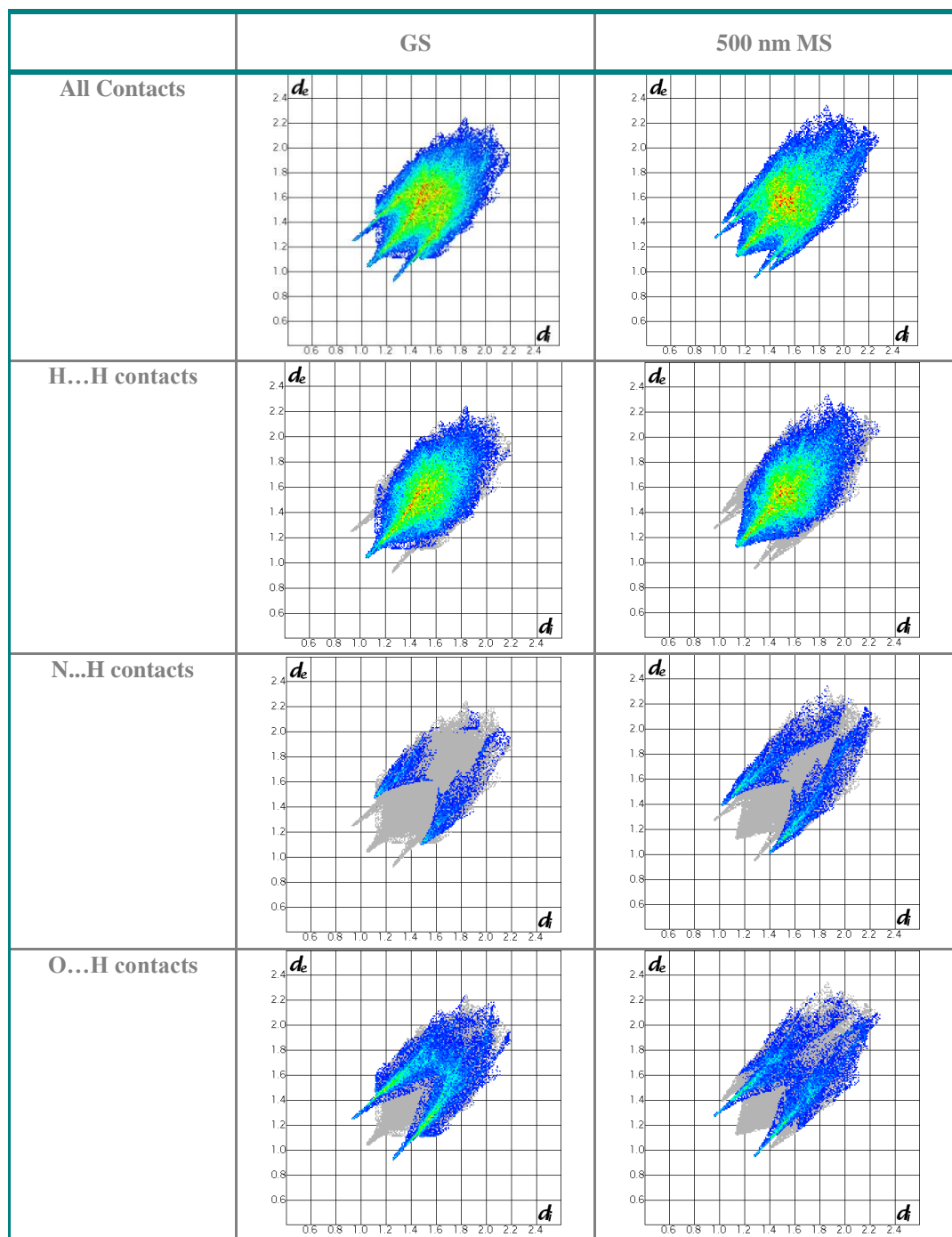
4.1.2. Complex [2]: Nitro-(*N,N,N',N'*-tetraethyldiethylenetriamine)palladium(II) tetraphenylborate hydrate

Complex [2] was synthesised as described in § 9.2.2 and single-crystals were grown from a tetrahydrofuran / toluene mixture *via* slow evaporation. Tetraphenylborate was chosen as the counter-ion as it is similar in size to the cationic nitrite species. It is usually the case that good multi-component crystals are formed when the constituent components are similar in size, as these are likely to pack most efficiently. A crystal was mounted with minimum light exposure and flash cooled to 100 K before a standard X-ray dataset was collected.

Crystal Structure and Bonding

[2] crystallises in the monoclinic space group $P2_1/n$ with one palladium cation, one tetraphenylborate anion and one solvent water molecule in the asymmetric unit. Figure 4.8 shows the atomic arrangement for the cation. The palladium centre is square planar, coordinating to one *N,N,N',N'*-tetraethyldiethylenetriamine ligand and one nitrite group with an RMS deviation of 0.046 from the plane for Pd(1), N(1), N(2), N(3) and N(4). The nitrite ligand adopts solely nitro-(η^1-NO$_2$) configuration in this flash cooled structure. Crystal data are given in Table 4.11.
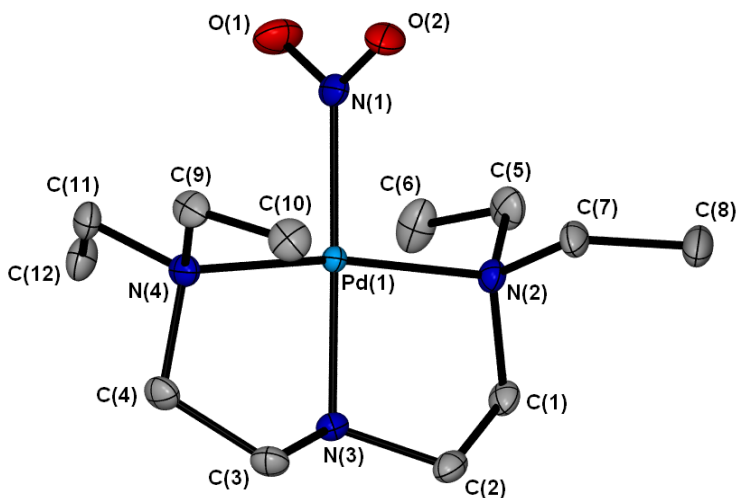
Figure 4.8: Single-crystal X-ray structure showing the atomic arrangement for the metal cation in [2]. Ellipsoids at 50% probability and hydrogen atoms removed for clarity

Figure 4.9 shows the overall crystal packing arrangement for complex [2]. The crystal structure may be viewed as an extended network of tetraphenylborate anions, surrounding channels within which the palladium cations are positioned (Figure 4.9(a)).
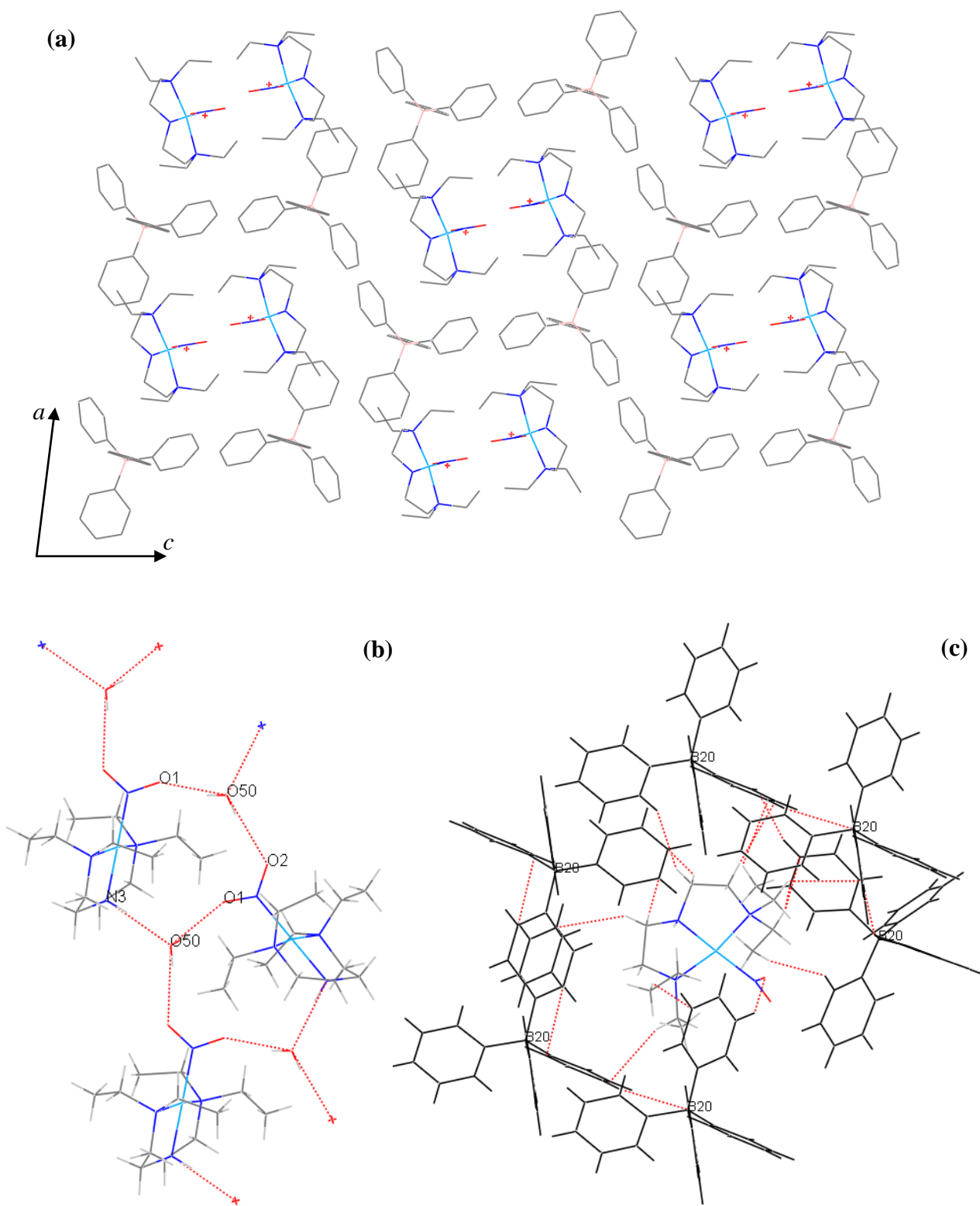
Figure 4.9: Crystal packing arrangement for [2]; **(a)** packing diagram, viewed along the *b*-axis, *c*-axis horizontal, **(b)** hydrogen bonded cation chains extending parallel to the *b*-axis, *c*-axis horizontal, **(c)** cation – anion close-contact interactions.

The cations are aligned in chains running parallel to the *b*-axis, with the nitrite ligands oriented towards the centre of the channel. Each palladium moiety is linked to its symmetry-related cation neighbour *via* a hydrogen bonded network extending along the *b*-axis, which also involves two solvent water molecules (Figure 4.9(b)). The hydrogen bonds that comprise this network may be described in Graph Set notation[131] as one discrete $D_1^1(2)$ motif between N(3) and a water oxygen, O(50), and a second $C_2^2(6)$ chain motif linking each nitrite ligand to two neighbouring water molecules. Full hydrogen bond data are given in Table 1, Appendix 2, and all three interactions are described as medium strength hydrogen bonds.[132] It is, therefore, apparent that the nitrite group is involved in a number of moderately strong interactions, which could potentially be unfavourable for photoinduced isomerism in the system. Each palladium cation is also involved in a number of C-H...H and C-H...π close-contact interactions with six tetraphenylborate anions (Figure 4.9(c)), localised on the phosphine side of the molecule. Despite the number of close-contact interactions observed, calculations indicate a small amount of void space is present in the lattice, comprising 2.1% of the unit cell volume (74.15 $Å^3$) when a probe radius of 1.2 Å and grid spacing of 0.1 Å are used. This indicates there is some free space in the static lattice, which potentially could assist the atomic rearrangements necessary for linkage isomerism.

Steady-State Photocrystallography

The solid-state UV/vis spectrum for complex [2] (Figure 1, Appendix 2) was used to identify a suitable excitation wavelength for steady-state photocrystallographic studies. As discussed previously for complex [1], a wavelength in the tail of the main, MLCT absorption is considered the most likely to induce maximum photoisomerisation,[23, 71, 130] and this analysis indicated that 400 nm LED light was most appropriate choice for photoactivation.

The flash cooled structure of [2] obtained previously was used as the GS structure for photocrystallographic studies. The same crystal was held at 100 K and irradiated with 400 nm LED light, *in-situ* on the diffractometer. After 1 hr irradiation, the LEDs were switched off and a new dataset collected. This revealed that photoactivated nitro – nitrito conversion had been induced in the crystal, with 68% of the cations now adopting nitrito-(η^1-ONO) coordination (Figure 4.10(a)). The ES nitrito isomer is disordered over two positions, creating three separate sites for each atom of the nitrite group in this partially excited structure (Figure 4.10(b)).
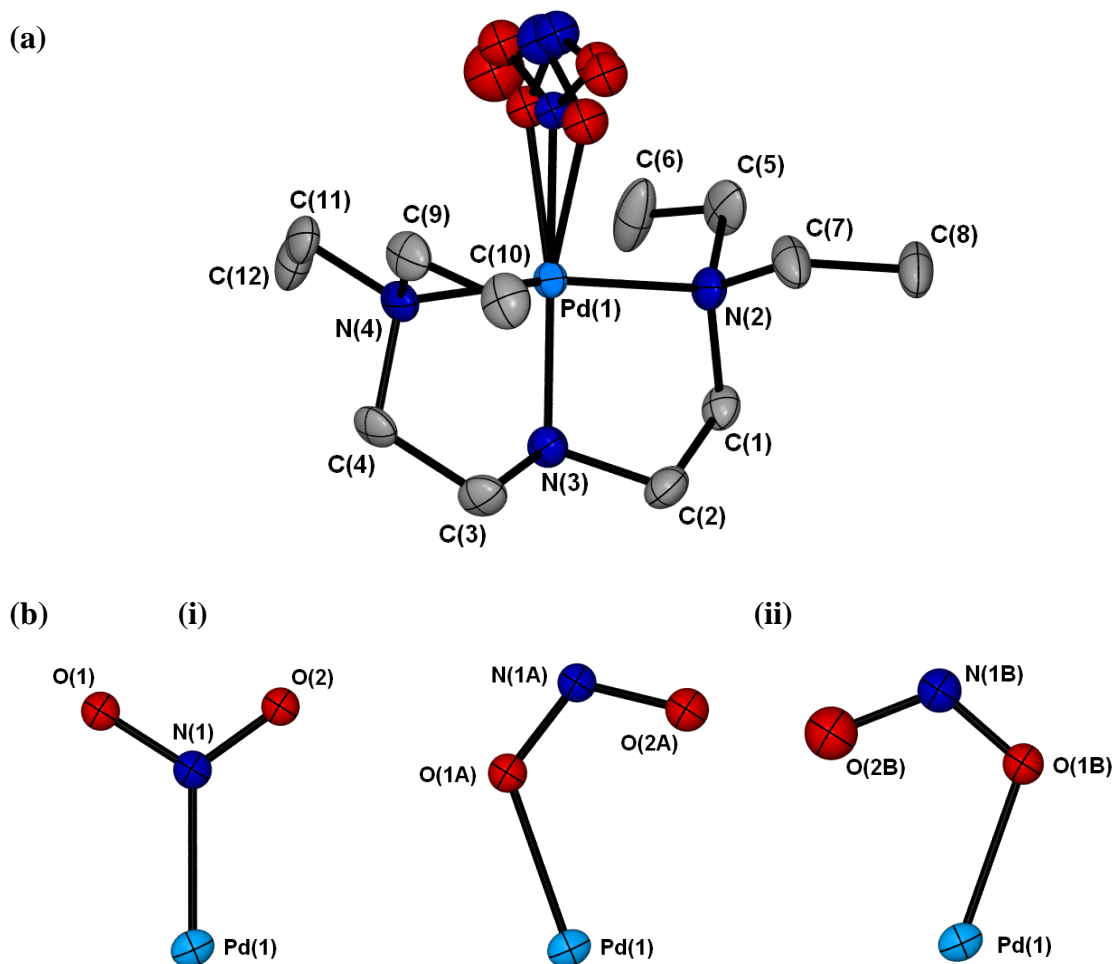
Figure 4.10: (a) Single-crystal X-ray structure for the MS state of [2] showing the atomic arrangement for the cation, ellipsoids at 50% probability and hydrogen atoms removed for clarity. **(b)** Atomic arrangements for nitrite isomers, (i) GS nitro-(η^1-NO$_2$) and (ii) disordered MS nitrito-(η^1-ONO) components.

The same crystal was irradiated further and subsequent datasets show that a photostationary state is reached after 3 h, with a maximum excitation of 73%. The excitation level remains constant when the crystal is held at 100 K in the dark, confirming the ES to be metastable. The diffraction quality is reduced after photoactivation, particularly at higher resolution, suggesting some crystal decay on irradiation. Crystal data for both the GS and MS structures are given in Table 4.11.

Figure 4.11 displays the photodifference map for [2]. Negative electron density surrounding the nitro-(η^1-NO$_2$) ligand, represented by red contours, confirms the reduction of this isomer on photoactivation, while green contours show an increase in electron density at the positions of O(1A), O(1B), N(1A) and N(1B), confirming the production of the MS. There is some overlap between the positions of O(2A), O(2B) and the GS oxygen atoms, which could explain why no positive electron density is evident at these positions despite being expected from the MS structure.

Table 4.11: Crystal data for the GS and photoactivated MS structures of [2]

	Ground State	400 nm Metastable State
Photoconversion	0%	73%
Temperature	100(2) K	100(2) K
Radiation source	Synchrotron	Synchrotron
Wavelength	0.77490 Å	0.77490 Å
Empirical formula	C36 H51 B1 N4 O3 Pd1	C36 H51 B1 N4 O3 Pd1
Formula weight	705.02	705.02
Crystal size	0.05 x 0.04 x 0.02 mm^3	0.05 x 0.04 x 0.02 mm^3
Crystal system	Monoclinic	Monoclinic
Space group	$P2_1/n$	$P2_1/n$
Unit cell dimensions	a = 12.5938(7) Å α = 90° b = 9.5609(6) Å β = 94.5260(10)° c = 29.0970(17) Å γ = 90°	a = 12.570(3) Å α = 90° b = 9.643(3) Å β = 94.735(4)° c = 28.983(8) Å γ = 90°
Volume	3492.6(4) Å^3	3501.2(16) Å^3
Z	4	4
Density (calculated)	1.341 M g m^{-3}	1.337 M g m^{-3}
Absorption coeff. μ	0.571 mm^{-1}	0.647 mm^{-1}
F(000)	1480	1480
R(int)	0.0753	0.1122
R1 (obs. data)	0.0469	0.0650
wR2 (all data)	0.1374	0.1773
Reflections (indep.)	10617	7398
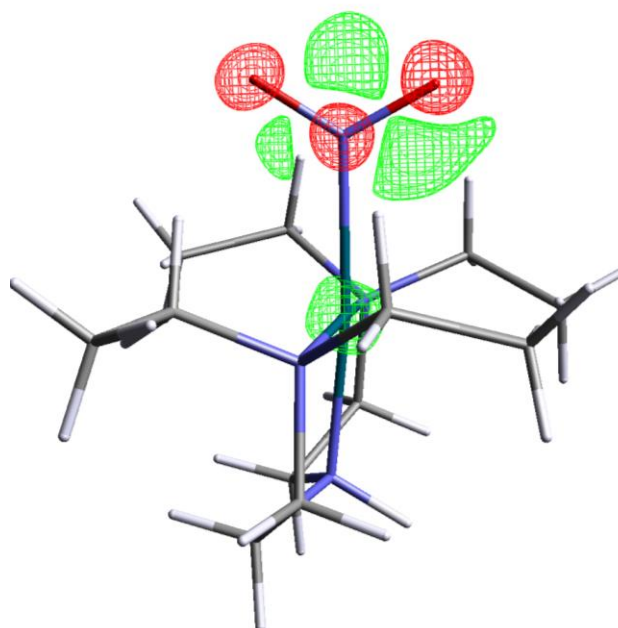
Figure 4.11: Photodifference map showing the change in Fourier electron density distribution between the GS and MS of [2]; red = negative contours at -2.5 eÅ^{-3}, green = positive contours at +1.6 eÅ^{-3}

Finally, variable temperature parametric studies were conducted to determine the MS range. The overall nitrito-(η^1-ONO) occupancy remains constant on warming from 100 to 180 K, but a slight reduction is observed by 200 K. At 220 K and above the *endo*-nitrito isomer can no longer be detected and the cation returns to its 100% nitro-(η^1-NO$_2$) GS. Table 4.12 gives the excitation achieved in all photocrystallographic experiments with [2].

Table 4.12: Crystallographically determined ratios of nitro and nitrito linkage isomer components in [2] as a function of irradiation time

Irradiation time / h	Temp / K	Refined Occupancy			
		GS nitro-(η^1-NO$_2$)	MSa nitrito-(η^1-ONO)	MSb nitrito-(η^1-ONO)	Overall MS nitrito-(η^1-ONO)
0	100	1.00*	0.00*	0.00*	0.00*
1	100	0.32(1)	0.48(1)	0.20(1)	0.68(2)
2	100	0.29(1)	0.51(1)	0.20(1)	0.71(2)
3	100	0.27(1)	0.51(1)	0.22(1)	0.73(2)
3.5	100	0.27(1)	0.51(1)	0.22(1)	0.73(2)
3.5	160	0.26(1)	0.53(1)	0.21(1)	0.74(2)
3.5	180	0.27(1)	0.51(1)	0.22(1)	0.73(2)
3.5	200	0.34(1)	0.46(1)	0.20(1)	0.66(2)
3.5	220	1.00*	0.00*	0.00*	0.00*

* No esd is reported for full occupancy or zero occupancy as these ratios were not refined

Crystal Packing and Sterics

The overall packing arrangement is largely unchanged on excitation; the crystal retains the same $P2_1/n$ space group and the photoactivated structure closely resembles that shown in Figure 4.9. There is a small increase of 0.25% ($\Delta V = 8.6(17)$ Å^3) in the unit cell volume, which is smaller than the increase found for complex [1] upon photoactivation (§ 4.1). The difference is still statistically significant however, with a value of $\Delta V / \sigma(\Delta V) = 5.21$ when the 3σ rule is applied. Interestingly, Table 4.11 shows the cell expansion to be anisotropic, increasing only in the *b*-axis while the *a*- and *c*-axes both decrease slightly on photoactivation. This anisotropy is indicative that the cell changes result from the isomerisation, as both the nitro – nitrito rearrangement and the extension of the hydrogen bonded cation chains occur along the *b*-direction. Additionally, calculations again determine some void space in the photoexcited structure. Voids in the MS structure comprise 1.8% of the unit cell volume (62.33 Å^3), which is slightly less than that found in the GS despite the small increase in unit cell volume.

GS nitro-(η^1-NO$_2$)   MSa nitrito-(η^1-ONO)   MSb nitrito-(η^1-ONO)
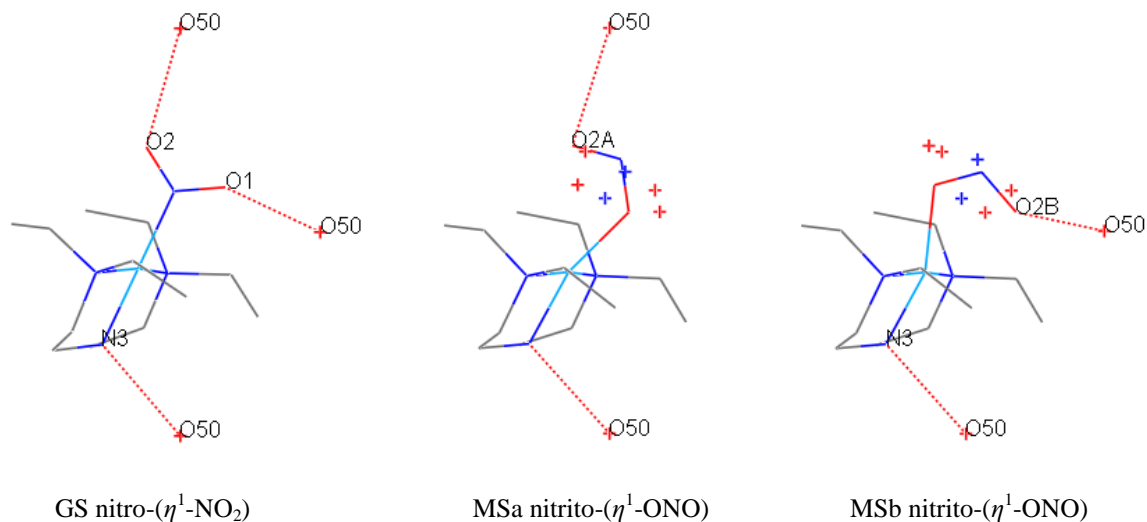
Figure 4.12: Changes in hydrogen bonding to the cation following photoactivation of [2]

Photoconversion between the isomers necessarily disrupts the hydrogen bond network in [2]. Figure 4.12 and Table 4.13 describe the hydrogen bond changes on excitation. Interactions between the nitro-(η^1-NO$_2$) ligand and the water molecule, O(50)…O(2) and O(50)…O(1), are broken upon conversion to the nitrito-(η^1-ONO) isomer and are replaced by new hydrogen bonds between O(50) and the unbound oxygen atoms of the disordered nitrito groups, O(2A) and O(2B). There is a small variation in D…A contacts to the nitro isomer between GS and MS, as expected due to expansion of the lattice on photoactivation. A better comparison to describe hydrogen bond changes caused by the photoisomerisation is made between GS nitro and MS nitrito D…A distances. Figure 4.12 shows that comparison should be made between (i) GS O(50)…O(1) and MS O(50)…O(2B), and (ii) GS O(50)…O(2) and MS O(50)…O(2A) distances. For (i), a significant reduction of 0.38(2) Å is observed, while for (ii) a small change of +0.04(1) Å is found that is within error and so insignificant. In general, the shorter interaction (i) formed upon photoactivation should have a stabilising effect on the MS *endo*-nitrito isomer. Full hydrogen bond data for the MS are recorded in Table 2, Appendix 2.

Table 4.13: Changes in hydrogen bond D…A distances in the cation following photoactivation of [2]

	Isomer	GS / Å	MS / Å
N(3)-H(3)...O(50)	N/A	2.87(1)	2.90(1)
O(50)-H(50B)...O(2) **#1**	Nitro-(η^1-NO$_2$)	2.90(1)	2.99(2)
O(50)-H(50A)...O(1) **#2**		2.88(1)	2.79(2)
O(50)-H(50B)...O(2A) **#1**	Nitrito-(η^1-ONO)	N/A	2.94(1)
O(50)-H(50A)...O(2B) **#2**		N/A	2.50(2)

Symmetry operations for equivalent atoms: **#1** = (x, y-1, z)   **#2** = (-x+1/2, y-1/2, -z+3/2)

It is interesting that this number of hydrogen bonds must be rearranged in order for linkage isomerisation to occur in [2]. The extra energy required to affect the changes is expected to disfavour the isomerisation reaction, and this could provide some explanation for why excitation does not proceed to 100%. In spite of this, in terms of the literature,[20, 35, 52] 73% is still a relatively high level of single-crystal-to-single-crystal photoconversion and, as such, suggests that the photoreaction in [2] is not strongly limited by the degree of hydrogen bonding to the nitrite group.

Finally, Crystal Explorer fingerprint plots help to assess differences in intermolecular contacts upon photoactivation in [2] (Table 4.14). For these diagrams the Hirshfeld surface is calculated about the isomerising palladium cation only. There is little change between the plots for all contacts confirming that the overall structure is largely unchanged, with the exception of a missing hydrogen bond "spike" for the MS plot (expected at d_i / d_e = 1.1 / 0.8 Å). This is due to the incomplete modelling of the water molecule in the MS structure, as hydrogen atoms could not be located due to the reduction in data quality. Similarly to complex [1], the N…H and O…H contacts relate to changes involving the nitrite ligand, while C…H and H…H contacts represent the rest of the structure. While there are no strong features apparent in the GS N…H plot, a number of new close contacts are formed on excitation, as would be expected on rearrangement of N(1) to N(1A) or N(1B). Changes in the O…H contacts are less pronounced, which is again to be expected as the presence of the two disordered nitrito components causes only a small overall change in the oxygen atom positions. The C…H and H…H plots are near identical for GS and MS structures, indicating that the only differences indicated by these plots are those relating to the isomerising ligands.

Of additional interest is the non-symmetrical appearance of the C…H plot for both GS and MS structures. The d_i / d_e points represent hydrogen atoms on the internal molecule (d_i), *i.e.* the cation, interacting with carbon atoms external to the Hirshfeld surface (d_e). A lack of reciprocal contacts, which would render the plot more symmetrical, indicates that these interactions are only "one-way" across the Hirshfeld surface. This result actually supports the description of the intermolecular interactions given above in Figure 4.9(c), where the C-H…H-C and C-H…π contacts are only observed between a cation and its adjacent anion moieties. As the anions are not encompassed by the calculated Hirshfeld surface, reciprocal contacts will not be represented by the fingerprint plot.

Table 4.14: Crystal Explorer fingerprint plots representing changes in intermolecular contacts to the cation moiety on photoactivation of [2]

	GS	400 nm MS
All Contacts		
N...H contacts		
O…H contacts		
C…H contacts		
H…H contacts		
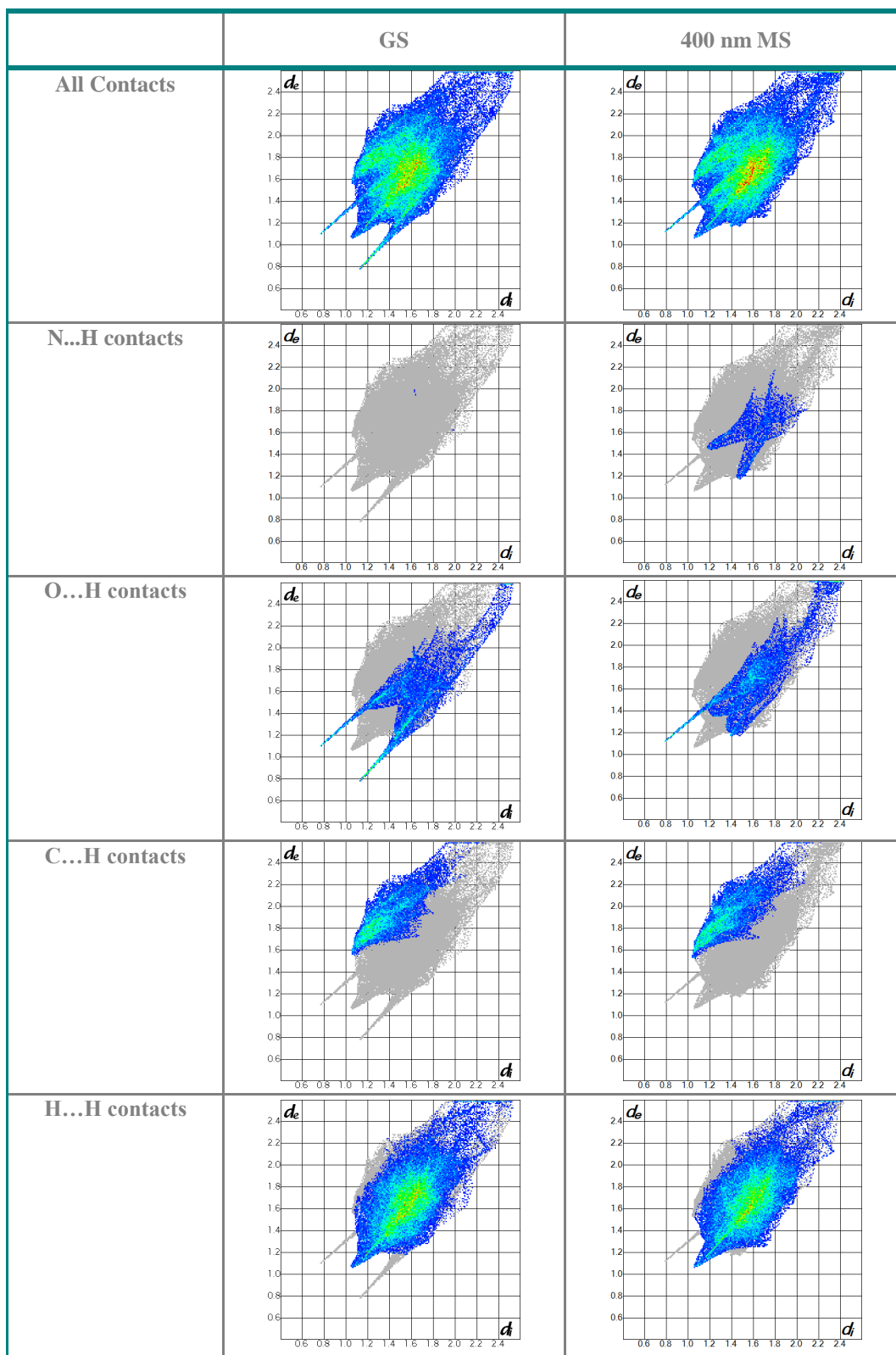
4.1.3 Complex [3]: Nitro-(*N,N,N',N'*-tetraethyldiethylenetriamine)platinum(II) tetraphenylborate hydrate

Complex [3] was synthesised by the procedure outlined in § 9.2.3 and single-crystals obtained *via* slow evaporation from a tetrahydrofuran / toluene mixture at room temperature. A crystal was mounted with minimal light exposure and flash cooled to 100 K, before a single-crystal X-ray dataset was collected.

Crystal Structure and Bonding

Complex [3] is isostructural with [2], crystallising in the same monoclinic space group $P2_1/n$ with one platinum cation, one tetraphenylborate anion and one solvent water molecule in the asymmetric unit. The metal centre adopts square planar geometry with a RMS deviation of 0.042 from the plane for Pt(1), N(1), N(2), N(3) and N(4). Figure 4.13 shows the slight distortion from the perfect square planar arrangement at platinum, due to restrictions imposed by the chelating amine ligand. The fourth coordination site is occupied by the nitrite ligand, which is bound solely as the nitro-(η^1-NO$_2$) isomer in this flash cooled structure. Crystal data are given in Table 4.16.
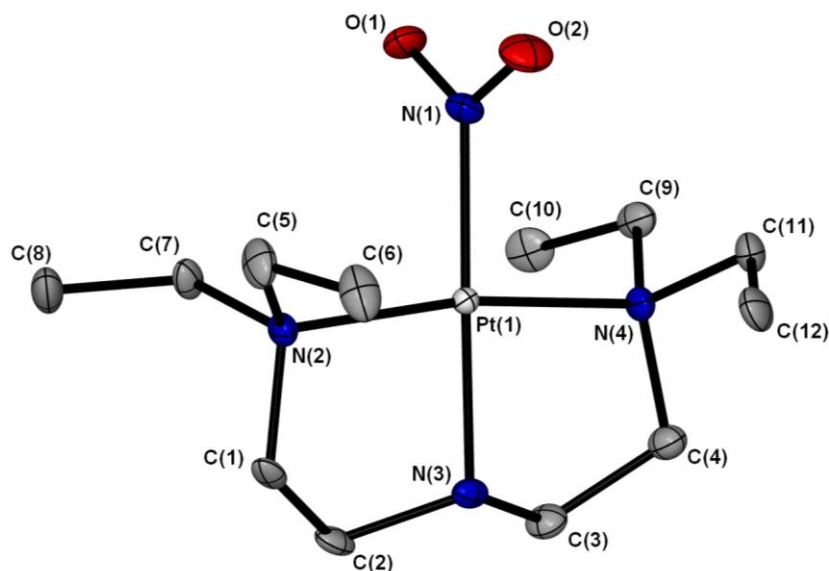
Figure 4.13: Single-crystal X-ray structure showing the atomic arrangement for the platinum cation in the flash cooled GS of [3]. Ellipsoids set a 50% probability and hydrogen atoms removed for clarity

Crystal Packing and Sterics

As complex [3] is isostructural with its palladium analogue [2], the crystal packing arrangement is identical to that described by Figure 4.9, with each cation involved in several of close contacts with neighbouring anion moieties. The platinum cations in [3] are linked by a similar hydrogen bond network to that shown in Fig 4.9(b), again comprising of $D_1^1(2)$ and $C_2^2(6)$ motifs with hydrogen bonds similar within error to those of [2] (Table 1, Appendix 3). This comparison is perhaps unsurprising, considering that the radii of Pd(II) and Pt(II) are similar.[133] It is again evident that the nitrite group is involved in several intermolecular interactions in the GS nitro-(η^1-NO_2) structure, which could be unfavourable for photoconversion in the complex.

However, as for [2], void space calculations indicate the presence of small voids in the flash cooled GS of [3], when the static crystal structure is considered. Using a probe radius of 1.2 Å and grid spacing of 0.1 Å void space comprising 2.0% of the unit cell volume (70.3 Å^3) is calculated, indicating that, on average, there exists some free space within the lattice that potentially could assist the atomic rearrangement necessary for linkage isomerisation.

Steady-State Photocrystallography

A solid-state UV/vis spectrum was recorded for [3] (Figure 1, Appendix 3) and used to identify suitable excitation wavelengths for photocrystallographic studies with the system. A wavelength in the tail of the largest, MLCT absorption was chosen as, from previous results, this is expected to induce maximum photoconversion.[23, 71, 130] As such, a wavelength of 365 nm was selected.

The flash cooled crystal structure obtained for [3] was used as the GS for photocrystallographic experiments. The same crystal was then held at 100 K and subjected to 1 h irradiation with 365 nm light, *in-situ* on the diffractometer, before a second single-crystal X-ray dataset was collected in the absence of external light. After 1 h of irradiation the system was found to be partially excited, with 27% of the crystal now adopting *endo*-nitrito-(η^1-ONO) coordination (Figure 4.14).

The crystal was irradiated further, and repeat datasets show that conversion is increased with irradiation time, with a maximum excitation of 51% achieved after a total of 8 h. This value remained constant when the crystal was held at 100 K in the dark, showing the photostationary state to be metastable at this temperature. The diffraction quality is reduced for the MS, suggesting some crystal degradation. Table 4.16 gives crystal data for the GS and MS structures.
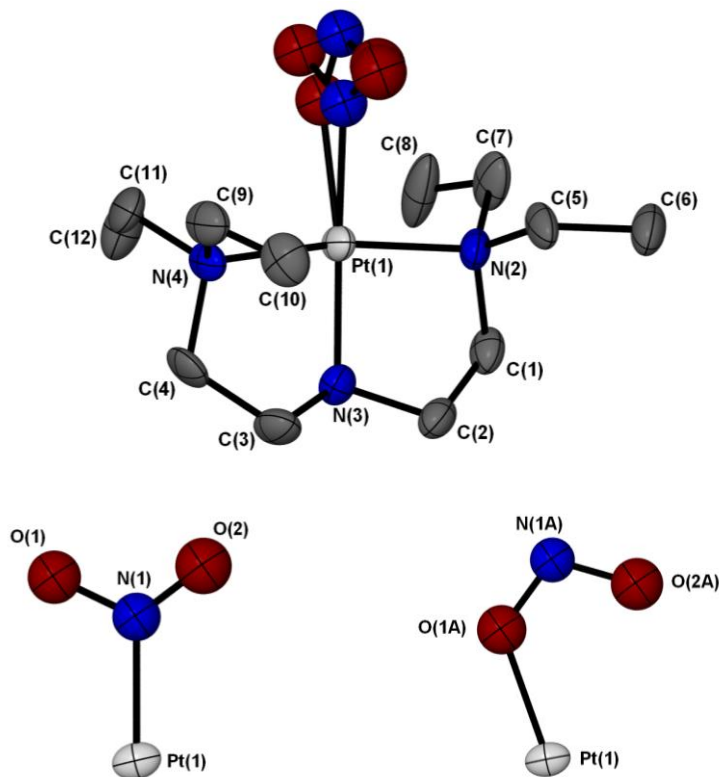
Figure 4.14: (a) Single-crystal X-ray structure showing the atomic arrangement of the cation in the photoactivated structure of [3], ellipsoids at 50% probability and hydrogen atoms removed for clarity. **(b)** Individual arrangements for nitro-(η^1-NO$_2$) and nitrito-(η^1-ONO) isomers of the photoactivated structure.

Table 4.16: Crystal data for GS and photoactivated MS structures of [3]

	GS	365 nm MS
Photoconversion	0%	51%
Temperature	100(2) K	100(2) K
Radiation source	Mo K$_\alpha$	Mo K$_\alpha$
Wavelength	0.71073 Å	0.71073 Å
Empirical formula	C36 H51 B1 N4 O3 Pt1	C36 H51 B1 N4 O3 Pt1
Formula weight	793.71 g mol^{-1}	793.71 g mol^{-1}
Crystal size	0.40 x 0.20 x 0.05 mm^3	0.40 x 0.20 x 0.05 mm^3
Crystal system	Monoclinic	Monoclinic
Space group	$P2_1/n$	$P2_1/n$
Unit cell dimensions	a = 12.6422(3) Å $\quad$ b = 9.5442(2) Å $\quad \beta$ = 94.411(2)° $\quad$ c = 29.0475(6) Å	a = 12.6131(5) Å $\quad$ b = 9.6446(5) Å $\quad \beta$ = 94.720(5)° $\quad$ c = 28.9293(16) Å
Volume	3494.48(13) Å^3	3507.3(3) Å^3
Z	4	4
Density (calculated)	1.509 Mg m^{-3}	1.503 Mg m^{-3}
Absorption coeff. μ	4.055 mm^{-1}	4.041 mm^{-1}
F(000)	1608	1608
R(int)	0.0751	0.0655
R1 (obs. data)	0.0408	0.0614
wR2 (all data)	0.0724	0.1357
Reflections (indep.)	10660	7143

The presence of the nitrito-(η^1-ONO) isomer is confirmed by the photodifference map (Figure 4.15). Red contours surrounding the atoms of the nitro-(η^1-NO$_2$) ligand indicate negative electron density, confirming the reduction of this isomer on photoactivation. Simultaneously, green contours at the expected positions of O(1A) and N(1A) show the increase in electron density as the MS is produced. The fact that no positive electron density is observed at the expected position of O(2A) is explained by the fact that atoms O(2) of the GS and O(2A) of the MS share approximately the same position, therefore little change in the electron density is seen in this region. The smaller area of negative electron density at O(2), in comparison to those at atoms N(1) and O(1), further supports this explanation.
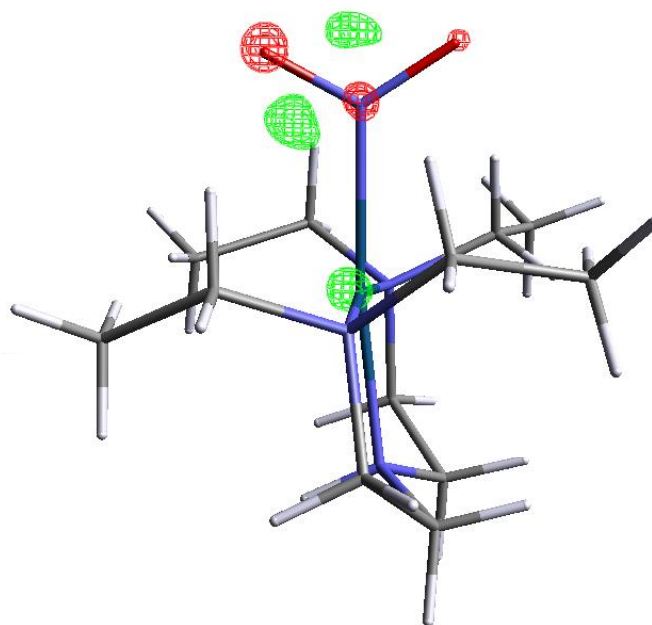
Figure 4.15: Photodifference map for the platinum cation in [3], showing the change in Fourier electron density between the GS and MS; red = negative contours at -6.5 eÅ^{-3}, green = positive contours at +3.5 eÅ^{-3}

Finally, variable temperature parametric studies were conducted with [3] to determine the MS range. The relative occupancies of the two linkage isomers varies slowly on raising the temperature, with the occupancy of the nitrito-(η^1-ONO) isomer decreasing from 51% at 100 K, to 44% by 240 K. On heating to 260 K however, the system reverts to its 100% nitro GS configuration, showing that the MS limit for complex [3] exists between 240 and 260 K. The relative occupancy levels for each of the two linkage isomers, as refined from the X-ray data, for all of the photocrystallographic experiments with [3] are given in Table 4.17.

Table 4.17: Crystallographically determined ratios of nitro and nitrito linkage isomer components in photocrystallographic experiments with [3]

Experiment type	Temperature / K	Irradiation time / h	Refined Occupancy	
			Nitro-(η^1-NO$_2$)	Nitrito-(η^1-ONO)
GS	100	0	1.00*	0.00*
MS	100	1	0.73(1)	0.27(1)
MS	100	4	0.54(1)	0.46(1)
MS	100	8	0.49(1)	0.51(1)
VT	160	8	0.49(1)	0.51(1)
VT	180	8	0.51(1)	0.49(1)
VT	200	8	0.52(1)	0.48(1)
VT	220	8	0.54(1)	0.46(1)
VT	240	8	0.56(1)	0.44(1)
VT	260	8	1.00*	0.00*

* No esd is reported for full occupancy or zero occupancy as these ratios were not refined

Crystal Packing and Sterics

As expected the overall structure shows little change, excepting the nitro – nitrito rearrangement. The crystal remains in the same $P2_1/n$ space group and only a small change in the unit cell is observed, with an increase of 0.37% ($\Delta V = 12.8(3)$ Å^3) on photoactivation. This increase is statistically significant, with a value of $\Delta V / \sigma(\Delta V) = 38.8$ when the 3σ rule is applied. As determined for isostructural [2], the unit cell changes in [3] are anisotropic, with an increase observed in the *b*-axis and small decreases for both *a* and *c* parameters. The increase along *b* is again in line with the direction of nitro – nitrito isomer conversion and so indicates that the unit cell expansion is a result of the isomerisation. In addition, void space calculations conducted on the static crystal structure determine that void space still exists within the lattice following photoactivation. For [3] there is little change in the amount of free space available in the static crystal lattice between GS and MS photostationary structures, with voids comprising 68.7 Å^3 (2.0% of the unit cell) determined for the MS structure that are identical to those calculated in the GS. This result indicates that the amount of void space available in the lattice is not directly affected by nitro – nitrito linkage isomerism in [3].
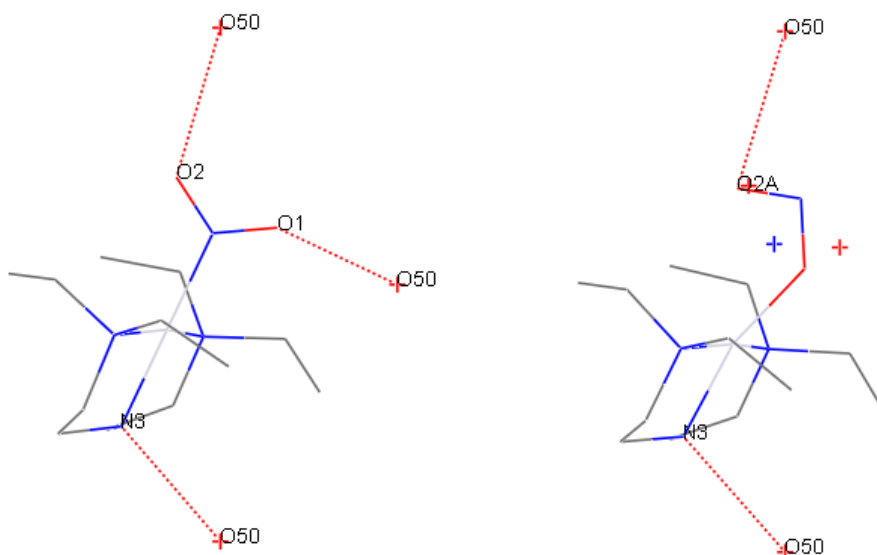
Figure 4.16: Changes in hydrogen bonding to the cation following photoactivation of [3]

In contrast to the analogous palladium complex [2], in [3] one hydrogen bonding interaction is lost upon photoactivation, due to the fact that only one nitrito-(η^1-ONO) orientation is present in the MS (Figure 4.16). Table 4.18 shows that this D…A distance, O(50)…O(2A), is longer in the MS structure than the corresponding GS interaction, O(50)…O(2), and overall the number and length of favourable interactions to the nitrite group is reduced following photoactivation. Full hydrogen bond data for the MS structure are given in Table 2, Appendix 2.

Table 4.18: Changes in hydrogen bond D…A distances in the cation following photoactivation of [3]

	Isomer	GS / Å	MS / Å
N(3)-H(3)...O(50)	N/A	2.88(1)	2.91(1)
O(50)-H(50B)...O(2) **#1**	Nitro-(η^1-NO$_2$)	2.90(1)	2.94(3)
O(50)-H(50A)...O(1) **#2**		2.88(1)	2.76(2)
O(50)-H(50B)...O(2A) **#1**	Nitrito-(η^1-ONO)	N/A	3.04(3)

Symmetry operations for equivalent atoms: **#1** = (x, y-1, z) **#2** = (-x+1/2, y-1/2, -z+3/2)

Finally, Crystal Explorer fingerprint plots are used to assess the changes in intermolecular interactions on photoactivation, and again the plots are similar to those observed for complex [2]. The plots displayed in Table 4.19 are calculated for a Hirshfeld surface encompassing the isomerising cation moiety only. The overall fingerprint plot is largely similar for GS and MS structures, confirming that the overall crystal structure is largely unchanged on excitation in agreement with crystal packing comparisons made previously. Additionally, the C…H and H…H plots do not change on excitation and the only key differences are found for N…H and O…H contacts. These observations agree with those made for complex [2] and indicate that the only changes in close contacts on photoactivation are those involving the isomerising ligands.

Table 4.19: Crystal Explorer fingerprint plots showing changes in intermolecular contacts to the cation moiety on photoactivation of [3]

	GS	365 nm MS
All Contacts		
N...H contacts		
O…H contacts		
C…H contacts		
H…H contacts		
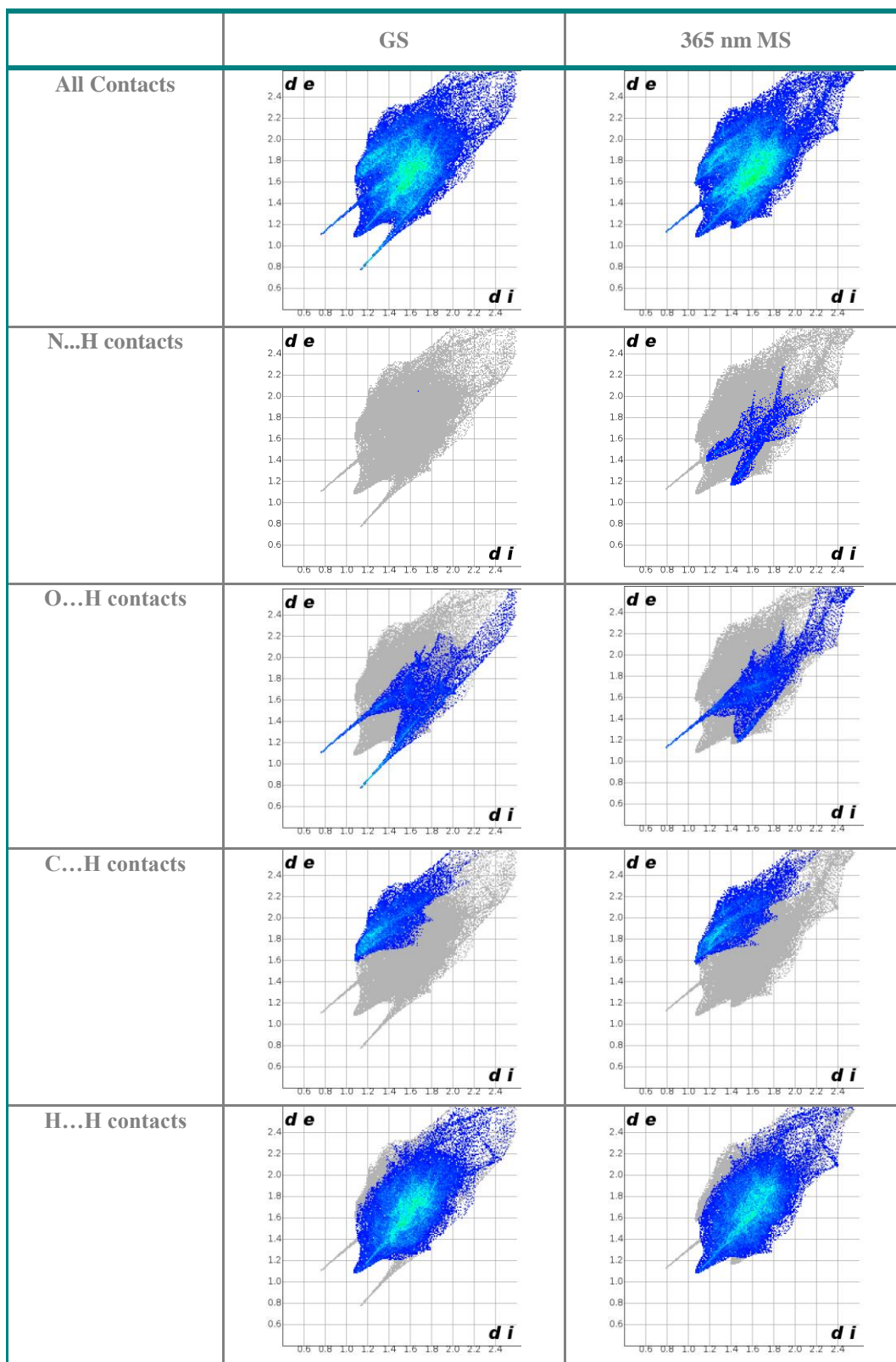
4.1.4 Comparisons: Complexes [1] to [3]

Complexes [1], [2] and [3] are related in terms of their constituent components: all contain a *N,N,N',N'*-tetraethyldithethylenetriamine ancillary ligand and nitrite ligand capable of nitro – nitrito isomerism, but significantly they differ in the choice of transition-metal (TM) centre. The result of moving down Group 10 is a change in the coordination number and therefore the charge on the photoactive species, which necessarily causes a change in crystal form from complex [1] to that of [2] and [3]. In addition, whilst complex [1] is not solvated, [2] and [3] are both hydrate species. The three complexes are nevertheless worthy of comparison and trends in their isomerism behaviour will be discussed in terms of the four factors identified in Chapter 2 as key potential influences on the solid-state isomerisation process: steric strain, electronic structure, kinetic and light absorption properties.

Crystallisation Geometries

A first point of comparison between complexes [1] to [3] can be made between the geometric arrangements they preferentially crystallise into under ambient conditions. This relates both to the coordination geometry at the metal and the preferred isomeric arrangement of the ambidentate nitrite ligand, and in both cases complex [1] is set apart from its heavy metal analogues.

Firstly, the fact that nickel complex [1] adopts octahedral geometry, while [2] and [3] (palladium and platinum respectively) are square planar, is an unsurprising result of moving to second and third row TMs. Group 10 metals have a d^8 electron configuration and therefore most commonly adopt either octahedral or square planar geometry depending on the crystal field. Where no very strong field ligands are present, in first row complexes such as [1] the crystal field is relatively weak and so the ligand field splitting parameter (Δ) is low enough for an octahedral environment to be favourable. By contrast values of Δ are higher for heavy TMs, in line with the expansion of the $4d$ and $5d$ orbitals, and this increase in crystal field strength favours a low spin, square planar geometry in [2] and [3].[133]

Harder to explain is the interesting behaviour of the monodentate nitrite group in [1], crystallising with a mixture of nitro-(η^1-NO$_2$) and *endo*-nitrito-(η^1-ONO) isomers under ambient conditions. [2] and [3] crystallise as exclusively nitro-(η^1-NO$_2$) isomers, which is unsurprising considering the affinity of heavier TMs, as "softer" lewis acids, for the "softer" nitrogen donor as expected by the HASB concept.[134, 135] Invoking the same theory, having a smaller atomic radius but still the same charge, nickel(II) is thought of as a "harder" lewis acid than palladium(II) or platinum(II).

Therefore, it should be unsurprising that the nickel complex shows more affinity for the nitrito-(η^1-ONO) arrangement than either [2] or [3]. However, not only does [1] crystallise with the nitro-(η^1-NO$_2$) form as the major isomer, but thermal studies with [1] also show the *N*-bound arrangement is thermodynamically more stable. Both of these observations do not correlate with an explanation based solely on HASB theory, and as such suggest there are further factors which contribute to the choice of linkage isomer upon crystallisation for the nickel system.

Photoconversion Level

The second and most important comparison is the maximum level of photoexcitation that can be achieved for each complex in the single-crystal. At this point it is important to highlight that the crystal structure of [1] differs from that of isostructural [2] and [3] and indeed while [1] is a neutral species, [2] and [3] contain a charged photoactive species accompanied by a bulky tetraphenylborate anion. Any comparisons, particularly in reference to the crystal packing and steric interactions in the systems, are therefore made in light of these limiting factors.

The maximum level of photoexcitation achievable in the single-crystal decreases with increasing size of the heavy metal centre, with Ni > Pd > Pt. A possible explanation for this behaviour relates to the kinetic lability of ligands bound to a TM complex, which is expected to decrease on moving down a group. Complexes of the 4*d* and 5*d* metals are generally considered to be less labile than their 1st row counterparts, due to both the increase in crystal field splitting (increased Δ) and the relative increase in metal – ligand bond strength expected on descending the group.[133] However, this explanation considers only the metal centre and does not account for the effect of the overall crystalline environment, which must also strongly influence the solid-state reaction.

A number of parameters may be compared in order to assess the degree to which steric strain within the crystal lattice affects the level of photoconversion in [1] to [3]. Firstly, in all three systems the unit cell volume is observed to increase on photoactivation, with a change of $\Delta V =$ +2.04% for [1] and even smaller differences of $\Delta V =$ +0.25% and +0.37% for [2] and [3] respectively. In this case a direct comparison may be made between the volume of the whole unit cell, as all three systems have Z = 4. For each complex the increase is small in terms of the overall crystal volume, and the overall crystal packing arrangement is largely unchanged between GS and MS for [1] to [3], indicating there is little strain induced in the lattice as a result of linkage isomerisation. This correlates with the fact that single-crystal integrity is maintained during all of the photocrystallographic experiments reported in this section, and could suggest some steric control of the solid-state isomerisation. As discussed in Chapter 1, the Topochemical Postulate[1]

states that a solid-state reaction will occur with the minimal amount of atomic or molecular movement. An application of the postulate in this case would assert that, where the structure is most dominated by inert fragments, *i.e.* the sterically demanding ancillary amine ligand, and additionally for [2] and [3] the inclusion of a bulky tetraphenylborate anion, then the maximum level of photoconversion will be achieved in that system. The atomic rearrangements required for the isomerisation of the much smaller nitrite ligand can therefore occur without disrupting the overall crystal structure, causing only small changes in the lattice volume. However, the argument does not account for the fact that the maximum photoconversion is achieved for complex [1], but at the same time this system undergoes the significantly larger volume change. A smaller proportion of the neutral complex [1] is made up of inert auxiliary fragments than that of the tetraphenylborate salts [2] and [3]. Therefore, if the photoisomerisation was governed solely by the steric factors already discussed above, it would be expected that [2] and [3] should achieve the higher level of conversion.

Next, a comparison of changes in intermolecular interactions can also provide insight into the level of steric strain induced in each crystal system and the degree to which this correlates with the conversion trend. A comparison of hydrogen bonding changes on excitation is of interest to help to rationalise the conversion levels observed. While no intermolecular hydrogen bonds are disturbed on 100% nitro – nitrito conversion in complex [1], a number of interactions must be broken and reformed to facilitate the rearrangement in [2] and [3]. As hydrogen bonds are considered to be comparatively strong interactions, these changes should cost energy and so provide a barrier to the photoreaction. This may help to explain, in part, the lower conversion level observed in both [2] and [3].

A comparison of the amount of void space present in the overall lattice for [1] to [3], between GS and MS structures, shows no correlation with the level of photoactivation achieved. However, the void space tool in Mercury can additionally be used to assess the relevance of the "reaction cavity" concept to the solid-state linkage isomerism reaction. This concept was discussed in Chapter 2 with reference to the design of the crystalline species for study in this project, and it was highlighted that high levels of photoactivation are expected to correlate with small changes in the reaction cavity region. For the present analysis, an assessment of the reaction cavity volume is made in Mercury by removing the atoms of the nitrite ligand and conducting a void space calculation. For [2] and [3], the void space already present is subtracted from the value obtained for these calculations, in order to provide the volume for the reaction cavity region only. In this

instance, values have also been normalised by dividing by the value of Z, to represent the reaction cavity for a single photoactive molecule. Results are displayed in Table 4.20.

Table 4.20: Reaction cavity volumes calculated from steady state photocrystallographic data for *N,N,N',N'-*tetraethylditheylenetriamine complexes

Complex	Conversion / %	Reaction cavity (% of unit cell volume / Z)		
		GS	MS	ΔV_c
[1]	100	2.1	2.3	0.2
[2]	73	1.0	1.3	0.3
[3]	51	0.5	1.2	0.7

In reference to the reaction cavity discussion in Chapter 2, the value of greatest relevance is the change in reaction cavity volume on photoexcitation in each system, ΔV_c. ΔV_c is found to increase with decreasing photoconversion level, with the largest change occurring in platinum complex [3]. This observation correlates effectively with the rationale of both the reaction cavity principle and the Topochemical Postulate, showing that the system displaying the highest level of photoconversion causes the least disruption to the surrounding crystal lattice on photoactivation.

Whilst this last observation appears to neatly rationalise the trend for photoactivation in species [1] to [3], when taking the above observations as a whole it is evident that arguments based on steric strain alone are insufficient to fully explain the complexities of the solid-state nitro − nitrito linkage isomerisation reaction. It is evident that a more complicated interplay of a number factors are likely to govern the overall outcome of the photoreaction in each system, and other potential steric, electronic and kinetic influences will be further investigated in later sections.

4.2. Other Nickel – Triamine Complexes

Following on from the success of complex [1], a number of nickel – nitrite complexes containing other triamine ancillary ligands were investigated for their potential to display high levels of nitro – nitrito conversion. Candidates were identified from the literature (Search 1) and novel systems were also synthesised. The findings of these studies are reported here-in, with analysis focussing on the techniques shown to be most effective in § 4.1.

4.2.1. Complex [4]: Dinitro-(*N,N,N',N'',N''*-pentamethyldiethylenetriamine) nickel(II)

Crystal Structure and Bonding

Complex [4] was synthesised by the procedure given in § 9.2.4 and bright green crystals grown from a dichloromethane and propan-2-ol mixture, *via* slow evaporation at room temperature. Several crystals were screened before the most suitable was selected, flash cooled to 100 K and a full, single-crystal X-ray dataset obtained (Figure 4.17).
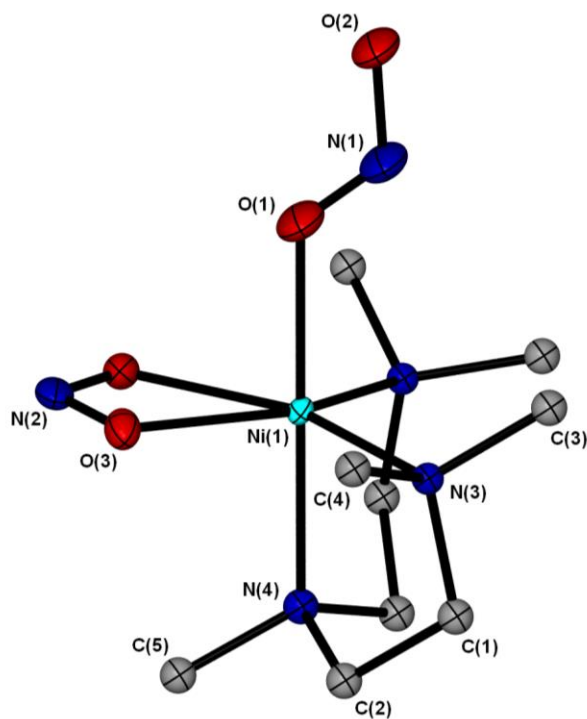
Figure 4.17: Single-crystal X-ray structure for complex [4] showing the atomic arrangement for one disorder component, at 100 K. Ellipsoids at 50% probability and hydrogen atoms removed for clarity

The compound crystallises in the monoclinic space group $P2_1/m$, with half a molecule in the asymmetric unit. The mirror plane runs through the centre of the molecule, bisecting Ni(1), O(1), O(2), N(1), N(2) and N(4), and the second half of the molecule is generated by mirror symmetry. All crystals of [4] screened gave structures that were heavily disordered in the amine auxiliary ligand, with two sites determined for atoms C(1), C(2), C(3), C(4) and N(3). The methyl group C(5) is disordered across the mirror plane, with the second disorder site generated by the crystallographic symmetry. Although the data quality is slightly diminished as a result of this disorder, the atomic connectivity is clearly evident from the X-ray data.

As observed for analogous complex [1], the nickel centre adopts pseudo-octahedral geometry, surrounded by one tridentate amine ligand and one bidentate nitrito-(η^2-O,ON) group. The last coordination site is occupied by a monodentate nitrite ligand, but in [4] this group adopts an *exo*-nitrito-(η^1-ONO) arrangement in the initial, flash cooled structure. Contrasting with the geometry of complex [1], the amine ligand is bound in a facial arrangement, causing the two nitrite ligands to adopts sites approximately *cis* to one another. Crystal data are given in Table 4.21.

Table 4.21: Single-crystal X-ray data for the flash cooled structure of [4]

Temperature	100(2) K
Radiation source	MoK$_\alpha$
Wavelength	0.71073 Å
Empirical formula	C4.5 H11.5 N2.5 Ni0.5 O2
Formula weight	162.02
Crystal size	0.20 x 0.20 x 0.05 mm^3
Crystal system	Monoclinic
Space group	$P2_1/m$
Unit cell dimensions	$a = 7.128(5)$ Å $b = 10.153(5)$ Å $\beta = 94.889(5)°$ $c = 10.295(5)$ Å
Volume	742.3(7) Å^3
Z	4
Density (calculated)	1.450 M g m^{-3}
Absorption coeff. μ	1.324 mm^{-1}
F(000)	344
R(int)	0.0850
R1 (obs. data)	0.0527
wR2 (all data)	0.1518
Reflections (indep.)	2144
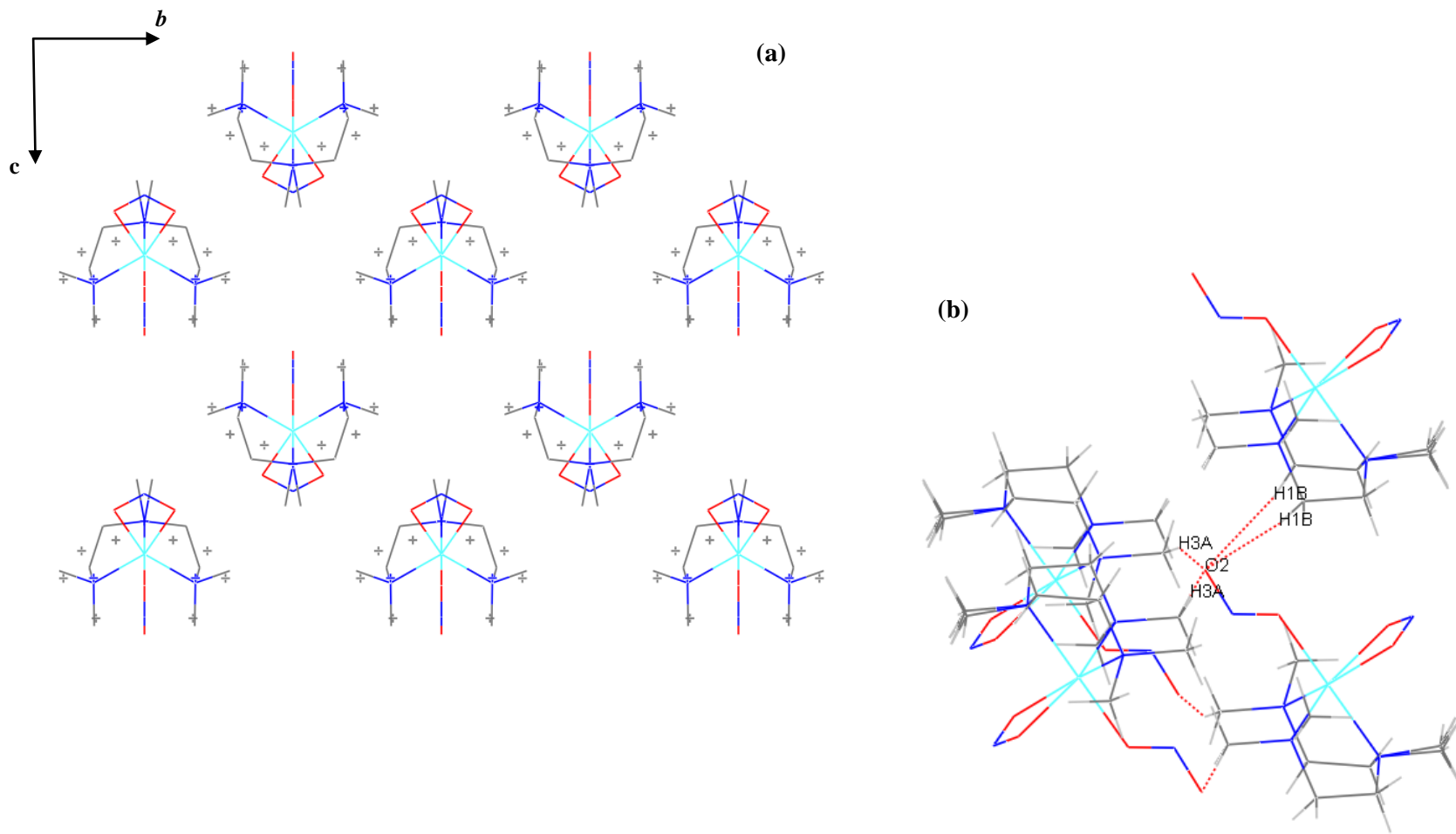
Figure 4.18: Crystal packing diagrams for complex [4]. **(a)** Overall packing arrangement viewed down the *a*-axis, *b*-axis horizontal. **(b)** Short contacts to the *exo*-nitrito ligand, forming links between layers of molecules.

The crystal packing arrangement for complex [4] is shown in Figure 4.18. The two molecules in the unit cell are offset from one another by half a cell length and are related by inversion. This forms rows of similarly oriented molecules running parallel to the crystallographic *b*-axis, with molecules in adjacent rows offset and inverted with respect to one another (Figure 4.18(a)). There are no hydrogen bonds present, but the *exo*-nitrito group is involved in four C-H…O close contact interactions to the amine ligands of nearest neighbour molecules (Figure 4.18(b)). The presence of these interactions indicates the crystal is tightly packed in this region and suggests there is little free space surrounding the nitrite group.

Steady-State Photocrystallography

Numerous recrystallisation attempts were conducted for [4] with a variety of solvent systems and methods, but unfortunately no better quality crystals were obtained. While a GS structure that is already heavily disordered is not ideal for photocrystallographic studies, where successful analysis relies on the clear resolution of small changes between GS and ES structures, the available crystals were sufficient to determine whether [4] undergoes some change on irradiation.

The solid-state UV/vis spectrum for complex [4] was obtained (Figure 1, Appendix 4) and used to guide the selection of a suitable excitation wavelength. A characteristic MLCT absorption band is identified in the data and, as MLCT transitions are shown to be involved in similar isomerisation processes,[71] excitation in the tail region of this band is expected to be most likely to induce a photoreaction.[23, 130] As such, preliminary photocrystallographic experiments were conducted with wavelengths in the region of 400 to 500 nm.

The crystal structure remained entirely unchanged upon photoactivation with 400, 470 or 500 nm LED light at 100 K, suggesting that the *exo*-nitrito-(η^1-ONO) isomer in [4] is photostable, at least under the standard, steady-state experimental conditions used.

In light of these results, and the relatively poor quality of the crystals that could be obtained, no further photocrystallographic experiments were conducted for complex [4].

4.2.2. Complex [5]: Dinitro-(*N*-isopropyldiethylenetriamine)nickel(II)

Crystal Structure and Bonding

Complex [5] was synthesised *via* the preparation outlined in § 9.2.5 and purple single-crystals grown by slow evaporation from a propan-2-ol solution. A plate-like single-crystal was flash cooled to 100 K before a standard X-ray dataset was collected (Figure 4.19).
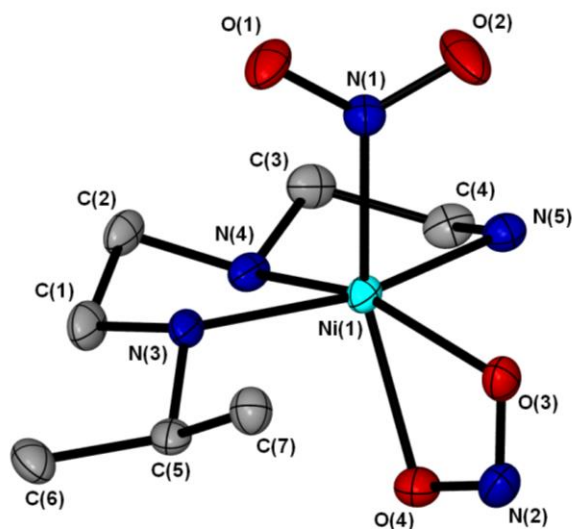
Figure 4.19: Single-crystal X-ray structure showing the atomic arrangement in the flash cooled GS structure of [5] at 100 K. Ellipsoids shown at 50% probability and hydrogen atoms removed for clarity

[5] crystallises in the monoclinic space group $P2_1/c$ with one molecule in the asymmetric unit. The nickel(II) centre is again six-coordinate, bound to one *N*-isopropyldiethylenetriamine group and one monodentate nitrite group, with the pseudo-octahedral coordination sphere completed by a bidentate nitrito-(η^1-O,ON) ligand. The monodentate nitrite ligand is bound solely through nitrogen as the nitro-(η^1-NO$_2$) isomer in this flash cooled structure. As the results of § 4.1 indicate that a nitro-(η^1-NO$_2$) GS arrangement is often susceptible to photoactivation, this system is a promising candidate for photocrystallographic studies. Crystal data are given in Table 4.22.

Figure 4.20(a) describes the packing arrangement for [5], showing molecules aligned in rows with adjacent rows inverted with respect to one another. Molecules within a row are linked by a N(4)-H(4C)…O(3) hydrogen bond, forming $C_1^1(4)$ chains parallel to the *c*-axis. The amine ligands are oriented such that their isopropyl branches point directly into channels between rows, with isopropyl groups of adjacent rows oriented towards one another due to inversion. As such, the rows can be thought of in pairs extending along the *a*-axis. Because inverted molecules are offset by 0.25 of a unit cell however, steric hindrance is minimised between these bulky alkyl groups.
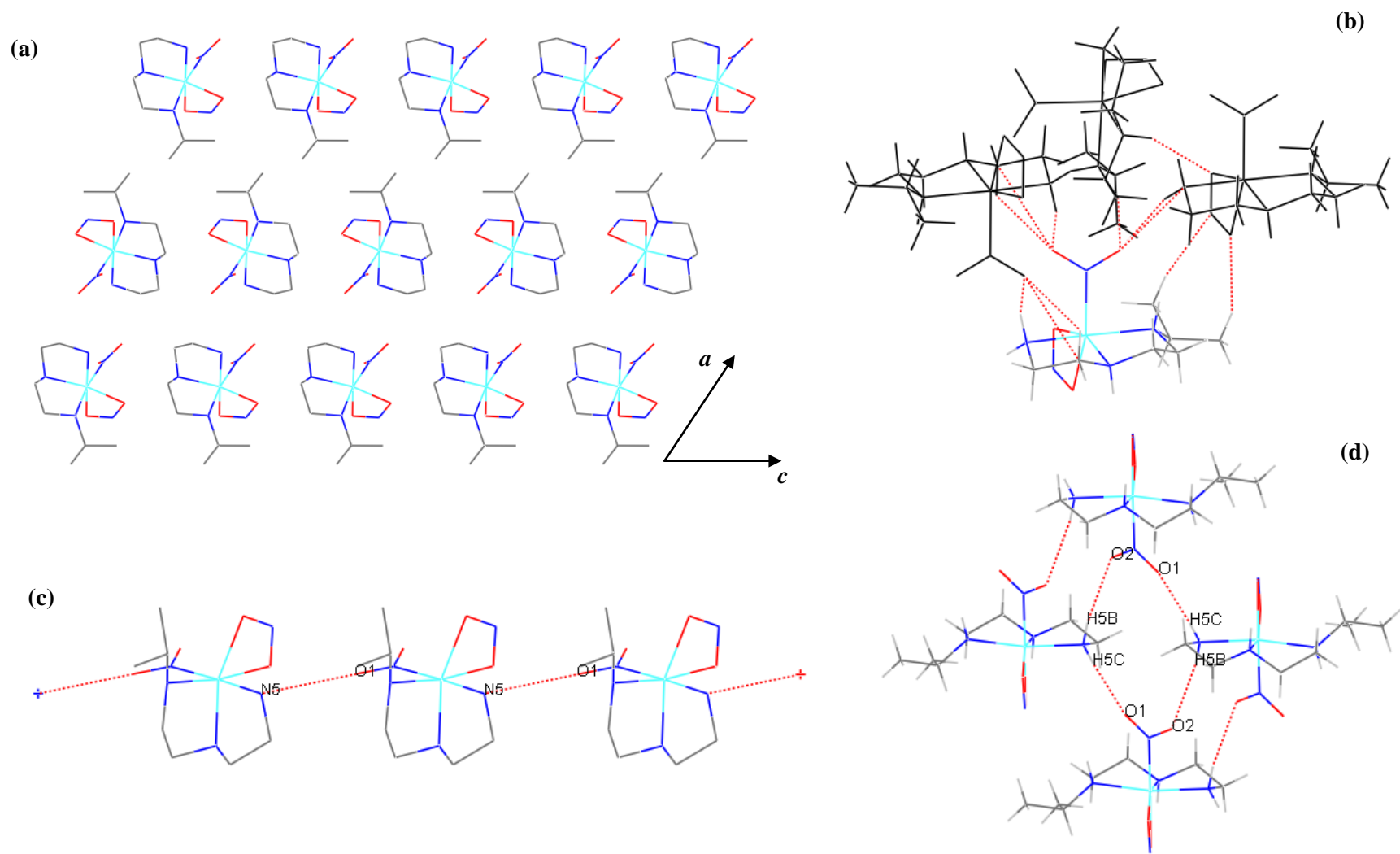
Figure 4.20: Crystal packing diagrams for [5]: **(a)** packing arrangement viewed along the *b*-axis, *c*-axis horizontal, **(b)** close contacts to the nitro-(η^1-NO$_2$) ligand, **(c)** 1-D hydrogen bonded chains parallel to the *b*-axis, viewed along the *a*-axis, **(d)** hydrogen bonded ring motif involving nitro-(η^1-NO$_2$) groups, viewed in the *a-b* plane

The nitro ligands point away from the isopropyl groups, into separate channels on the opposite side of each row. Figure 4.20(b) shows a number of short intermolecular contacts exist between each nitrite and three neighbouring molecules, suggesting the structure is tightly packed in these regions. In addition, each nitro group is involved an extended network of intermolecular hydrogen bonds: while a N(5)-H(5C)…O(1) interaction forms one-dimensional $C_1^1(5)$ chains parallel to the b-axis (Figure 4.20(c)), additionally a N(5)-(H5B)…O(2) hydrogen bond is formed across the channel between rows, extending parallel with the a-axis. The combination of these interactions constructs a $R_4^4(12)$ ring motif in the a-b plane, as shown in Figure 4.20(d). Full hydrogen bonding tables for complex [5] are given in Table 1, Appendix 5.

The presence of short contacts to the nitro ligand could suggest only a restricted amount of linkage isomerism will be possible in [5], particularly as hydrogen bonds to the nitrite are moderately strong[132] and these must be overcome before any structural rearrangement can occur. However, these observations should be considered carefully as they are made only on the static, time-averaged structure and no consideration of dynamic behaviour in the lattice is made.

Steady-State Photocrystallography

A suitable excitation wavelength for photocrystallographic experiments was chosen according to the solid-state UV/vis spectrum (Figure 1, Appendix 5). A strong absorption for [5], occurring in the soft UV to visible region, is characteristic of an MLCT transition and, as such processes are expected to be involved in the isomerisation,[71] excitation under this peak is most likely to induce excitation. As such, wavelengths of 365, 400 and 430 nm were chosen for test experiments. The most promising response was achieved with 400 nm light, expectedly near the tail of the band,[23, 130] and a full photocrystallographic study was conducted for [5] at this wavelength.

A single-crystal was held at 100 K and irradiated *in-situ* for 1 h with 400 nm LED light, using the experimental set-up described in § 3.2.2. A subsequent X-ray dataset revealed that photoinduced linkage isomerism had occurred in the system, with 53% of the crystal now converted to an *endo-*nitrito-(η^1-ONO) isomer (Figure 4.21). The diffraction quality was noticeably reduced following irradiation of the crystal, suggesting that light exposure had caused crystal degradation. Longer irradiation periods showed no further increase in the excitation level and in fact caused further degradation of the sample, eventually preventing structure solution. As such 53% is the maximum level of photoconversion that can be achieved in [5], after 1 h irradiation.
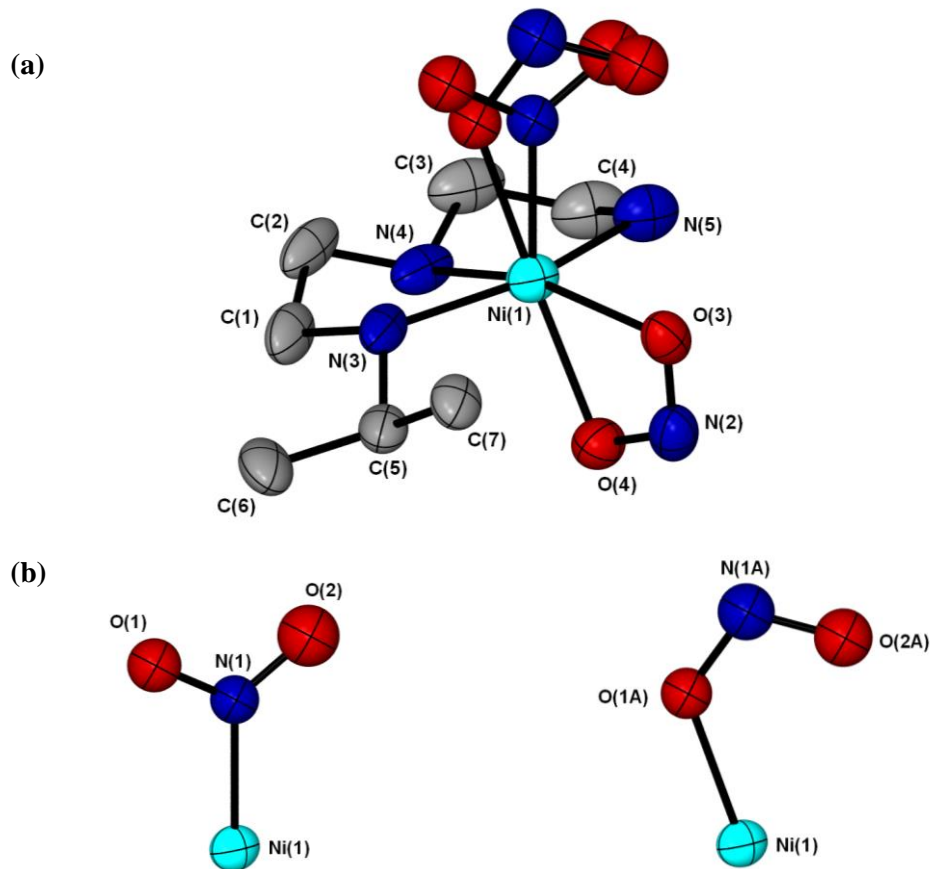
Figure 4.21: **(a)** Single-crystal X-ray structure showing the atomic arrangement in the MS structure of [5], following irradiation with 400 nm LED light at 100 K, **(b)** Individual arrangements for the nitro-(η^1-NO$_2$) and *endo*-nitrito-(η^1-ONO) isomers present

A second crystal was also irradiated for 1 h and a repeat dataset revealed a similar level of photoconversion, showing the result is reproducible. When the crystal was held at 100 K in the dark no change in the excitation level was observed, indicating that the nitrito-(η^1-ONO) isomer is metastable at this temperature. Table 4.22 gives the crystal data for the MS structure.

A photodifference map was constructed between the GS coordinates and photoactivated data (Figure 4.22), which clearly shows the production of the nitrito-(η^1-ONO) isomer. Regions of red contours surrounding the positions of the nitro-(η^1-NO$_2$) isomer indicate negative electron density and confirm the reduction of this isomer on irradiation, while the green contours at the expected positions of O(1A) and N(1A) represent positive electron density, showing the production of the nitrito-(η^1-ONO) isomer. As discussed for previous photoactivated systems in this Chapter, a lack of positive electron density at the expected position of O(2A) is likely explained by the fact that there is little change in oxygen atom position upon rearrangement from O(2) to O(2A).

Table 4.22: Crystal data for the flash cooled GS and photoinduced MS structures of [5], at 100 K

	Ground State	400 nm Metastable State
Photoconversion	0%	52%
Temperature	100(2) K	100(2) K
Wavelength	0.71073 Å	0.71073 Å
Empirical formula	C7 H19 N5 Ni1 O4	C7 H19 N5 Ni1 O4
Formula weight	295.98	295.98
Crystal size	0.3 x 0.3 x 0.04 mm^3	0.3 x 0.3 x 0.04 mm^3
Crystal system	Monoclinic	Monoclinic
Space group	$P2_1/c$	$P2_1/c$
Unit cell dimensions	$a = 15.2858(9)$ Å $b = 6.8724(3)$ Å $\quad \beta = 107.879(6)°$ $c = 12.6927(7)$ Å	$a = 15.856(5)$ Å $b = 6.571(5)$ Å $\quad \beta = 107.920(5)°$ $c = 12.781(5)$ Å
Volume	1269.0(1) Å^3	1267.0(12) Å^3
Z	4	4
Density (calculated)	1.549 M g m^{-3}	1.552 M g m^{-3}
Absorption coeff. μ	1.542 mm^{-1}	1.544 mm^{-1}
F(000)	624	624
R(int)	0.0356	0.0443
R1 (obs. data)	0.0452	0.0522
wR2 (all data)	0.1042	0.1139
Reflections (indep.)	4233	2563
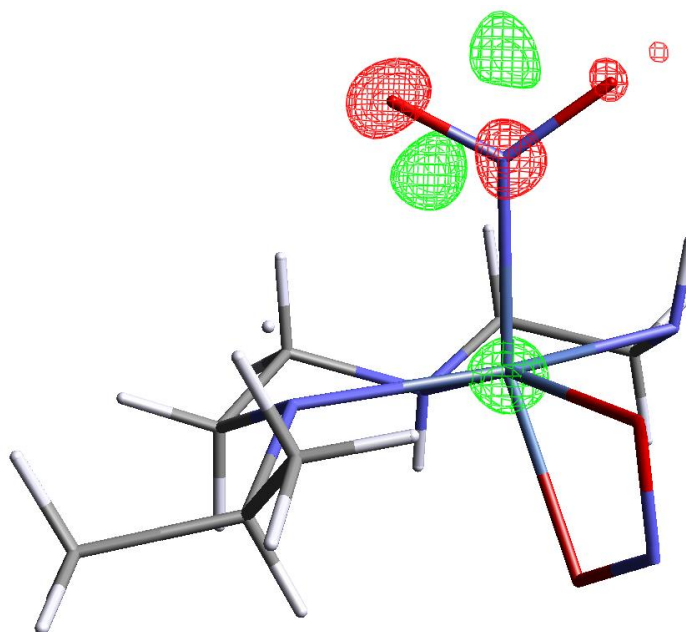
Figure 4.22: Photodifference map for the MS structure of [5], red = –2.7 e Å^{-3}, green = +2.5 e Å^{-3}

Variable temperature parametric studies were then completed with the same crystal, showing that the *endo*-nitrito-(η^1-ONO) isomer in [5] is only metastable over a small temperature range. On heating to 120 K the photoactivated isomer has already begun to decay, with an nitrito occupancy of 48% determined by a steady-state data collection at this temperature. By 140 K the system returns to the 100% nitro-(η^1-NO$_2$) GS arrangement. A full list of linkage isomer occupancies for all photocrystallographic experiments with [5] is given in Table 4.23.

Table 4.23: Crystallographically determined ratios of nitro and *endo*-nitrito isomers in [5] as a function of exposure to 400 nm LED light in steady-state photocrystallographic studies

Irradiation time / h	Temp / K	Refined Occupancy	
		Nitro-(η^1-NO$_2$)	Nitrito-(η^1-ONO)
0	100	1.00*	0.00*
1	100	0.47(1)	0.53(1)
1	120	0.52(1)	0.48(1)
1	140	1.00*	0.00*

* No esd is reported for full occupancy or zero occupancy as these ratios were not refined

Crystal Packing and Sterics

There is little change in the overall structure following photoexcitation; the crystal retains the same *P*2$_1$/*c* space group and the MS packing diagram closely resembles that of Figure 4.20(a), excepting the change in nitrite coordination. Comparison of the GS and MS unit cell parameters reveals that there is a 2.0(12) Å^3 reduction (0.16%) on excitation, which is again contrary to changes observed in all other systems discussed previously in this Chapter. In [5] the changes are anisotropic, with the only reduction occurring along the *b*-axis whilst both the *a*- and *c*-axes expand on irradiation. The reduction of the *b*-axis is in line with the direction of hydrogen bond arrays involving nitro-(η^1-NO$_2$) (Figure 4.20(c) and (d)), so could be a result of the isomerisation. However, no firm conclusions can be based on these observations as in fact the volume reduction is statistically insignificant by the 3σ rule, with value of $\Delta V / \sigma(\Delta V) = 1.67$ (*i.e.* < 3).

Several intermolecular hydrogen bonds are rearranged on nitro – nitrito conversion (Figure 4.23). Two contacts to the GS nitro ligand are broken and replaced by one N(5)-H(5B)...N(1A) bond to the nitrito isomer. No trend is observed for D…A distances, with some lengthening whilst other shorten (Table 4.24). However, the overall rearrangement of four hydrogen bonds into two for the nitrito isomer may suggest why the MS limit is low for [5], as more stabilising interactions exist for the GS. Full hydrogen bond data for the MS are given in Table 2, Appendix 5.

Table 4.24: Changes in hydrogen bond D…A distances following photoactivation of [5]

	Isomer	GS / Å	MS / Å
N(4)-H(4C)...O(3) **#1**	N/A	3.09(1)	3.09(1)
N(3)-H(3C)...O(1)	Nitro-(η^1-NO$_2$)	2.94(1)	3.01(1)
N(5)-H(5B)...O(2)		2.99(1)	2.82(1)
N(5)-H(5C)...O(1) **#2**		2.96(1)	2.83(1)
N(5)-H(5B)...O(2) **#3**		3.31(1)	3.32(1)
N(5)-H(5B)...O(2A)	Nitrito-(η^1-ONO)	N/A	3.05(1)
N(5)-H(5B)...N(1A) **#3**		N/A	3.27(1)

Symmetry operations for equivalent atoms: **#1** = (x ,-y+1/2, z+1/2), **#2** = (x, y+1, z), **#3** = (-x+1, -y, -z+2)
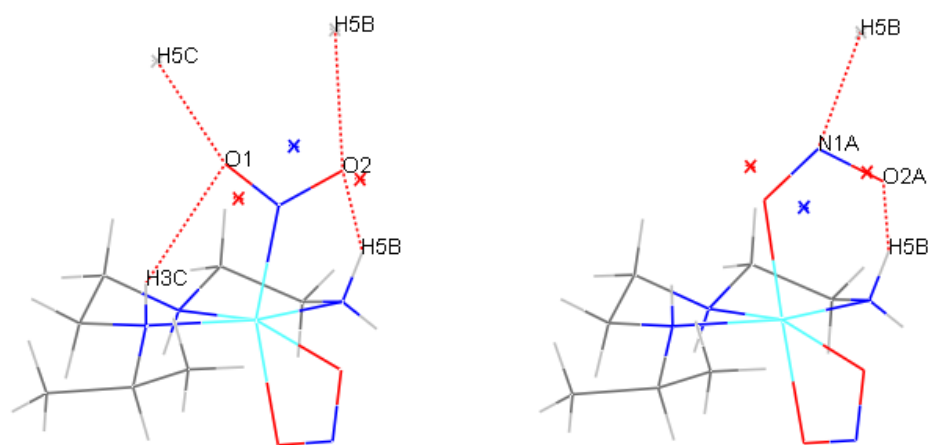
Figure 4.23: Changes in hydrogen bonding following photoactivation of [5]

Finally, Crystal Explorer fingerprint plots are used to assess changes in intermolecular contacts in [5] on photoactivation (Table 4.25). Only three types of close contact occur in [5]: N…H, O…H and H…H interactions. While N…H and O…H contacts necessarily involve the isomerising nitrite ligands, H…H contacts represent the rest of the structure. The overall shapes of the GS and MS plots are noticeably different in the case of [5], suggesting that the structure does change on excitation. However, it is clear by comparing the O…H plots that it is these interactions govern the shape of the overall fingerprint plots. Large difference in O…H contacts between GS and MS structures are due to the numerous hydrogen bond rearrangements, discussed in detail previously. Additionally, N…H contacts become both more frequent and shorter on conversion to the MS, in line with the rearrangement of N(1) to N(1A). The H…H plots, representing the overall structure, show little change between GS and MS and confirm the conclusions made from Mercury packing diagrams that there is little change in the overall crystal structure following excitation.

Table 4.25: Crystal Explorer fingerprint plots showing changes in intermolecular interactions on photoactivation of [5]

	GS	400 nm MS
All Contacts		
N...H contacts		
O…H contacts		
H…H contacts		
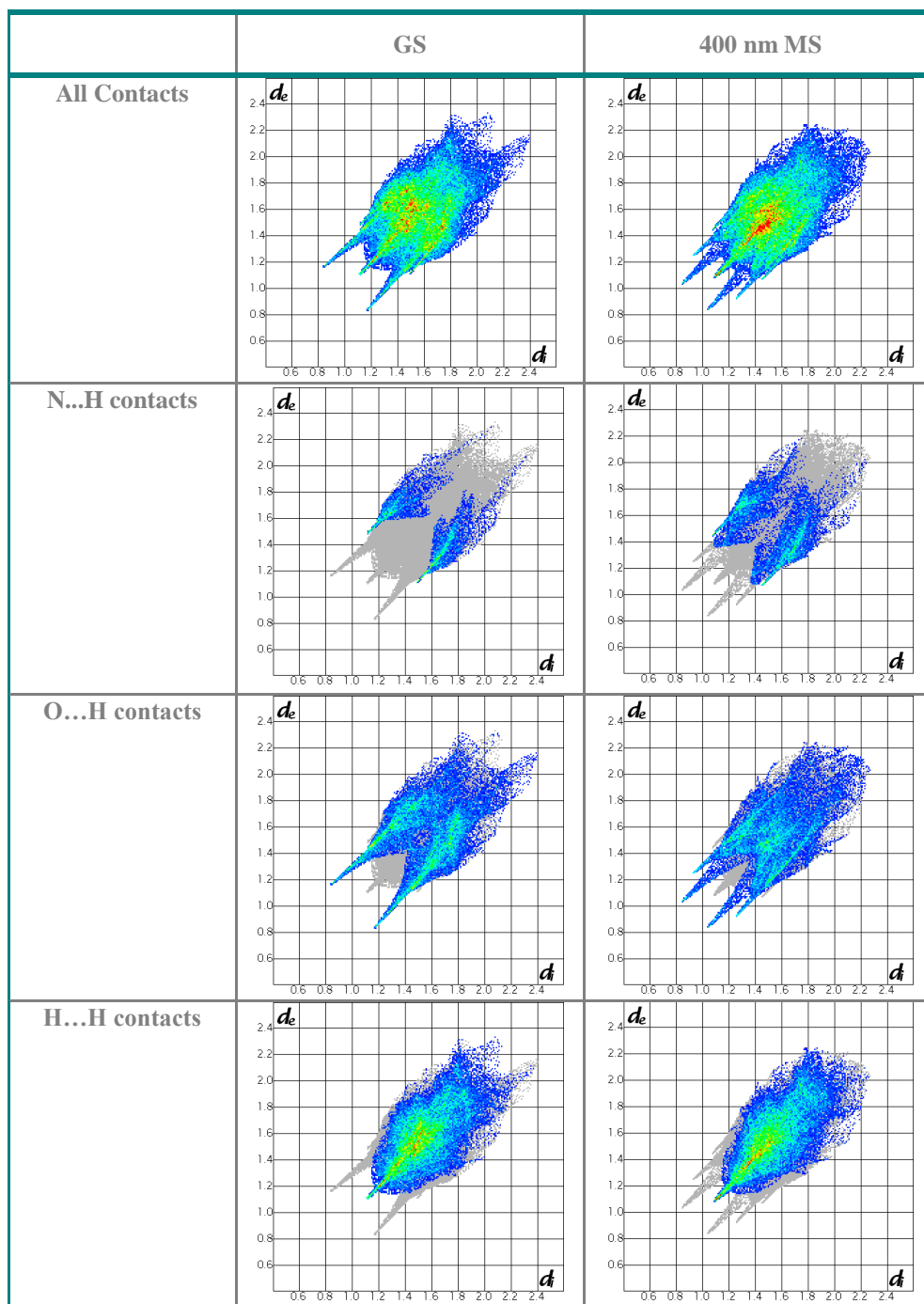
4.2.3. Complex [6]: Dinitro-(2,2'-diamino-*N*-methyldiethylamine)nickel(II)

Crystal Structure and Bonding

Complex [6] was synthesised by the procedure outlined in § 9.2.6. and blue plate-like crystals grown *via* slow evaporation from propan-2-ol. A crystal was mounted with minimal light exposure and flash cooled to 100 K, before a single-crystal X-ray experiment was conducted.
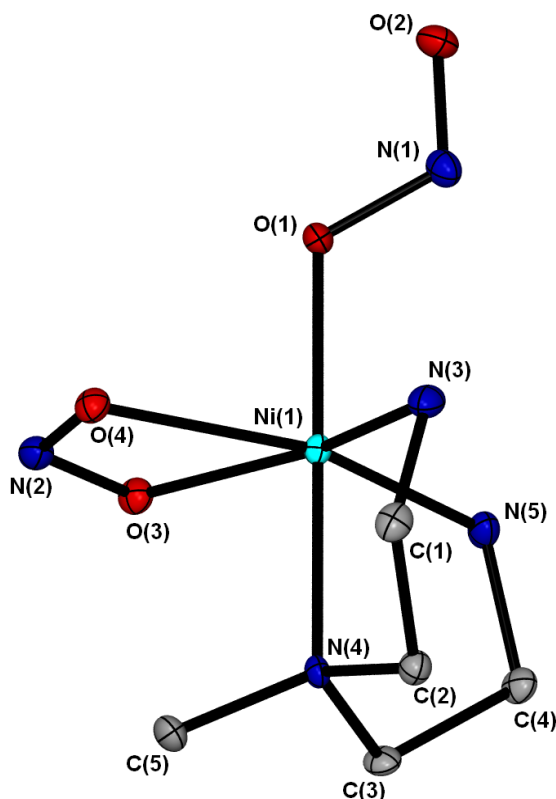
Figure 4.24: Single-crystal X-ray structure for complex [6] showing the atomic arrangement in the flash cooled structure at 100 K. Ellipsoids shown at 50% probability and hydrogen atoms removed for clarity

[6] crystallises in the triclinic space group *P*-1 with a single molecule in the asymmetric unit (Figure 4.24). As observed for analogous nickel – amine complexes the metal centre is six-coordinate, bound to one 2,2'-diamino-*N*-methyldiethylamine ligand, one nitrito-(η^2-O,ON) ligand and with the final site occupied by a second nitrite group coordinated solely as *exo*-nitrito-(η^1-ONO). The complex adopts a distorted octahedral geometry, mostly likely due to strain caused by the bite angle of the tridentate amine ligand. The amine is bound in a facial arrangement, similarly to the analogous complex [4], which is also found to crystallise as an *exo*-nitrito linkage isomer in the GS crystal structure. Crystal data for [6] are given in Table 4.26.

Table 4.26: Single-crystal X-ray data for the flash cooled structure of [6]

Temperature	100(2) K
Radiation source	MoK$_\alpha$
Wavelength	0.71073 Å
Empirical formula	C5 H15 N5 Ni1 O4
Formula weight	267.93 g mol^{-1}
Crystal size	0.30 x 0.20 x 0.02 mm^3
Crystal system	Triclinic
Space group	P-1
Unit cell dimensions	a = 7.2725(5) Å α = 86.610(9)°
	b = 7.3026(8) Å β = 86.295(7)°
	c = 10.1457(11) Å γ = 69.570(8)°
Volume	503.49(8) Å^3
Z	2
Density (calculated)	1.767 M g m^{-3}
Absorption coeff. μ	1.932 mm^{-1}
F(000)	280
R(int)	0.0431
R1 (obs. data)	0.0367
wR2 (all data)	0.0685
Reflections (indep.)	3079

The crystal packing arrangement is displayed in Figure 4.25. The structure packs in layers, with rows of molecules running directly parallel to the crystallographic *b*-axis and adjacent rows stacked along the *c*-direction (Figure 4.25(a)). Only one weaker interaction forms a link between adjacent layers: a C(5)–H(5A)…O(2) contact between the *exo*-nitrito ligand and a methyl group of a molecule from the next layer (Figure 4.25(b)). Within each layer molecules are linked by an extended hydrogen bond network. A $R_2^2(8)$ ring motif, comprising of two symmetry equivalent N(3)–H(3C)…O(4) interactions, firstly groups molecules into hydrogen bonded "dimers" (Figure 4.25(c)). These pairs are then linked to neighbouring units *via* other discrete hydrogen bonds involving acceptor atoms from both mono- and bidentate nitrite ligands (Table 1, Appendix 6).

Steady-State Photocrystallography

Although the analogous *exo*-nitrito complex [4] is photostable under steady-state conditions, test experiments were conducted to determine whether photoisomerisation could be induced in [6]. A solid-state UV/vis spectrum was collected (Figure 1, Appendix 6) and used to guide the choice of excitation wavelength. This indicated that wavelengths between 365 and 470 nm might be suitable for photoactivation in [6], however no photoreaction could be induced. The negative results of photocrystallographic studies with both [4] and [6] indicate that systems crystallising preferentially as the *exo*-nitrito-(η^1-ONO) isomer are stable with respect to photoisomerisation.
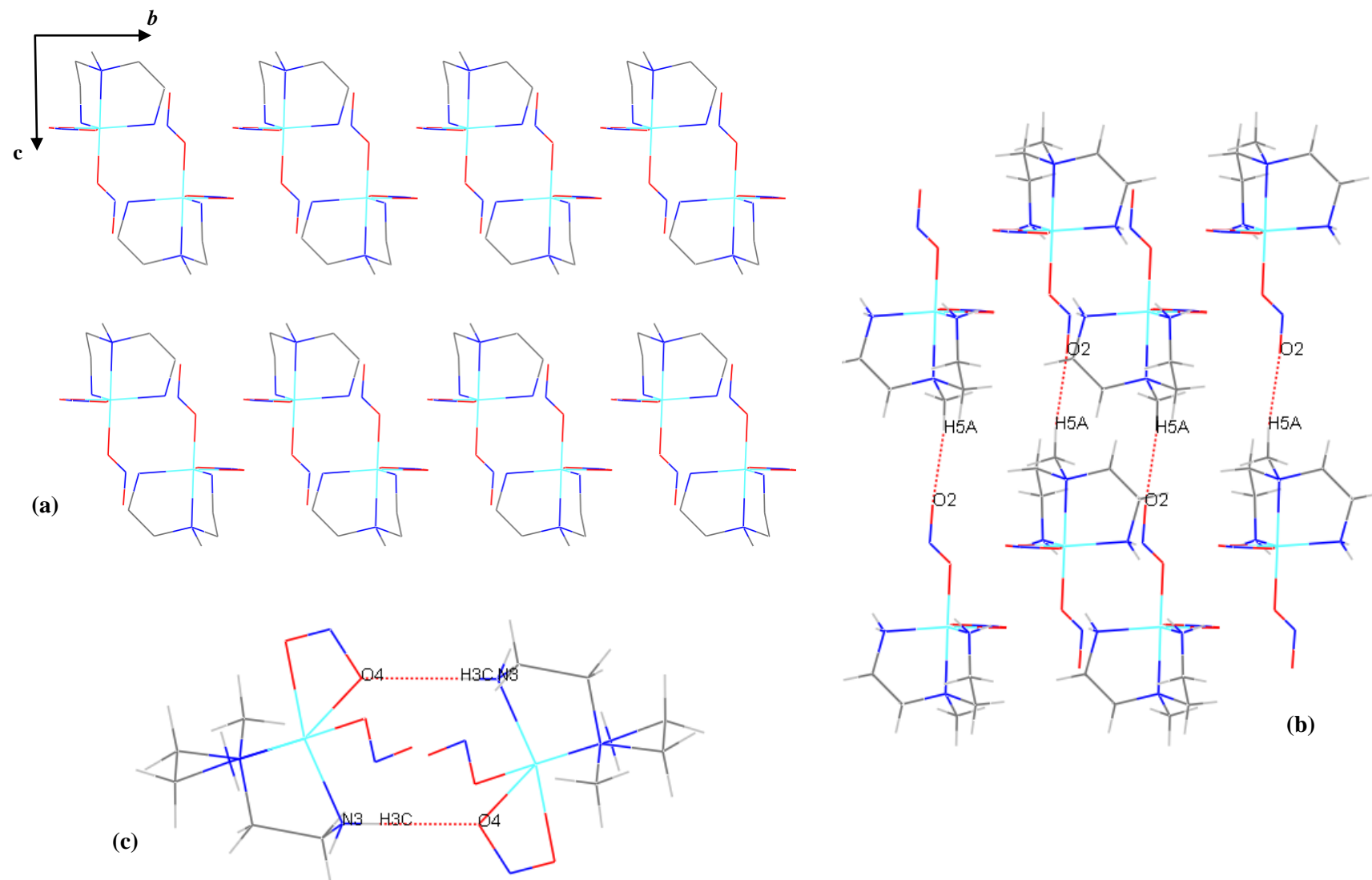
Figure 4.25: Crystal packing arrangement for complex [6]: **(a)** packing diagram, viewed along the *a*-axis, *b*-axis horizontal; **(b)** C-H...O close-contact interactions (red dotted lines) between adjacent layers; **(c)** hydrogen bonded ring motif (red dotted lines) forming hydrogen bonded "dimer" pairs of molecules

4.2.4. Complex [7]: Dinitro-(3,3'-diamino-*N*-methyldipropylamine)nickel(II)

Complex [7] is the first nickel–dipropylamine system investigated in this project and was originally reported by Wen *et. al.* in 1998 (CSD ref. MEHNES). The authors first studied [7] as part of a series of systems thought to follow unusual crystallisation pathways, particularly to understand an apparent preference for conglomerate crystallisation.[136] The potential for linkage isomerism is not discussed in this previous work, making [7] an ideal candidate for the current study.

Crystal Structure and Bonding

[7] was synthesised following the literature,[136] with violet crystals obtained by evaporation from methanol. In comparison with the previous study, a room temperature dataset was first collected.
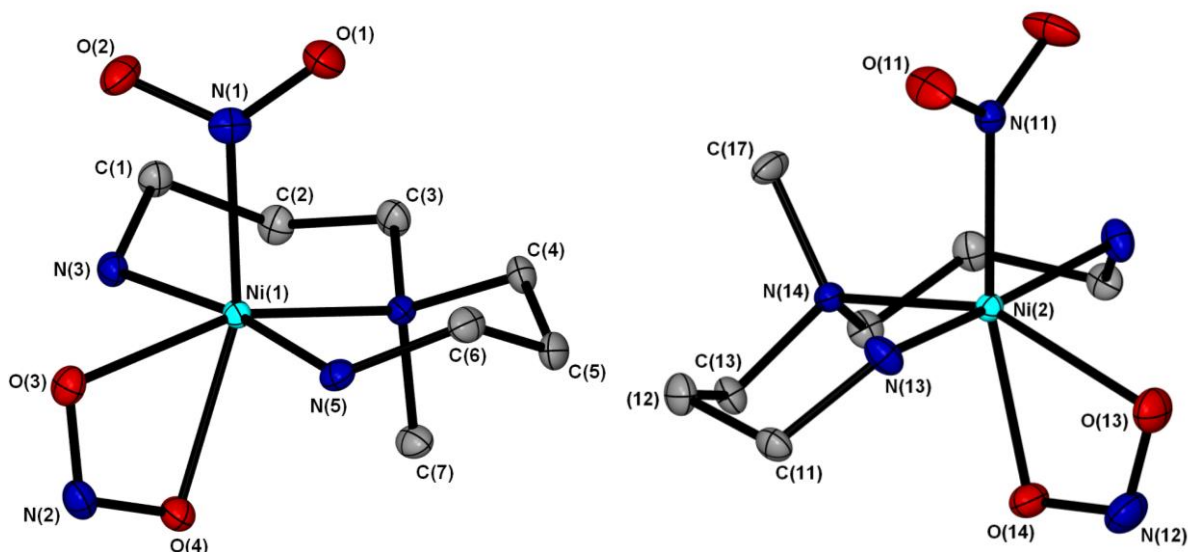
Figure 4.26: Single-crystal X-ray structures for the two independent molecules in the GS structure of [7] at 100 K, molecule A (**right**) situated on a general position and molecule B (**left**) situated at a mirror plane. Ellipsoids at 50% probability and hydrogen atoms and disorder components are removed for clarity.

[7] crystallises in the monoclinic space group $P2_1/m$ with 1.5 molecules in the asymmetric unit, giving a value of Z = 6 (Figure 4.26). While molecule A occupies a general position, molecule B is located on the mirror plane such that the mirror bisects Ni(2), N(11), N(12), N(14), O(13), O(14) and C(17). As such there is a 2 : 1 ratio of A to B molecules in the crystal. Both nickel centres are six-coordinate, bound to one monodentate nitrite, one nitrito-(η^2-O,ON) group and one tridentate amine ligand. Although identical in their constituent components, the two independent molecules are in fact geometric isomers of one another. In molecule A the amine binds meridionally such that the *N*-methyl substituent points downwards away from the monodentate

nitrite. However in molecule B the amine, though also meridionally coordinated, is inverted such that its *N*-methyl group points upwards towards the nitrite. This geometric difference was not identified in the original study, but it provides an explanation as to why the two molecules must adopt crystallographically distinct environments. Wen *et al.* do remark that octahedral Ni(II) species are known to be labile in solution, and this could suggest a formation pathway to this mixed crystal form. The monodentate nitrite ligand adopts nitro-(η^1-NO$_2$) geometry as the major form in both species and, while this is the sole isomer present for molecule B, in molecule A a minor *endo*-nitrito-(η^1-ONO) component is also identified at 22%. No evidence of this partially occupied *endo*-nitrito isomer was reported in the 1998 study. Table 4.27 gives the crystal data.

Table 4.27: Single-crystal X-ray data for the room temperature structure of [7]

Temperature	100(2) K
Radiation source	Mo K$_\alpha$
Wavelength	0.71073 Å
Empirical formula	C7 H19 N5 Ni1 O4
Formula weight	443.97
Crystal size	0.50 x 0.40 x 0.10 mm^3
Crystal system	Monoclinic
Space group	$P2_1/m$
Unit cell dimensions	$a = 7.235(5)$ Å
	$b = 23.768(5)$ Å $\beta = 103.920(5)°$
	$c = 11.072(5)$ Å
Volume	1848(2) Å^3
Z	6
Density (calculated)	1.596 M g m^{-3}
Absorption coeff. μ	1.588 mm^{-1}
F(000)	936
R(int)	0.0265
R1 (obs. data)	0.0305
wR2 (all data)	0.0724
Reflections (indep.)	5760

Figure 4.27(a) describes the crystal packing in the room temperature structure of [7]. Molecules of the same isomer align in rows along the *a*-axis (into the page in Figure 4.27(a)) and there are no strong interactions between molecules within each row. The symmetry-related nitro oxygen atoms O(11) of molecule B are involved in a N(5)-H(5D)…O(11) contact to a neighbouring molecule A. This creates hydrogen bond chains throughout the structure, involving both species and running parallel to the *b*-axis. By contrast, no hydrogen bonds exist to the nitrite in molecule A and these are oriented away from the bulky amine groups. The lack of strong intermolecular contacts to molecule A could suggest why a mix of linkage isomers is found only for this isomer.

114
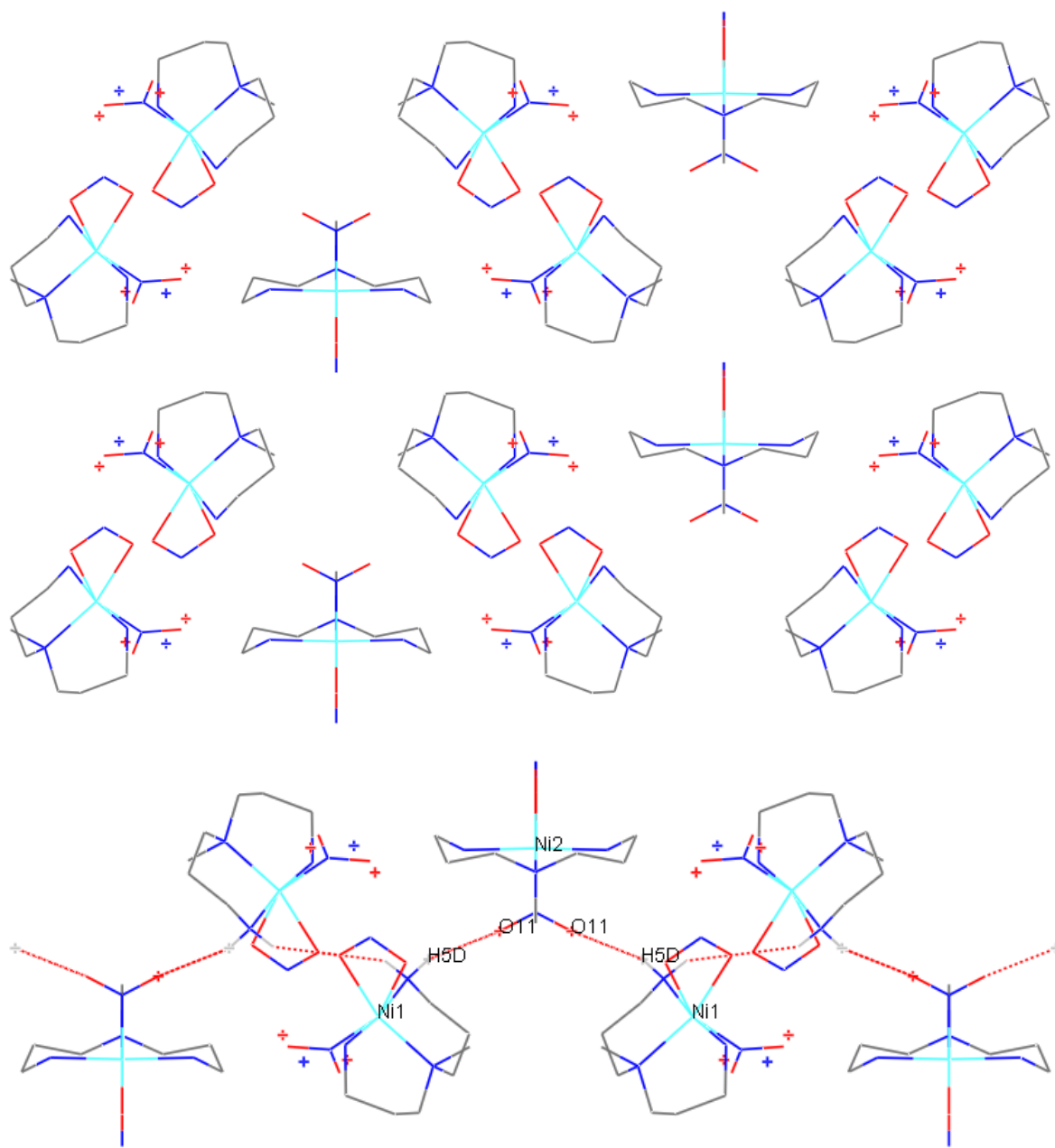
Figure 4.27: (a) Crystal packing arrangement for the room temperature structure of [7], **(b)** hydrogen bonding interactions to the nitro-(η^1-NO$_2$) ligand in molecule B.

Thermal Studies

Given the precedent, set by complex [1], for a thermodynamic equilibrium existing between nitro and nitrito isomers when both are present under ambient conditions, [7] was first the subject of thermal studies to assess the effect of temperature on the nitro : nitrito ratio in molecule A.

The crystal was slowly cooled from 298 to 100 K, *in*-situ on the diffractometer and in the absence of any light. Cooling was paused at regular intervals to allow collection of a full single-crystal X-ray dataset, from which the nitro : nitrito isomer ratio for molecule A was then refined at each temperature. The crystal was held at each stage for 5 min to allow the temperature to equilibrate, before a new experiment was conducted. Table 4.28 collates the results of these studies.

Table 4.28: Crystallographically determined nitro : nitrito ratios for molecule 1 of [7] as a function of temperature on cooling

Temp / K	Occupancy (esd)	
	Nitro-(η^1-NO$_2$)	Nitrito-(η^1-ONO)
298	0.78(1)	0.22(1)
250	0.89(1)	0.11(1)
200	0.96(1)	0.04(1)
150	1.00*	0.00*
100	1.00*	0.00*

* No esd is reported for full occupancy or zero occupancy as these ratios were not refined

The nitro : nitrito ratio was observed to change on cooling, with conversion to the nitro-(η^1-NO$_2$) isomer increasing as the temperature was lowered. By 150 K no evidence of the *endo*-nitrito-(η^1-ONO) isomer could be found in difference maps, confirming that a 100% nitro isomer had been achieved on cooling. As for complex [1], this result indicates the two linkage isomers exist in a thermodynamic equilibrium at ambient temperature and the position of this equilibrium can be shifted by varying the temperature. Once again, the nitro-(η^1-NO$_2$) isomer appears to be the more thermodynamically stable arrangement, as it is preferred at low temperature.

Although only limited data were obtained in the VT experiment, these allow approximate kinetic analysis of the equilibrium. A Van't Hoft plot (explained in § 4.1.1.) can be constructed for the data between 298 and 200 K and used to approximate thermodynamic data using Equation 4.4.

$$(-R)\ln(K_{eq}) = \Delta H (\frac{1}{T}) - \Delta S$$

$$y \quad = \quad m \quad x \quad + \quad C$$

Equation 4.4
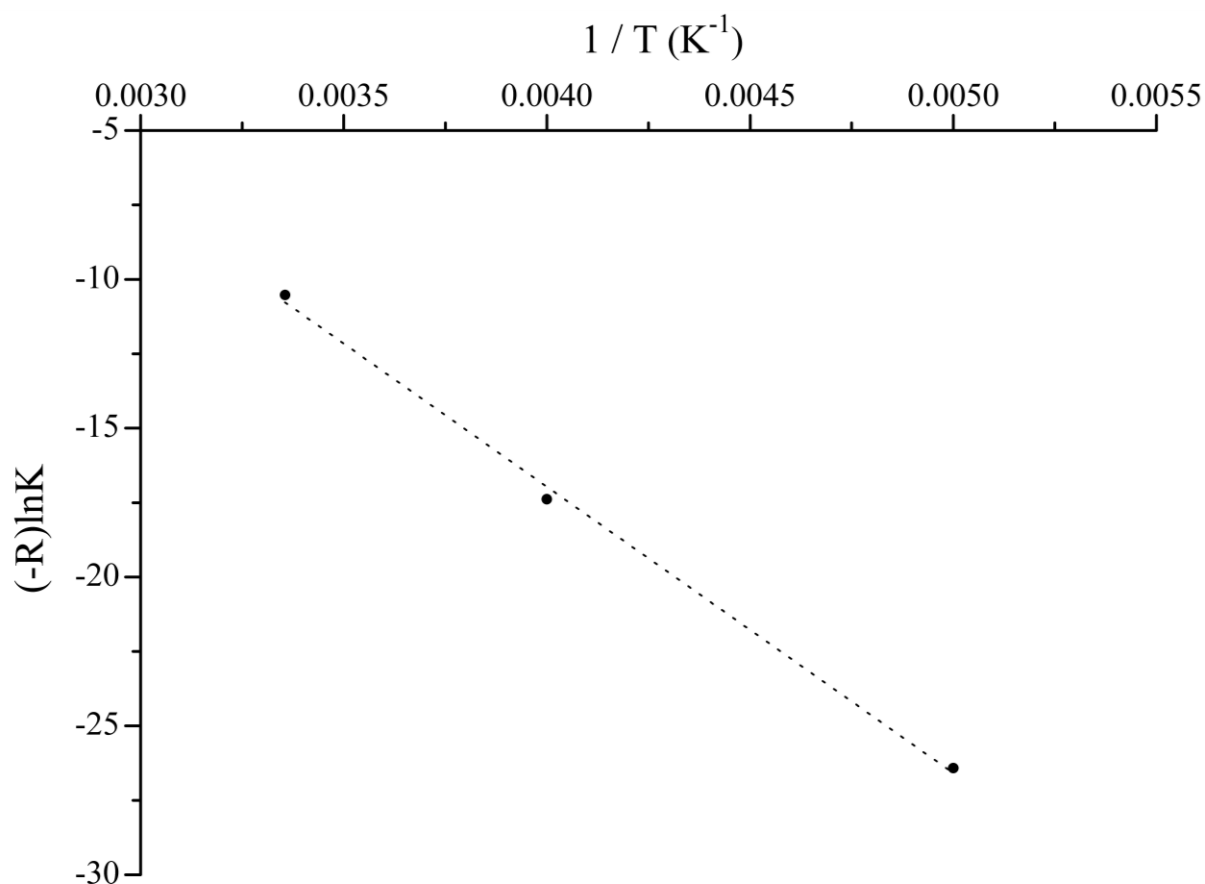
Figure 4.28: Van't Hoft plot for the thermodynamic equilibrium in complex [7]. Slope m = standard enthalpy (ΔH) = −9.6 (± 0.4) kJ mol^{-1}, intercept C = entropy (ΔS) = −21.5 (± 1.8) J K^{-1} mol^{-1}, R^2 = 0.996

The Van't Hoft plot (Figure 4.28) shows good linear regression, with R^2 = 0.996. The negative slope confirms the nitro-(η^1-NO$_2$) isomer is enthalpically favoured by ΔH = −9.6 (± 0.4) kJ mol^{-1}, while a value of ΔS = −21.5 (± 1.8) J K^{-1} mol^{-1} is obtained for the entropy change on nitrito − nitro conversion. These values are comparable to those obtained for complex [1] (§ 4.1.1.).

An Arrhenius plot may also be constructed, allowing an estimate of the activation energy E$_A$ for the thermal isomerisation process. Figure 4.29 again shows good linear correlation between Equation 4.6 and the data, returning an estimation of E$_A$ = −1.6 (± 0.05) kJ mol^{-1}. This value is smaller than that obtained for complex [1], but is still comparable. The values for ΔH, ΔS and E$_A$ are all indicative of a low energy barrier between the isomers, suggesting they are close in energy. This is expected on considering that both isomers co-exist in the crystal under ambient conditions.

$$\ln(k_{eq}) = -E_A\left(\frac{1}{RT}\right) + \ln(A)$$

<div align="right">Equation 4.6</div>

$$y \quad = \quad m\ x\ + \quad C$$
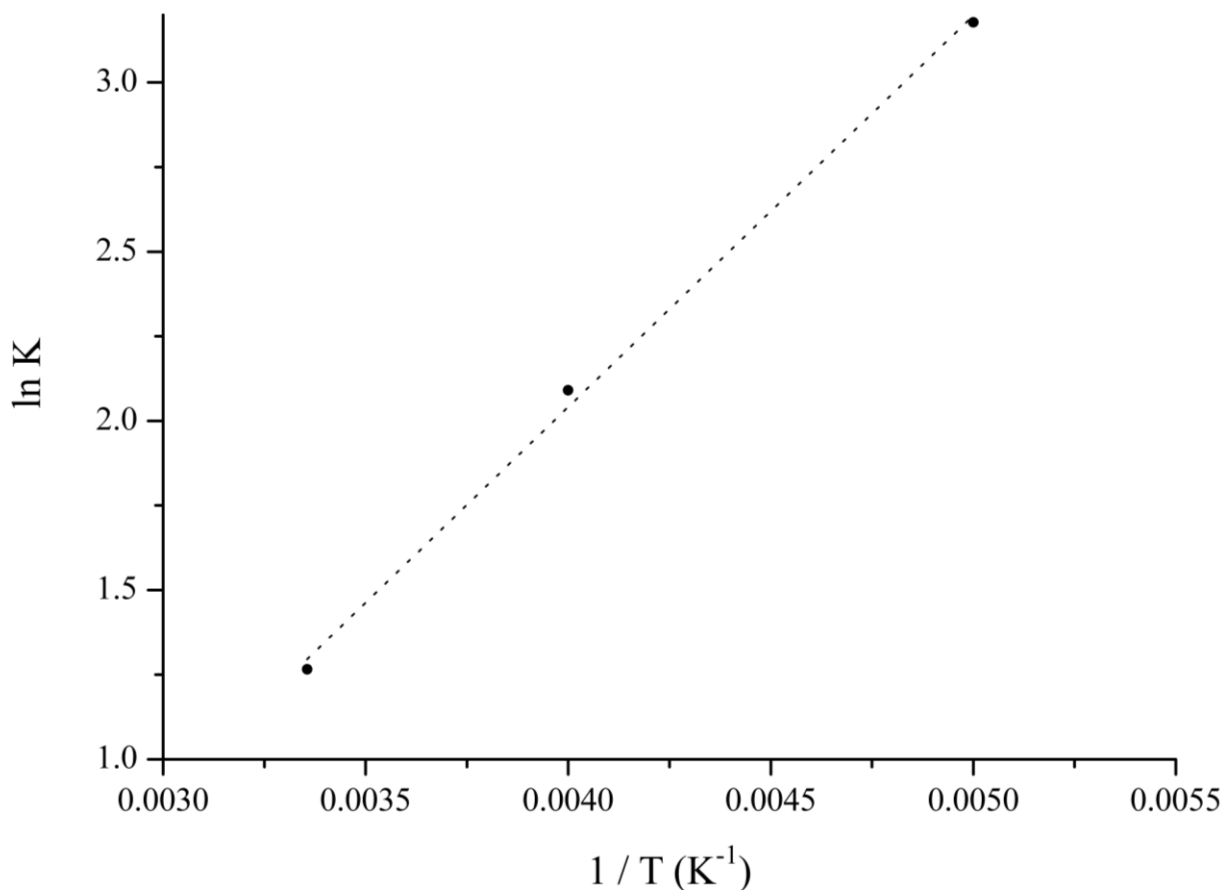
Figure 4.29: Arrhenius plot for the thermally induced isomerisation reaction in complex [7]. Activation energy $E_A = -1.16 \, (\pm \, 0.05) \, kJ \, mol^{-1}$, $R^2 = 0.996$

Steady-State Photocrystallography

A UV/vis spectrum was first collected for [7] and used to guide the selection of an appropriate excitation wavelength for photocrystallographic studies with the complex (Figure 1, Appendix 7). A dominant absorption at 361 nm is characteristic of an MLCT transition and as such wavelengths in this range are thought to be most likely to induce linkage isomerism in the system.[71] In light of previous success using a wavelength in the tail of the absorption band,[23, 130] 400 nm light was chosen as the most appropriate wavelength for excitation of complex [7].

A crystal was first slow cooled to 100 K, in the dark, to ensure both molecules A and B adopt the 100% nitro-(η^1-NO$_2$) linkage isomer arrangement in the GS. The crystal was then irradiated with 400 nm LED light at 100 K for a period of 1 h, using the experimental set up described previously (§ 3.2.2). A second X-ray dataset was then collected in the absence of further light. This dataset revealed that a change in both molecules is induced on excitation. Whilst 89% conversion to a nitrito-(η^1-ONO) isomer had been achieved for molecule A, a minor 32% nitrito isomer was also

118

identified for molecule B. Linkage isomerism in molecule B necessarily breaks the mirror symmetry required at this site in $P2_1/m$ and the photoactivated data was best solved in the non-centrosymmetric space group $P2_1$. Additionally the *N*-methyl group C(17) now also breaks the original symmetry, preferring to sit just out of the lost mirror plane in the ES structure (Figure 4.30). The reduction in symmetry raises the number of molecules in the asymmetric unit to $Z' = 3$ and, as only molecule B breaks the symmetry of the original GS cell, the other two molecules are essentially similar. This is confirmed by the fact that they are the same geometric isomer (molecule A) and their nitro : nitrito ratios refine to similar values. As such conversion levels reported for molecule A are an average over the two, now assigned as molecules A and A'.
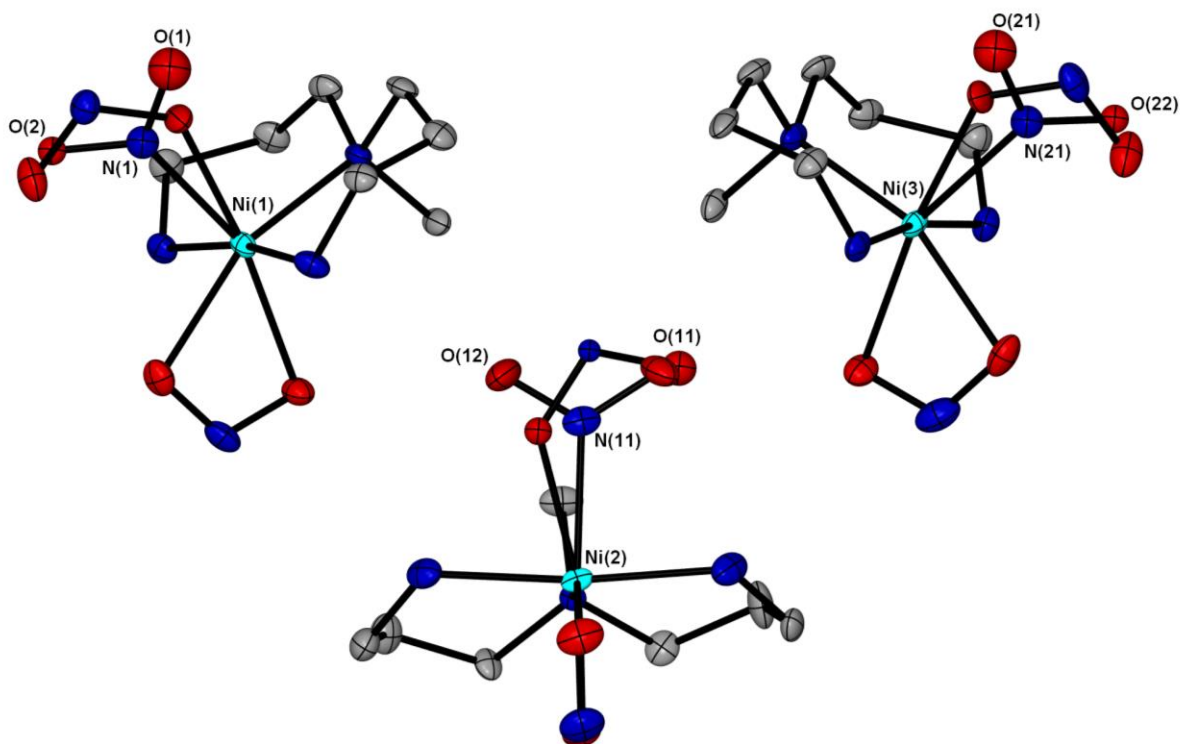
Figure 4.30: Single-crystal X-ray structure showing the atomic arrangement for the three independent molecules in the MS structure of [7], ellipsoids at 50% probability and hydrogen atoms removed for clarity.

To confirm the space group assignment a MORE 3 instruction was used to obtain the highest correlation coefficients for the $P2_1$ structure in Shelxl-97.[137] The largest values involve the nitrites of molecules A and A', further confirming that these are similar. Despite this, no stable solution was obtained for the MS data in the original centrosymmetric space group, indicating the $P2_1$ solution is a better model. Table 4.29 gives crystal data for both GS and MS.

Table 4.29: Crystal data for the flash cooled GS and photoinduced MS structures of [7], at 100 K

	Ground State	400 nm Metastable State
Photoconversion	Molecule A = 0%, B = 0%	Molecule A = 89%, B = 32%
Temperature	100(2) K	100(2) K
Wavelength	0.71073 Å	0.71073 Å
Empirical formula	C7 H19 N5 Ni1 O4	C7 H19 N5 Ni1 O4
Formula weight	443.97	443.97
Crystal size	0.50 x 0.40 x 0.10 mm^3	0.50 x 0.40 x 0.10 mm^3
Crystal system	Monoclinic	Monoclinic
Space group	$P2(1)/m$	$P2(1)$
Unit cell dimensions	a = 7.119(5) Å b = 23.688(5) Å β = 103.360(5)° c = 10.909(5) Å	a = 7.100(5) Å b = 23.968(5) Å β = 103.945(5)° c = 10.935(5) Å
Volume	1790(2) Å^3	1806(2) Å^3
Z	6	6
Density (calculated)	1.648 M g m^{-3}	1.633 M g m^{-3}
Absorption coeff. μ	1.639 mm^{-1}	1.625 mm^{-1}
F(000)	936	936
R(int)	0.0229	0.0398
R1 (obs. data)	0.0251	0.0328
wR2 (all data)	0.0607	0.0753
Reflections (indep.)	5590	7582

No further change in the excitation level for any of the molecules could be induced on further irradiation, confirming that a photostationary state had been achieved. The ES remained constant on holding the crystal at 100 K in the dark, confirming it to be metastable under these conditions.

Table 4.30: Crystallographically determined nitro : nitrito ratios as a function of exposure to 400 nm LED light during steady-state photocrystallographic experiments with [7]

Irradiation time / h	Temp / K	Molecule A Occupancy		Molecule B Occupancy	
		Nitro-(η^1-NO$_2$)	Nitrito-(η^1-ONO)	Nitro-(η^1-NO$_2$)	Nitrito-(η^1-ONO)
0	100	1.00*	0.00*	1.00*	0.00*
1	100	0.11(1)	0.89(1)	0.68(1)	0.32(1)
2	110	0.12(1)	0.88(1)	0.68(1)	0.32(1)
2	115	0.14(1)	0.86(1)	0.70(1)	0.30(1)
2	120	0.25(1)	0.75(1)	0.84(1)	0.16(1)
2	125	0.57(1)	0.43(1)	1.00*	0.00*
2	130	0.92(1)	0.08(1)	1.00*	0.00*
2	135	1.00*	0.00*	1.00*	0.00*

* No esd is reported for full occupancy or zero occupancy as these ratios were not refined

Variable temperature parametric studies were then conducted to determine the temperature range over which the ES is metastable. The nitrito isomers in both molecules remain constant on warming to 110 K, but begin to decrease on further heating. By 150 K molecule B has regained its GS arrangement and the structure is now best solved in the original $P2_1/m$ unit cell. On further warming the nitrito isomer occupancy in molecule A continues to decrease, until at 135 K this molecule also returns to the GS nitro-(η^1-NO$_2$) arrangement. The nitro : nitrito ratios refined from all photocrystallographic data for molecules A and B are given in Table 4.30.

Crystal Packing and Sterics

The crystal packing for [7] is largely unchanged on excitation and similar to that shown in Figure 4.27(a), excepting the change in nitrite coordination for molecule B and the concomitant reduction in symmetry. Despite the space group change, Table 4.29 confirms there is no dramatic shift in cell parameters, although a +16(3) Å^3 (0.9%) increase in cell volume is observed on excitation. This difference is just significant, with a value of $\Delta V / \sigma(\Delta V) = 5.33$ for the 3σ rule.
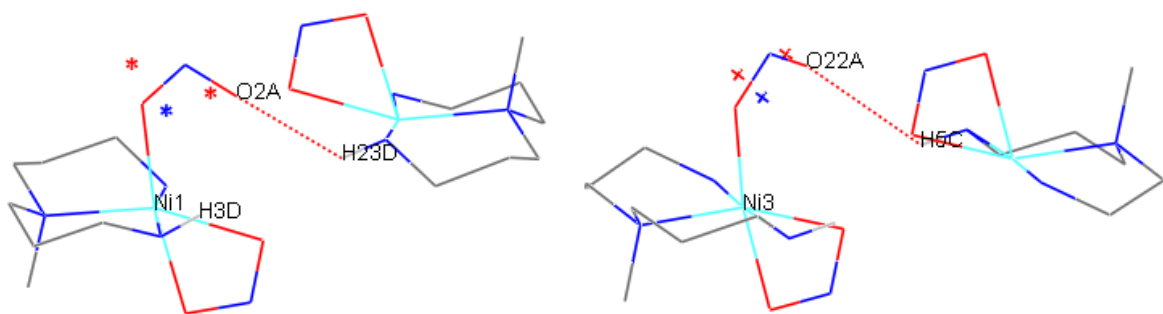
Figure 4.31: New intermolecular hydrogen bonds formed in the MS to nitrito-(η^1-ONO) in molecule A and A'

As noted in thermal studies, the hydrogen bond network in [7] could provide an explanation for the considerably lower photoconversion level achieved for molecule B. Hydrogen bond data for the GS and MS are given in Tables 1 and 2, Appendix 7. Several intermolecular hydrogen bonds are rearranged following photoconversion in complex [7]. No hydrogen bonds to the nitrite ligand exist in the GS arrangement for molecule A, suggesting it is better situated to undergo isomerisation as there are fewer strong contacts providing a barrier to conversion. However, excitation to the nitrito isomer creates new intermolecular hydrogen bonds involving these groups in molecules A and A' (Figure 4.31). Formation of these new interactions will be energetically favourable and so should favour the formation of the ES nitrito-(η^1-ONO) isomer in both cases.
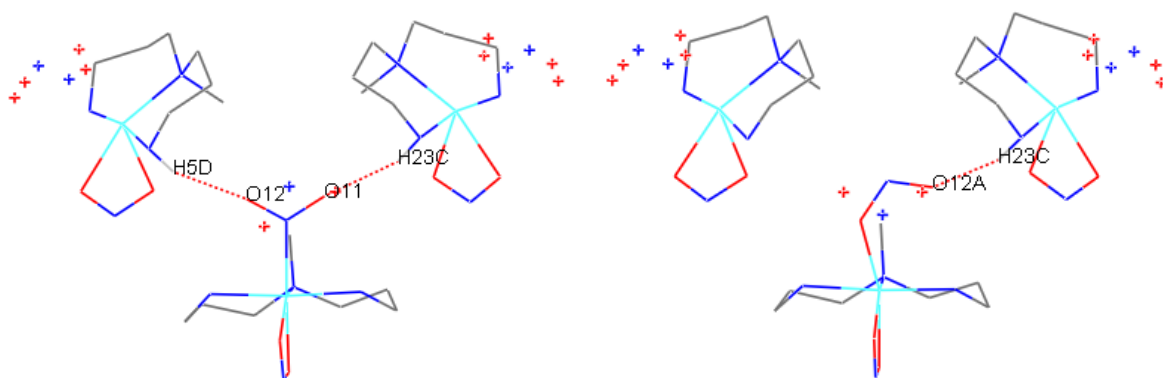
Figure 4.32: Changes in intermolecular hydrogen bonding to the nitrite in molecule B on excitation

Additionally, the nitrite ligand in molecule B is constrained in the GS by two symmetry-related N(5)-H(5D)…O(11) contacts, becoming bonds N(23)-H(23C)…(O11) and N(5)-H(5D)…O(12) when the mirror symmetry is lost upon excitation (Figure 4.32, left). These must be broken for isomerisation to occur and in their place a new intermolecular N(23)-H(23A)…(O12A) hydrogen bond to the nitrito isomer must additionally be formed (Figure 4.32, right). The breaking and re-forming of these bonds requires extra energy, making conversion in molecule B less favourable.

In addition, Hirshfeld surfaces were constructed separately around molecules A and B in turn, such that fingerprint plots could be generated for each of these geometric isomers individually (Table 4.31). Firstly, the overall plots are significantly different for molecules A and B, confirming that they occupy quite different environments within the crystal. Considering each molecule individually, the overall plot shapes are similar for GS and MS, confirming there is little change in the overall structure on excitation. For both molecules A and B, only three key types of interaction contribute to the fingerprint plot: while N…H and O…H contacts must include changes involving the nitrite groups, H…H close contacts will solely represent the rest of the structure. Both the N…H and O…H plots display sharp, spike features that represent hydrogen bonding.[138] For molecule A, a subtle increase in these features is observed on moving to the MS reflecting the formation of new hydrogen bonds to the ES nitrito ligands while none exist to the GS nitro isomer, as discussed previously. For molecule B, a difference between GS and MS contacts is also evident and in particular the formation of a single, shorter O…H hydrogen bond is observed, comparing well with the observations described by Figure 4.32. By contrast, the H…H plots for both molecules show little change between GS and MS, again confirming that the key differences are only the result of the photochemical linkage isomerisation.

Table 4.31: Crystal Explorer fingerprint plots showing changes in intermolecular interactions on photoactivation of [7]

	Molecule A		Molecule B	
	GS	400 nm MS	GS	400 nm MS
All contacts				
N...H contacts				
O…H contacts				
H…H contacts				

123
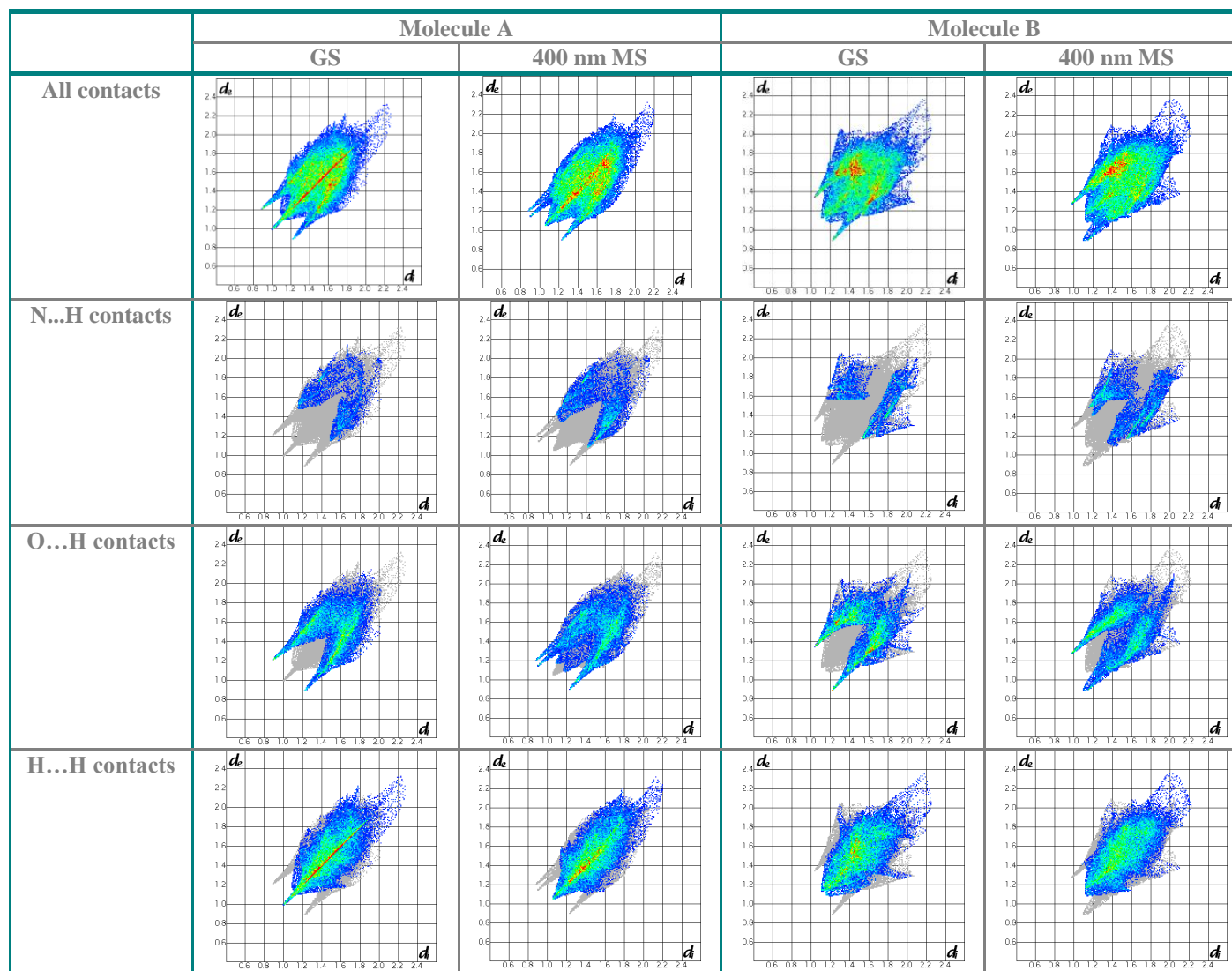
4.2.5. Complex [8]: (*μ*-Oxalato)-di-[nitro-(3,3'-diamino-*N*-methyldipropylamine) nickel(II)]

Previous work has shown that [8] is obtained in two different crystalline forms, one adopting *exo*-nitrito coordination and the other crystallising as the nitro-(η^1-NO$_2$) isomer (CSD reference LIJSIG and LIJSUS).[139] No photocrystallographic studies with these species are reported in the literature, therefore [8] was chosen as a candidate for steady-state photocrystallographic studies.

(i) (*μ*-Oxalato)-di-[(*exo*-nitrito)-(3,3'-diamino-*N*-methyldipropylamine)nickel(II)] [8a]
Crystal Structure and Bonding

Complex [8] was synthesised by the literature procedure[139] (§ 9.2.8.) and blue-green crystals of [8a] were obtained *via* slow evaporation. A single-crystal was mounted with minimum light exposure, flash cooled to 100 K and a standard X-ray dataset collected (Figure 4.33).
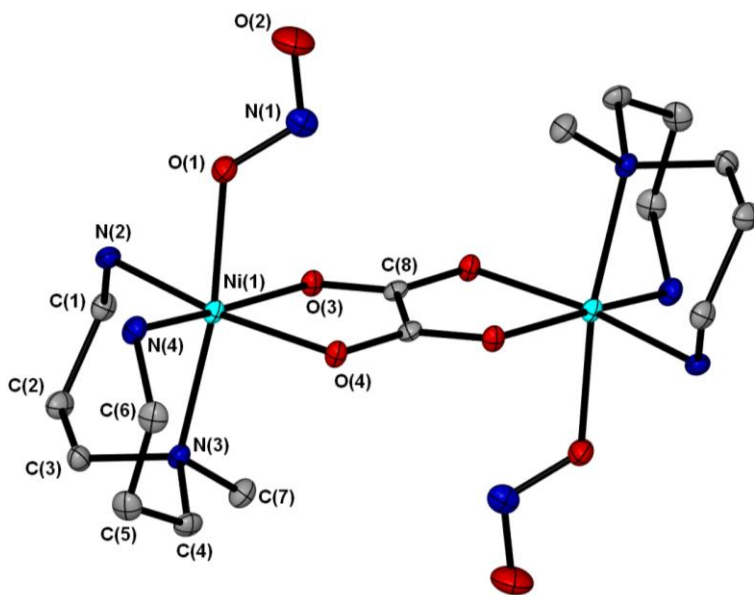
Figure 4.33: Single-crystal X-ray structure showing the atomic arrangement in the flash cooled structure of [8a] at 100 K. Ellipsoids at 50% probability and hydrogen atoms removed for clarity

[8a] crystallises in the triclinic space group *P*-1 with half a molecule in the asymmetric unit. The structure is the same as reported in the literature,[139] with the molecule situated on the inversion centre. The second half of the dimer is generated by inversion, such that both metals occupy crystallographically identical environments. The nickel adopts distorted octahedral geometry, bound to one *exo*-nitrito-(η^1-ONO) ligand, one *fac*-triamine and the remaining sites occupied by the bridging oxalate group. This arrangement is comparable to *exo* complexes [4] and [6], whose triamine group also adopts facial coordination. Table 4.32 displays crystal data for [8a].

Table 4.32: Crystal data for the flash cooled structure of [8a]

Temperature	100(2) K
Radiation source	MoK$_\alpha$
Wavelength	0.71073 Å
Empirical formula	C8 H19 N4 Ni1 O4
Formula weight	293.98
Crystal size	0.15 x 0.08 x 0.02 mm^{-1}
Crystal system	Triclinic
Space group	*P*-1
Unit cell dimensions	$a = 7.3994(7)$ Å^3 $\alpha = 91.222(7)°$
	$b = 7.7050(7)$ Å^3 $\beta = 95.548(7)°$
	$c = 10.3925(9)$ Å^3 $\gamma = 99.062(8)°$
Volume	581.96(9) Å^3
Z	2
Density (calculated)	1.678 M g m^{-3}
Absorption coeff. μ	1.678 mm^{-1}
F(000)	310
R(int)	0.0467
R1 (obs. data)	0.0355
wR2 (all data)	0.0749
Reflections (indep.)	3541

Figure 4.34(a) describes the packing arrangement in [8a], showing a simply ordered crystal structure in which discrete molecules are related only by translation in each direction, with the required inversion symmetry of the unit cell operating on the dimer itself. Individual molecules are linked by a single N(2)-H(2C)…O(3) hydrogen bond, repeated by symmetry to form chains of molecules extending parallel to the *a*-axis (Figure 4.34(b)). Atoms O(1) and O(2) of the nitrito ligand are also involved hydrogen bonds to a neighbouring dimer (Figure 4.34(c)). The presence of these short contacts to the nitrite ligand suggests that the crystal structure is tightly packed. Full hydrogen bond data for [8a] is given in Table 1, Appendix 8.

Steady-State Photocrystallography

Given that the analogous complexes [4] and [6], which also crystallise solely as the *exo*-nitrito-(η^1-ONO) isomer, show no change in nitrite coordination on photoexcitation, it was not expected that nitro – nitrito conversion would be induced in [8a]. A solid-state UV/vis spectrum was obtained (Figure 1, Appendix 8) and used to select appropriate excitation wavelengths. As expected, no change in the *exo*-nitrito isomer could be induced on irradiation at any wavelength, showing again that systems crystallising solely as this isomer are photoinert under the steady-state photocrystallographic conditions employed.
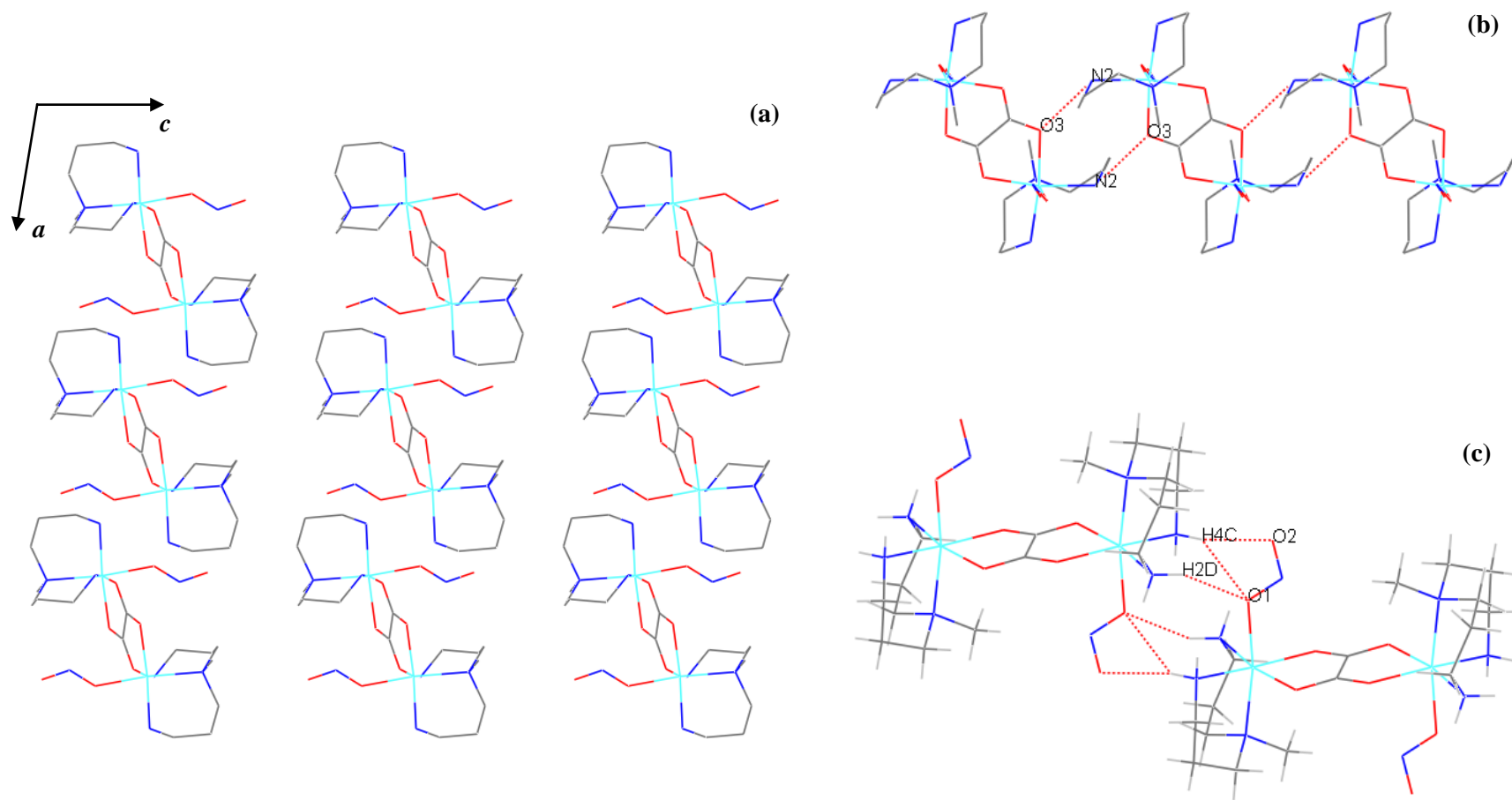
Figure 4.34: **(a)** Crystal packing diagram for the flash cooled structure of [8a], viewed along the *b*-axis, *c*-axis horizontal; **(b)** hydrogen-bonded chains parallel to the *a*-axis; **(c)** hydrogen bonding interactions to the nitrito-(η^1-ONO) ligand.

(ii) (*μ*-Oxalato)-di-[nitro-(3,3'-diamino-*N*-methyldipropylamine)nickel(II)] dihydrate [8b]

Crystal Structure and Bonding

Violet crystals of complex [8b] were obtained from the same crystallisation vial as those of [8a] and separated by hand. The yield of [8b] is increased by repeated recrystallisation from aqueous solutions, suggesting that [8b] is the slightly thermodynamically favoured crystal form in this solvent system. A crystal was mounted and flash cooled to 100 K, with minimum light exposure, and a full single-crystal X-ray dataset collected.
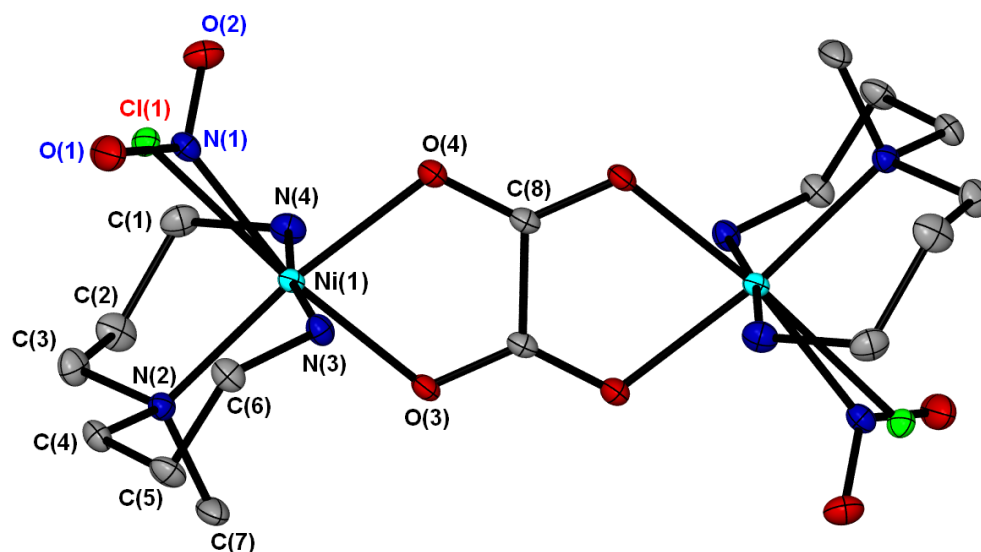
Figure 4.35: Single-crystal X-ray structure showing the atomic arrangement for the nickel dimer in [8b], highlighting the disordered nitro-(η^1-NO$_2$) and chlorine groups. Ellipsoids set a 50% probability and hydrogen atoms removed for clarity

[8b] crystallises as a dihydrate species in the triclinic space group *P*-1, with the asymmetric unit comprising of half the dimer molecule and a water molecule of crystallisation. As for [8a], the complex molecule is positioned on the inversion centre such that the second half of the dimer is generated by symmetry and as such both nickel atoms again occupy crystallographically identical environments (Figure 4.35). The nickel centre is pseudo-octahedral, bound to one tridentate amine ligand, one nitrite group adopting nitro-(η^1-NO$_2$) coordination and with the final two sites filled by the bridging oxalate. Contrary to the arrangement for [8a], in [8b] the amine is bound meridionally, forcing the nitro group to adopt a site *cis* to the plane of the tridentate ligand.

The crystal form is identical to that reported previously,[139] as shown by unit cell parameters reported in Table 4.33. However, in their previous study Wen *et al.* determine unusual thermal parameters for the nitro-(η^1-NO$_2$) ligand. No comment is made in their analysis, but as irregular ellipsoids are often indicative of some issue with the solution as reported, the structure of [8b] was examined more closely in the current analysis. This led to the proposal of a disorder model, as shown in Figure 4.35, indicating that the nitro species is in fact co-crystallised with 33% of an analogous chloride dimer. The chloride species is a reasonable side product from the synthetic route to [8] and, as the incorporation of this disorder model leads to dramatically improved thermal parameters in both components, the model appears to fit the data well.

Figure 4.36(a) describes the crystal packing arrangement for [8b]. The dimeric molecules align in rows, with water of crystallisation occupying space in narrow channels running parallel to the *a*-axis. Within each row, dimers linked by hydrogen bonding to the water molecules, forming $C_2^2(7)$ chains extending parallel to the *a*-axis (Figure 4.36(b)). These chains make up a small part of an extensive hydrogen bonding array in [8b] (Table 2, Appendix 8), and of particular importance is the number of interactions involving the nitro-(η^1-NO$_2$) ligand. Figure 4.37(a) shows the nitro group is involved in three hydrogen bonds to N-H groups on neighbouring dimers, as well as its interactions with water molecules. All but one of these hydrogen bonds are moderately strong,[132] tending to suggest that the structure is tightly packed in the region surrounding the nitrite ligand. This may be unfavourable for any potential linkage isomerism in the system upon photoactivation. Additionally to contacts involving the 67% occupied nitro-(η^1-NO$_2$) ligand, Figure 4.37(b) shows that a number of analogous hydrogen bonding interactions exist between the surrounding molecules and the 33% occupied chloride ligand.

A second, non-solvated crystal form of [8b] was obtained from a smaller scale reaction procedure, whose structure was solved to show it contained solely the nitro-(η^1-NO$_2$) derivative. Unfortunately these crystals were of poor quality and displayed heavy disorder, therefore were unsuitable for use in photocrystallographic studies. It is possible that the presence of the extra, stabilising interactions in [8b] to both the water molecules and the chloride ligand make the co-crystallisation of the nitro- and chloro- derivatives more favourable, therefore producing a better ordered crystalline material.
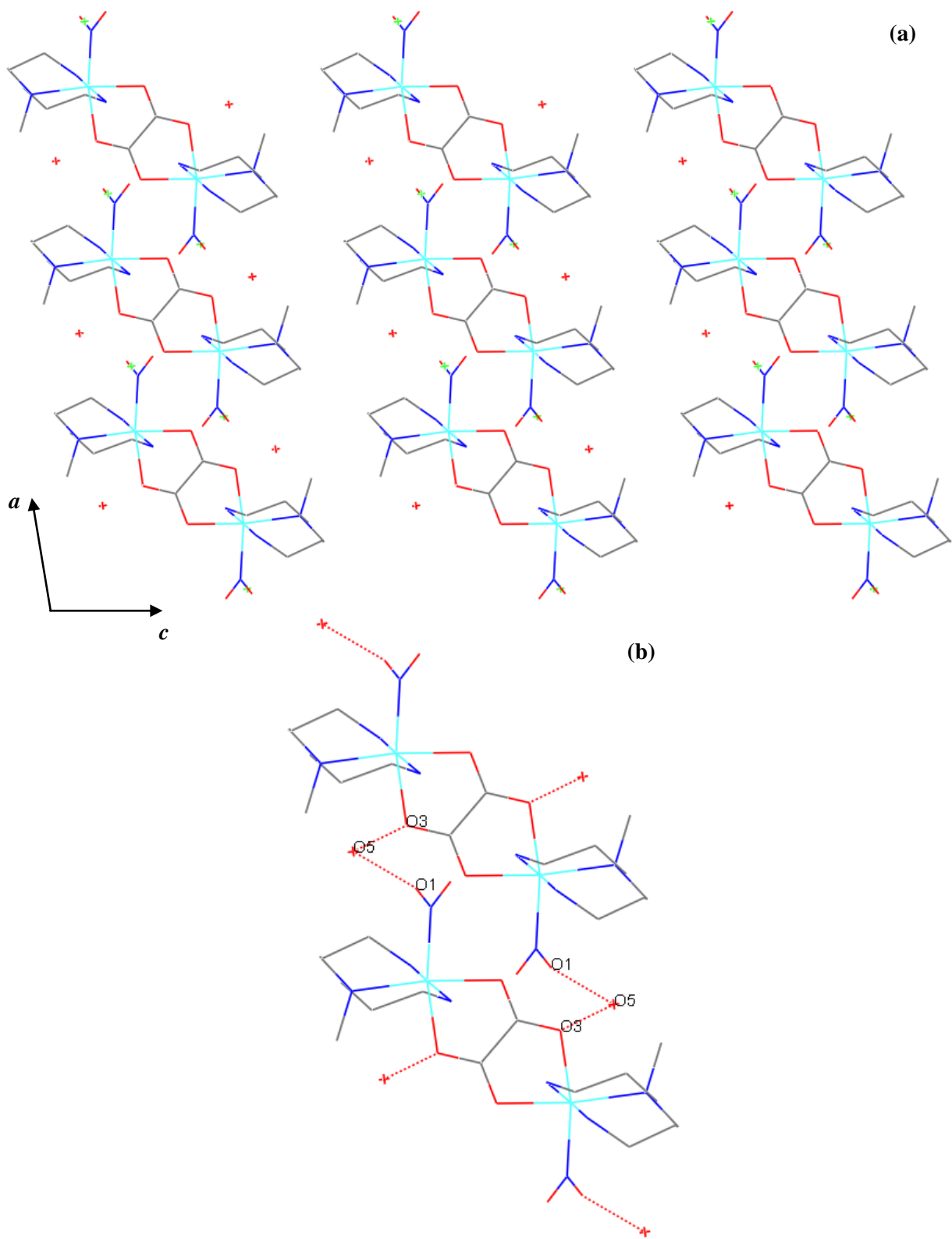
Figure 4.36: (a) Crystal packing diagram for the flash cooled structure of [8b] at 100 K, viewed along the *b*-axis, *c*-axis horizontal **(b)** Hydrogen bonded chains involving water molecules of crystallisation, extending parallel to the *a*-axis
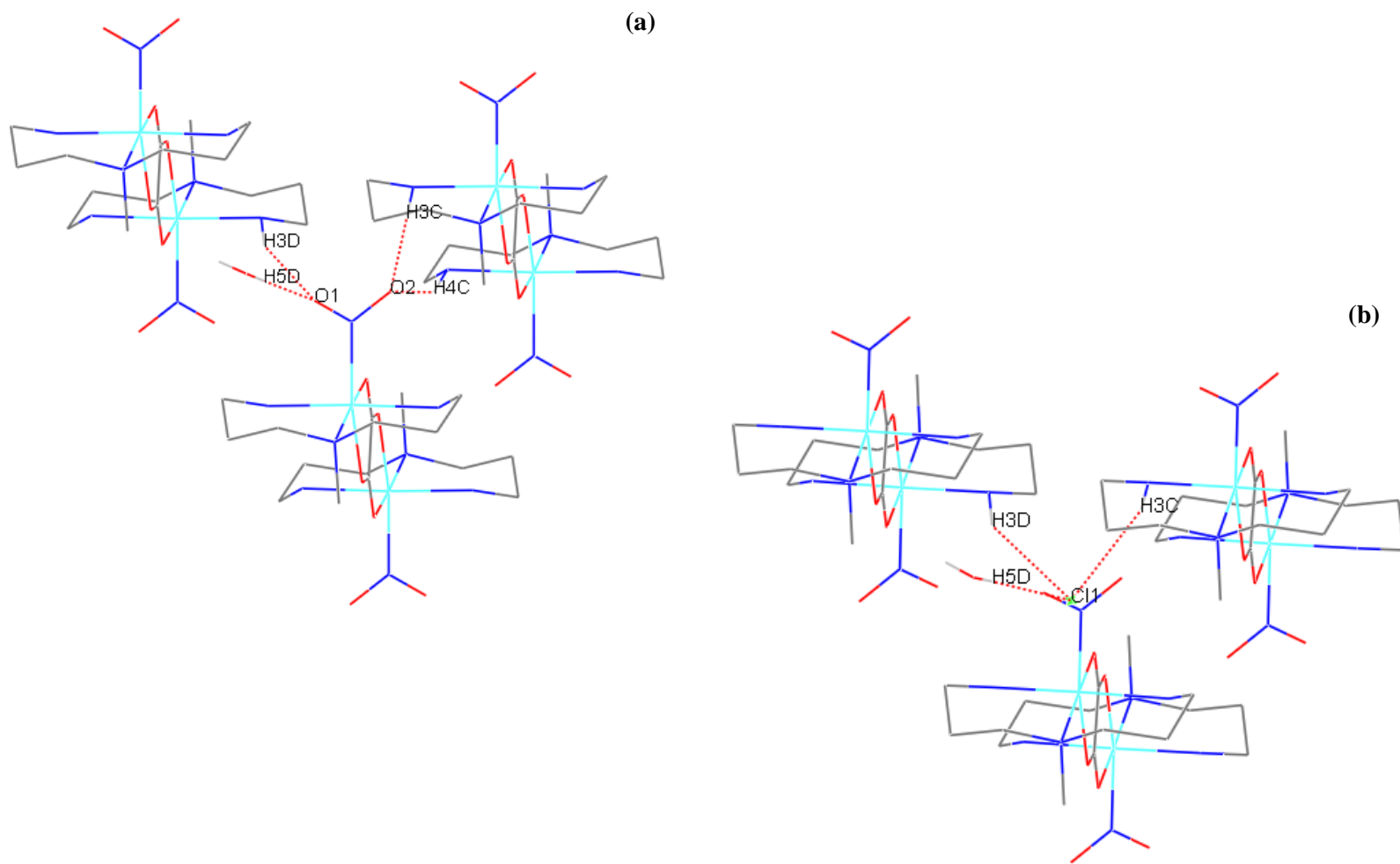
Figure 4.37: Hydrogen bonding interactions to the **(a)** 67% nitro-(η^1-NO$_2$) and **(b)** 33% chloride disorder components in the flash cooled structure of [8b] at 100 K

Steady-State Photocrystallography

The solid-state UV/vis spectrum was first used as a guide to select an appropriate excitation wavelength (Figure 1, Appendix 8). As expected from previous results and the literature,[23, 130] preliminary experiments suggested that $\lambda = 400$ nm was most suitable and a full steady-state photocrystallographic experiment was conducted using this wavelength.

A crystal was held at 100 K and irradiated with 400 nm LEDs light for a period of 1 h. A subsequent X-ray dataset revealed that, while the same 33% chloride impurity was retained, the nitro-(η^1-NO$_2$) derivative had been partially converted to an *endo*-nitrito-(η^1-ONO) isomer, with 15% of the crystal now adopting this ES arrangement (Figure 4.38). The crystal was further irradiated and conversion to the nitrito-(η^1-ONO) isomer continued to rise with increased irradiation time, until a photostationary state was achieved. A final occupancy of 35% was determined after 3.5 h of 400 nm light. This ES is metastable at 100 K, remaining constant when held at this temperature in the absence of external light. Little change in the refined occupancy for the chloride impurity was found for any of the structures obtained, further confirming that this is an appropriate model for the system. Table 4.33 gives crystal data for both the GS and MS.

Table 4.33: Crystal data for the flash cooled GS and photoinduced MS structures of [8b], at 100 K

	Ground State	400 nm Metastable State
Photoconversion	0%	35%
Temperature	100(2) K	100(2) K
Wavelength	0.77490 Å	0.71073 Å
Empirical formula	C8 H21 Cl0.34 N3.67 Ni1 O4.35	C8 H21 Cl0.34 N3.67 Ni1 O4.35
Formula weight	308.77	308.77
Crystal size	0.07 x 0.05 x 0.03	0.07 x 0.05 x 0.03
Crystal system	Triclinic	Triclinic
Space group	*P*-1	*P*-1
Unit cell dimensions	$a = 6.760(1)$ Å, $\alpha = 79.716(2)°$ $b = 8.667(1)$ Å, $\beta = 79.254(2)°$ $c = 11.706(2)$ Å, $\gamma = 69.940(2)°$	$a = 6.843(5)$ Å, $\alpha = 79.273(5)°$ $b = 8.656(5)$ Å, $\beta = 78.851(5)°$ $c = 11.766(5)$ Å, $\gamma = 67.819(5)°$
Volume	628.1(2) Å^3	628.3(6) Å^3
Z	2	2
Density (calculated)	1.632 M g m^{-3}	1.632 M g m^{-3}
Absorption coeff. μ	1.972 mm^{-1}	1.628 mm^{-1}
F(000)	326	326
R(int)	0.0492	0.0210
R1 (obs. data)	0.0453	0.0317
wR2 (all data)	0.1357	0.0724
Reflections (indep.)	3822	4127
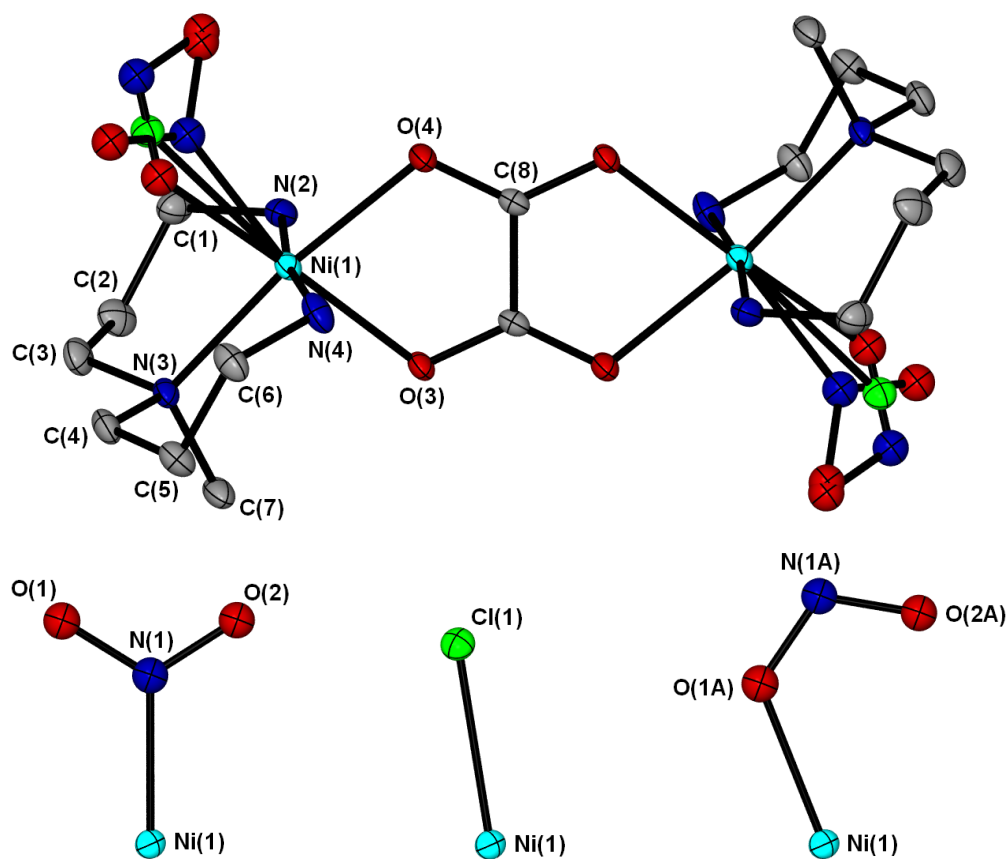
Figure 4.38: (a) Single-crystal X-ray structure showing the atomic arrangement in the MS structure for [8b], ellipsoids set at 50% probability and hydrogen atoms removed for clarity, **(b)** individual arrangements for the disordered components of the MS structure
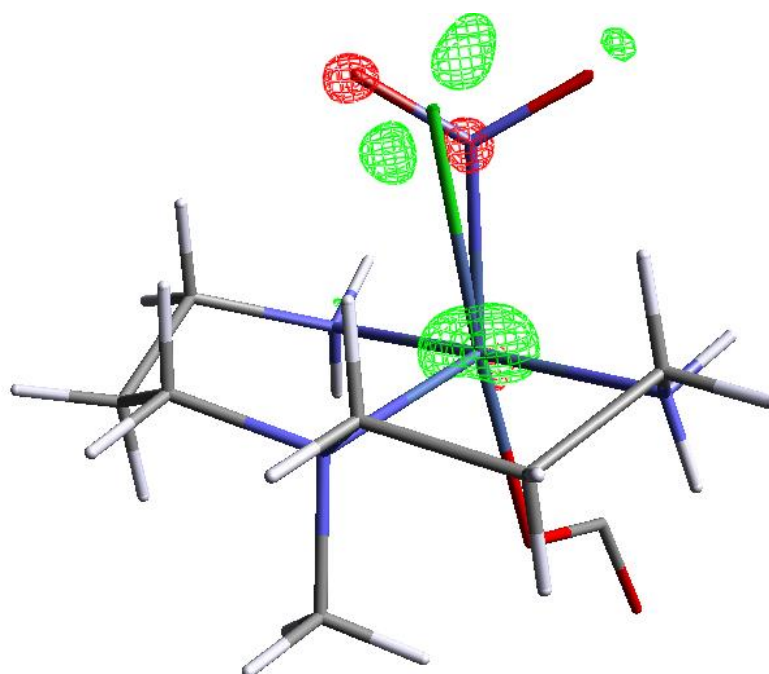
Figure 4.39: Photodifference map for the MS structure of [8b], red = −3.5 e Å^3, green = +3.9 e Å^3

The photodifference map in Figure 4.39 confirms the production of this ES *endo*-nitrito-(η^1-ONO) linkage isomer. Red contours at the positions of N(1) and O(1) of the GS nitro ligand indicate the disappearance of this isomer on irradiation, while green contours show the increase in electron density at the positions of N(1A), O(1A) and O(2A), in line with the production of the MS state. The absence of red contours at the position of O(2) might again be explained by the fact that there is very little atomic displacement required for the arrangement of O(2) to O(2A) and this is additionally supported by the considerably smaller point of increased electron density for O(2A).

Finally, variable temperature parametric studies were conducted to determine the temperature range over which the ES is metastable. The *endo*-nitrito-(η^1-ONO) isomer is only metastable over a small temperature range; on warming to 110 K the MS state has already begun to decay and the system fully regains its GS arrangement by 130 K. The crystallographically determined ratios for each ligand component from photocrystallographic data are given in Table 4.34.

Table 4.34: Crystallographically determined ratios of ligand components in [8b] as a function of exposure to 400 nm LED light in steady-state photocrystallographic studies

Irradiation time /	Temp /	Refined Occupancy		
h	K	Nitro-(η^1-NO$_2$)	Nitrito-(η^1-ONO)	Chloride
0	100	0.67(1)	0.00*	0.33(1)
1	100	0.52(1)	0.15(1)	0.33(1)
2	100	0.39(1)	0.28(1)	0.33(1)
3.5	100	0.32(1)	0.35(1)	0.33(1)
3.5	110	0.36(1)	0.31(1)	0.33(1)
3.5	120	0.50(1)	0.17(1)	0.33(1)
3.5	130	0.68(1)	0.00*	0.32(1)

* No esd is reported for full occupancy or zero occupancy as these ratios were not refined

Crystal Packing and Sterics

There is little change in the overall crystal structure following photoactivation, with the packing arrangement closely resembling that of the GS structure shown in Figure 4.36(a), excepting the change in nitrite ligand coordination. The crystal retains the same *P*-1 space group and there is no significant change in the overall unit cell volume between GS and MS structures.
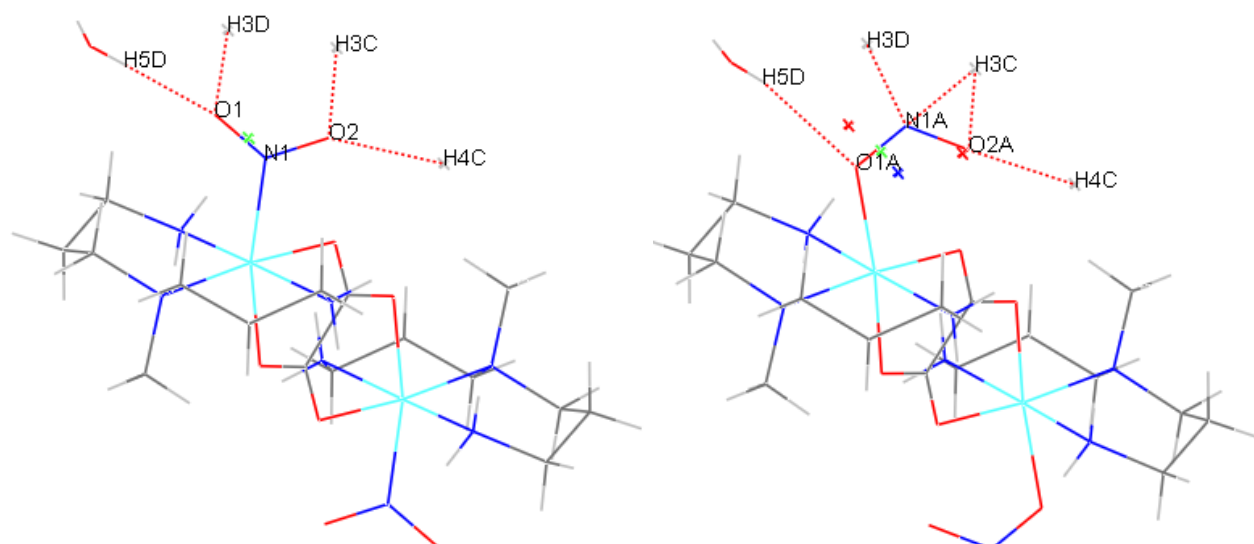
Figure 4.40: Changes in hydrogen bonding interactions to the nitrite ligand in [8b] upon photoactivation

Despite a lack of evidence for much change in the overall structure, some movement must occur in the region surrounding the nitrite group on conversion between isomers. In particular several hydrogen bonding interactions must be broken and re-formed during isomerisation. Figure 4.40 and Table 4.35 show the hydrogen bonding changes due to photoconversion. Overall, four interactions to the nitro-(η^1-NO$_2$) ligand must be broken, and in the MS structure five new interactions to the *endo*-nitrito-(η^1-ONO) ligand are created. These changes will require additional energy to be implemented, before linkage isomerism can occur in the system. Full hydrogen bond data for the MS structure of [8b] are found in Table 3, Appendix 8.

Table 4.35: Changes in hydrogen bond D…A distances to the nitrite following photoactivation of [8b]

	Isomer	GS / Å	MS / Å
O(5)-H(5D)...O(1) **#1**		2.80(1)	2.63(1)
N(3)-H(3D)...O(1) **#2**	Nitro-(η^1-NO$_2$)	3.19(1)	3.19(1)
N(3)-H(3C)...O(2) **#3**		3.09(1)	3.13(1)
N(4)-H(4C)...O(2) **#4**		3.33(1)	3.28(1)
O(5)-H(5D)...O(1A) **#1**		N/A	3.24(1)
N(3)-H(3D)...N(1A) **#2**		N/A	3.25(1)
N(3)-H(3C)...N(1A) **#3**	Nitrito-(η^1-ONO)	N/A	2.99(1)
N(3)-H(3C)...O(2A) **#3**		N/A	3.06(1)
N(4)-H(4C)...O(2A) **#4**		N/A	3.20(1)

Symmetry operations for equivalent atoms:
#1 = (x+1, y-1, z), **#2** = (-x, -y+2, -z), **#3** = (x+1, y, z), **#4** = (-x, -y+1, -z)

Crystal Explorer fingerprint plots also provide a quick, visual summary of the differences in key intermolecular interactions on photoconversion (Table 4.36). While N…H, O…H and Cl…H contacts across the Hirshfeld surface are indicative of interactions involving the isomerising ligands, the remaining interactions represent the rest of the crystal structure, with C…C and C…O contacts the result of interactions involving the oxalate bridging ligand. The overall shape of the plots is comparable between GS and MS, supporting the observation that there is little change in the overall crystal structure on photoactivation. However, some differences between the plots are evident and can be directly attributed to the linkage isomerisation. The O…H plots show some subtle differences between GS and MS, but much more striking is the change in N…H contacts. There is both an increase in the number of N…H interactions but also a dramatic reduction in their d_i / d_e distance, corresponding to the rearrangement from N(1) to the position of N(1A) where it is more exposed to interaction with surrounding molecules. Of additional interest is the marked reduction in the number of Cl…H interactions observed for the 33% occupied chloro-derivative. This reduction also reflects the isomerisation as, while in the presence of the GS nitro ligand the chloride is not shielded from interaction with neighbouring molecules, in the presence of the MS *endo*-nitrito ligand the chloride is blocked by the positioning of N(1A), which now interacts with the surrounding lattice in its place. Finally, the remaining fingerprint plots for C…C, H…H, and C…O interactions are essentially identical between GS and MS structures, confirming that the only key differences in the crystal structure on photoactivation are those relating to the isomerising groups.

Table 4.36: Crystal Explorer fingerprint plots showing changes in intermolecular interactions on photactivation of [8b]

	GS	400 nm MS
All Contacts		
N...H contacts		
O…H contacts		
C…C contacts		
H…H contacts		
C…O contacts		
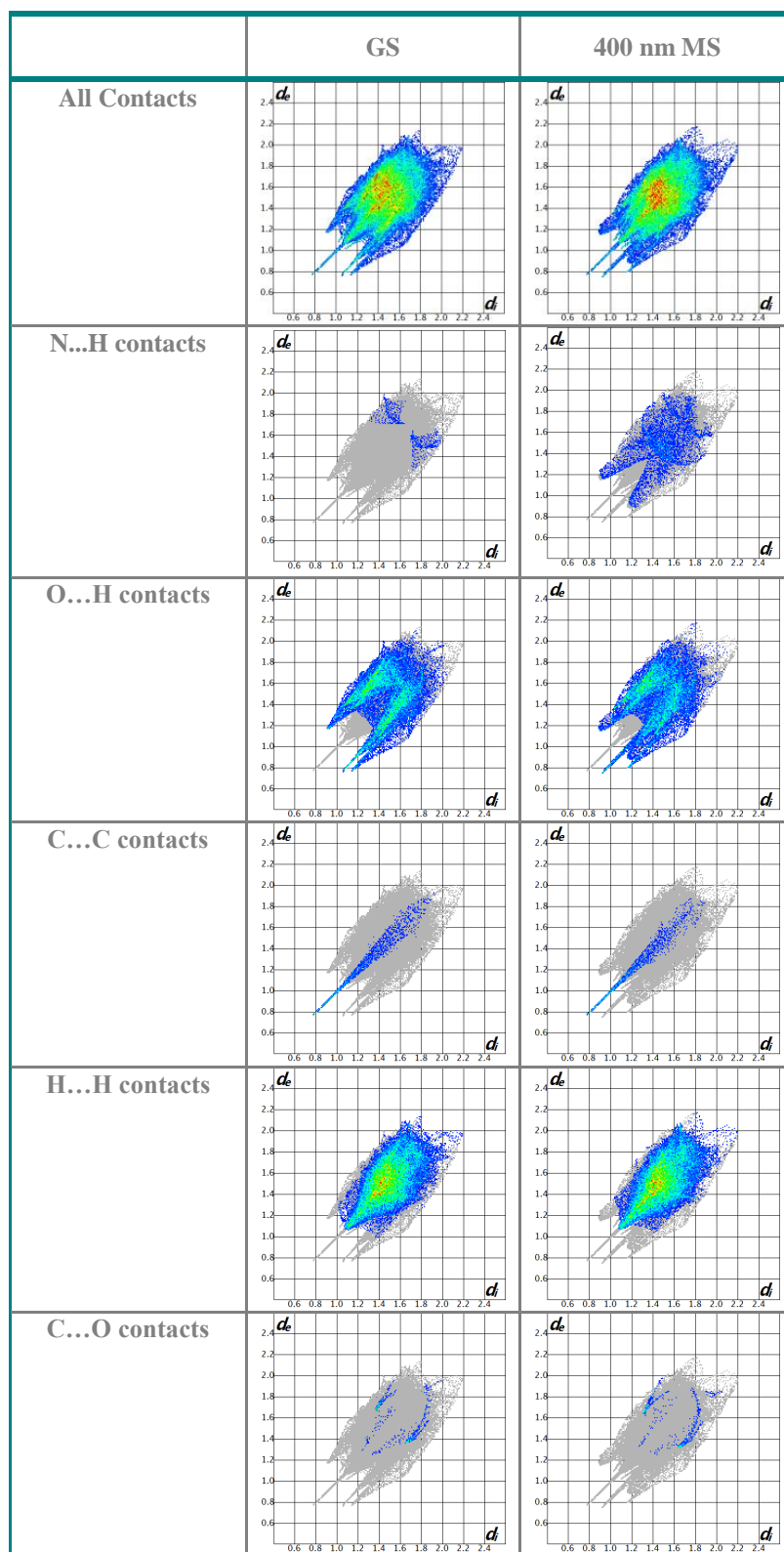
4.2.6. Comparisons: Complexes [1] and [4] to [8]

Comparison can be made between [1] and [4] to [8], given that they are universally neutral, six-coordinate nickel – nitrite species containing triamine ligands. Together these represent an extensive set of such systems, considering that a search (2) of the CSD, using the fragment shown in Figure 4.41, returned only three other unique triamine structures, two of which were polymeric.

$$N-\text{---}Ni-\text{---}N$$
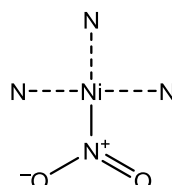
Figure 4.41: Fragment used to conduct Search 2 of the Cambridge Structural Database (CSD)

Crystallisation Geometries

An interesting comparison between all of the nickel – triamine species studied in Chapter 4 is the apparent preference for each system to crystallise either as a majority nitro-(η^1-NO$_2$) isomer, or instead as a solely *exo*-nitrito-(η^1-ONO) compound. Given that the nitrite group is theoretically capable of an extensive range of binding modes,[61] it is interesting that only these two arrangements crystallise preferentially. Additionally, given that nitro-(η^1-NO$_2$) displays nitro – nitrito isomerism while *exo*-nitrito remains photoinert, it is of interest for the current study to understand why a system will crystallise as one linkage isomer in preference to the other.

It is apparent that a trend exists between the preferred nitrite isomer on crystallisation and the geometry of the triamine ligand. In all cases where the nitro isomer is dominant the amine binds meridionally, while conversely *exo*- isomers always contain a triamine adopting facial geometry. There is no obvious trend in either hydrogen bonding or other steric influences that appears to account for this observation, again suggesting there is a limit to the efficacy of these arguments to conclusively explain the behaviour of the nitrite group. Instead, a potential explanation could be made by considering electronic influences in the molecular species itself. The *trans*-effect theorem is based on the assumption that ligands occupying sites *trans*- to one another in a complex use the same metal orbitals for bonding and are therefore in competition. The *trans*-influence is the manifestation of the effect in ground state properties of the system, such as metal – ligand bond lengths and geometries.[133] This would suggest that the most stable arrangement for a complex should involve a compromise, with a strong donor preferring to occupy a position *trans*- to a weaker donor such that the orbital might be best shared.

The *trans*-influence argument agrees well with the geometric preferences observed in [1] and [4] to [8]. The *N*-donor nitro-(η^1-NO$_2$) ligand is higher in the spectrochemical series that the *O*-donor *exo*-nitrito group, indicating that nitro-(η^1-NO$_2$) is the stronger field ligand.[133] It appears that nitro-(η^1-NO$_2$) preferentially crystallises with a *mer-* amine, as this places a weaker field oxygen atom of the bidentate nitrito-(O,ON) ligand at the *trans-* position. The bidentate ligand is likely to be fairly weak-field as its –1 charge is formally delocalised over the three atoms. Additionally, the *exo*-isomer arrangement is also in agreement with the expected *trans*-influence: in the presence of a *fac-* amine the weak-field *exo*-nitrito ligand is positioned *trans-* to the central nitrogen atom of the amine ligand, which should be a stronger donor than nitrito-(η^2-O,ON).

Although it is not certain which ligand, the amine or nitrite group, directs the formation of a particular isomer, it is likely that the geometry of the tridentate amine is the governing factor. Due to the chelate effect[133] greater stability is gained from amine bonding than from the nitrite, therefore the preferred arrangement of the larger group is likely to dictate the nitrite binding mode.

As the *trans*-influence can affect the relative metal – ligand bond lengths of a species, these might also be used to assess the applicability of the hypothesis. The average Ni-N and Ni-O bond lengths of 2.038 Å and 2.053 Å, respectively, from compounds reported in the CSD,[127] are very similar and so direct comparison of their values appears reasonable. General comparison of Ni-N and Ni-O bonds for all six species is not applicable as there are other factors, such as the differing steric demands of *N*-substituted groups on the amine ligands, which may contribute to bond length variations. The best comparison may be made between complexes [8a] and [8b], given that they are chemically the same compound but differ only in their crystallisation geometry.

Table 4.39: Relevant metal – ligand bond lengths for *trans*-influence in complexes [8a] and [8b]

	[8a] *exo*-nitrito	[8b] nitro
Ni(1)-O(1) / Ni(1)-N(1)	2.134(1)	2.072(5)
Ni(1)-O(3)	2.081(1)	2.116(2)
Ni(1)-N(3)	2.184(1)	2.162(2)

To assess the likelihood of *trans*-influence the following distances should be compared: (i) nitro bond Ni(1)-N(1) of [8a] to *exo*-nitrito Ni(1)-O(1) of [8b], (ii) Ni(1)-O(3) to the bidentate nitrite in both complexes, and (iii) Ni(1)-N(3) to the central amine nitrogen in both systems (Table 4.39). All differences are statistically significant[15] and both (i) and (ii) show support of *trans*-influence. For (i) as expected Ni(1)-N(1) in [8a] is considerably shorter than Ni(1)-O(1)

of [8b], while for (ii) the Ni(1)-O(3) bond of the bidentate (η^2-O,ON) ligand is considerably longer in the nitro isomer, in-line with a weakening of this bond when it is situated *trans-* to the nitro-(η^1-NO$_2$) ligand. Conversely, the results of comparison (iii) do not support the presence of *trans*-influence, with the Ni(1)-N(3) bond in the *exo-* system [8a] not shortened as expected but in fact still longer than the same bond in the nitro isomer. This latter discrepancy is possibly the result of constraints imposed by the *fac-* arrangement of the amine, which is necessarily heavily distorted due to strain imposed by this tight coordination mode. However, further evidence is required to conclusively determine the validity of the *trans*-influence hypothesis in these complexes.

Photoconversion Level

Despite success with [1], 100% excitation was not achieved in any other nickel – amine species investigated. Given their chemical similarity, it is interesting that those compounds undergoing photoisomerisation: [1], [5], [7] and [8b], do so to varied levels of conversion. This indicates that solid-state effects must strongly influence the photoreaction, and comparison may suggest the degree to which the crystalline environment can affect the level of achievable photoconversion.

The simplest parameter for comparison is first the overall change in unit cell volume ΔV on photoactivation. As discussed in § 4.1.4, it has long been thought that solid-state photoreactions proceed topochemically,[1] therefore the system undergoing the smallest change is necessarily expected to achieve highest photoconversion. For all nitro – nitrito systems so far studied ΔV is small and the overall crystal structure does not change greatly on excitation, observations both seemingly in-line with the Topochemical Postulate. However, the relative changes in ΔV do not effectively explain the photoconversion trend in [1], [5], [7] and [8b], with the largest change of +2.04% occurring alongside 100% conversion in complex [1]. [5], [7] and [8b] show no correlation between conversion and ΔV, with values of –0.16%, +0.9% and +0.03% respectively, suggesting that this parameter alone does not effectively account for the trends observed.

It is also apparent that the degree of hydrogen bonding to the nitrite affects the level of achievable isomerisation. The highest converting species, [1] and molecule A of [7], show no intermolecular hydrogen bonding to the nitrite ligand in the GS. By contrast, the nitrite groups in the other three species are hydrogen bonded and here excitation is limited to *ca.* 50%. For conversion to occur these strong contacts must first be overcome, which necessarily requires extra energy. As such, it is perhaps intuitive that such interactions provide a barrier to excitation (Table 4.37).

Table 4.37: Comparison of hydrogen bonding and maximum conversion level for nickel – triamine species

Complex	Max. conversion level / %	GS intermolecular hydrogen bond lengths / Å
[1]	100	None
[5]	52	2.96(1), 3.31(1)
[7] (molecule A)	89	None
[7] (molecule B)	32	3.06(1), 3.06(1)
[8b]	35	2.80(1), 3.19(1), 3.09(1), 3.33(1)

In addition, comparison of fingerprint plots for all of the isomerising species reported in Chapter 4 has indicated that a number of intermolecular interactions to the nitrite ligand are rearranged between GS and MS, while the remaining crystalline environment appears largely unchanged. These results are pleasing as the triamines were chosen as bulky, photoinert fragments that it was hoped would dominate the packing and facilitate nitro – nitrito rearrangement more efficiently.

As the "reaction cavity" concept[99] was shown to agree well with the photoconversion trend observed for [1], [2] and [3] (§ 4.1.4), the same analysis was applied to [5], [7] and [8b]. As before, the reaction cavity is defined as the region surrounding the photoactive part of the system, and it is expected that the cavity that undergoes the least change should represent the most favourable photoreaction. Table 4.38 gives the results for all the photoactive nickel – triamines. Reaction cavity data are reported as a percentage of unit cell volume and have been normalised by dividing by Z, so that the reaction cavity for an individual photoactive molecule is represented.

Table 4.38: Reaction cavity data from steady-state photocrystallographic studies with nickel – triamines

Complex	Conversion / %	ΔV_c (% of unit cell volume / Z)
[1]	100	0.20
[5]	52	0.33
[7]	89, 32	0.17
[8b]	35	0.75

Although the results are less convincing that those of the *N,N,N',N'-*tetraethyldiethylenetriamine systems of § 4.1.4, they are generally in agreement with the Topochemical Postulate, with lower converting systems displaying larger values of ΔV_c. The only anomalous result is determined for [7], unexpectedly returning the smallest ΔV_c despite

having incomplete conversion in either independent molecule. It is perhaps the fact that there are two independent photoactive species co-existing in [7] that causes this discrepancy; given that the two sites have differing photoresponses it is perhaps unrealistic to assess them together. However, analysis on molecules A and B separately also returns inconsistent results. This could suggest that excitation of the two molecules is somehow correlated, perhaps *via* intermolecular interactions in the lattice. The anomaly indicates that, although the reaction cavity concept generally fits well with conversion trends, there are likely other processes occurring that also affect the photoisomerisation.

4.3.   Summary

The results of Chapter 4 have begun to suggest which factors more strongly affect the progress of linkage isomerism within the crystal, and which are less influential. From § 4.1 it is apparent the identity of the TM centre has some influence on linkage isomerisation, although it is evident this factor alone cannot explain the trends observed and further investigation on this point is desirable.

In terms of the steric influences within the lattice, it appears that comparison of the overall change in lattice volume on excitation has limited efficacy in explaining the trends. The degree to which the isomerising groups are involved in intermolecular contacts, and most particularly hydrogen bonding, has been shown to play a more key role in assisting or hindering conversion, as is evident both from fingerprint plots and hydrogen bond analysis. This suggests that, when designing systems to undergo maximum photoconversion, it is better to employ auxiliary ligands containing fewer potential hydrogen bond donors, so as to reduce the possibility of unfavourable interactions for the isomerising groups. Conversely, void space analysis on the overall crystal structure is not shown to correlate with photoconversion. This is likely due to the fact that calculations are made only on the static, time- and space-averaged structures of photostationary GS and MS states, and therefore take no account of the dynamic behaviour of the lattice over the shorter length and time-scales that are likely more relevant to individual isomerisation events.[101] Void space calculations are better employed in reaction cavity analysis, which appears to better explain the trends observed in reference to changes occurring in more localised regions. Overall, the results indicate that, while arguments based on steric influences go some way to explaining the trends in isomerisation behaviour observed, these alone are not sufficient. It is apparent that other influences, such as kinetic and electronic factors, must also be investigated to obtain a more complete understanding of the nitro – nitrito photoisomerism process.

Chapter 5.

Steady-state Crystallographic Studies of Group 10 Complexes with a Tridentate Phosphine Ligands

Chapter 5. Steady-state Crystallographic Studies of Group 10 Complexes with a Tridentate Phosphine Ligands

By analogy to the metal – triamine species of Chapter 4, Chapter 5 is concerned with nitro – nitrito isomerisation in metal – triphosphine systems. Descending Group 15 necessarily causes a change in the electronic influence from the ancillary ligand. Phosphines are generally better strong-field ligands than the equivalent amines, leading to complexes with higher values of Δ.[133] For nickel(II), the increased ligand field stabilisation energy (LFSE) assists a geometry change from the octahedral environment observed in triamine species and the d^8 metal centre can now adopt square planar configuration.
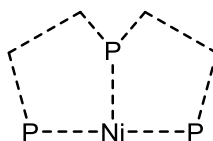
Figure 5.1: Fragment used to conduct Search 3 of the CSD

To allow comparison between the complexes of Chapters 4 and 5, phosphine ligands were chosen to be as similar as possible to the triamine species. CSD Search 3 was conducted using the fragment in Figure 5.1, with no additional geometric constraints. This returned 62 hits, 43 of which are tridentate species. 33 contain *bis*-(2-diphenylphosphinoethyl)phenylphosphine, or "triphos" (Figure 5.2), showing this to be a popular ligand for nickel – triphosphine synthesis. Of these 33 systems, although a range of ligands are found at the fourth coordination site, interestingly none are nitrite species.
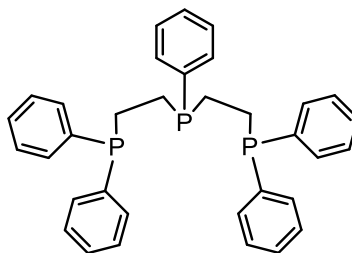
Figure 5.2: *bis*-(2-diphenylphosphinoethyl)phenylphosphine, or "triphos" ligand

Triphos is also a good ligand for use in the current study, when considering both the requirements for auxiliary ligands outlined in Chapter 2 and the recommendations arising from the results of Chapter 4. Its suitability lies in the fact that it is highly substituted, with five phenyl groups bonded to phosphorus. As such, this bulky ligand is highly desirable as a photoinert fragment to be incorporated into metal – nitrite species, as it should dominate crystal packing and assist isomerisation in the smaller nitrite ligand whilst minimising the overall changes in the lattice. Additionally, being highly substituted, triphos has no hydrogen donor capability, a feature recommended in Chapter 4 when designing systems to undergo high levels of photoconversion (§ 4.2.6).

5.1. *bis*-(2-Diphenylphosphinoethyl)phenylphosphine Complexes

5.1.1. Complex [9]: Nitro-(*bis*-(2-diphenylphosphinoethyl)phenylphosphine) nickel(II) tetraphenylborate

Complex [9] was first synthesised during earlier linkage isomer studies involving a selection of Ni(II) systems with mainly mono- and di-phosphine ancillary ligands, and was the only tridentate species investigated.[140] [9] was prepared *via* a novel synthetic route, in which equal portions of triphos and potassium hexanitronickelate(II) in methanol / THF were heated under reflux in a dry N_2 atmosphere. The product was dissolved in acetone / water and sodium tetraphenylborate added to give an orange precipitate of [9]. Irradiation at $\lambda = 400$ nm and 100 K induced 85% nitro – nitrito conversion in the single-crystal, however no further photoactivation could be achieved. [9] is studied further in the current project, aiming to better understand why photoactivation remains incomplete at $\lambda = 400$ nm.

Crystal Structure and Bonding

A crystal of [9] was flash cooled to 100 K and an X-ray dataset collected (Table 5.1). [9] crystallises in the triclinic space group *P*-1 with one nickel cation and one tetraphenylborate anion in the asymmetric unit. The nickel centre is square planar, bound to one nitrite and one *bis*-(2-diphenylphosphinoethyl)phenylphosphine (Figure 5.3). A mixture of isomers is found for the flash cooled structure, similar to the nickel complexes [1] and [7]. The major isomer at 88% occupancy adopts nitro-(η^1-NO_2), while the minor isomer is *endo*-nitrito-(η^1-ONO).

Table 5.1: Single-crystal X-ray data for the flash cooled structure of [9]

Temperature	100(2) K
Radiation source	Mo K$_\alpha$
Wavelength	0.71073 Å
Empirical formula	C58 H53 B1 N1 Ni1 O2 P3
Formula weight	958.44 g mol^{-1}
Crystal size	0.25 x 0.20 x 0.11 mm^3
Crystal system	Triclinic
Space group	*P*-1
Unit cell dimensions	$a = 11.441(5)$ Å $\alpha = 96.185(5)°$
	$b = 14.381(5)$ Å $\beta = 105.333(5)°$
	$c = 17.105(5)$ Å $\gamma = 113.091(5)°$
Volume	2424.8(15) Å^3
Z	2
Density (calculated)	1.313 Mg m^{-3}
Absorption coeff. μ	0.544 mm^{-1}
F(000)	1004
R(int)	0.0299
R1 (obs. data)	0.0454
wR2 (all data)	0.1036
Reflections (indep.)	14759
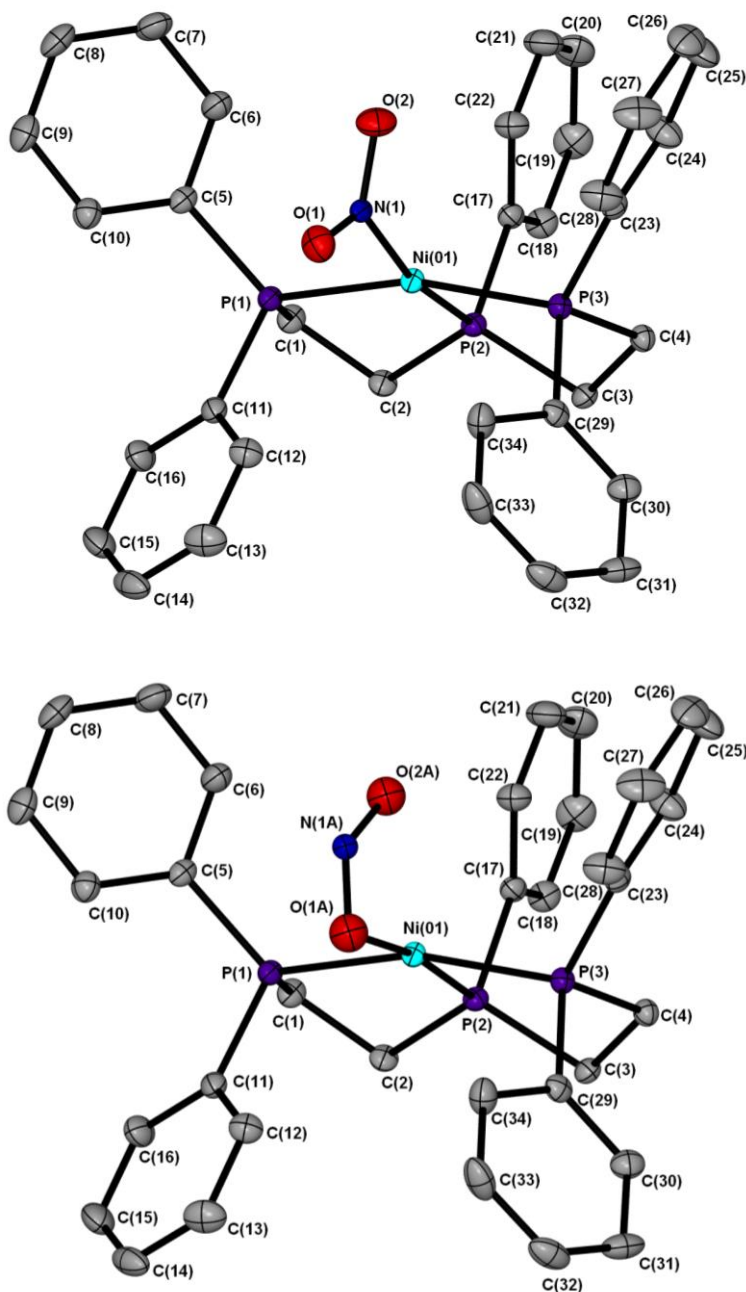
Figure 5.3: Single-crystal X-ray structure of the nickel cation in [9] showing the atomic arrangement for the two linkage isomers present in the flash cooled crystal; **(a)** 88% nitro-(η^1-NO$_2$) and **(b)** 12% *endo*-nitrito-(η^1-ONO). Ellipsoids at 50% probability and hydrogen atoms removed for clarity

The crystal packing arrangement for complex [9] is shown in Figure 5.4. Nickel cations are arranged in rows running parallel to the *b*-axis with cations in adjacent rows inverted with respect to one another due to the crystallographic symmetry, causing the nitrite ligands in adjacent rows to face towards one another. The isomerising groups are not close in space however, as inverted pairs of cations (comprising one unit cell) are offset from one another along the *b*-direction.
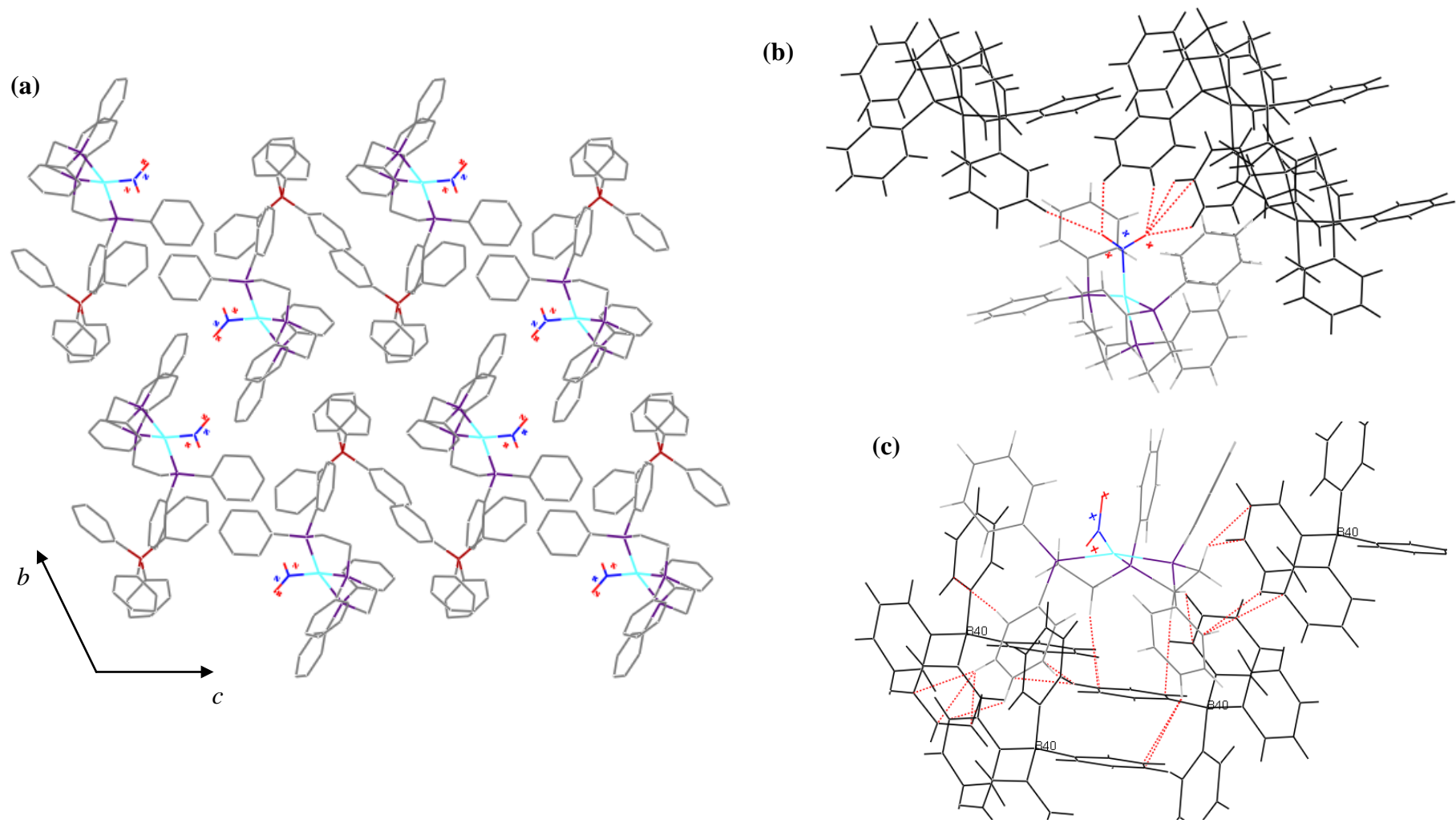
Figure 5.4: Crystal packing arrangement for the flash-cooled structure of [9]; **(a)** complete packing diagram viewed along the *a*-axis, *c*-axis horizontal, **(b)** close contact interactions (red dotted lines) to the nitrite ligand, **(c)** cation – anion close contact interactions

As expected, there are no hydrogen bonds in the structure, although each nitro-(η^1-NO$_2$) ligand is involved in six close contacts with three other neighbouring cations (Figure 5.4(b)), indicating the crystal is tightly packed in the region of the nitrite ligand. Each nickel cation is also involved in several C-H…C-H and C-H…π interactions with four neighbouring tetraphenylborate anions (Figure 5.4(c)). These contacts involve only the triphosphine ligand of the cation and so the bulky anions are positioned well away from the isomerising nitrite groups. No anion – anion interactions occur, with each tetraphenylborate only forming close contacts with neighbouring cation species.

Thermal Studies

As thermal studies with [1] and [7] have shown that a thermodynamic equilibrium exists between nitrite isomers co-existing in these systems on crystallisation, similar experiments are appropriate to investigate if comparable behaviour occurs in [9] on varying the temperature.

A crystal was mounted with minimal light exposure and a room temperature dataset collected. A series of identical datasets were then collected at regular intervals between 298 and 100 K, with the crystal held for 5 min at each temperature to allow the system to equilibrate. At 298 K the nitro : nitrito ratio is very similar to that determined for the flash cooled structure of [9], comparing well to analogous experiments with [1]. This indicates that, on flash cooling, the system is cryo-trapped into a similar arrangement to that seen under ambient conditions. Slow cooling causes a decrease in nitrito isomer occupancy and at 200 K and below this minor component can no longer be modelled satisfactorily, showing that a clean, 100% nitro-(η^1-NO$_2$) isomer has been produced. Repeat datasets were then collected, and in the second repeat set the crystal was warmed between 225 and 298 K to investigate the possibility of hysteresis. Finally the crystal was re-cooled in the third set of experiments. Isomer ratios are reproducible at each temperature, showing no hysteresis for the thermal process in [9]. A full summary of ratios obtained in repeat experiments is found in Table 1, Appendix 9.

In a separate series of experiments a new crystal was heated to determine the nitro : nitrito ratio above 298 K. As expected from the preceding thermal trend, raising the temperature further increased conversion to nitrito-(η^1-ONO), with a maximum level of 31% achieved at 370 K. Above this temperature crystallinity was irretrievably lost. The nitro : nitrito ratios for all thermal studies with [9] are given in Table 5.2. The results again suggest that the isomers exist in thermodynamic equilibrium, the position of which can be altered on varying the temperature. While high temperatures promote conversion to nitrito-(η^1-ONO), low temperatures favour nitro-(η^1-NO$_2$) suggesting this is the thermodynamically favoured arrangement.

147

Table 5.2: Crystallographically determined ratios of nitro-(η^1-NO$_2$) and nitrito-(η^1-ONO) isomers in [9] as a function of temperature (100 – 298 K = average over 3 repeat sets)

Temp / K	Occupancy (esd)	
	Nitro-(η^1-NO$_2$)	Nitrito-(η^1-ONO)
100	1.00*	0.00*
150	1.00*	0.00*
200	1.00*	0.00*
225	0.95(1)	0.05(1)
250	0.92(1)	0.08(1)
275	0.89(1)	0.11(1)
298	0.84(1)	0.16(1)
350	0.73(2)	0.27(2)
370	0.69(2)	0.31(2)

* No esd is reported for full occupancy or zero occupancy as these ratios were not refined

As for [1] and [7], kinetic data can be approximated for the thermodynamic equilibrium in [9]. A Van't Hoft plot was constructed for the data between 298 and 225 K (Figure 5.5).
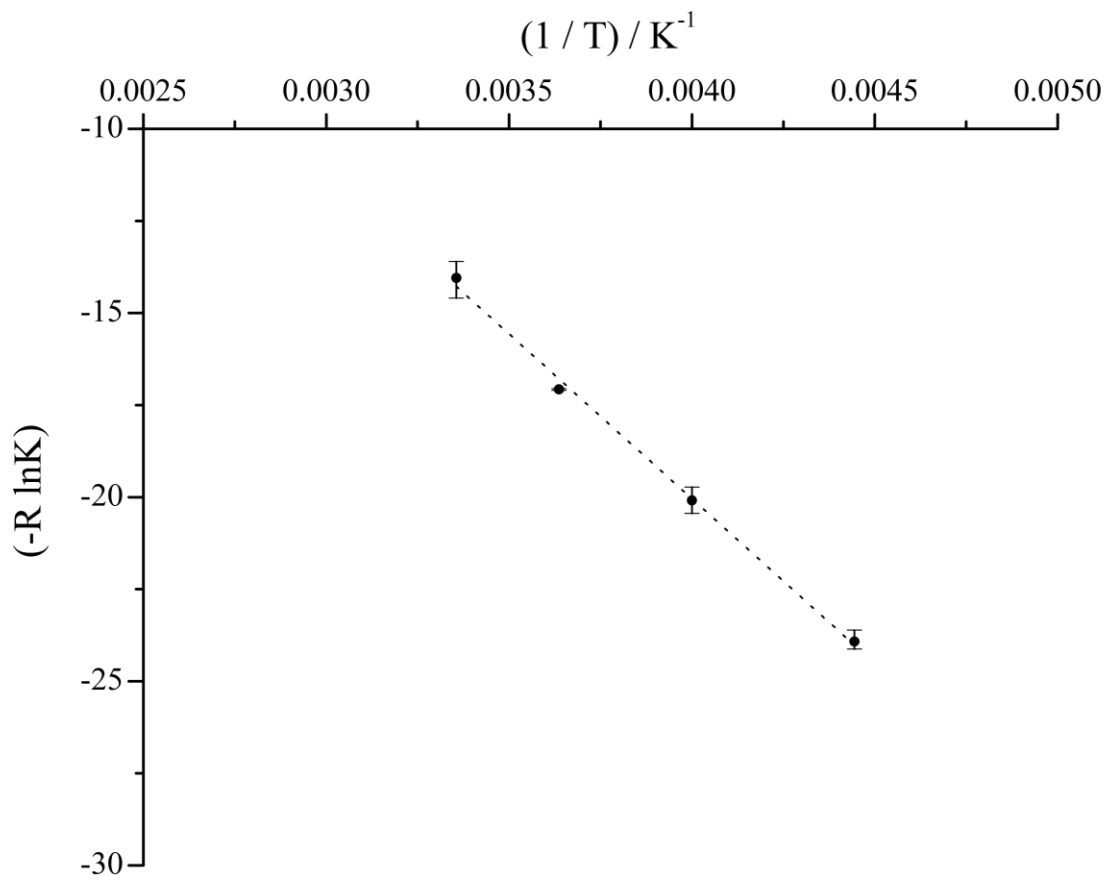
Figure 5.5: Van't Hoft plot for the thermodynamic equilibrium in complex [9]. Slope m = standard enthalpy (ΔH) = −8.9 (± 0.3) kJ mol^{-1}, intercept C = entropy (ΔS) = −15.7 (± 1.0) J K-1 mol^{-1}, R^2 = 0.991

$$(-R)\ln(K_{eq}) = \Delta H(\frac{1}{T}) - \Delta S$$

$$\text{y} \qquad = \text{m} \quad x \quad + \quad C$$

Applying Equation 4.4 to the data allows an estimation of the enthalpy ΔH and entropy change ΔS on thermal isomerisation. There is good linear correlation between Equation 4.4 and the data (R^2 = 0.991), and estimates of ΔH = −8.9 (± 0.3) kJ mol^{-1} and ΔS = −15.7 (± 1.0) J K^{-1} mol^{-1} both compare well to the results obtained for complexes [1] and [7] in Chapter 4.
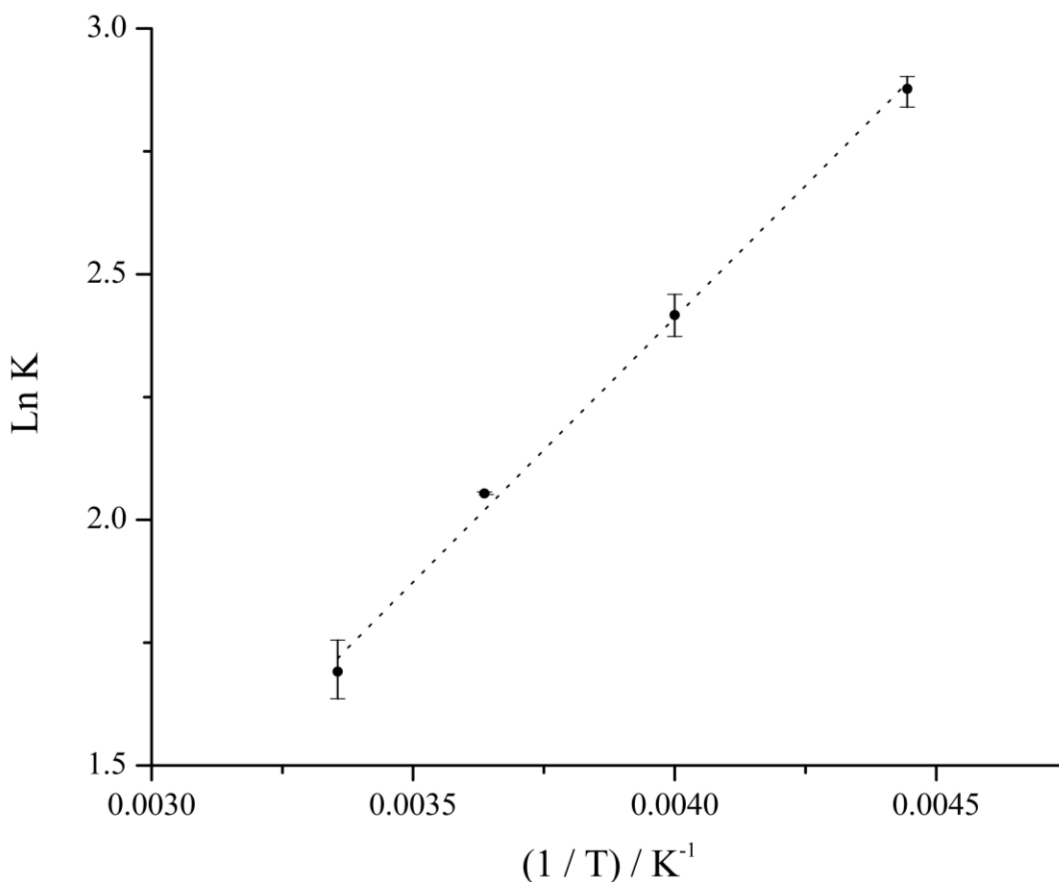
Figure 5.6: Arrhenius plot for the thermally induced isomerisation reaction in complex [9]. Activation energy E_A = −1.08 (± 0.04) kJ mol^{-1}, R^2 = 0.996

An Arrhenius plot can also be constructed, allowing an estimate of the activation energy E_A to be made for the thermal isomerisation (Figure 5.6). Again, there is strong linear correlation between Equation 4.6 and the data (R^2 = 0.996) and an estimate of E_A = −1.08 (± 0.04) kJ mol^{-1} is obtained. This value is very similar to that obtained for complex [7] and is comparable to both complex [1] and estimations of E_A for similar processes in the literature.[141]

$$\ln(k_{eq}) = -E_A(\frac{1}{RT}) + \ln(A)$$

$$\text{y} \quad = \quad \text{m} \ x \ + \quad C$$

Steady-State Photocrystallography

A UV/vis spectrum was collected on a solid sample of [9] and used to identify an appropriate excitation wavelength (Figure 1, Appendix 9). In line with previous results and discussion,[23, 71, 130] a wavelength in the tail of the main, MLCT absorption is likely to induce high conversion, and in test experiments irradiation at λ = 470 nm induced the most promising photoresponse. A full, steady-state photocrystallographic experiment was then conducted with 470 nm light.

A crystal was mounted at room temperature and slowly cooled to 100 K, before an X-ray dataset was collected in the dark. As expected a clean, 100% nitro-(η^1-NO$_2$) isomer had been produced. This structure is used as the GS for photocrystallographic studies. The same crystal was then irradiated with 470 nm LED light and, after a period of 2 h, the LEDs were switched off and a second, identical data collection was conducted. This second dataset showed that complete conversion to a metastable, 100% *endo*-nitrito-(η^1-ONO) isomer had been achieved. The crystal was held at 100 K in the dark for a further 1 h and a subsequent dataset confirmed that the 100% nitrito isomer remained present, showing the ES is metastable under these conditions. Crystal data for both GS and MS structures of [9] are given in Table 5.3.

Table 5.3: Crystal data for GS and MS structures of [9] in steady-state photocrystallographic experiments, following irradiation with 470 nm LED light

	Ground state	470 nm Metastable state
Photoconversion	0%	100%
Temperature	100(2) K	100(2) K
Radiation source	Mo K$_\alpha$	Mo K$_\alpha$
Wavelength	0.71073 Å	0.71073 Å
Empirical formula	C58 H53 B1 N1 Ni1 O2 P3	C58 H53 B1 N1 Ni1 O2 P3
Formula weight	958.44	958.44
Crystal size	0.15 x 0.10 x 0.02 mm^3	0.15 x 0.10 x 0.02 mm^3
Crystal system	Triclinic	Triclinic
Space group	*P*-1	*P*-1
Unit cell dimensions	a = 11.441(5) Å α = 96.219(5)° b = 14.378(5) Å β = 105.272(5)° c = 17.098(5) Å γ = 113.179(5)°	a = 11.456(5) Å α = 95.356(5)° b = 14.377(5) Å β = 105.708(5)° c = 17.089(5) Å γ = 112.581(5)°
Volume	2421.9(15) Å^3	2439.4(15) Å^3
Z	2	2
Density (calculated)	1.314 M g m^{-3}	1.305 M g m^{-3}
Absorption coeff. μ	0.544 mm^{-1}	0.540 mm^{-1}
F(000)	1004	1004
R(int)	0.0469	0.0548
R1 (obs. data)	0.0552	0.0628
wR2 (all data)	0.0986	0.1108
Reflections (indep.)	9855	9936

Figure 5.7: Photodifference map for the nickel cation in [9] showing the change in Fourier electron density distribution between the GS and MS; red = –4.5 eÅ^{-3}, green = +4.5 eÅ^{-3}

Figure 5.7 displays the photodifference map for [9], confirming the production of the MS. Red contours show areas of negative electron density surrounding the GS nitro isomer, showing its occupancy level decreases on photoactivation, while green contours show positive electron density at the atomic positions of the *endo*-nitrito isomer, confirming its formation.

Variable temperature parametric studies were then conducted using the same crystal, to determine the MS range. 100% nitrito-(η^1-ONO) occupancy is retained on warming between 100 and 160 K, but the system reverts to the 100% nitro-(η^1-NO$_2$) GS configuration by 180 K, indicating that the MS limit for [9] lies between 160 and 180 K (Table 5.4).

Table 5.4: Crystallographically determined nitro : nitrito ratios as a function of exposure to 470 nm LED light in steady-state photocrystallographic experiments with [9]

Irradiation time / h	Temp / K	Occupancy	
		Nitro-(η^1-NO$_2$)	Nitrito-(η^1-ONO)
0	100	1.00	0.00
2	100	0.00	1.00
2	140	0.00	1.00
2	160	0.00	1.00
2	180	1.00	0.00

Crystal Packing and Sterics

The overall packing arrangement is again largely unchanged following irradiation, with the photoactivated structure closely resembling that described by Figure 5.4, excepting the rearrangement of the nitrite ligand. The cell volume increases on photoactivation, with a value of $\Delta V = +17.5(21)$ $Å^3$ between GS and MS. This equates to a 0.72% increase, which is comparable to the changes observed in the triamine systems of Chapter 4. The difference is statistically significant, with a value of $\Delta V / \sigma(\Delta V) = 8.25$ on application of the 3σ rule. Considering the unit cell parameters separately, the lattice expansion occurs anisotropically, with only the *a*-axis increasing after irradiation while the *b*- and *c*-axes both decrease very slightly. It is difficult to relate these anisotropic changes to the isomerisation process directly, since the nitro − nitrito rearrangement does not occur specifically in the *a*-axis direction.

As there are no hydrogen bonds present in the structure of [9], analysis of the intermolecular interactions can instead be used to assess the changes in other close contacts as a result of the isomerisation. Crystal Explorer fingerprint plots are again used for this analysis, providing a quick, visual assessment of the difference between GS and MS structures.

The overall plots are again highly similar, showing there to be little change in the overall structure on photoactivation, although some very subtle differences are noticeable that appear clearer on separating the plots to show individual constituent interactions (Table 5.5). Four main types of intermolecular contacts occur in [9]: O…H and N…H contacts, involving interactions with the isomerising nitrite ligands; and C…H and H…H contacts, which solely represent the rest of the crystal structure. The N…H and O…H plots show marked changes between GS and MS. Excitation causes simultaneously a decrease in the number of O…H contacts and a dramatic increase in the number and length of N…H interactions, with new "spike" features at *ca.* $d_e = 1.4$ Å, $d_i = 1.1$ Å becoming apparent in the N…H plot for the photoactivated structure. These observations are expected on the rearrangement of N(1) to its new position as N(1A) following the nitro − nitrito rearrangement. Conversely, the C…H and H…H plots are nearly identical for both the GS and MS structures, confirming that the main changes in intermolecular interactions occur as a result of linkage isomerisation in [9].

Table 5.5: Crystal Explorer Fingerprint Plots representing the changes in intermolecular contacts in the GS and MS structures of [9]

	GS	470 nm MS
All Contacts		
N...H contacts		
O...H contacts		
C...H contacts		
H...H contacts		
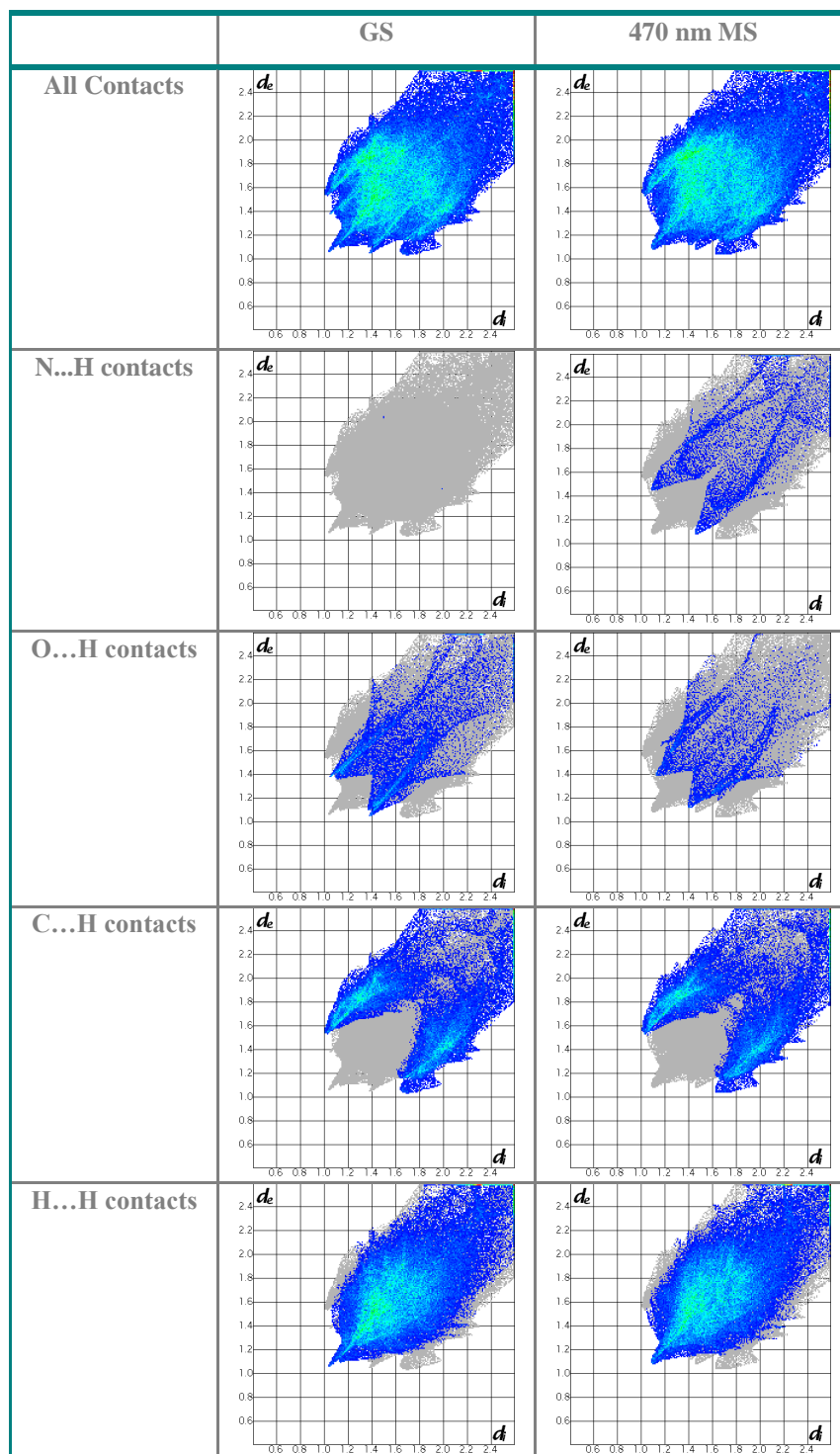
5.1.2. Complex [10]: Nitro-(*bis*-(2-diphenylphosphinoethyl)phenylphosphine) palladium(II) tetraphenylborate

Crystal Structure and Bonding

[10] was synthesised *via* the procedure outlined in § 9.2.10 and colourless crystals obtained by slow evaporation from a dichloromethane and toluene mixture. A crystal was flash cooled to 100 K before a standard X-ray data collection was then conducted (Figure 5.8).
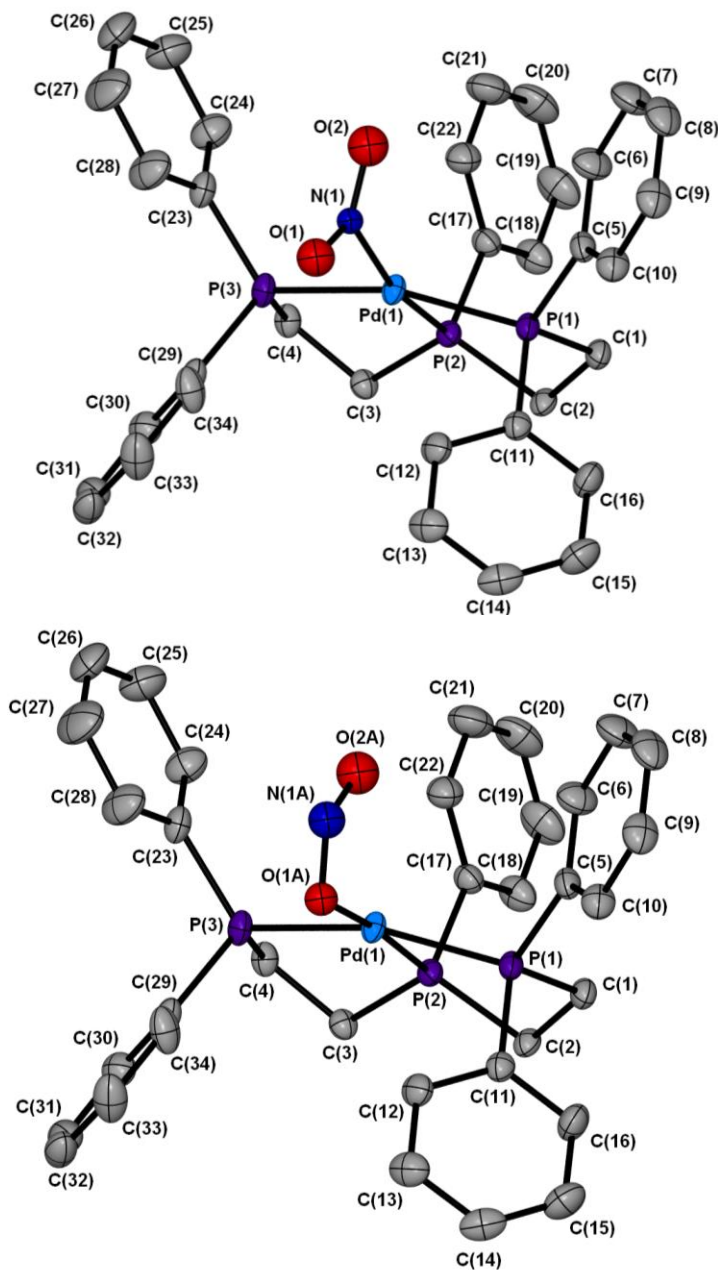
Figure 5.8: Single-crystal X-ray structure of the palladium cation in [10] showing the atomic arrangement for the two linkage isomers present in the flash cooled crystal; **(a)** 52% nitro-(η^1-NO$_2$) and **(b)** 48% *endo*-nitrito-(η^1-ONO). Ellipsoids at 50% probability and hydrogen atoms removed for clarity

154

Complex [10] is isostructural with its nickel analogue [9] and so crystallises in the same triclinic space group *P*-1, with one palladium cation and one tetraphenylborate anion in the asymmetric unit. The cation adopts square planar geometry, attached to one *bis*-(2-diphenylphosphinoethyl)phenylphosphine ligand while the remaining coordination site is occupied by a monodentate nitrite group. Similarly to [9], the nitrite is disordered over two positions in the flash cooled structure, with both nitro-(η^1-NO$_2$) and *endo*-nitrito-(η^1-ONO) isomers present. The ratio of isomers is more equal here than for the nickel complex, with nitro and nitrito occupancies of 52 : 48 respectively in [10]. Table 5.6 gives the crystal data.

Table 5.6: Crystal data for flash cooled structure of [10]

Temperature	100(2) K
Radiation source	Synchrotron
Wavelength	0.77490 Å
Empirical formula	C58 H53 B1 N1 O2 P3 Pd1
Formula weight	1006.13 g mol^{-1}
Crystal size	0.05 x 0.02 x 0.01 mm^3
Crystal system	Triclinic
Space group	*P*-1
Unit cell dimensions	a = 11.356 (2) Å α = 97.625(2)° b = 14.487(2) Å β = 104.780(2)° c = 17.192(2) Å γ = 111.007(2)°
Volume	2473.2(6) Å^3
Z	2
Density (calculated)	1.351 M g m^{-3}
Absorption coeff. μ	0.586 mm^{-1}
F(000)	1040
R(int)	0.0619
R1 (obs. data)	0.0572
wR2 (all data)	0.1789
Reflections (indep.)	14822

Being isostructural with [9], the crystal packing arrangement for complex [10] closely resembles that described by Figure 5.4, excepting the exchange of the metal centre from nickel to palladium.

Again, no hydrogen bond interactions occur in the structure of [10], as expected due to the lack of hydrogen bond donor groups on the ancillary triphos ligand. Instead, the nitrite ligand is again involved in a number of close contact interactions with hydrogen atoms on three neighbouring cation molecules, suggesting that the crystal packing is fairly tight in the regions surrounding the isomerising groups in the static, space- and time-averaged crystal structure.

Thermal Studies

The presence of two nitrite arrangements in the flash cooled structure suggest potential for thermally-induced linkage isomerism in [10], as has been observed in nickel – nitrite complexes [1], [7] and [9], for which more than one linkage isomer is found to co-exist in system on crystallisation. As such, similar thermal studies are appropriate for complex [10].

The same crystal was first warmed to 298 K and a room temperature dataset obtained. This revealed a 50 : 50 isomer ratio, showing there is no preference for either linkage isomer under ambient conditions. The crystal was then slow cooled *in-situ*, with cooling stopped at regular intervals to allow repeat datasets to be collected. Contrary to the results obtained for the nickel – nitrite species, little change in the nitro : nitrito ratio is observed in [10] on cooling, with a maximum difference of 55 : 45 nitro to nitrito isomers respectively obtained by 100 K. A 5% difference in occupancy is small and, as it is accumulated over several repeat X-ray experiments, cannot be considered significant. As such, it appears that slow cooling does not induce significant thermal nitrito – nitro isomer conversion in the palladium – nitrite species.

Steady-State Photocrystallography

The solid-state UV/visible absorption spectrum of [10] (Figure 1, Appendix 10) was used to guide the selection of excitation wavelength photocrystallographic studies. The position of the main, MLCT absorption suggested that wavelengths between 300 and 430 nm were most likely to induce high levels of photoisomerisation,[23, 71, 130] and test experiments led to the selection of 400 nm light.

A crystal was flash cooled to 100 K and a single-crystal X-ray dataset confirmed the same, mixed structure containing a 52 : 48 ratio of nitro to nitrito isomers for the GS. The same crystal was then subject to 1 h irradiation at $\lambda = 400$ nm and a subsequent dataset revealed that conversion had been induced, with 89% of the crystal now occupying *endo*-nitrito-(η^1-ONO) configuration. A maximum photoinduced *endo*-nitrito occupancy of 90% was achieved after 2 h photoactivation, with further irradiation causing no appreciable change. Additionally, no change was observed when the crystal was held at 100 K in the dark, confirming the ES to be metastable at this temperature. Table 5.7 gives the crystal data for GS and MS structures.

Additionally, the photodifference map in Figure 5.9 clearly shows the production of the MS. Red contours surrounding the atoms of the nitro group confirm the reduction of this ligand, while regions of positive density (green) surrounding the atoms of the *endo*-nitrito ligand reflect the increased conversion to this isomer on photoactivation.

156

Table 5.7: Crystal data for GS and MS structures of [10] in steady-state photocrystallographic experiments, following irradiation with 400 nm LED light

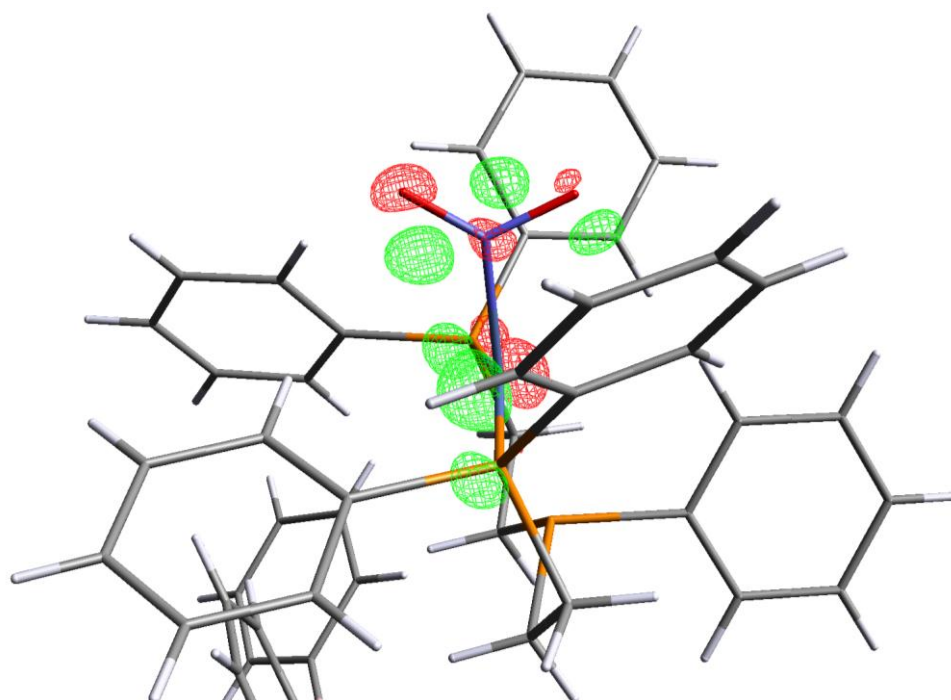|	Ground state	400 nm Metastable state
Nitrito occupancy	52%	90%
Temperature	100(2)	100(2)
Radiation source	Synchrotron	Synchrotron
Wavelength	0.77490 Å	0.77490 Å
Empirical formula	C58 H53 B1 N1 O2 P3 Pd1	C58 H53 B1 N1 O2 P3 Pd1
Formula weight	1006.13 g mol^{-1}	1006.13 g mol^{-1}
Crystal size	0.05 x 0.02 x 0.01 mm^3	0.05 x 0.02 x 0.01 mm^3
Crystal system	Triclinic	Triclinic
Space group	*P*-1	*P*-1
Unit cell dimensions	a = 11.356(2) Å α = 97.625(2)° b = 14.487(2) Å β = 104.780(2)° c = 17.192(2) Å γ = 111.007(2)°	a = 11.361(1) Å α = 96.928(1)° b = 14.478(1) Å β = 105.175(1)° c = 17.172(2) Å γ = 110.857(1)°
Volume	2473.2(6) Å^3	2474.9(4) Å^3
Z	2	2
Density (calculated)	1.351 M g m^{-3}	1.350 M g m^{-3}
Absorption coeff. μ	0.586 mm^{-1}	0.585 mm^{-1}
F(000)	1040	1040
R(int)	0.0619	0.0623
R1 (obs. data)	0.0572	0.0610
wR2 (all data)	0.1789	0.1870
Reflections (indep.)	14822	14850
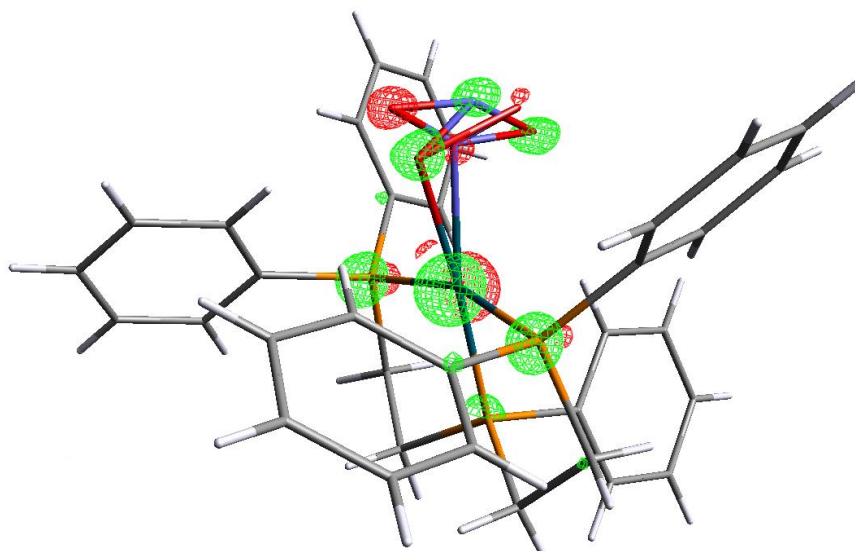
Figure 5.9: Photodifference map for the palladium cation in [10], showing the change in Fourier electron density distribution between the GS and MS; red = −2.8 eÅ^{-3}, green = +2.8 eÅ^{-3}

Finally, variable temperature parametric studies were conducted to determine the MS range. *Endo*-nitrito remains the major isomer until 180 K, but warming to 200 K causes the system to return to a ratio similar to that of the GS. The MS limit therefore exists between 180 and 200 K. Table 5.8 gives the isomeric ratios for photocrystallographic studies with [10].

Table 5.8: Crystallographically determined ratios of nitro and nitrito linkage isomers as a function of irradiation time in photocrystallographic experiments with [10]

Irradiation time / h	Temperature / K	Occupancy (esd)	
		Nitro-(η^1-NO$_2$)	Nitrito-(η^1-ONO)
0	100	0.52(1)	0.48(1)
1	100	0.11(1)	0.89(1)
2	100	0.10(1)	0.90(1)
2	140	0.10(1)	0.90(1)
2	160	0.11(1)	0.89(1)
2	180	0.18(1)	0.82(1)
2	200	0.55(1)	0.45(1)

* No esd is reported for full occupancy or zero occupancy as these ratios were not refined

Crystal Packing and Sterics

Very little change in the overall structure is observed on photoactivation in [10], with the system retaining the same *P*-1 space group and the packing arrangement still closely resembling that shown in Figure 5.4. A comparison of the unit cell parameters also confirms there to be little difference between the GS and MS, with a small volume increase of $\Delta V = +1.7(7)$ Å^3 (0.07%) that is statistically insignificant on application of the 3σ rule, returning a value of $\Delta V / \sigma(\Delta V) = 2.36$. The cell changes are anisotropic, with an increase observed in the *a*-axis but decreases in both *b*- and *c*-axes, showing expansion only along the *a*-direction. The changes are similar to those of [9], but again cannot be a direct result of the isomerisation as the nitro – nitrito rearrangement occurs in a plane that intersects with all three axes.

Crystal Explorer fingerprint plots are also used to assess the changes in intermolecular interactions on excitation (Table 5.9). Again, in line the crystal packing diagrams, the overall plot shape is very similar for both GS and MS, indicating little change in the overall structure. On decomposing these plots into the individual constituent interactions some subtle differences are identified, however, that can be attributed to the nitro – nitrito rearrangement. N…H and O…H close contacts include interactions involving the nitrite groups, while C…H and H…H plots represent solely the remaining structure. There is generally an increase in the number of close N…H and O…H contacts on photoactivation and it is particularly event that O…H interactions also become shorter. These differences are in line with the MS rearrangement, as the atoms of the *endo*-nitrito isomer are in general further from the palladium centre and are more exposed to interaction with the surrounding environment. By contrast, the C…H and H…H plots are unchanged, confirming that the differences in intermolecular contacts are the result of nitro – nitrito isomerisation.

158

Table 5.9: Crystal Explorer fingerprint plots showing changes in intermolecular contacts to the cation moiety on photoactivation of [10]

	GS	400 nm MS
All Contacts		
N...H contacts		
O…H contacts		
C…H contacts		
H…H contacts		
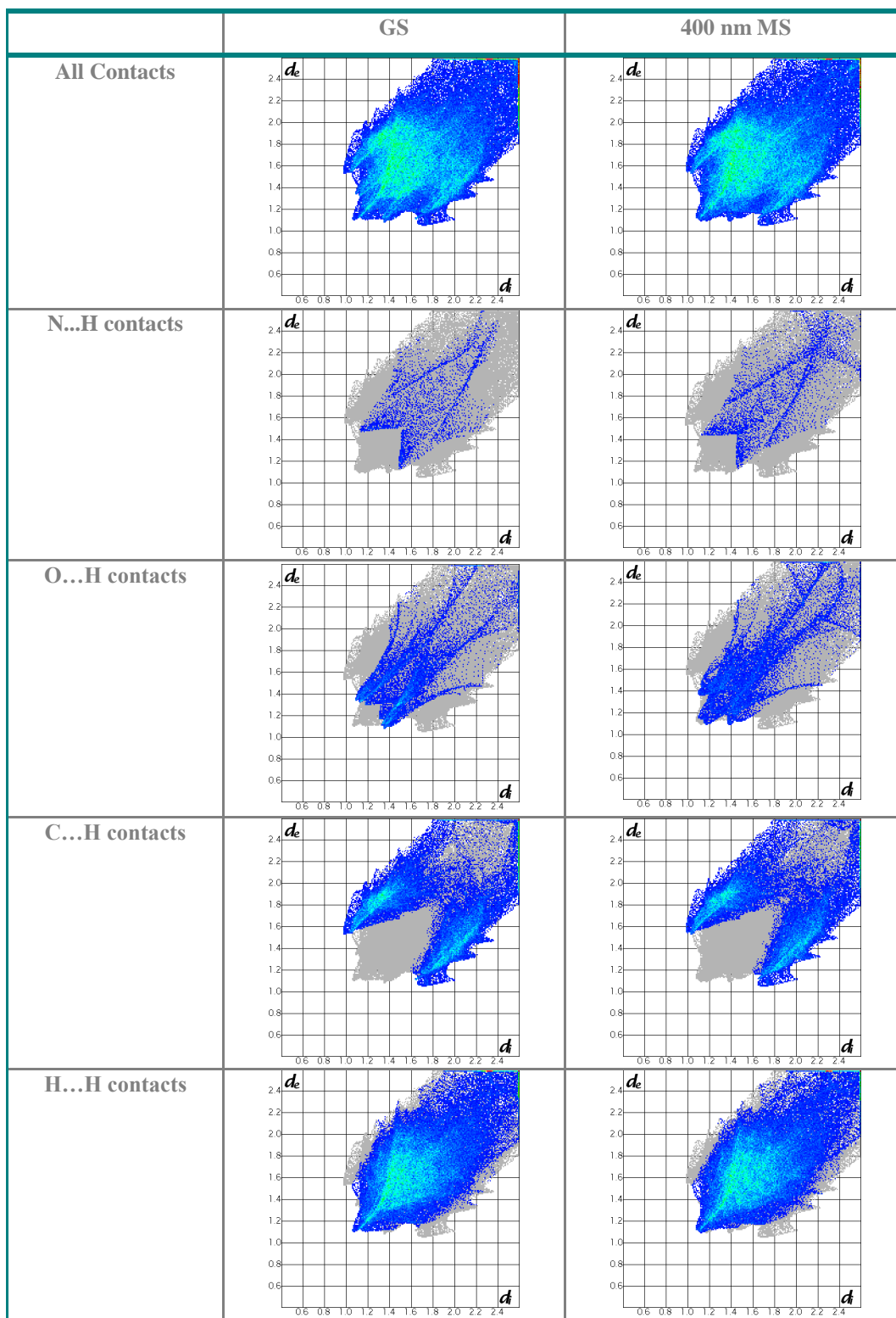
5.1.3. Complex [11]: Nitro-(bis-(2-diphenylphosphinoethyl)phenylphosphine) platinum(II) tetraphenylborate

Crystal Structure and Bonding

Complex [11] was synthesised *via* the procedure outlined in § 9.2.11 and colourless crystals were grown by slow evaporation from a dichloromethane and toluene mixture. A suitable crystal was flash cooled to 100 K and a standard single-crystal X-ray dataset collected.
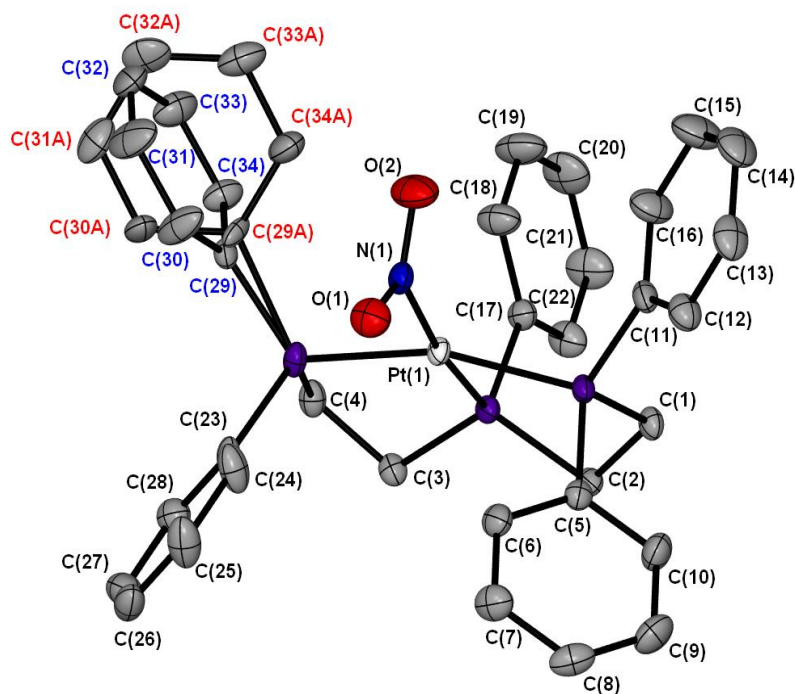
Figure 5.10: Single-crystal X-ray structure of the platinum cation in [11] showing the atomic arrangement in the flash-cooled structure. Ellipsoids at 50% probability and hydrogen atoms removed for clarity

Complex [11] is isostructural with [9] and [10], crystallising in the same triclinic space group, *P*-1, with similar cell parameters. The asymmetric unit contains one cation and one tetraphenylborate anion and Figure 5.10 shows the atomic arrangement in the cation. As expected the d^8 platinum centre is square planar, with the single nitrite ligand adopting solely nitro-(η^1-NO$_2$) configuration while the remaining coordination sites are occupied by the triphosphine ligand. One phenyl group is disordered over two positions, with a 80 : 20 ratio between the two components.

Crystal Packing and Sterics

Being isostructural with [9] and [10], the packing arrangement in [11] is similar to that of Figure 5.4. Again, no hydrogen bonds exist in the structure, as expected due to the lack of effective hydrogen bond donors on the triphos ligand. In addition, the molecules are involved in similar intermolecular interactions to those described previously for this crystal form.

Steady-State Photocrystallography

The UV/vis spectrum, collected on a solid sample of [11], was used to help optimise the excitation wavelength for use in photocrystallographic experiments with the complex (Figure 1, Appendix 11). The spectrum indicates that wavelengths between 300 – 430 nm are most likely to induce high levels of nitro – nitrito conversion in [11], as these are found to be under the main, MLCT absorption band for the system.[71] Test experiments indicated that irradiation at λ = 400 nm induced the most promising photoresponse for [11], which is expected as this wavelength occurs in the tail of the dominant absorption band.[23, 130] As such a full, steady-state photocrystallographic experiment was conducted for [11] using 400 nm light.
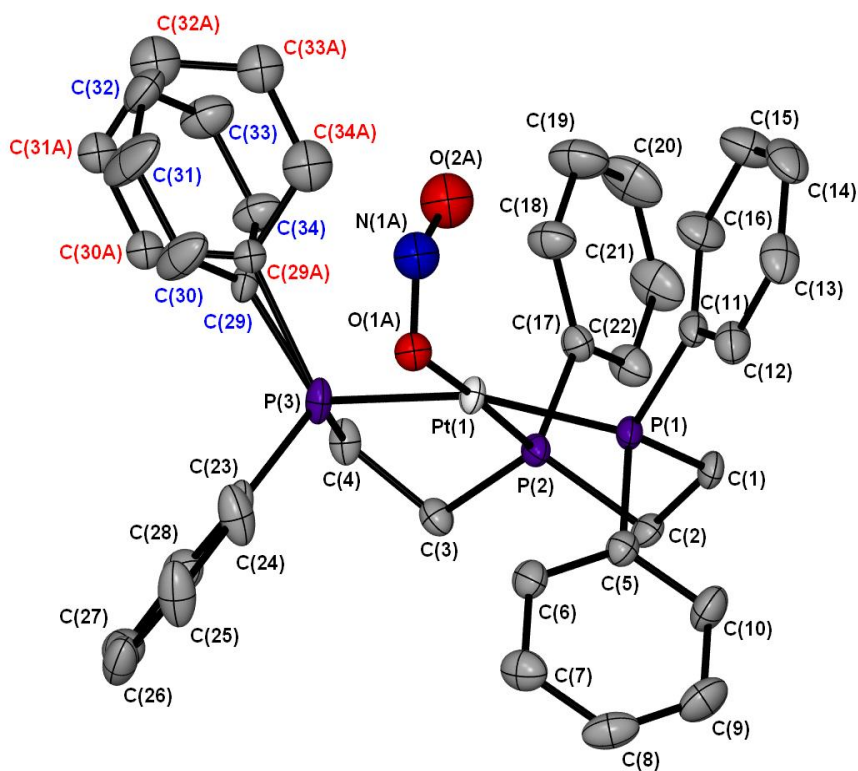
Figure 5.11: Single-crystal X-ray structure showing the atomic arrangement of the 90% *endo*-nitrito-(η^1-ONO) isomer in the MS of [11]. Ellipsoids at 50% probability and hydrogen atoms removed for clarity

The same crystal was held at 100 K and irradiated *in-situ* with 400 nm LED light for 1 h. A second X-ray dataset then confirmed that photoactivation had occurred, with 90% of the crystal now converted to *endo*-nitrito-(η^1-ONO). The atomic arrangement for this photoactivated state is shown in Figure 5.11. Further irradiation caused no appreciable increase in excitation, confirming this to be the photostationary state for [11] using 400 nm light. Additionally, no change in the nitro : nitrito ratio was observed when the crystal was held at 100 K in the dark, confirming the ES to be metastable under these conditions. Crystal data for the GS and MS are given in Table 5.10.

Table 5.10: Single-crystal X-ray data for the GS and MS structures of [11]

	Ground state	400 nm Metastable state
Photoconversion	0%	90%
Temperature	100(2) K	100(2) K
Radiation source	Mo K$_\alpha$	Mo K$_\alpha$
Wavelength	0.71073 Å	0.71073 Å
Empirical formula	C58 H53 B1 N1 O2 P3 Pt1	C58 H53 B1 N1 O2 P3 Pt1
Formula weight	1094.82 g mol^{-1}	1094.82 g mol^{-1}
Crystal size	0.28 x 0.23 x 0.02 mm^3	0.28 x 0.23 x 0.02 mm^3
Crystal system	Triclinic	Triclinic
Space group	*P*-1	*P*-1
Unit cell dimensions	a = 11.3546(3) Å α = 98.612(2)° b = 14.4891(3) Å β =104.491(2)° c = 17.1499(4) Å γ = 111.197(2)°	a = 11.3894(2) Å α = 96.919(2)° b = 14.5178(3) Å β = 105.215(2)° c = 17.1546(5) Å γ = 110.986(2)°
Volume	2455.1(1) Å^3	2482.1(1)
Z	2	2
Density (calculated)	1.481 M g m^{-3}	1.465 M g m^{-3}
Absorption coeff. μ	3.000 mm^{-1}	2.967 mm^{-1}
F(000)	1104	1104
R(int)	0.0332	0.0443
R1 (obs. data)	0.0338	0.0415
wR2 (all data)	0.0782	0.0954
Reflections (indep.)	14905	15058
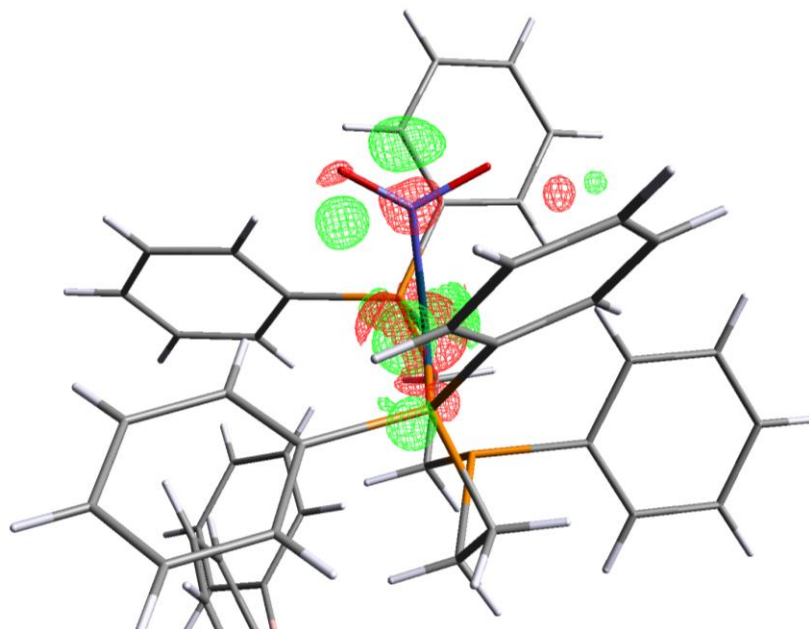
Figure 5.12: Photodifference map of the platinum cation in [11], showing the change in Fourier electron density distribution between the GS and MS; red = −3.8 eÅ^{-3}, green = +3.8 eÅ^{-3}

Figure 5.12 shows the photodifference map for complex [11]. Green regions show positive electron density at the positions of atoms O(1A) and N(1A), confirming the production of the photoactivated *endo*-nitrito isomer. Conversely, regions of negative electron density at atoms N(1) and O(1) of the nitro ligand confirm the disappearance of this isomer on irradiation.

A new crystal was irradiated for 1 h at 100 K, before variable temperature parametric studies were conducted to determine the MS range. The crystal was warmed and repeat datasets collected at intervals between 160 and 220 K. The photoinduced *endo*-nitrito isomer is retained as the major component at 100 – 180 K. On further warming to 200 K, the nitrito occupancy decreases and by 220 K the system returns to the 100% nitro-$(\eta^1$-$NO_2)$ GS. Nitro : nitrito ratios for all photocrystallographic experiments with [11] are given in Table 5.11.

Table 5.11: Crystallographically determined ratios of nitro-$(\eta^1$-$NO_2)$ and *endo*-nitrito-$(\eta^1$-ONO) isomers in [11] as a function of irradiation time and experiment temperature

| Irradiation time / h	Temperature / K	Refined Occupancy	
		Nitro-$(\eta^1$-$NO_2)$	Nitrito-$(\eta^1$-ONO)
0	100	1.00*	0.00*
1	100	0.10(1)	0.90(1)
2	160	0.12(1)	0.88(1)
2	180	0.12(1)	0.88(1)
2	200	0.61(1)	0.39(1)
2	220	1.00*	0.00*

* No esd is reported for full occupancy or zero occupancy as these ratios were not refined

Crystal Packing and Sterics

The crystal structure is largely unchanged on excitation, excepting nitro – nitrito conversion, and the MS packing diagram closely resembles that shown in Figure 5.4. A small volume increase of 1.10%, or +27.0(1) Å^3, is found on photoactivation that, although slightly larger than the changes observed for [9] and [10], is still comparable to the analogous systems. For [11], the volume change is significant, with $\Delta V / \sigma(\Delta V) = 270$ on application of the 3σ rule. Unlike complexes [9] and [10], the cell expansion occurs isotropically, with all three axes increasing on irradiation.

Additionally, Crystal Explorer fingerprint plots for the GS and MS also suggest little change [11], with the overall plots remaining largely similar after isomerisation (Table 5.12). N…H and O…H plots include interactions involving the nitrite groups, while C…H and H…H plots represent the rest of the structure. The number of N…H contacts dramatically increases between GS and MS, in line with changes expected on the rearrangement of N(1) to its new position as N(1A) in the nitrito-$(\eta^1$-ONO) isomer. The changes in O…H interactions are less striking between the GS and MS, but small differences are noticeable, confirming these contacts are rearranged on excitation. Conversely, the C…H and H…H plots are very similar for GS and MS structures, confirming the main rearrangements in close contacts occur only to those atoms of the isomerising nitrite groups.

Table 5.12: Crystal Explorer Fingerprint plots showing the changes in intermolecular interactions between the GS and 400 nm photoactivated state in [11]

	Ground state	400 nm Metastable state
All Contacts		
N...H contacts		
O…H contacts		
C…H contacts		
H…H contacts		
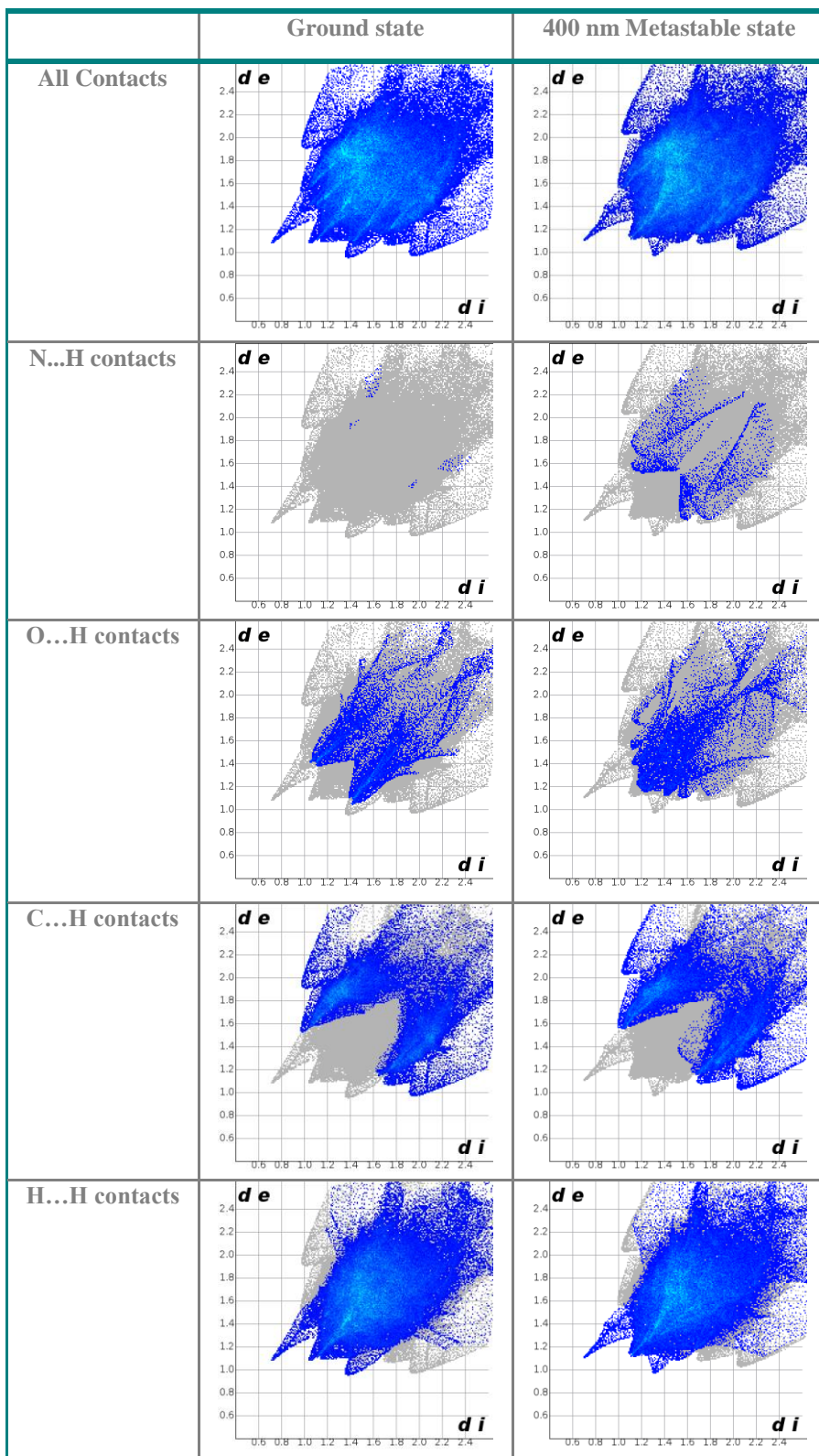
5.1.4. Comparisons: Complexes [9] to [11]

Direct comparison can be made between complexes [9], [10] and [11] given that they not only contain the same constituent components, excepting the change in metal, but are also entirely isostructural in their preferred crystal form. Despite their similarities, these compounds are shown to display some different and interesting linkage isomerism behaviour. A review of these contrasts in reference to potential influential factors, outlined in Chapter 2, can help suggest which processes are key in controlling the solid-state nitro – nitrito linkage isomerisation.

Nitro : Nitrito Ratios on Crystallisation

An interesting first point of comparison is the observation that all three triphos complexes crystallise with differing ratios of nitro : nitrito isomers under ambient conditions (Table 5.13). While the nickel and palladium species contain a mixture of nitro and *endo*-nitrito linkage isomers, platinum complex [11] crystallises solely as the nitro form.

Table 5.13: Summary of nitro : nitrito ratios for triphos complexes on crystallisation, determined by X-ray crystallography under ambient conditions

Complex	TM Centre	Occupancy (esd)	
		nitro-(η^1-NO$_2$)	nitrito-(η^1-ONO)
[9]	nickel	0.84(1)	0.16(1)
[10]	palladium	0.50(1)	0.50(1)
[11]	platinum	1.00*	0.00*

* No esd is reported for full occupancy or zero occupancy as these ratios were not refined

A possible explanation for the preference of platinum(II) for nitro-(η^1-NO$_2$) coordination is based on HASB theory, which would expect the $5d$ centre to be the "softest" metal atom and therefore show highest affinity for the "softer" nitrogen donor.[133] By this same reasoning nickel(II) should display strongest affinity for the "hard" oxygen donor and so the highest nitrito-(η^1-ONO) occupancy should be observed in [9]. However, this is not the case and instead the palladium species [10] crystallises with the highest 50% *endo*-nitrito occupancy, suggesting HASB theory alone is insufficient to explain the isomer trend on crystallisation.

Although, as discussed, no strong hydrogen bonds are present in [9] to [11], there exist a number of intermolecular C-H…O interactions to the nitrite groups. Despite some debate in the literature, C-H…O contacts are often thought of as weaker hydrogen bonding interactions.[132] As such, a comparison of C-H…O contacts to the isomerising ligands might help to rationalise the trend in

nitro : nitrito ratio for [9] and [10] on crystallisation. Figure 5.13 shows C-H…O interactions to each of the nitro-(η^1-NO$_2$) and nitrito-(η^1-ONO) ligand arrangements for complexes [9] and [10]. Rather than room temperature data, contacts in the flash cooled, 100 K structures are compared, where the ambient temperature arrangement is cryo-trapped. It should be noted that only those interactions whose length are less than the sum of the Van de Waals radii for the two atoms are highlighted in the figure. In [9], five C-H…O contacts are determined between the nitro-(η^1-NO$_2$) ligand and aromatic C-H groups from the surrounding lattice. This is compared to just two such interactions for the nitrito-(η^1-ONO) arrangement. The presence of more interactions to nitro-(η^1-NO$_2$) is in-keeping with the observation that this isomer is thermodynamically preferred, as the formation of C-H…O contacts should be energetically favourable and so act to stabilise this arrangement at ambient temperature. By similar reasoning, it would be expected that more C-H…O contacts with nitrito-(η^1-ONO) should exist for [10] than for [9], given that the palladium analogue crystallises with the greater proportion of this linkage isomer. Figure 5.13 shows this is not the case, however, with only two C-H…O contacts determined, within the limits, between Pd-ONO and the surrounding lattice. As such, it is difficult to draw any firm conclusion as to the influence of C-H…O contacts on the crystallisation behaviour of these two species.
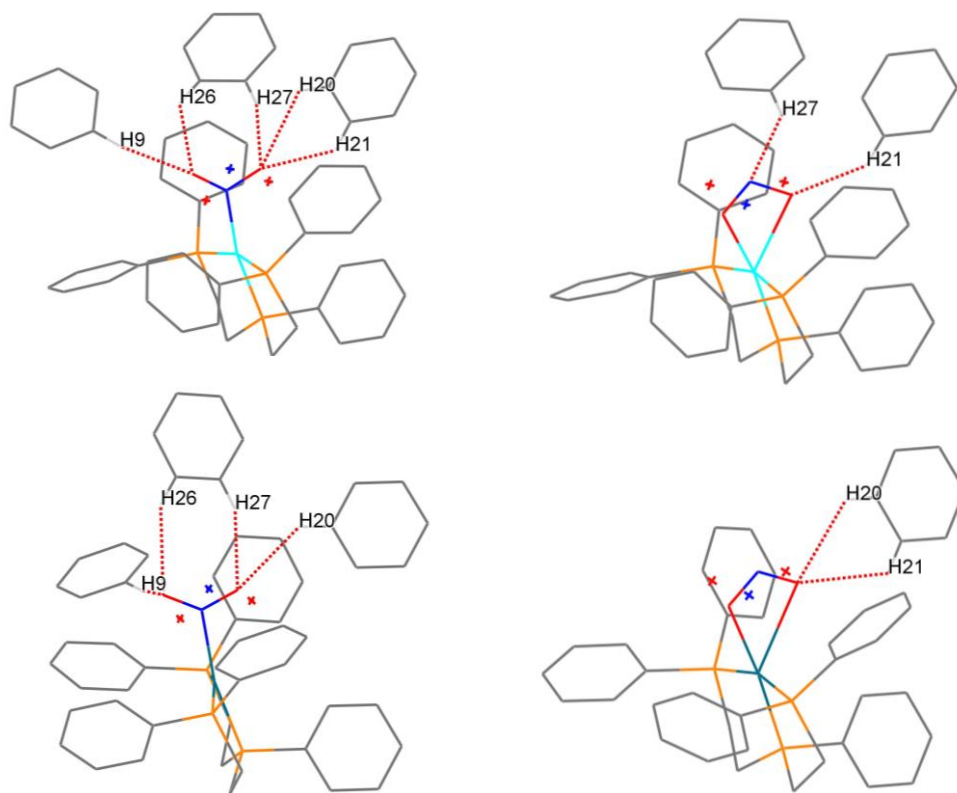
Figure 5.13: C-H…O interactions (< sum of Van de Waals radii) to the nitrite ligands in [9] and [10]:
top left = Ni–NO$_2$; **top right** = Ni–ONO; **bottom left** = Pd–NO$_2$, **bottom right** = Pd–ONO

It is also interesting that, while for nickel – nitrite systems [1], [7] and [9] linkage isomers appear exist in a thermodynamic equilibrium that is easily controlled with temperature, the palladium species [10] cannot be manipulated in a similar manner. When also considering that [9] and [10] are isostructural, it is possible that their different thermal isomerisation behaviour is again a result of changing the metal. The nickel system would be expected to undergo more effective nitrito – nitro conversion in the temperature range than the palladium analogue, confirming the greater expected lability of the nitrite when attached to a first-row TM centre.[133] Another possible explanation for the unexpected thermal behaviour in [10] again relates to the relative stabilities of the two nitrite isomers. While there is a marked preference for the nitro-(η^1-NO$_2$) arrangement on crystallisation of [9], with an 84 : 16 nitro : nitrito ratio, the same is not true of the palladium – nitrite system as it crystallises with equal amounts of each isomer. Additionally Figure 5.13 shows that, in contrast to the relative environments in [9], for complex [10] there are a similar number of close contacts formed to the two isomers, with four interactions to nitro-(η^1-NO$_2$) and five to the *endo*-nitrito arrangement. These factors indicate that the two nitrite arrangements are closer in energy in complex [10] and it is therefore possible that neither isomer is preferred thermodynamically, explaining why no appreciable thermal isomerisation can be induced on slow cooling.

Photoconversion Level

Although high excitation levels are achieved in complexes [9] to [11], the observation that photoisomerisation does not proceed to completion in all three systems is again of interest considering that they are isostructural. Their behaviour on photoactivation can again be compared to the identity of the TM centre, with the maximum photoconversion level following a trend of nickel > palladium ≈ platinum. The observation of similar properties for 4d and 5d complexes, while being distinct from the related first-row compound, is common amongst TM coordination complexes and is attributed to the effect of the Lanthanide Contraction.[133] The intervention of the 4f elements between 2nd and 3rd row TM series causes the atomic radii of 5d metals to be smaller than expected and comparable to their 4d counterparts, due to the poor shielding capabilities of the 4f orbitals. As such, it is common to observe similar properties in related palladium and platinum compounds, helping to rationalise their similar photoconversion. Additionally, as previously discussed it is expected that nickel species [9] should show the strongest photoresponse, given the increased expected lability of the nickel – nitrite bond and also considering that HASB theory predicts nickel to have the highest affinity for the "harder" nitrito-(η^1-ONO) isomer.[133]

Despite these observations, the > 90% photoconversion achieved in these three triphos complexes indicates their structure is conducive to nitro − nitrito rearrangement. Given the rationale of choosing sterically-demanding, photoinert ancillary species was that these should dominate the structure so that the photoreaction may proceed topotactically, lattice changes for [9] to [11] should also be compared in reference to the conversion trend. The unit cell volume increases on photoactivation in all three complexes, in general agreement with those observed for the amine species studied in Chapter 4. However, the trend for ΔV observed for the triphos systems does not correlate with photoconversion, with expansions of +0.72%, +0.07% and +1.10% observed for [9], [10] and [11], respectively. ΔV is comparatively small for all three complexes, suggesting that isomerisation proceeds topotactically.[1-3] However, thorough application of the Topochemical Postulate to these data would expect that the system achieving maximum photoconversion should simultaneously undergo least expansion. It is palladium complex [10] that is again anomalous, undergoing the smallest lattice change despite an incomplete photoreaction. It appears, therefore, that comparison of the overall cell change does not account for the observed photoactivation level.

Table 5.14: Reaction cavity data from steady-state photocrystallographic studies with triphos systems

Complex	Conversion / %	ΔV_c (% of unit cell volume / Z)
[9]	100	0.1
[10]	90	0.1
[11]	90	0.5

The Reaction Cavity principle considers steric influences in the photoactive region of the crystal alone,[99] and can additionally be used to rationalise the photoconversion trend observed for [9], [10] and [11]. As discussed in Chapter 4 (§ 4.1.4 and 4.2.6) the value of greatest relevance is the change in reaction cavity volume between the GS and MS structures ΔV_c, as this provides a measure of the distortion, and therefore strain imparted to the lattice, in order for the photoisomerisation to be achieved. Table 5.14 gives the results of reaction cavity analysis for the triphos species. Calculations were made on the flash cooled GS and MS structures at 100 K, to best account for the fact that a clean, 100% nitro GS could not be achieved for [10]. The results for [9] and [11] correlate well, with the lower converting platinum species displaying largest ΔV_c. Once again however the palladium system proves anomalous, with a ΔV_c value smaller than expected and the same as [9], despite a 10% difference in their photoconversion. The assessment of steric influences in the crystal lattice on the photoisomerisation is therefore somewhat inconclusive for the triphos species, and this again suggests that other factors must additionally influence the isomerisation reaction in these species. As remarked previously however, it should

168

be remembered that here only the static, time- and space-averaged structures are considered, as steady-state methods only provide information on photostationary states. No assessment of the dynamic lattice behaviour over shorter length- or time-scales can be made, which might be more relevant to an individual isomerisation event.[101]

Finally, as well as investigating steric influences on photoactivation levels, the likelihood of electronic influences on the isomerisation might also be considered. Given the indication, in Chapter 4, of some *trans*-influence between the metal – nitrite ligand and the site *trans* to this position, a similar effect can be investigated across the series of complexes in this Chapter. The analysis is, in fact, less ambiguous for the triphos species, given that all three complexes are isostructural and the photoisomerisation is very close to completion in each case. If some *trans*-influence is induced as a result of isomerisation, this should be reflected in bond length differences between GS and MS structures. Nitro – nitrito isomerisation is expected to induce a change in the ligand field strength at the metal, given that nitro-(η^1-NO_2) is expected to be a stronger-field ligand than nitrito-(η^1-ONO).[133] As such, the GS M^{2+} – N(1) should be stronger and shorter than the corresponding MS M^{2+} – O(1A) bond. These changes should also be accompanied by a shortening in the M^{2+} – P(2) distance between GS and MS, in-line with the expected strengthening of this bond as the *trans*-nitrite ligand is exchanged for a weaker-field, nitrito-(η^1-ONO) arrangement. Table 5.15 lists the M^{2+} – P(2) and M^{2+} – N(1) / O(1A) bond lengths for the GS and MS structures, respectively, for each of the triphos complexes. For [9], GS bond lengths were taken from the flash cooled structure at 100 K, to be comparable to the flash cooled GS for [10] and [11].

Table 5.15: Changes in metal – ligand bond lengths to *trans*-oriented ligands as a result of nitro – nitrito isomerisation complexes [9] to [11]

Complex	Conversion / %	GS M^{2+} – N(1) / Å	MS M^{2+} – O(1A) / Å	GS M^{2+} – P(2) / Å	MS M^{2+} – P(2) / Å
[9]	100	1.923(2)	1.966(3)	2.127(1)	2.117(1)
[10]	90	2.163(5)	2.135(3)	2.215(1)	2.206(1)
[11]	90	2.111(3)	2.129(3)	2.219(1)	2.201(1)

As expected, there is an increase in the metal – nitrite bond length as a result of the change in coordination on photoactivation in all three complexes. In addition, a decrease is observed for M^{2+} – P(2) bond lengths between GS and MS structure in all of the compounds, with a 0.010 Å change for [9] and [10] and an even larger decrease of 0.018 Å for complex [11]. On considering the reported esd of 0.001 on each M^{2+} – P(2) measurement, the changes are found to be statistically significant on application of the 3σ rule, suggesting some evidence of *trans*-influence in these

169

systems. However, to provide comprehensive evidence of some electronic influence over the progress of isomerisation, it would also be expected that the greatest value of $\Delta[M^{2+} - P(2)]$ should correlate with the highest photoconversion level. Table 5.15 shows this is not the case, suggesting these data do not determine conclusively that electronic effects from the ancillary ligands have an influence over the isomerisation reaction in these systems.

5.2.   Summary

Building on the results of Chapter 4, the investigation of triphosphine species in Chapter 5 further highlights which analyses are most effective in rationalising the observed linkage isomerism trends, and additionally which key influential factors appear to control the nitro – nitrito isomerisation process in the single-crystal. It is again evident that the choice of metal incorporated into the photoactive species strongly influences linkage isomerisation behaviour, and results indicate that the inclusion of a first-row TM centre leads to a more reliable photoisomerisable species. In both Chapters 4 and 5, 100% photoconversion has only been observed in nickel(II) species and, additionally, the thermal isomerisation in nickel complexes [1], [7] and [9] is better explained and more controllable than for palladium complex [10].

It is additionally apparent, however, that other factors must also be considered when designing systems to undergo photoconversion to a maximum and reliable level. Steric analyses conducted in Chapter 5 have further confirmed that the presence of intermolecular interactions to the nitrite ligand strongly influence the preference for a particular nitrite isomer under certain conditions. The combination of these observations and hydrogen bonding analysis in Chapter 4 strongly suggests that the introduction of potential interactions to the nitrite ligand should be carefully considered when choosing ancillary fragments. Additionally, although reaction cavity analysis for complexes [9], [10] and [11] is not entirely conclusive, the results are still indicative that minimising ΔV_c, *i.e.* the amount of movement required in the photoactive region of the crystal, is also key to promoting high photoconversion levels. As such, potential complexes should include groups that best protect this photoactive area, and again Chapter 5 has indicated that the inclusion of bulky, photoinert ancillary ligands and counterions is one effective way to achieve these ends.

Despite some success, the results of Chapter 5 are not entirely conclusive and again suggest that other influences, such as kinetic factors and light absorption properties, should also be investigated to obtain a more complete understanding of the linkage isomerisation reaction in the solid-state.

Chapter 6.

Photocrystallographic Kinetics Studies

Chapter 6. Photocrystallographic Kinetics Studies

Chapters 4 and 5 have shown that steady-state photocrystallographic studies are highly valuable in understanding the changes induced on photoactivation. The data from high quality, single-crystal experiments allow relevant parameters to be measured precisely, facilitating effective comparison between photostationary GS and MS arrangements. However, a disadvantage of the steady-state method is that photostationary states can only elucidate the environment before and after isomerisation and no information is available on the transient changes occurring as the reaction progresses. In reality, photoinduced linkage isomerism is a dynamic process and so it is desirable to investigate any changes as they occur. The kinetics of nitro – nitrito isomerisation are particularly of interest and Chapter 6 is concerned with developing photocrystallographic methods allowing the photoreaction to be followed with time. Analysing the profiles in reference to solid-state kinetic models can also provide mechanistic information for the isomerisation process.

While a number of spectroscopic studies into the kinetics of solid-state linkage isomerisations exist in the literature,[142-144] comparatively few examples are found where single-crystal X-ray methods are applied. The majority of single-crystal kinetic studies have focussed on irreversible photodimerisation processes and as early as 1998 Feeder *et al.* were able to follow [2+2] cycloaddition in crystals of 2-benzyl-5-benzylidenecyclopentanone (BCCP).[145, 146] While these earlier studies rely on traditional, first order kinetics to model the photodimerisation, more recent studies have employed Johnson, Mehl, Avrami and Kolmogorov (JMAK) theory.[141, 147-149] JMAK analysis originates from Avrami's early studies of solid-state phase transformations[150-152] and is based on a nucleation and growth mechanism. The kinetic profile obtained for photodimerisation is best described by a sigmoidal function,[141, 147-149] similar to the general equation of JMAK theory

$$\alpha(t) = 1 - \exp(-kt^n) \qquad\qquad \text{Equation 6.1}$$

$\alpha(t)$ is the "conversion fraction", or level of ES present at a time t. For incomplete reactions a modified equation is proposed, allowing the initial and final conversions to be parameterised[149]

$$\alpha(t) = \alpha_f - (\alpha_f - \alpha_0)\exp(-kt^n) \qquad\qquad \text{Equation 6.2}$$

where k = rate constant, n = order of reaction (or "Avrami constant"), α_0 = initial conversion and α_f = final conversion. The value of n describes the dimensionality (D) of ES growth.

$$D = n - 1 \qquad\qquad \text{Equation 6.3}$$

Therefore, $n = 2$ indicates 1-D growth, $n = 3$ 2-D growth *etc*. $n = 1$ suggests a homogeneous transformation where there is equal probability of an event occurring throughout the sample.[147]

6.1. Following Photoactivated Nitro – Nitrito Conversion with Time

For the photodimerisation reactions reported in the literature, the use of full, single-crystal X-ray experiments for kinetic studies is straightforward as the photoreaction is irreversible. The situation is more complicated for kinetic experiments in the current project, as solid-state linkage isomerism is a reversible process. However, as a MS is generated at low temperature, the use of time-averaged techniques is still feasible providing the experimental conditions are carefully controlled and the data are collected efficiently. Despite this, it would still be highly beneficial to follow the isomerisation *in-situ*, and therefore § 6.1 contains reports of both photocrystallographic kinetic studies of nitro – nitrito isomerism with steady-state methods and the development of preliminary "single-spot" techniques allowing the photoreaction to be followed in real time.

6.1.1. Complex [1]: Kinetics of the Photoisomerisation at λ = 500 nm

As discussed previously in § 4.1.1, 100% nitro – nitrito photoconversion can be achieved in nickel – nitrite complex [1] on irradiation with 500 nm LED light, with the photoreaction complete within a 2 h period. The fact that the photoreaction in [1] proceeds to completeness, is highly reproducible and additionally the observation that no appreciable crystal decay occurs on repeated exposure to light, X-ray and temperature variation, makes this compound an ideal first candidate for steady-state photocrystallographic kinetic studies.

A crystal of [1] was mounted at room temperature and slow cooled to 100 K in the absence of light, before a single-crystal X-ray dataset was collected to confirm that a 100% nitro-(η^1-NO$_2$) isomer had been produced, as per § 4.1.1. The crystal was then held at 100 K and irradiated with 500 nm LED light for 2 min, at which point the LEDs were switched off and a second dataset collected to determine the nitro : nitrito ratio after illumination. The crystal was then irradiated for a further 2 min, giving a total exposure time of 4 min, before another full single-crystal dataset was obtained. This procedure was repeated for total irradiation periods of 8, 16, 32, 64 and 128 min, by which time the photoreaction was expected to have reached completeness. The structures were solved to determine the nitro : nitrito ratio at each time point and these results are shown in Figure 6.1. A table of nitro : nitrito ratios is also given in Table 1, Appendix 12. The data were then analysed using JMAK theory. As [1] undergoes complete conversion, $\alpha_f = 1$ and $\alpha_0 = 0$ and Equation 6.2 simplifies to the general Equation 6.1, which is applied to the data.
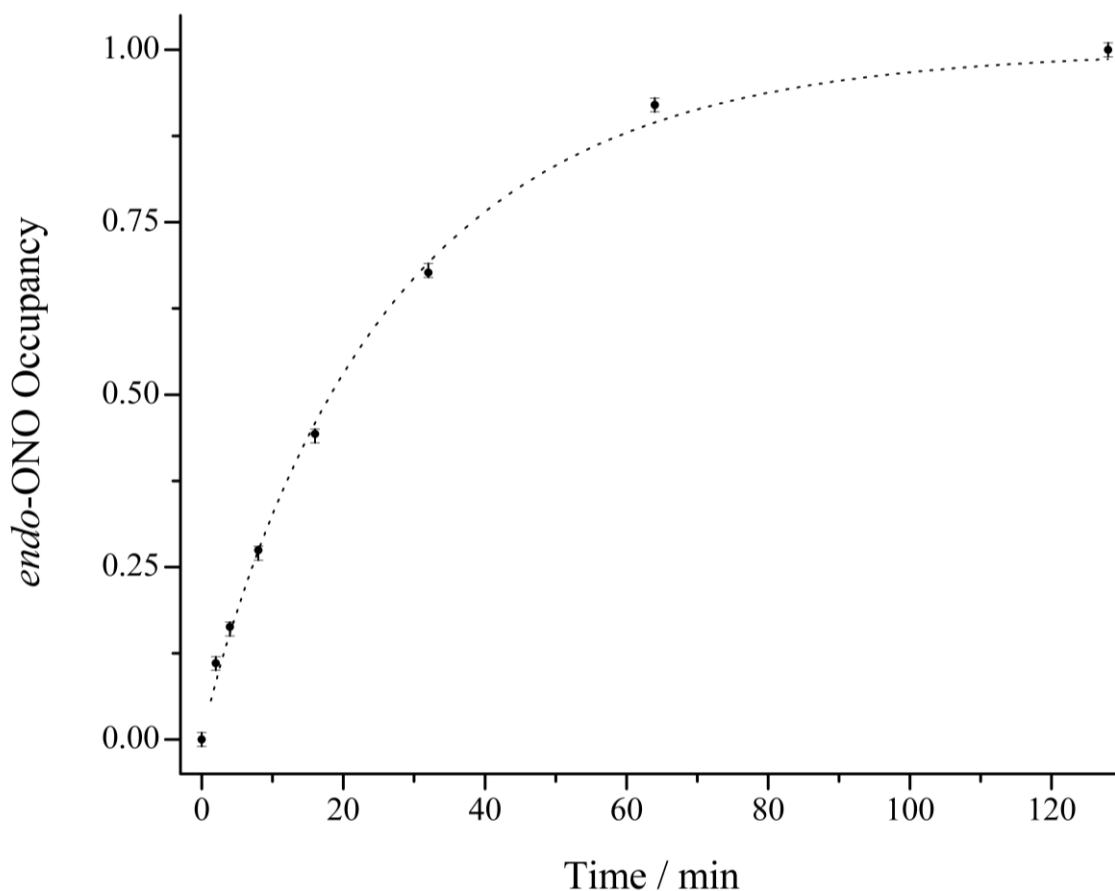
Figure 6.1: Photokinetic plot of ES *endo*-nitrito occupancy vs. total irradiation time with 500 nm LED light. Least squares fitting of $y = 1 - \exp(-kt^n)$: $k = 0.037$ ($\pm\ 0.001$) min^{-1}, $n = 0.94$ ($\pm\ 0.04$), $R^2 = 0.997$

The sigmoidal shaped curve indicates that isomerisation initially occurs quickly, with the rate of reaction decreasing as irradiation progresses. This is expected, considering that the photoreaction is self-limiting: while at the start all molecules are in the GS and have the potential to be converted, as isomerisation proceeds there is an increasingly smaller likelihood that an incoming photon will meet with a GS molecule as there are now fewer left in the sample, leading to a progressively slower rate of reaction with time. The current analysis assumes a first order process, where one incident photon interacts with one complex molecule, which is a reasonable expectation when using low flux LED light for photoactivation. The data show good agreement with Equation 6.1, with a value of $R^2 = 0.997$ indicating JMAK theory provides a good model for photoactivation in the crystal. The analysis returns a value for $n = 0.94$ ($\pm\ 0.4$), which is close to unity and therefore indicates a homogeneous process where there is equal likelihood of an isomerisation event occurring throughout the crystal. The value of $n \approx 1$ also suggests that 500 nm light penetrates well through the crystal and there is little absorption in the outer, photoactivated layers that could inhibit the progress of light through to the centre of the sample.

6.1.2. Complex [1]: Kinetics of the Photoisomerisation at λ = 400 nm

It has been shown that isomerisation can also be induced in crystals of [1] with 400 nm light, although photoactivation remains incomplete at this wavelength (§ 4.1.1). The kinetics of the isomerisation reaction at λ = 400 nm is also of interest, as the profile of the photoreaction with time may help to suggest why conversion cannot proceed to 100% under these conditions.

A crystal was again mounted at room temperature and slow cooled to 100 K, where a single-crystal X-ray dataset confirmed that the 100% nitro-(η^1-NO$_2$) isomer had been isolated. This crystal was then held at 100 K and subject to steady-state photocrystallographic kinetic studies, as outlined in § 6.1.1 above, at λ = 400 nm allowing the nitro : nitrito ratio to be determined at intervals during excitation. Full details of the nitro : nitrito isomer ratios obtained in all kinetic experiments with 400 nm light are given in Table 2, Appendix 12.
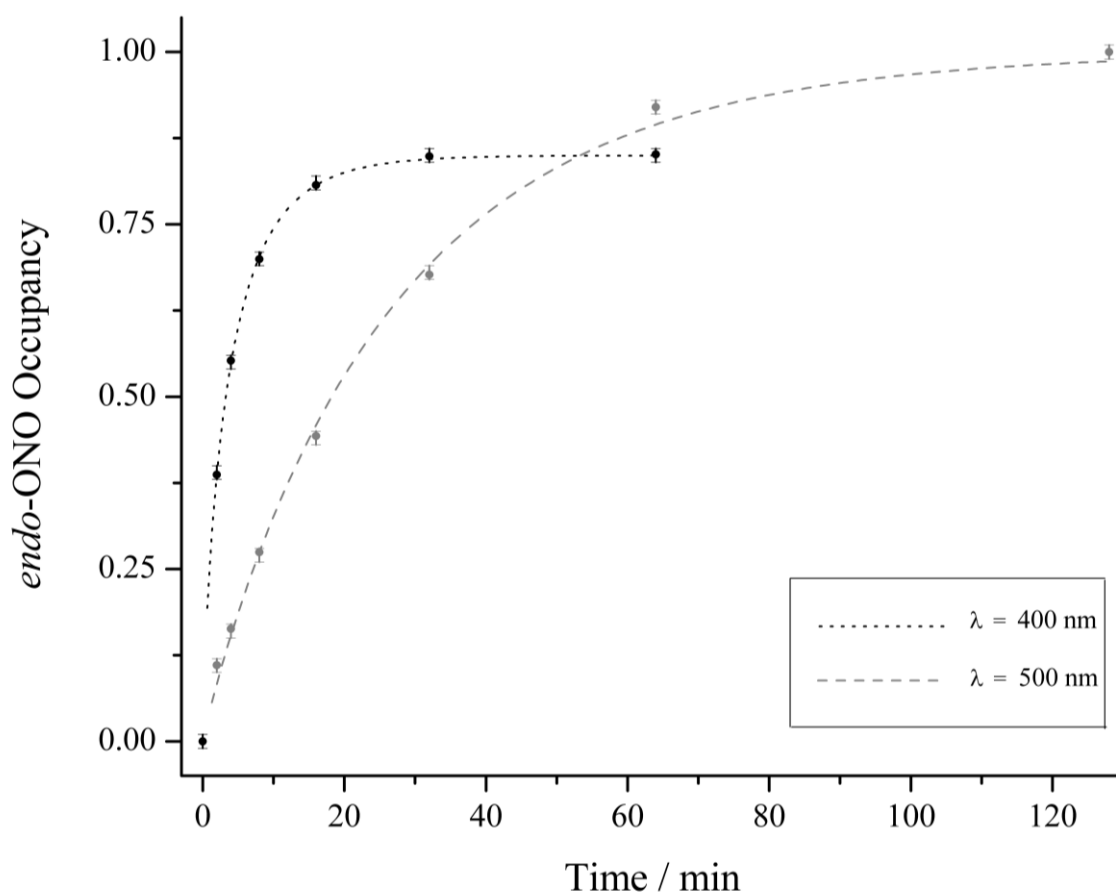
Figure 6.2: Kinetic plots of *endo*-nitrito occupancy vs. irradiation time, comparing λ = 400 nm **(black, dotted)** and 500 nm **(grey, dashed)**. Least squares fitting of y = 1 − exp(−kt^n): **400 nm**, k = 0.262 (± 0.003) min^{-1}, n = 0.76 (± 0.01), R^2 = 0.999; **500 nm**, k = 0.037 (± 0.001) min^{-1}, n = 0.94 (± 0.04), R^2 = 0.997

Figure 6.2 compares the kinetic profiles obtained for complex [1] on irradiation with both 400 nm and 500 nm LED light. The data for $\lambda = 400$ nm are again fitted to Equation 6.1 and a value of R^2 = 0.999 reflects strong correlation with the JMAK expression. On comparing the two plots it is apparent that excitation occurs more rapidly with 400 nm light, producing a much steeper excitation curve at short irradiation times and a value of $k = 0.262$ (± 0.003) min^{-1} in comparison to the smaller value of $k = 0.037$ (± 0.001) min^{-1} at $\lambda = 500$ nm. However, the curve for 400 nm excitation also levels out more abruptly and a maximum conversion of 85% to the *endo*-nitrito isomer is achieved after 32 min total irradiation time, remaining constant on further irradiation. This plot shape is indicative that a faster reaction is occurring near the surface of the crystal with this higher energy radiation, but at the same time this wavelength of light has only a finite penetration depth through the bulk crystal, leading to an incomplete photoreaction. This observation is supported by the UV/vis absorption spectrum for [1] (Figure 1, Appendix 1), showing that 400 nm light is strongly absorbed by the complex and so is unlikely to penetrate fully throughout the crystal (§ 4.1.1). Regression analysis returns a value of $n = 0.76$ (± 0.01), indicating negative dimensionality for the growth of the ES, *i.e.* $D = -0.24$. This value of D is unphysical and as such suggests that simple JMAK theory cannot effectively explain the progress of excitation at $\lambda = 400$ nm. The most likely explanation for this discrepancy is the absorption issue with 400 nm light. This necessarily means that there is a higher likelihood of an excitation event occurring closer to the surface than in the centre of the crystal. As such, excitation can no longer be homogeneous throughout the sample and is actually disfavoured in some regions, leading to a reduced value for the Avrami constant of $n < 1$. Previous studies in the literature have also hypothesised that non-integer values of n are the result of hybrid mechanisms[141, 148] or additional processes occurring in the system that retard the progress of the photoreaction,[149] further supporting the proposed explanation.

The results of kinetic studies at both excitation wavelengths further support observations made in previous sections, agreeing that incomplete photoconversion in the single-crystal can be explained by absorption problems using a particular excitation source. These results highlight the importance of choosing the correct wavelength for photocrystallographic studies and confirm that spectroscopic techniques are invaluable to complement crystallographic methods for a successful outcome in these types of experiments.

6.1.3. Following the Photoreaction in Real Time: Development of Single-Spot Techniques

For the experiments described so far in Chapter 6, the steady-state photocrystallographic method is easily adapted to obtain kinetic information on complex [1], as the ES is metastable at the low temperatures used. However, these methods are not transferrable to all reversible single-crystal-to-single-crystal reactions and for those systems where the ES cannot be made to exist indefinitely there is a requirement to develop kinetic methods allowing the photoreaction to be followed directly. As such, § 6.1.3 describes the development of preliminary "single-spot techniques" to study the isomerisation in real time. These methods exploit the fact that the intensity of certain reflections is observed to change markedly as a result of excitation. Kinetic information can then be obtained by following the change in a single diffraction spot with irradiation, which is achieved by repeated collection of the same, single frame and allows the photoreaction to be followed *in-situ* as it occurs. The kinetic experiment is conducted on a crystal of [1] at $\lambda = 500$ nm, to enable comparison with steady-state studies in § 6.1.1.

There are three key areas that must be optimised to achieve the most reliable results from this technique: (i) a systematic method is required to identify reflections undergoing the largest change as a direct result of isomerisation; (ii) a data collection procedure must be devised both to identify the best frame containing the target reflection and to collect this frame repeatedly whilst the crystal is continuously irradiated; and (iii) the data from these non-standard X-ray experiments must be efficiently processed so that kinetic information can be interpreted.

(i) Identifying suitable reflections

A list of selection criteria has been outlined previously.[140] A suitable reflection must:

1. undergo a large intensity change between the GS and MS *(either increase or decrease)*
2. always be present to some degree in both the GS and MS data *(to enable fair comparison)*
3. be moderately strong *(intensity changes will be hard to determine if the reflection is weak to begin with, but intense spots close to saturating the detector are equally unsuitable)*
4. be found at a suitable resolution *(reflections at very high angle are most susceptible to changes resulting from crystal deterioration, but those at very low angle could be subject to strong corrections (high Lorentz factors, masked regions etc.) and so should also be avoided)*
5. correspond to an *hkl* plane that intersects the isomerising ligand *(providing extra assurance that the intensity change is a direct result of the isomerisation).*

To satisfy criteria 1. to 3. a list of calculated intensities are compiled as .fcf files from the GS and MS structures of [1]. These are compared using the program LOGLOG,[153] which creates scatterplots to allow quantitative comparison of two input reflection files. Calculated reflections are compared as the only difference between GS and MS structure models is the change of nitrite coordination, therefore any differences observed should be a direct result of the isomerisation.
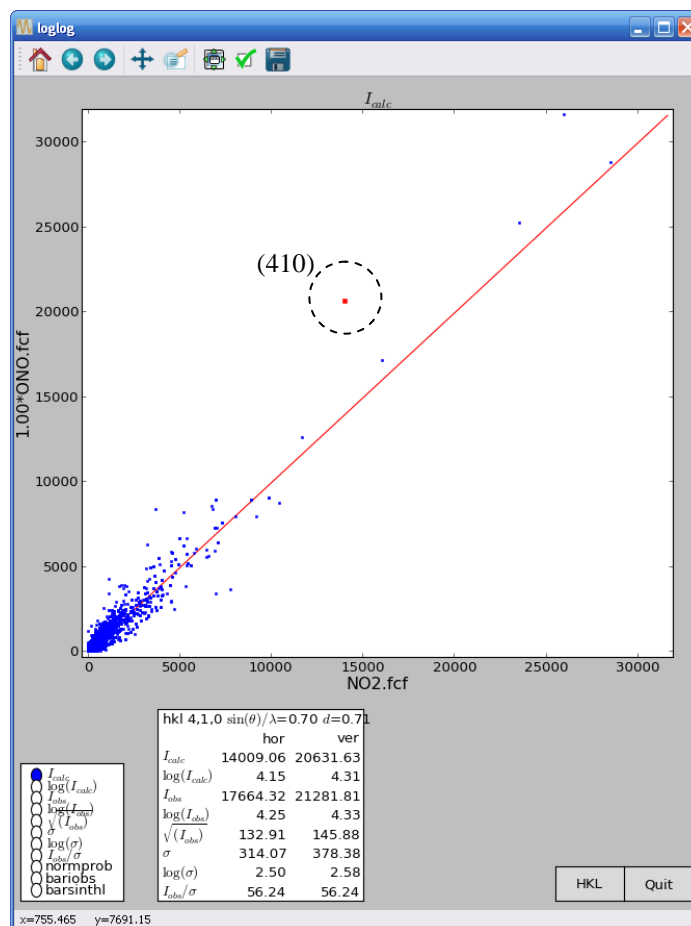
Figure 6.3: Histogram output from LOGLOG comparing calculated reflection files for GS nitro (NO2.fcf) and *endo*-nitrito (ONO.fcf) with a 1 : 1 scale factor, showing the choice of the (410) reflection

Figure 6.3 shows the histogram output from LOGLOG for [1]. It is those reflections lying away from the diagonal (red) that satisfy criterion 1., with those found above increasing in intensity on irradiation, whilst those below are observed to decrease. Reflections on or close to the diagonal are not greatly affected by the isomerisation. Criterion 2. is directly satisfied by using the histogram, as only reflections appearing in both GS and MS .fcf files are included. The most likely reflections to satisfy criterion 3. are those occurring in the mid-range of the plot. Considering the criteria collectively, the (410) reflection is selected, as highlighted in Figure 6.3.

178
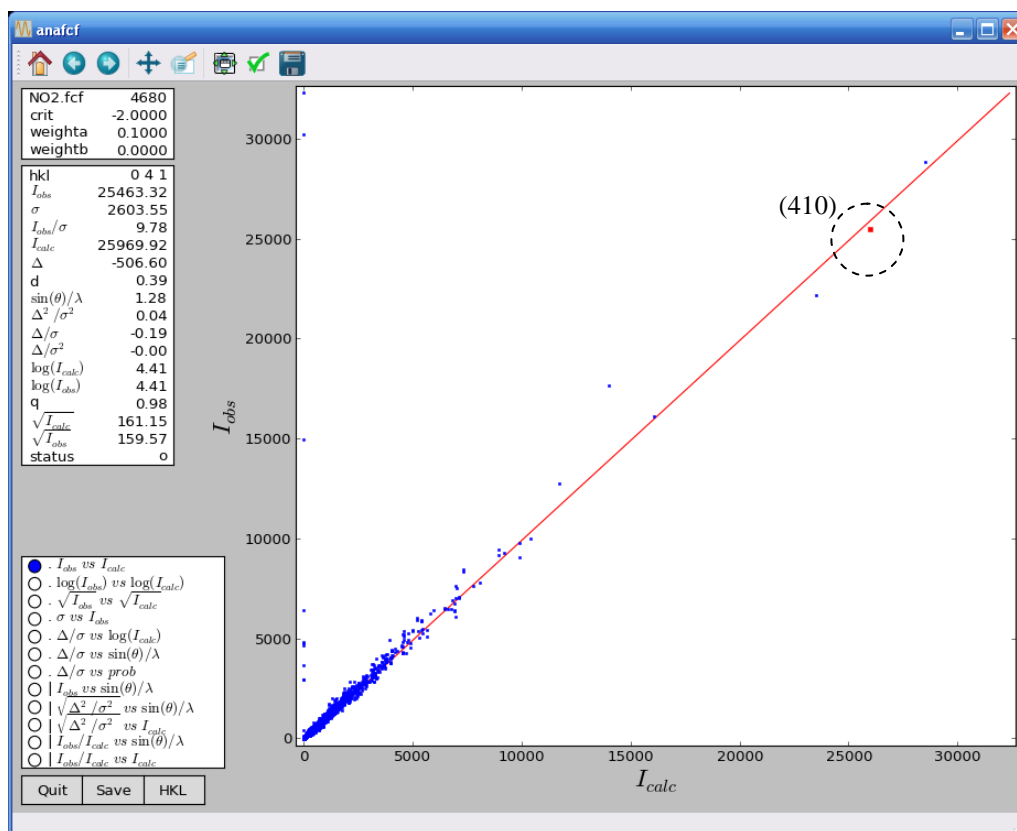
Figure 6.4: Histogram output from ANAFCF comparing calculated and observed intensities for the GS structure of complex [1]

ANAFCF[154] is also used to further confirm the suitability of the (410) reflection. The program plots a histogram comparing calculated and observed intensities for an input structure, which is used to identify reflections that do not fit the model. For the purposes of the current analysis (410) should lie close to the diagonal, as observed in Figure 6.4, confirming it is not anomalous.
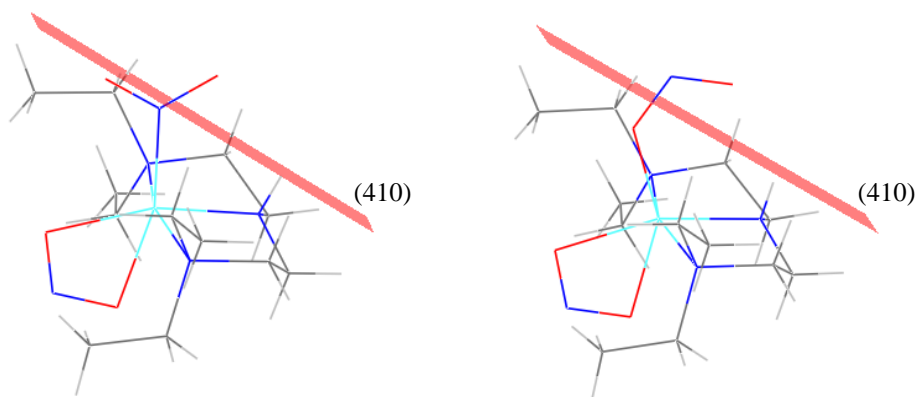
Figure 6.5: Intersection of the (410) plane with nitrite in GS **(left)** and MS **(right)** structures of [1]

Criteria 4. and 5. must also be considered. As [1] is orthorhombic, (410) has 8 equivalents that could all be suitable for the kinetic experiment. While equivalent reflections are expected to occur at the same resolution, some may be better situated in a data collection frame than others (avoiding masked regions *etc.*). Criterion 5. is satisfied by analysing the structures of [1] using Mercury[127] to confirm the (410) plane intersects with the nitrite ligand (Figure 6.5).

(ii) Data collection procedure

A crystal was mounted at room temperature and slow cooled to 100 K, before a single-crystal X-ray dataset was collected to confirm the presence of a 100% nitro-(η^1-NO$_2$) isomer. This data was collected with the LED ring in place to ensure no frames are masked by the experimental set-up. The GS dataset was then searched for frames containing the (410) and equivalent reflections, using the "Find HKL" tool in CrysAlis Pro. Once the most suitable frame was identified, its position (ω, θ, κ, and φ) was recorded and used to design the kinetic experiment. The data collection strategy is constructed manually, with the θ, κ, and φ positions kept at those recorded from the chosen GS frame. A wide-sliced ω-scan is set to collect data over 2° either side of the selected ω position, making a total scan width of 4°. The scan width is optimised to ensure that the whole reflection is included in the frame and to compensate for any unit cell changes, and hence peak position, on photoactivation. The X-ray exposure time is chosen as a compromise between achieving enough diffraction that an intensity change is easily identified whilst also obtaining data quickly so that several data points can be recorded before the reaction is complete. Once all of these parameters are optimised, the single frame is collected repeatedly as the crystal is irradiated. 10 frames are first collected in the dark to be averaged as an estimate of the error.

(iii) Data processing

Before the kinetic data can be processed the orientation matrix must first be set. This is required as only one unique image has been collected and so the software has insufficient information to calculate the crystal position relative to the diffractometer axes. The orientation matrix from the GS data can be used, as the crystal is not moved between data collections. Once the orientation matrix is set the kinetic data can be indexed to obtain the correct unit cell and the reflection of interest can then be highlighted in every frame using the "Find HKL" tool in CrysAlis Pro. Once identified, the reflection can be integrated to obtain the individual intensity and the process is then repeated for every frame. When all the data have been processed a plot of intensity *vs.* irradiation time gives the kinetic profile for the photoisomerisation reaction. Finally, the crystal is held at 100 K and a final, full X-ray data collection is used to determine the final *endo*-nitrito occupancy.

The frame at ω = –24º, θ = –25º, κ = 10º, φ = –120º was selected for the kinetic experiment, as it contained the most suitable equivalent (410) reflection (Figure 6.6). A data collection strategy was constructed using these fixed values of θ, κ and φ, with the wide-sliced ω-scan running from ω = –26 to –22º and an X-ray exposure time of 50 s per image. 80 of these 4º frames were collected in sequence, with the first 10 frames collected in the dark to be averaged as initial intensity, I_0. The 500 nm LEDs were switched on at the start of frame 11, and irradiation was continued until the end of frame 70. Frames 71 to 80 were then also collected in the dark and averaged to provide the final intensity, I_f. Finally, another full X-ray dataset was then collected at the end of the experiment, confirming that 100% conversion to the *endo*-nitrito MS had occurred.
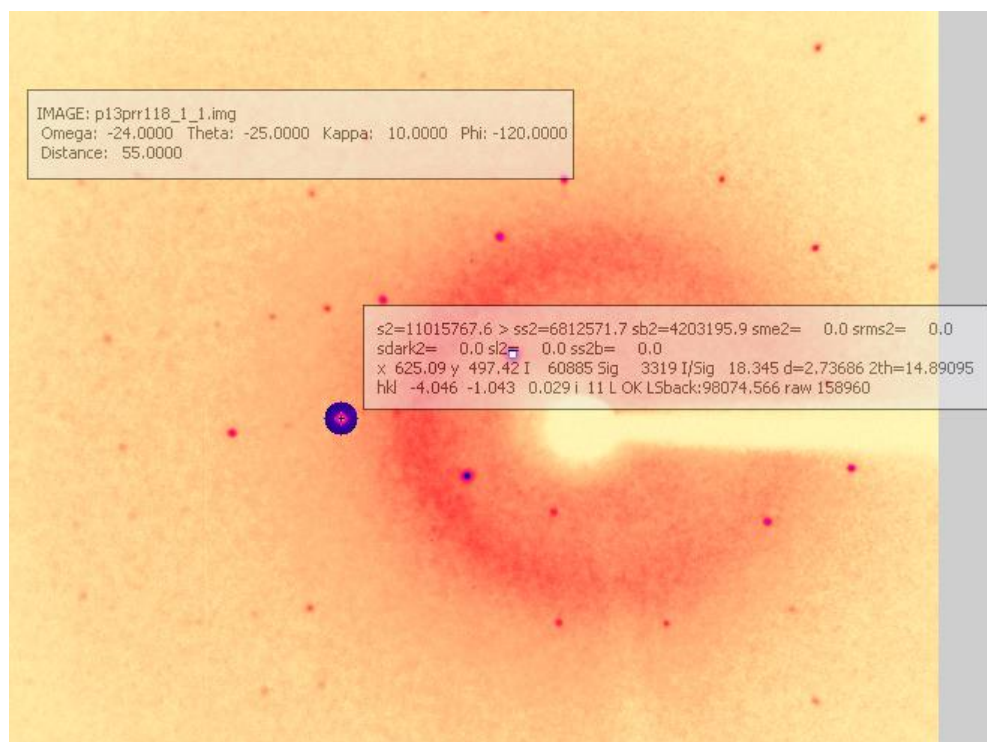
Figure 6.6: Data collection image from kinetic experiments following the change in the (410) reflection as a function of irradiation time

The data were processed as described and the kinetic profile obtained is shown in Figure 6.7. As expected by its position above the diagonal on the LOGLOG histogram in Figure 6.3, the reflection is observed to increase as photoactivation progresses. Although there is considerable noise observed in the data, the general trend again follows a sigmoidal profile, and can be analysed using JMAK theory. Equation 6.2 may be used directly for the data obtained by single-spot techniques, but now α_0 becomes I_0, or 57787 counts, and α_f becomes I_f, or 76307 counts.

$$y = 76307 - (76307 - 57787)\exp(kt^n)$$

Equation 6.4
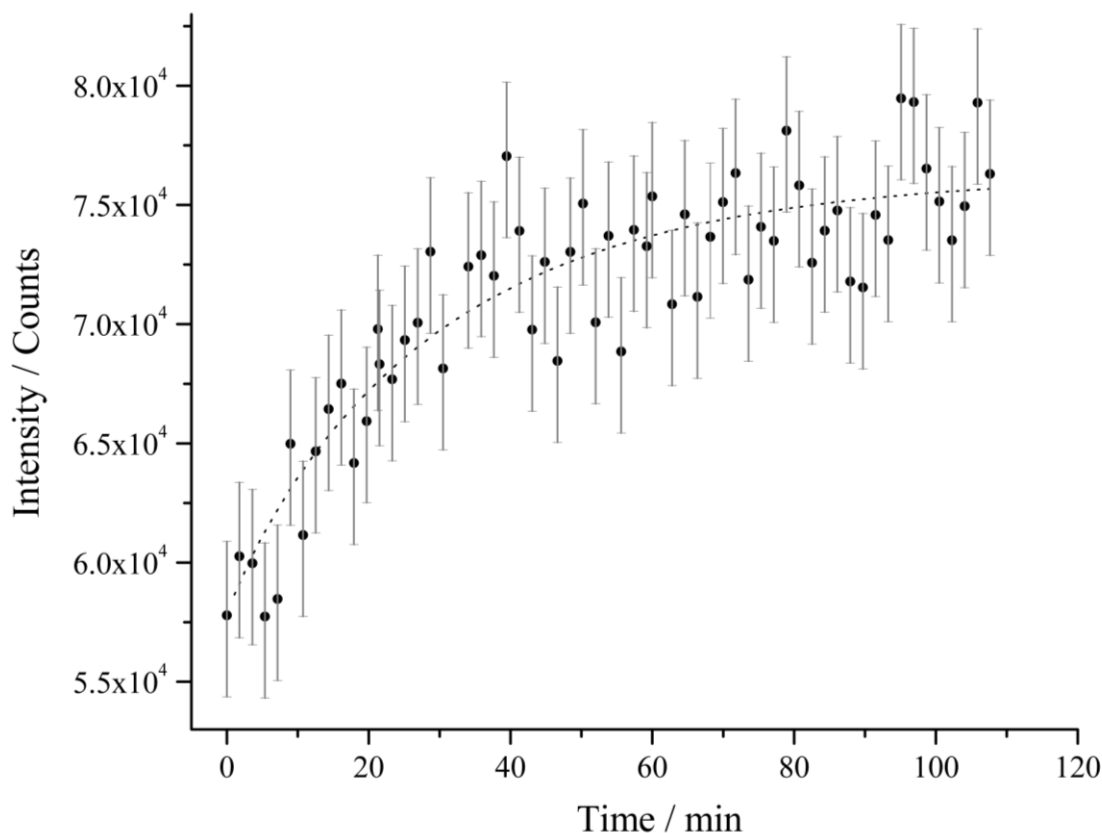
Figure 6.7: Kinetic plot following the (410) reflection with irradiation time in complex [1]. Least squares fitting of $y = 76307 - (76307 - 57787)\exp(kt^n)$: $k = 0.035$ ($\pm$ 0.002) min^{-1}, $n = 0.93$ ($\pm$ 0.09), $R^2 = 0.793$

The data show a poorer fit to the JMAK equation than profiles obtained using steady-state methods, reflecting considerable noise in the data. However, $R^2 = 0.793$ is still reasonable and esd values on both k and n are comparable to earlier results. The rate constant k determined by single-spot methods compares well to that of Figure 6.1, with respective values of $k = 0.035$ ($\pm$ 0.002) min^{-1} and $k = 0.037$ ($\pm$ 0.001) min^{-1} similar within error. Avrami constants n obtained by the two methods are also similar within error and both are close to unity, again suggesting that excitation occurs homogeneously throughout the crystal on irradiation with 500 nm LED light.

An estimation of the error in these measurements is made by considering the first 10 frames of the experiment. As well as providing an average value for I_0, the range of these measurements was used to construct error bars in Figure 6.7. This range should be more reliable than the 10 frames used to calculate I_f, as the crystal had not yet been irradiated. The size of the error bars suggests the spread of intensities observed is mostly attributed to inconsistency in the detector reading between frames, which is perhaps unsurprising as area detectors are not optimised to accurately record the intensity of a single reflection. This and other problems with the single-spot method are discussed further in § 6.3.

6.2.   Following Thermal Nitrito – Nitro Decay with Time

Variable temperature parametric studies conducted on photoactivated systems in Chapters 4 and 5 have shown that excitation is reversed on warming the crystal and nitrito – nitro decay occurs at temperatures above the MS limit. Investigation of this reverse processes is also required to better understand the full nitro – nitrito isomerism process and as such kinetic experiments to study the thermal nitrito – nitro decay process are conducted with a small selection of complexes.

6.2.1.   Complex [1]: Nitrito – Nitro Decay and the Effect of Temperature

Variable temperature parametric studies indicate that the MS limit for complex [1] exists at approximately 160 K (§ 4.1.1). It is interesting to note, however, that there is in fact a small temperature range over which the system reverts back to the GS arrangement, with the onset of *endo*-nitrito-(η^1-ONO) decay occurring at 150 K (Table 4.8). As steady-state methods were used for these studies, the ratios are refined from full, time-averaged X-ray datasets and so it is not possible to determine whether the *endo*-nitrito occupancies at 150 and 160 K represent a static ES population at that temperature. It is equally possible that the system is no longer truly metastable by 150 K and that instead the *endo*-nitrito isomer is decaying throughout the X-ray experiment. In this latter scenario the *endo*-nitrito occupancies at 150 and 160 K are actually an average of the decaying ES population over the full experiment.

To study the thermal nitrito – nitro process in [1] more carefully, decay experiments were conducted at temperatures between 150 and 160 K, using the same crystal. In each experiment, the crystal was first slow cooled to 100 K and then irradiated at λ = 500 nm for 2 h, before a data collection was conducted to confirm excitation to the 100% *endo*-nitrito-(η^1-ONO) MS. The crystal was then warmed and a new data collection started as soon as the required temperature was reached. A separate kinetic experiment was conducted at each of five temperatures; 150 K, 152.5 K, 155 K, 157.5 K and 160 K. Each experiment required *ca.* 20 h and within this time the data for four complete quadrants were obtained sequentially. As complex [1] is solved in the orthorhombic space group $P2_12_12_1$, this allowed a full single-crystal refinement to be conducted at four time intervals during the decay experiment so that the nitro : nitrito ratio was determined at each of these time points. For each of the five temperatures a decay curve was then constructed, which is a plot of *endo*-nitrito-(η^1-ONO) occupancy *vs*. time (Figure 6.8).
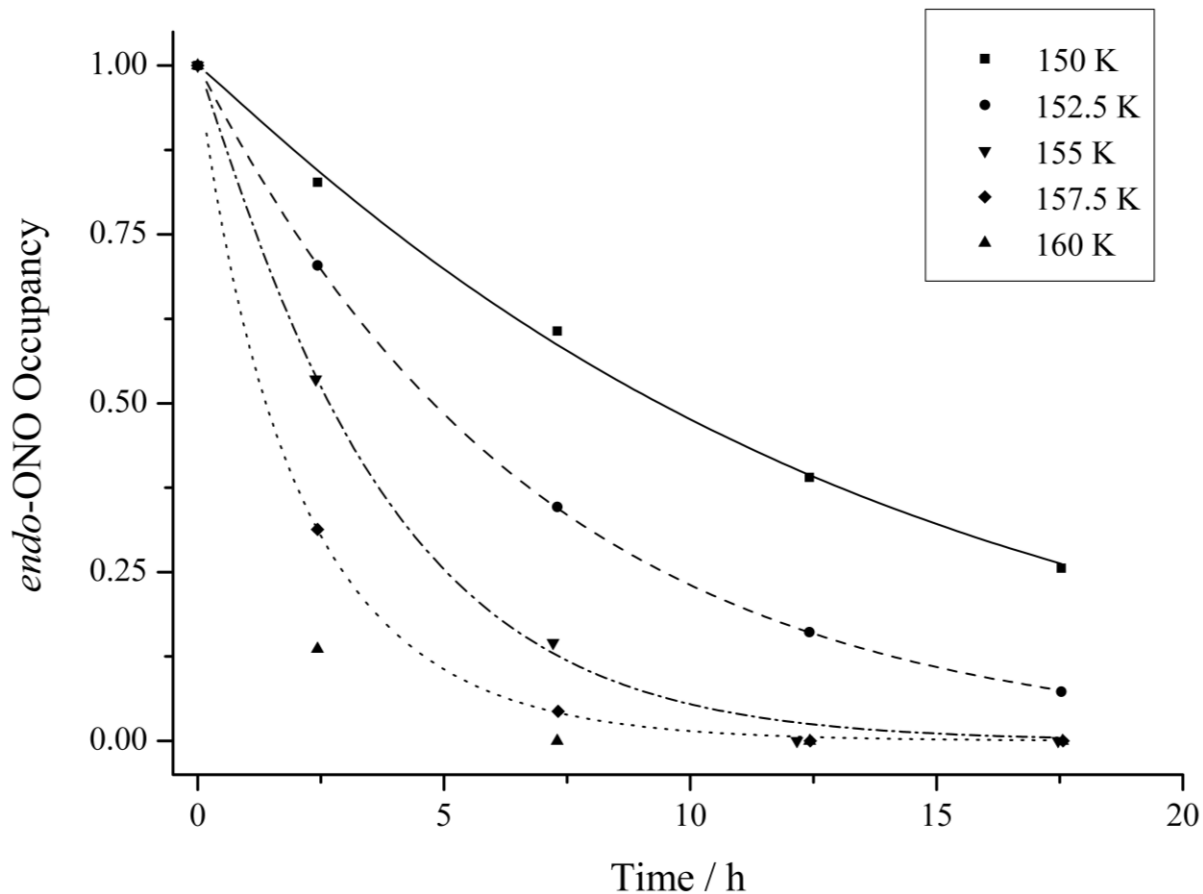
Figure 6.8: Kinetic curves describing MS decay in complex [1] between 150 and 160 K. Least squares fitting of y = exp($-kt^n$): **150 K:** $k = 0.08(1)$ h^{-1}, $n = 1.05(7)$, $R^2 = 0.994$; **152.5 K:** $k = 0.15(1)$ h^{-1}, $n = 1.02(1)$, $R^2 = 0.999$; **155 K:** $k = 0.27(1)$ h^{-1}, $n = 1.09(9)$, $R^2 = 0.992$; **157.5 K:** $k = 0.48(1)$ h^{-1}, $n = 0.92(3)$, $R^2 = 0.999$.

The decay data confirm that the photoactivated *endo*-nitrito isomer is no longer metastable above 150 K and nitrito − nitro decay is accelerated by raising the temperature. As for photoexcitation, the reverse decay process is best approximated by a sigmoidal function. If photoactivation is well modelled by JMAK theory, it is likely that the reverse decay process might occur by a similar mechanism and so the kinetic profiles in Figure 6.8 are fitted with the modified JMAK equation. As complete decay is achieved in complex [1], $\alpha_0 = 1$ and $\alpha_f = 0$ and so Equation 6.2 simplifies to

$$y = \exp(-kt^n) \hspace{3cm} \text{Equation 6.5}$$

The data correlate well with Equation 6.5, with $R^2 > 0.99$ at all temperatures fitted. Unfortunately regression analysis could not be completed at 160 K as there are too few data points before full decay to the GS is achieved. The value of *n* is close to unity in all cases, indicating homogeneous decay with equal likelihood of an event occurring throughout the crystal. This result is in agreement with excitation kinetics at λ = 500 nm and, additionally, profile shapes in both studies indicate that both photoactivation and decay processes occur by similar, first order mechanisms.
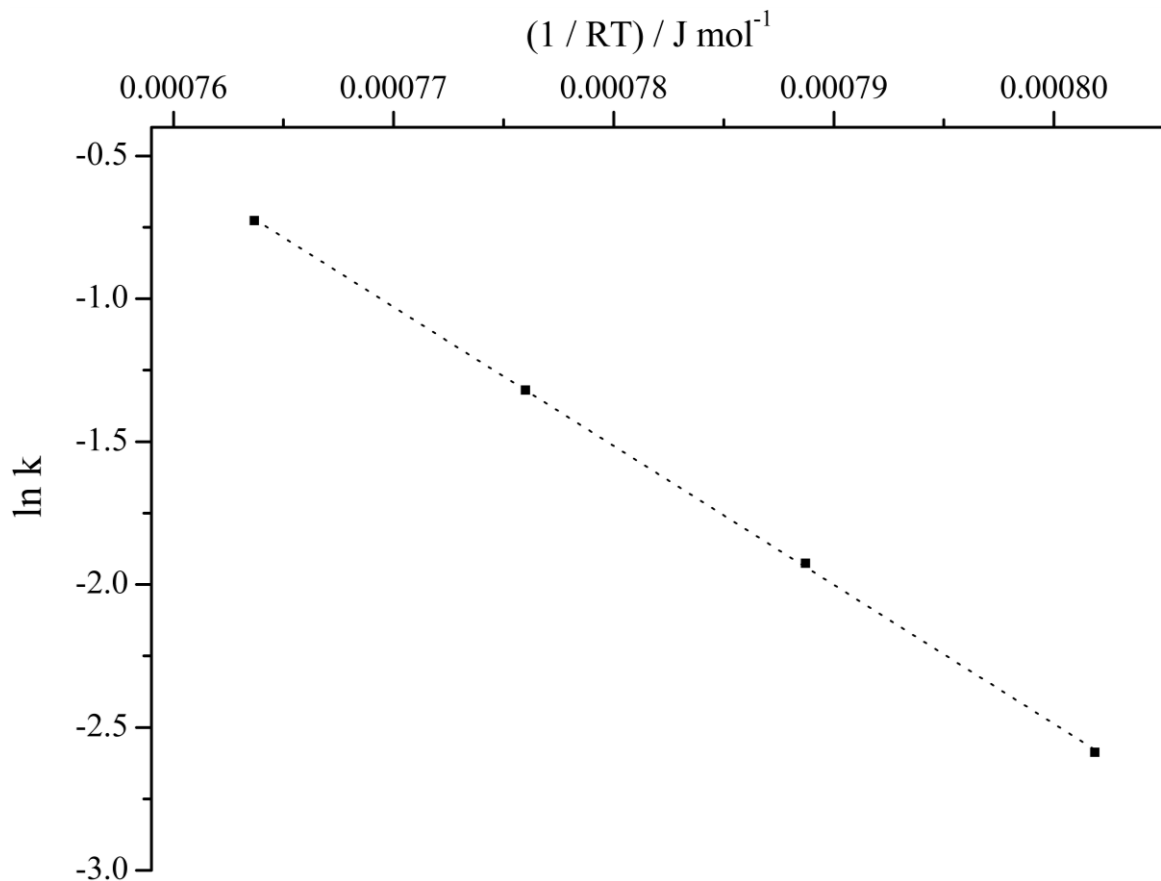
Figure 6.9: Arrhenius plot of ln(k) vs. (1 / RT) for kinetic data following *endo*-nitrito isomer decay in complex [1] between 150 and 160 K. E_A (– slope) = +48.6 (± 0.4) kJ mol⁻¹, R^2 = 0.999

The rate constants k obtained at each temperature can additionally be used to estimate the activation energy E_A for thermal nitrito – nitro decay. An Arrhenius plot of ln(k) vs. (1 / RT), where R = molar gas constant = 8.314 J K⁻¹ mol⁻¹, produces a straight line whose gradient represents E_A (Figure 6.9). The analysis provides an estimate of E_A = +48.6 (±0.4) kJ mol⁻¹, indicating an endothermic process. This is expected on considering that an input of thermal energy (*i.e.* warming) is required for nitrito – nitro decay to proceed. The estimate is in agreement with literature values found for other solid-state transformations: in 2010 Cao *et al.* report an energy of E_A = 32.5 kJ mol⁻¹ for the photodimerisation of 1,4-dimethyl-2-pyridinone,[148] and more recently Dumont *et al.* report a value of E_A = 46 kJ mol⁻¹ for cyanide : isocyanide linkage isomerism in iron(II) hexachromate(III) nanoparticles, from kinetic data obtained by FTIR.[16] While this comparable energy is calculated for the bulk material, the authors report that the value of E_A is highly dependent on particle size, an observation that highlights how important it is that the current analysis is completed using the same single-crystal for every data collection.

6.2.2. Complex [7]: Nitrito – Nitro Decay and the Effect of Crystallographic Environment

Steady-state studies in § 4.2.4 have shown that the degree of achievable photoisomerisation is highly dependent on the surrounding lattice, with varying excitation levels achieved for the two, crystallographically independent nitrite environments of complex [7]. Kinetic analysis of the reverse thermal process in [7] also allows the isomerisation behaviour at these two independent sites to be compared quantitatively, and as such the progress of nitrito – nitro decay in the two geometric isomers, A and B, has also been investigated as a function of time.

Variable temperature parametric studies with [7] (Table 4.30) indicate that the onset of MS decay occurs at 120 K for both molecules A and B, although it is evident that the decay process for each has a different temperature dependence. While molecule B achieves an average GS nitro-(η^1-NO$_2$) arrangement during a 7 h steady-state experiment at 125 K, the MS of molecule A decays over a larger temperature range of 120 to 135 K. In the attempt to make fair comparison between the two environments, a compromise temperature of 130 K was chosen for decay experiments conducted using synchrotron radiation, in which sufficient data for the refinement of a full, single-crystal X-ray structure for the monoclinic system in [7] could be collected in *ca.* 1 h. A crystal was mounted at room temperature and slow cooled to 100 K, then irradiated *in-situ* for 2 h with 400 nm LED light. An X-ray dataset was next collected at 100 K, confirming the photostationary state had been achieved for both molecules A and B, as per § 4.2.4. The crystal was then warmed to 130 K and a new data collection started as soon at the required temperature was reached. This kinetic data collection required *ca.* 12 h and in this time the data for 11 complete hemispheres was collected sequentially, allowing the nitro : nitrito ratios for each of molecules A and B to be refined, from full X-ray datasets, for 12 time intervals during the decay process.

Figure 6.10 shows the progress of *endo*-nitrito isomer decay with time for molecule A at 130 K. The kinetic profile is best approximated by a sigmodial function and the data are again analysed using JMAK theory. For molecule A, $\alpha_0 = 0.84$ and $\alpha_f = 0.20$ therefore Equation 6.2 becomes

$$y = 0.20 - (0.20 - 0.84)\exp(-kt^n) \qquad \text{Equation 6.6}$$

The data for molecule A correlate well with Equation 6.6, with a value of $R^2 = 0.989$. A value of $n = 0.95$ (± 0.05) is obtained for the Avrami exponent, which is again close to unity and so indicates homogeneous decay with equal probability of an event occurring throughout the crystal.
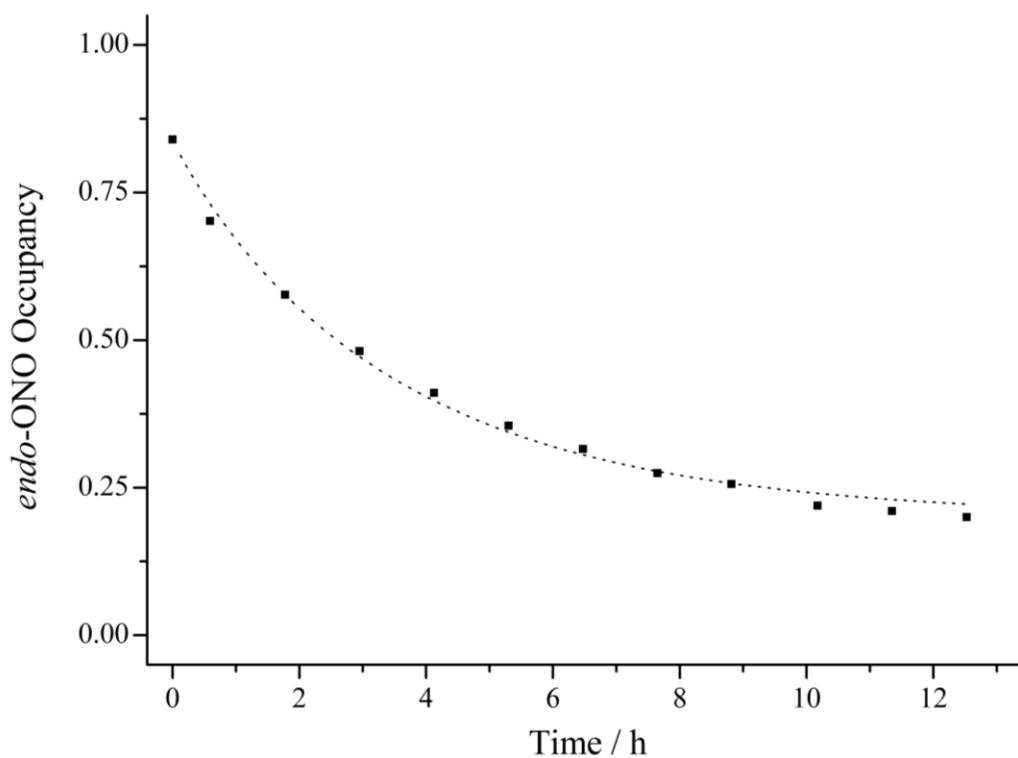
Figure 6.10: Kinetics of photoactivated *endo*-nitrito isomer in molecule A at 130 K. Least squares fitting of $y = 0.20 - (0.20 - 0.84)\exp(-kt^n)$: $k = 0.29$ (± 0.01) h^{-1}, $n = 0.95$ (± 0.05), $R^2 = 0.989$

The profile for nitrito – nitro decay in molecule B is again sigmoidal and is well approximated by JMAK kinetics (Figure 6.11). For molecule B $\alpha_0 = 0.31$ and $\alpha_f = 0$, thus Equation 6.2 simplifies to

$$y = (0.31)\exp(-kt^n) \hspace{4cm} \text{Equation 6.7}$$

A value of $R^2 = 0.978$ shows reasonable agreement between Equation 6.7 and the data, which again indicates that JMAK analysis is an effective model to describe the solid-state isomerisation. The Avrami constant $n = 0.94$ (± 0.09) can be approximated to unity within error, agreeing well with the result for molecule A and suggesting the decay of both independent nitrite ligands in [7] occurs homogeneously throughout the crystal. A comparison of the rate constants k for molecules A and B confirms that MS *endo*-nitrito isomer decay occurs at different rates for each distinct crystalline environment, with *ca.* four times faster decay occurring for molecule B. This observation could again be explained by considering the different intermolecular interactions involving the nitrite ligand in each environment. The GS nitro isomer in molecule B is involved in several hydrogen bonds, the re-formation of which should be energetically favourable. No such beneficial interactions exist to the GS of molecule A and in fact a new intermolecular hydrogen bond is also formed to the ES *endo*-nitrito isomer (Figure 4.31). Both of these factors suggest there is less energetic incentive for nitrito – nitro decay to occur in molecule A, which may explain the slower decay rate and so smaller observed value for k for this geometric isomer.
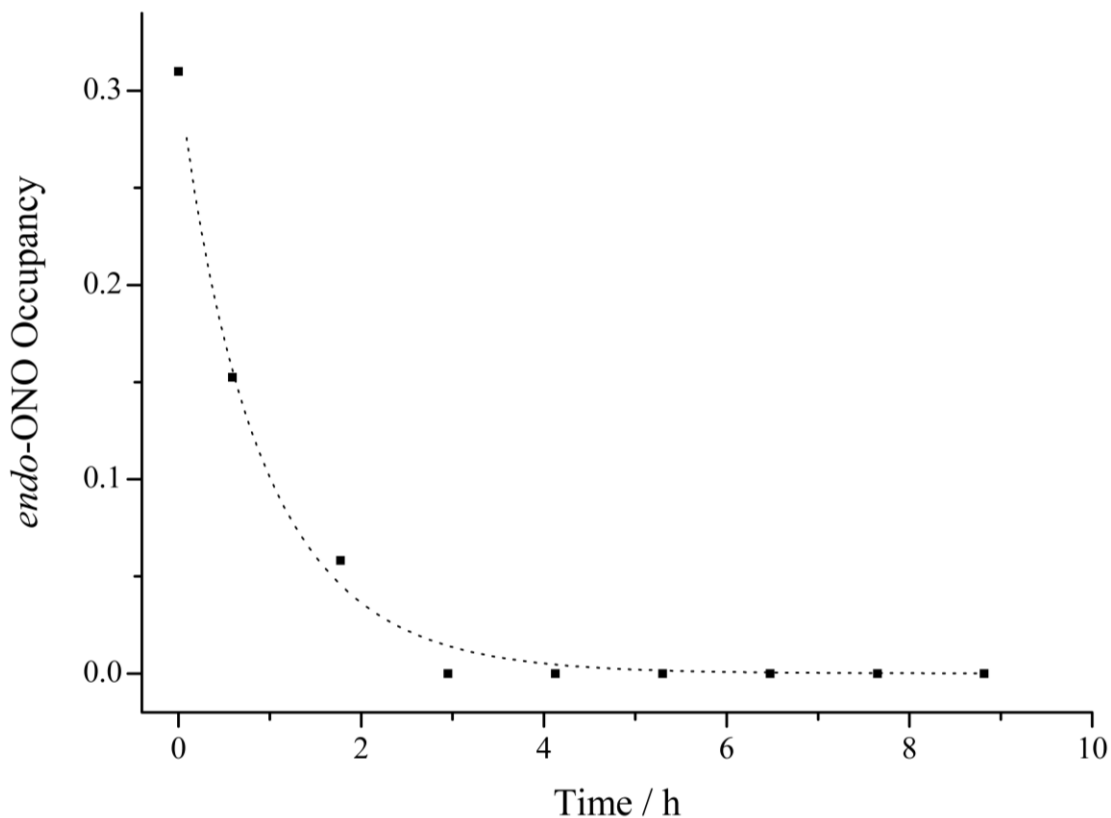
Figure 6.11: Kinetic curve for decay of the photoactivated *endo*-nitrito isomer in molecule B, complex [7] at 130 K. Least squares fitting of y = (0.31)exp(−kt^n): k = 1.13 (± 0.07) h^{-1}, n = 0.94 (± 0.09), R^2 = 0.978.

In summary, kinetic analysis of nitrito – nitrito decay in [7] again indicates that the isomerisation is highly dependent on the surrounding crystalline environment. The fact that molecules A and B undergo decay at considerably different rates indicates there is no correlation between the isomerisation at each of these sites and suggests they are converted independently. In terms of the "reaction cavity" concept discussed previously, an interpretation of these data would suggest that the two independent nitrite environments exist in different, unconnected reaction cavities. These independent cages appear unaffected by any change occurring in the other, that might occur as a result of isomerisation in the separate nitrite groups. This result does not agree with a suggestion, made in § 4.2.4 on considering steric influences, of possible correlation between the two distinct nitrite environments. The conclusions from kinetic analysis are most reliable however, as they are made on observation of the isomerisation in real time.

6.3. Summary

The kinetic data collected in Chapter 6 is generally well described by solid-state JMAK kinetics, with both photoexcitation and decay processes displaying sigmoidal profiles that fit well to model equations derived from JMAK theory. When the correct excitation wavelength is chosen, the results unambiguously suggest nitro − nitrito conversion occurs homogeneously throughout the crystal, with all values for the Avrami constant $n \approx 1$ indicating equal probability of an isomerisation event occurring in any region of the sample. Additionally, the observation of similar profile shapes, activation energies and kinetic rate constants for both excitation and decay studies with [1] indicate that both forward and reverse nitro − nitrito processes occur by similar mechanisms, and the observation of continuous profiles in all cases confirm a first order process. For photoexcitation, this result suggests that the interaction of one photon with one molecule in the GS arrangement is required to induce isomerisation, as suggests no cooperativity between molecules in the crystal to promote either photoexcitation or decay.

The results of Chapter 6 show the steady-state photocrystallographic method is sufficient to study both excitation and decay in metastable systems, where the ES lifetime can be manipulated by careful control of the experiment temperature. However, developing these methods to study the kinetics of shorter lifetime photoactivated species is more complicated. § 6.1.3 indicates that single-spot techniques show some promise, with preliminary kinetic data for complex [1] comparing well to the results obtained by steady-state methods. However, some issues with the method are highlighted that should be addressed for further improvement. Firstly, the considerable level of noise in the intensity data collected is attributed to the error in the CCD detector response, and highlights the fact that area detectors are not suitable for these types of measurements that require the accurate and repeated determination of single intensities. The single-spot method as outlined would be better carried out using a point detector system but, unfortunately for the current work, these detectors are no longer frequently available having been replaced by faster, modern CCD and pixel detectors. Secondly, the single-spot method is a considerably wasteful way of collecting X-ray data with the experimental set-up available. In terms of data collection, one of the main advantages of CCD detectors is the ability to collect many reflections quickly and so by collecting only a single reflection of interest per frame the single-spot procedure does not efficiently exploit the technology. Additionally, much of the data processing must be completed manually and is time-consuming. This latter issue might be solved in future by creating custom software to extract and record the required information efficiently.

There are a few ways that the data quality might be improved whilst still keeping the current available experimental set-up. Firstly, the noisy data of Figure 6.8 could be statistically improved by averaging each result over a small range of neighbouring data points (Figure 1, Appendix 12). This is effectively the action of a simple smoothing algorithm, reducing noise to achieve a better profile. However, whilst the results are aesthetically pleasing the actual gain in information is limited and as such this further data processing step is perhaps unnecessary. Additional improvement might be achieved by increasing the CCD detector binning from 2x2 to 4x4. The change to 4x4 binning improves the signal-to-noise ratio in each image as the same background count is spread over double the number of CCD pixels.[15] However, this also effectively reduces detector sensitivity and so this change is again perhaps wasteful of the available technology.

Addressing the issue of wasting resources, preliminary work has been started in collaboration with Dr. Pascal Parois and Dr Richard Cooper at the University of Oxford, developing software to predict the most suitable reflections and also frames that include several such reflections together. This will then allow several changing reflections to be monitored during a single kinetic experiment, greatly improving the efficiency of the single-spot technique. Additionally, some of the criteria for suitable reflections, including exclusions for spots in masked areas or with high Lorentz factors, can be incorporated into the selection process. At the time of writing this work is on-going and further investigation is planned for the future.

Despite these improvements, the results from single-spot methods would be further enhanced by changes to the experimental set-up and, in particular, the use of a different detecting method. It is possible that similar experiments might be achieved by using X-ray powder diffraction (XRPD), which would allow the peak height to be followed as a function of irradiation time *via* the quick determination of sequential XRPD patterns. However, given that the changes induced in the structure on isomerisation are comparatively small, preliminary tests with this technique have indicated that very high resolution data would be required to overcome the overlap between the diffraction peaks of interest and other reflections that remain unchanged. This would necessarily require the use of synchrotron radiation, which is not as readily available as a laboratory source.

Overall, the kinetic experiments outlined in Chapter 6 provide very useful information on the progress of the photoreaction in the single-crystal. Detailed mechanistic information has been inferred by applying solid-state kinetic theories to the data obtained and this information is integral to the further understanding of the solid-state isomerisation reaction.

Chapter 7.

Photocrystallographic Studies at Shorter Time Resolution

Chapter 7. Photocrystallographic Studies at Shorter Time Resolution

All of the photocrystallographic experiments so far described in this project have suggested the lifetime of the ES species in the crystal is highly temperature dependent. Careful control of the experimental conditions is required to maintain the metastable state. In particular, decay kinetic studies on complex [1] have shown that changing the temperature has a marked effect on the ES lifetime, with the decay rate noticeably accelerated on warming the crystal by just 2.5º (§ 6.2.1). This dynamic decay behaviour indicates that a spectrum of lifetimes can exist for photoactivated linkage isomers in the crystal; between low temperatures where metastable species are prevalent, to lifetimes on a min – h scale close to the MS limit, and moving to progressively more transient species on further warming towards ambient conditions. Support for this theory is provided by Woike *et al.* in a study using TR absorption spectroscopy to determine the presence of ns-lived nitrosyl isomers, in single-crystals of SNP at room temperature.[9] Considering that extensive work has shown metastable species to exist in SNP at low temperature,[34, 155] the observation of ultra-fast, reversible switching between η^1-NO (GS) and η^2-NO (MS$_2$) forms under ambient conditions provides further proof for the temperature dependence of the solid-state linkage isomerisation.

7.1.   Pseudo-Steady-State Experiments

Given this apparent temperature dependence, it should be possible to select the ES lifetime most suited to the set-up available for a particular photocrystallographic study, simply by careful control of the *in-situ* environment. To test this hypothesis, pseudo-steady-state studies were conducted with [1] in which a crystal was continuously irradiated while X-ray data was obtained at a variety of temperatures. Any difference in the system's response, to that seen by steady-state methods, may indicate the occurrence of shorter-lived processes that could not be previously observed by time-averaged techniques. Particular focus is given to temperatures near the MS limit, at *ca.* 160 K, where interesting decay behaviour has already been observed (§ 6.2.1).

Pseudo-steady-state experiments on Beamline I19

Initial pseudo-state-state studies of [1] were conducted as part of experiments helping to commission the TR crystallographic set-up in Experimental Hutch 2 (EH2) on Beamline I19 at Diamond Light Source.[156] Illumination of the sample throughout data collection was achieved using a pulsed Nd:YAG laser, tuned to 500 nm and focussed directly onto the sample position of the diffractometer (Figure 7.1). A full description of the experimental set-up is given in § 3.2.3.
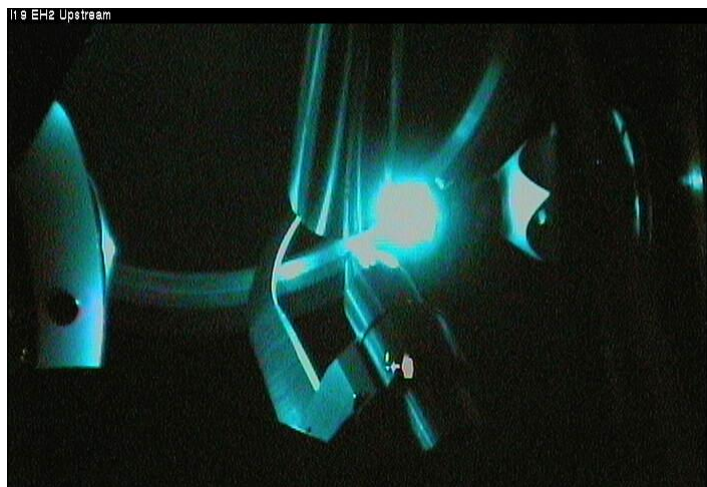
Figure 7.1: Experimental arrangement at the sample position for pseudo-steady-state studies conducted in EH2, Beamline I19, showing the delivery of light from the Nd:YAG laser ($\lambda = 500$ nm). The set-up facilitated the continuous illumination of a crystal throughout data collection

A crystal was first mounted on the diffractometer at room temperature and slow cooled to 100 K in the absence of any external light. A subsequent X-ray dataset then confirmed that the 100% nitro-(η^1-NO$_2$) GS had been achieved. Pseudo-steady-state data collections were then conducted at temperatures between 100 and 250 K, in which the crystal was continuously irradiated for the duration of a full, single-crystal X-ray experiment. Using the synchrotron X-ray radiation, a fully-complete dataset for [1] could be obtained in *ca.* 1 h at each temperature point. To ensure the removal of any residual metastable species at the end of each collection, the temperature was raised to 298 K and the crystal then re-cooled to the new temperature required between each dataset. As expected from previous steady-state results, irradiation at low temperatures of 100 – 150 K induced 100% conversion to the *endo*-nitrito-(η^1-ONO) MS isomer. On warming the crystal further however, the behaviour observed under pseudo-steady-state conditions began to differ from that seen previously. As in steady-state variable temperature experiments, conversion to the *endo*-nitrito isomer is decreased on heating towards the MS limit, however, at 160 K additional features are identified in the photodifference map that cannot be fully accounted for by expected reappearance of the nitro-(η^1-NO$_2$) GS. Additional difference peaks were assigned to the production of a new, *exo*-nitrito-(η^1-ONO) isomer (Figure 7.2), determined at low occupancy. This *exo*-nitrito isomer could be observed between 160 and 185 K, with a maximum occupancy of 12% determined at 170 K. In addition to the formation of the new isomer, the photoactivated *endo*-nitrito arrangement remains present over a wider temperature range under pseudo-steady-state conditions and is still observable at 190 K, while no trace of any ES arrangement can be found in steady-state data collected at the same temperature (§ 4.1.1). Nitrite isomer occupancies refined from these synchrotron data are shown in Table 7.1.
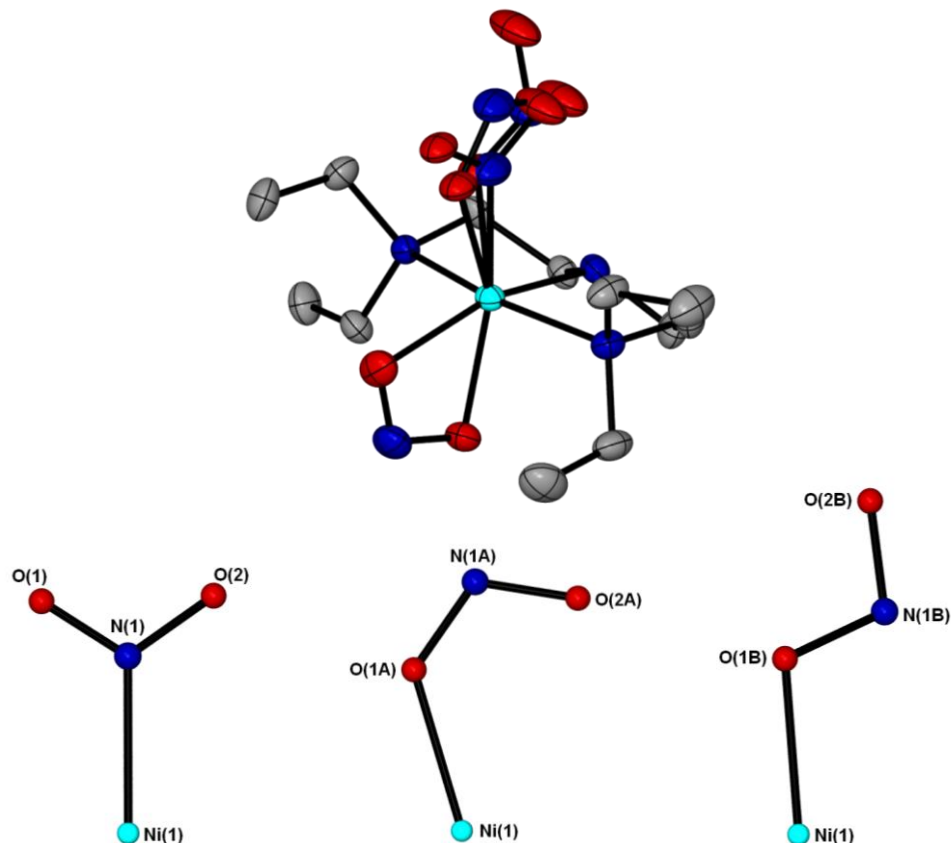
Figure 7.2: (Top) Single-crystal X-ray structure showing the atomic arrangement in complex [1] under pseudo-steady-state conditions, ellipsoids at 50 % probability and hydrogen atoms removed for clarity. **(Bottom)** Individual arrangements for the GS nitro, ES *endo*-nitrito and ES *exo*-nitrito linkage isomers

Table 7.1: Nitrite linkage isomer occupancies determined as a function of temperature during pseudo-steady-state photocrystallographic experiments with complex [1], conducted at Diamond Light Source

Temperature / K	Occupancy (esd)		
	nitro-(η^1-NO$_2$)	*endo*-nitrito-(η^1-ONO)	*exo*-nitrito-(η^1-ONO)
145	0.00*	1.00*	0.00*
150	0.00*	1.00*	0.00*
160	0.10(1)	0.82(1)	0.08(1)
170	0.14(1)	0.74(1)	0.12(1)
175	0.45(1)	0.46(1)	0.09(1)
180	0.59(1)	0.33(1)	0.08(1)
185	0.81(1)	0.15(1)	0.04(1)
190	0.91(1)	0.09(1)	0.00*
250	0.91(1)	0.09(1) ^	0.00*

* No esd is reported for full occupancy or zero occupancy as these ratios were not refined

^ Expected thermal occupancy of *endo*-nitrito-(η^1-ONO) at 250 K

194

Laboratory-based pseudo-steady-state experiments

To corroborate the synchrotron results, similar experiments were conducted with 500 nm LED light, using the laboratory-based photocrystallographic set-up described in § 3.2.3. The LED ring allows for *in-situ* illumination whilst a complete quadrant of data is obtained in *ca.* 4 h, which is sufficient to obtain a high quality single-crystal X-ray structure of [1]. These experiments were conducted with the same crystal as used in steady-state studies at $\lambda = 500$ nm (§ 4.1.1), enabling fair comparison between steady-state and pseudo-steady-state data. This crystal is *ca.* 5x larger than that necessary for synchrotron experiments.

The pseudo-steady-state data obtained with 500 nm LED light are shown in Figure 7.3. Excepting a small, systematic discrepancy in temperatures, the results are reproducible between the two pseudo-steady-state methods. This suggests that the new, *exo*-nitrito ES is not the product of non-linear processes, such as two-photon excitation, which might be induced by laser irradiation due to the higher incident flux. The temperature discrepancy between synchrotron and laboratory data might be attributed to a few different factors. Firstly, the fact that different crystal sizes were required for each method could be a cause of the differences, as this factor has been shown to affect the progress of isomerisation reactions in other single-crystal studies.[157] Secondly, considering that these two sets of data were obtained using different experimental set-ups involving different cryogenic equipment, it cannot be said for certain that the calibration of the two liquid nitrogen cooling devices was identical and, as such, the temperature discrepancy could be account for by this error. Finally, it has also been shown that prolonged laser exposure causes appreciable heating in the single-crystal, leading to temperature-based changes.[158] The lower-intensity light from LED illumination is not expected to cause such effects and so the different excitation methods could also account in part for the temperature differences observed.

For the larger crystal, the ES *endo*-nitrito-(η^1-ONO) isomer is observed on continuous irradiation between 100 and 180 K, with the onset of decay for the 100% MS arrangement occurring at *ca.* 145 K. The *exo*-nitrito-(η^1-ONO) isomer is observed between 145 and 165 K, with a maximum occupancy of 9% at 155 K. The graph shows that the appearance of this new isomer coincides with the onset of *endo*-nitrito isomer decay, while a stable model for GS nitro-(η^1-NO$_2$) arrangement cannot be refined until 150 K. Both this and the fact that the *exo*-nitrito form is not found in data obtained by steady-state methods, suggests the new isomer is a short-lived species that is only maintained at appreciable occupancy by continuous irradiation.

The results indicate that the *exo*-nitrito isomer lifetime is too short to be observed by steady-state data collections, which require an ES lifetime greater than *ca.* 4 h. However, irradiation of the sample during data collection induces a pseudo-steady-state arrangement in which the transient *exo*- isomer is continuously re-excited to a level that allows it to be identified in minor occupancy from the single-crystal X-ray experiment. Additional information about the *exo*-nitrito isomer lifetime can be inferred by considering the repetition rate of the pulsed Nd:YAG laser set-up used for irradiation in the synchrotron experiments. In these experiments the laser operates at 10 Hz, equating to a complete cycle time of 100 ms. As such, at temperatures where the *exo*- isomer is still observable under pseudo-steady-state conditions, its lifetime must be longer than 100 ms.
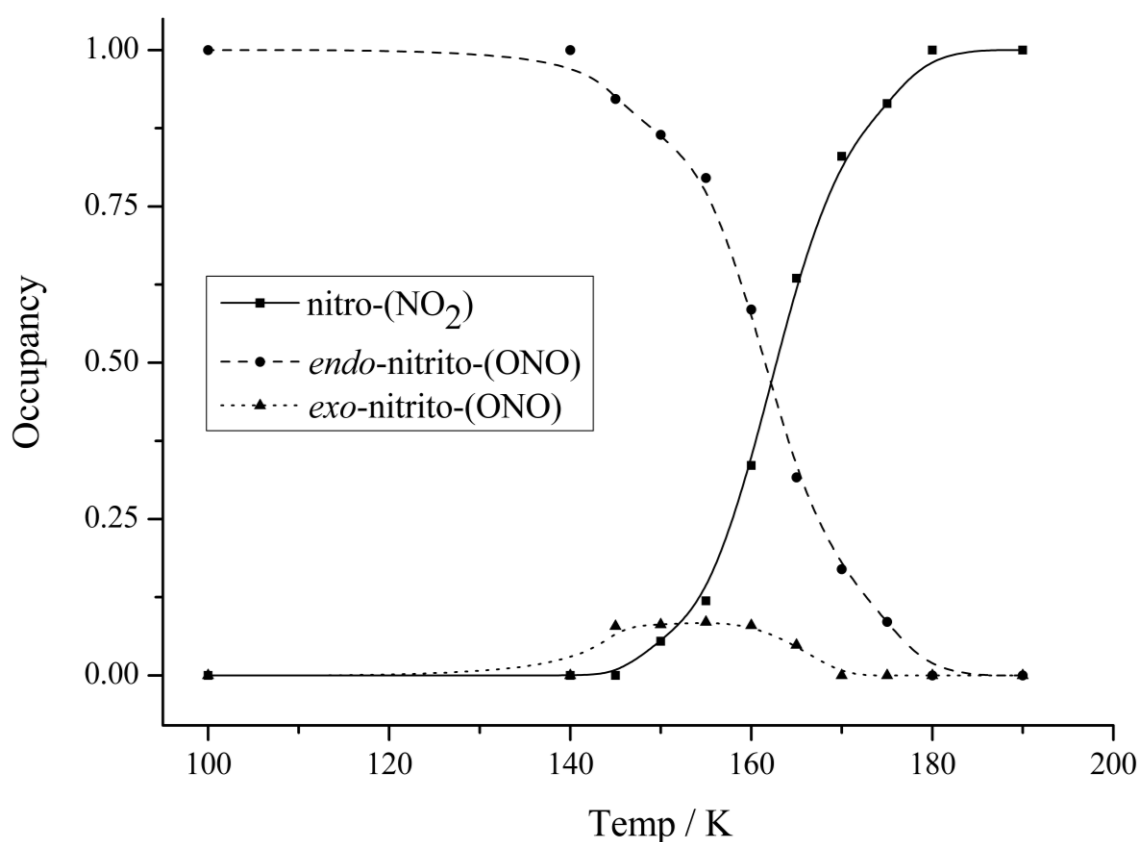
Figure 7.3: Nitrite linkage isomer occupancies determined as a function of temperature in laboratory pseudo-steady-state photocrystallographic experiments with complex [1], using 500 nm LED light

7.2.   Test Pump-Probe Experiments on Beamline I19

If a spectrum of lifetimes is expected for any linkage isomer induced in the single-crystal it therefore follows that photocrystallographic experiments at shorter time resolution, conducted just above the temperature at which the transient ES species could be previously observed, should allow the decay behaviour of that species to be investigated. Test pump-probe studies were conducted with [1], again in experiments helping to commission the TR set-up in EH2 on Beamline I19. These studies aimed to investigate the system at *ca.* 190 – 200 K, where ES isomers were longer observed under pseudo-steady-state conditions. The pump-probe set-up involves a dual-wheel mechanical chopper[123] (Figure 7.4), synchronised with the pulse train from the Nd:YAG laser. As described in detail in § 3.2.4, at the time these experiments were conducted the delay time between pump and probe pulses could be varied between 0 and 100 ms and the lowest time resolution achievable was 1 ms.
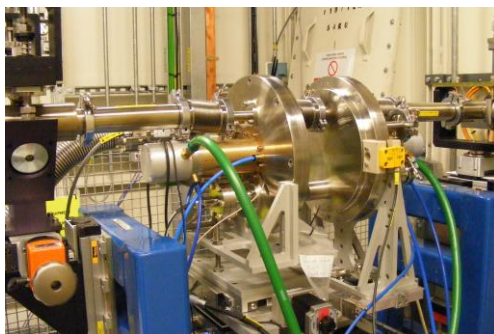
Figure 7.4: Dual-wheel mechanical chopper installed up-stream from the diffractometer in EH2, Beamline I19

A crystal was mounted at room temperature and slow cooled to 195 K. A subsequent X-ray dataset revealed the presence of a minor occupancy, thermally induced *endo*-nitrito-(η^1-ONO) isomer at 195 K, as expected by previous studies (§ 4.1.1). Pump-probe experiments were then conducted, with the pump – probe delay time varied between 0 and 50 ms. Unfortunately, the presence of the thermal species proved problematic for the photocrystallographic experiments, as it is not possible to differentiate between thermal and photoinduced *endo*-nitrito species. It is also likely that small temperature increases, induced in the crystal by laser irradiation, have an additional effect on the thermal *endo*-nitrito occupancy. These complications made it difficult to adequately resolve the *exo*-nitrito isomer from the photodifference map, and so the transient decay behaviour of this isomer also could not be investigated. Unfortunately, it is apparent that the overlap between thermal and photoinduced species make complex [1] unsuitable for pump-probe studies using the experimental set-up available. Future experiments should focus on systems that do not display thermal isomerisation, eliminating the possibility of such issues.

7.3. Summary

The TR crystallographic experiments described in Chapter 7 confirm that the lifetimes of linkage isomer species in the single-crystal are highly dependent on temperature. Careful control of this experimental variable has facilitated the investigation of complex [1] by pseudo-steady-state methods, showing these to be useful in determining further information on the complicated linkage isomerisation process occurring in this system. A new linkage isomer has been determined at minor occupancy, when the crystal is continuously irradiated at temperatures close to the MS limit. As no trace of this third ES arrangement was determined under steady-state conditions in Chapter 1, *exo*-nitrito-(η^1-ONO) is believed to be a transient species with a lifetime appreciably shorter than the *ca.* 4 h timeframe required to conduct a single-crystal X-ray data collection for [1] using the laboratory set-up. Under continuous illumination at $\lambda = 500$ nm, the average population of the *exo*-nitrito isomer is increased to a discernable level at temperatures between 145 and 165 K, allowing its characterisation by pseudo-steady-state techniques.

It is interesting to note that the *exo*- arrangement is only observable at temperatures between which the MS *endo*-nitrito isomer decays and the nitro-(η^1-NO$_2$) GS is regained (Figure 7.3). From this it might be inferred that the *exo*-nitrito isomer is in fact a transient species occurring in the decay pathway of the MS arrangement. This suggestion is supported by recently published DFT studies conducted on a related nickel – nitrite system, attempting to elucidate possible structural intermediates during nitro – nitrito conversion.[64] The calculations predict various intermediate nitrite arrangements as local energy minima in the conversion pathway, that closely resemble the *exo*-nitrito-(η^1-ONO) arrangement observed here by experiment. However, more convincing arguments would be required to support this proposed explanation for the *exo*-nitrito species. Possible complementary work might include TR spectroscopic evidence for the three linkage isomers by experiments conducted on single-crystal samples, or additionally parallel DFT studies conducted for a solid-state array. The latter calculations are computationally very expensive and as such are outside the remit of the current investigation.

It is apparent that TR crystallographic methods and their use to elucidate transient changes in solid-state linkage isomers remain at an early stage, with further progress required both in the crystallographic methodology and the application of complimentary techniques to obtain a more complete picture of the complicated processes occurring in the single-crystal on irradiation. However, Chapter 7 has illustrated that progress in the development of such methods at UK national facilities has been made and the method shows promise for the future.

Chapter 8.

Conclusions

Chapter 8. Conclusions

This project has aimed to identify the most influential factors that have a controlling effect on the progress of nitro – nitrito linkage isomerism in the solid-state, with a particular focus on maximising the photoconversion level that can be achieved in the single-crystal. This has been achieved *via* a simple crystal engineering approach, looking to maximise the available region surrounding the photoisomerisable ligand, or "reaction cavity", by incorporating sterically-demanding ancillary groups to dominate the crystal packing. On considering that, prior to the start of this project, there existed only a few reports in the literature of linkage isomer conversion that exceeded 50%,[36, 52] it is apparent that our approach has been largely successful. A substantial number of the complexes found to undergo photoactivated nitro – nitrito conversion in these studies proceed to high levels of photoactivation, with several of the species reported in Chapters 4 and 5 achieving conversion levels of 90% and greater. Analysis of the reaction cavity[99] volumes both before and after conversion indicates that the cavity has an appreciable degree of flexibility, but suggests that the highest photoactivation levels will be achieved in those systems that can incorporate nitro – nitrito rearrangement with the smallest overall change in cavity size. These results are in-keeping with early work by Schmidt and Cohen,[1-3] agreeing that the photoreactions progressing in a topotactic manner, *i.e.* with the least change in the photoactive region, will be most likely to succeed in the solid-state.

While the important effect of steric strain, induced in the lattice as a result of the atomic rearrangements, has been discussed in detail in Chapters 4 and 5 the analysis has also specifically highlighted the governing influence that individual intermolecular interactions can have on the progress of isomerisation in the single-crystal. The most important of these are hydrogen bonding interactions between the isomerising nitrite ligand and the surrounding crystalline array. The controlling influence of such interactions is particularly illustrated by complex [7], in which the two crystallographically independent molecules are shown to undergo differing photoresponses that correlate well with the degree of restrictive hydrogen bonding to the isomerising group. The results of Chapter 4 suggest it is beneficial to choose ancillary fragments that do not contain effective hydrogen bonding donors, and the efficacy of this approach is illustrated in the later investigation of the triphos complexes in Chapter 5. There are no effective hydrogen bonding groups present in these systems, which are all shown to achieve photoconversion levels of 90% and higher. Overall, the impact of all close intermolecular interactions between the photoactive fragment and the wider crystalline array is strongly evident from the results of Chapters 4 and 5,

highlighting, in agreement with some of the recent literature,[52, 58, 87, 159] the important effect that the surrounding environment will have on the progress of a photoreaction in the single-crystal.

This project also reports the first example of single-crystal kinetic studies involving nitro – nitrito linkage isomers and Chapter 6 provides some interesting new insights into the progress of the isomerisation reaction in real time. Further confirming the importance of the crystalline environment on photoreaction progress, kinetic investigation of the MS decay in complex [7] highlights the differing responses occurring at independent sites in the same crystal. This indicates the likelihood of different, unconnected reaction cavities for the two species crystallised together in this system. Chapter 6 also illustrates the effect different excitation wavelengths can have on the rate of photoisomerisation, highlighting the importance of choosing the correct type of irradiation to induce maximum photoactivation in complex [1]. These observations particularly underline the importance of obtaining a thorough understanding of the light absorption properties of the crystal before conducting photocrystallographic experiments. This provides an important reminder of the need for complementary spectroscopic measurements to obtain a more complete understanding of the photoactivation process. Possibly the key result of the kinetic experiments, however, is that for all of the complexes studied the photoinduced solid-state isomerisation proceeds as a first order reaction, with the results of JMAK analysis predicting that photoactivation occurs homogeneously throughout the crystal. These results suggest that the photoisomerisation is not cooperative, but that photo-switching in each, individual molecule occurs independently. This differs to the progress of other photoinduced solid-state transformations, for example LIESST processes in spin-crossover systems, which are known to occur cooperatively throughout the crystal.[160]

Finally, the possibility of some electronic contribution to linkage isomer formation has also been investigated, both in terms of the crystallisation preference for octahedral nickel(II)-amine complexes, and in reference to nitro – nitrito conversion. The evidence of some *trans*-influence over the preferred crystallisation geometry for the compounds of Chapter 4 is of particular interest, when considering the design of new compounds for photoactivation. It is important to be able to predict the most likely crystallisation geometry for a potential new species, as the *exo*- nitrito-(η^1-ONO) isomeric arrangement is shown to be photoinert under all tested photoactivation conditions.

Overall, these studies have made important progress towards a more detailed understanding of the key chemical and photophysical processes affecting nitro – nitrito isomerisation in the solid-state. Future efforts in this area will aim towards studying these processes in other solid-state forms,

beginning to reflect the possible applications for this chemistry in potential real-world devices. These studies will likely require the development of photocrystallographic techniques using other diffraction methods, and will additionally rely on the inclusion of complimentary spectroscopic data. In considering these goals, most importantly the results of the current project provide a strong basis for the future rational design of new TM coordination complexes for these purposes, which will routinely undergo high levels of photoactivation in a way that is both controllable and reproducible.

Chapter 9.

Experimental

Chapter 9. Experimental

9.1.   Synthetic Preparations of Intermediate Compounds

All chemicals purchased from commercial sources were used as received without further purification. All solvents were reagent grade.

9.1.1.   Preparation of (i): Potassium hexanitronickelate(II) monohydrate

$$NiCl_2 + 6KNO_2 \xrightarrow{\;H_2O\;} K_4[Ni(NO_2)_6].H_2O + 2KCl$$
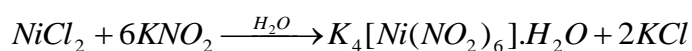
Scheme 9.1: Synthesis of Compound (i)

Excess potassium nitrite (5.11 g, 60 mmol) was dissolved in distilled water (2 mL) and added drop wise to an aqueous solution of nickel(II) chloride hexahydrate (1.19 g, 5 mmol) at room temperature. The green nickel(II) solution turned to violet on addition of potassium nitrite and an orange solid gradually precipitated on stirring. The solution was stirred for 2 h and the orange product then filtered and dried under vacuum (90 % yield).[161]

9.1.2.   Preparation of (ii): Potassium tetranitropalladate(II)

$$PdCl_2 + 4KNO_2 \xrightarrow{\;H_2O\;} K_2[Pd(NO_2)_4] + 2KCl$$
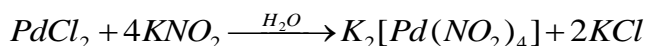
Scheme 9.2: Synthesis of Compound (ii)

This compound was prepared using a slightly modified literature procedure.[162] Excess potassium nitrite (2.55 g, 30 mmol) was dissolved in distilled water (2 mL) the added drop wise to a suspension of palladium(II) chloride (0.89 g, 5 mmol) in distilled water (5 mL) with stirring. The red/brown suspension initially dissolved to give a yellow solution, and a yellow precipitate formed with time. The mixture was stirred for 2 h before the yellow precipitate was filtered and dried under vacuum (60 % yield).

9.1.3. Preparation of (iii): Potassium tetranitroplatinate(II)

$$K_2[PtCl_4] + 4KNO_2 \xrightarrow{H_2O} K_2[Pt(NO_2)_4] + 4KCl$$
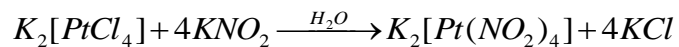
Scheme 9.3: Synthesis of Compound (iii)

An excess of potassium nitrite (2.55 g, 30 mmol) was dissolved in distilled water (2 mL), then added drop wise to a warm aqueous suspension of potassium tetrachloroplatinate(II) (2.08 g, 5 mmol) with stirring. The mixture was warmed until all of the reactants had dissolved, then quickly cooled to *ca.* 5 °C. After cooling for a few hours colourless crystals of the product are formed, which were filtered and dried under vacuum (90 % yield).

9.2. Synthetic Preparations of Final Compounds

All chemicals purchased from commercial sources were used as received without further purification. All solvents were reagent grade.

9.2.1. Preparation of Complex [1]: Dinitro-(*N,N,N',N'*-tetraethyldiethylenetriamine) nickel(II)

$$C_{12}H_{29}N_3 \quad + \quad K_4[Ni(NO_2)_6].H_2O \quad \xrightarrow{\;MeOH\;} \quad Ni(C_{12}H_{29}N_3)(NO_2)_2 \quad + \quad 4KNO_2$$
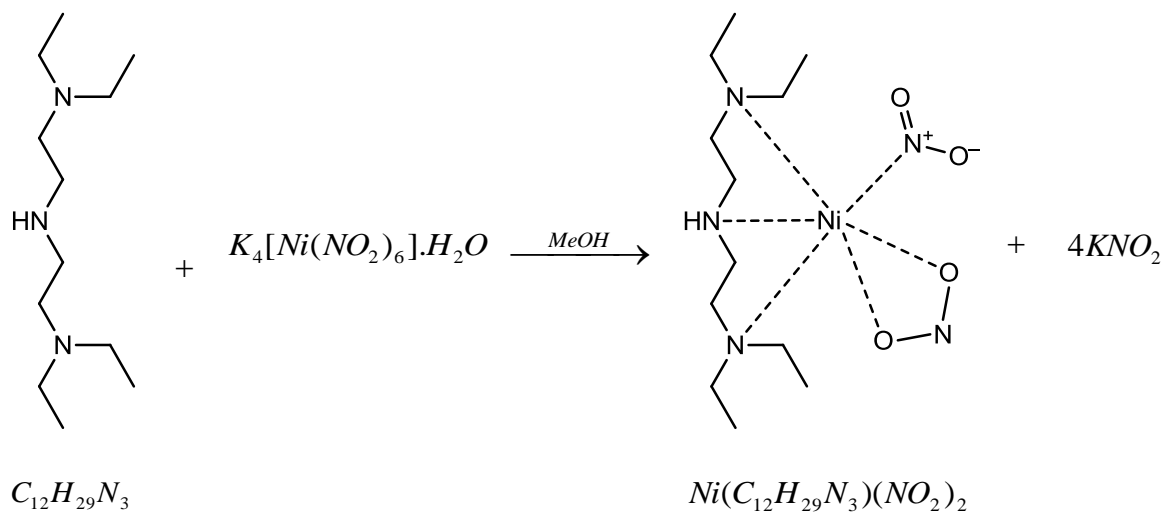
Scheme 9.4: Synthesis of Compound [1]

This compound was synthesised *via* a modified literature procedure.[69]   *N,N,N',N'*-tetraethyldiethylenetriamine (0.26 mL, 1 mmol) in methanol (5 mL) was slowly added dropwise to a suspension of potassium hexanitronickelate(II) monohydrate (0.51 g, 1 mmol) in methanol (5 mL) with vigorous stirring. The orange suspension gradually turned to a green solution on the addition of the amine. The mixture was stirred for 2 h, before the solvent was removed under vacuum. The resulting solid was taken up in dichloromethane and filtered to remove any insoluble inorganic salts.   The solvent was again removed under vacuum and the green product recrystallised by slow evaporation from methanol.

CHN: calcd (%) for $C_{12}H_{29}N_5Ni_1O_4$: C 39.37, H 7.98, N 19.13; found (%): C 39.20, H 8.10, N 19.32

FT-IR: ν(NO) = 1363, 1208, 974, 737 cm^{-1}; ν(NH) = 3238 cm^{-1}

UV/vis: 646, 366 nm

9.2.2. Preparation of Complex [2]: Nitro-(*N,N,N',N'*-tetraethyldiethylenetriamine) palladium(II) tetraphenylborate

N,N,N',N'-tetraethyldiethylenetriamine (0.26 mL, 1 mmol) in acetone (5 mL) was added dropwise to a solution of potassium tetranitropalladate(II) (0.37 g, 1 mmol) in distilled water (5 mL), with stirring. The homogeneous colourless solution turned initially cloudy on addition of the amine with the formation of a cream precipitate, but this re-dissolved on further stirring. The mixture was stirred for 3 h.

$$C_{12}H_{29}N_3 \qquad\qquad [Pd(C_{12}H_{29}N_3)(NO_2)]NO_2$$

Counterion exchange

$$[Pd(C_{12}H_{29}N_3)(NO_2)]NO_2 + NaBPh_4 \xrightarrow{\ Acetone/H_2O\ } [Pd(C_{12}H_{29}N_3)(NO_2)]BPh_4 + NaNO_2$$
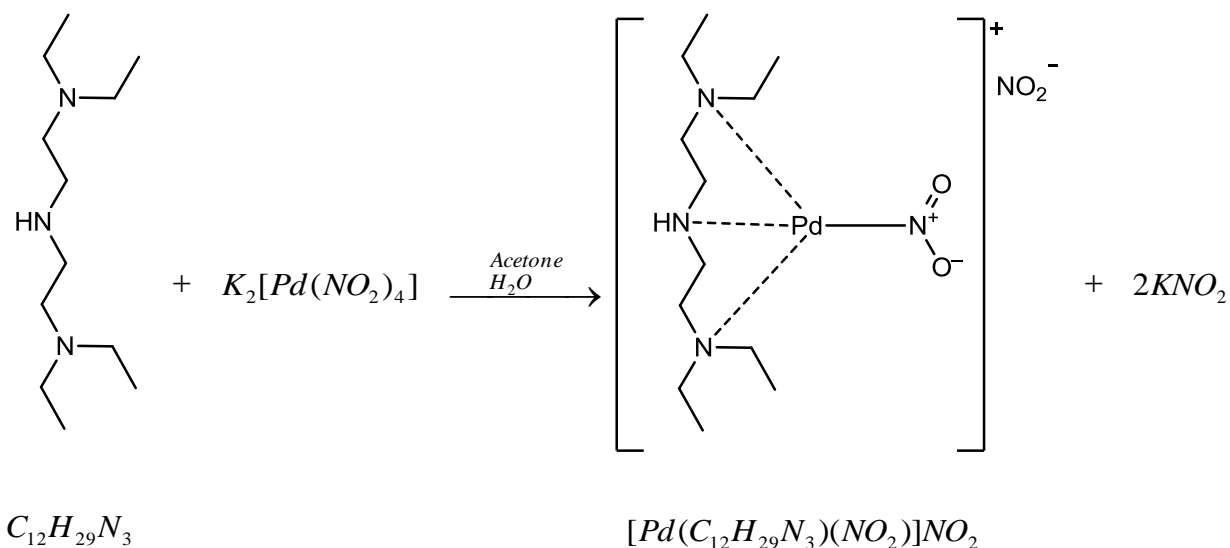
Scheme 9.5: Synthesis of Compound [2]

An excess of sodium tetraphenylborate (0.69 g, 2 mmol) was dissolved in a distilled water: acetone mix (30 : 1) and added dropwise to the reaction. A cream precipitate formed, which was collected by vacuum filtration and washed with a little cold distilled water. The cream powder was recrystallised *via* slow evaporation from a tetrahydrofuran / toluene mixture.

CHN: calcd (%) for $C_{36}H_{49}B_1N_4O_2Pd_1 . H_2O$: C 61.33, H 7.29, N 7.95; found (%): C 62.2, H 7.35, N 8.01

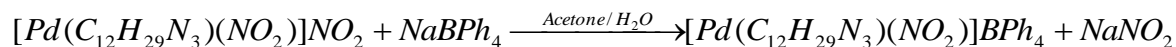FT-IR: v(NO) = 1455, 1372, 733, 704 cm^{-1}; v(NH) = 3659 cm^{-1}

UV/vis: 321 nm

9.2.3. Preparation of Complex [3]: Nitro-(*N,N,N',N'*-tetraethyldiethylenetriamine) platinum(II) tetraphenylborate

N,N,N',N'-tetraethyldiethylenetriamine (0.26 mL, 1 mmol) in acetone (5 mL) was added dropwise to an aqueous solution (3 mL) of potassium tetranitroplatinate(II) (0.46 g, 1 mmol), and the resulting colourless solution was stirred for 24 h.

$$C_{12}H_{29}N_3 \qquad\qquad\qquad [Pt(C_{12}H_{29}N_3)(NO_2)]NO_2$$

Counter ion exchange

$$[Pt(C_{12}H_{29}N_3)(NO_2)]NO_2 + NaBPh_4 \xrightarrow{\text{Acetone/}H_2O} [Pt(C_{12}H_{29}N_3)(NO_2)]BPh_4 + NaNO_2$$
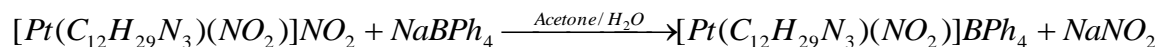
Scheme 9.6: Synthesis of Compound [3]

An excess of sodium tetraphenylborate (0.69 g, 2 mmol) was dissolved in a distilled water: acetone mixture (30 : 1) and added drop wise to the reaction mixture. A white precipitate was formed on addition of the borate, which was collected by vacuum filtration and washed with a little cold distilled water. The white product was recrystallised from a tetrahydrofuran / toluene mixture, *via* slow evaporation.
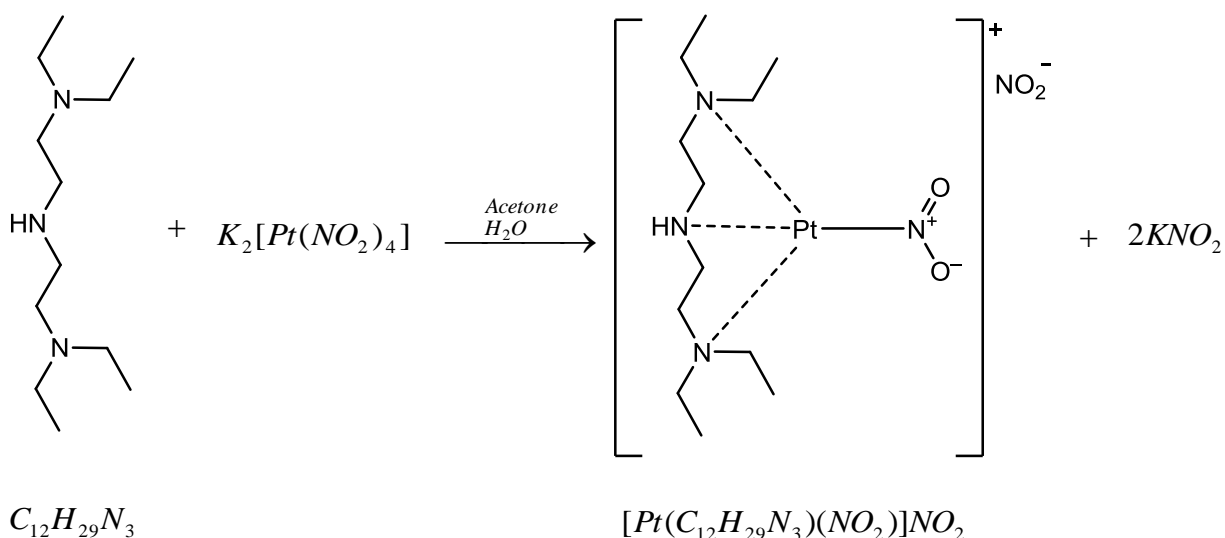
CHN calcd (%) for $C_{36}H_{49}B_1N_4O_2Pt_1 \cdot H_2O$: C 54.48, H 6.48, N 7.06; found (%): C 55.84, H 6.42, N 7.11

FT-IR: $v(NO)$ = 1455, 1378, 1323, 732, 703 cm^{-1}; $v(NH)$ = 3424 cm^{-1}

UV/vis: 321 nm

9.2.4. Preparation of Complex [4]: Dinitro-(*N,N,N',N'',N''*-pentamethyl-diethylenetriamine)nickel(II)

$$C_9H_{23}N_3 \quad + \quad K_4[Ni(NO_2)_6].H_2O \quad \xrightarrow{\;MeOH\;} \quad Ni(C_9H_{23}N_3)(NO_2)_2 \quad + \quad 4KNO_2$$
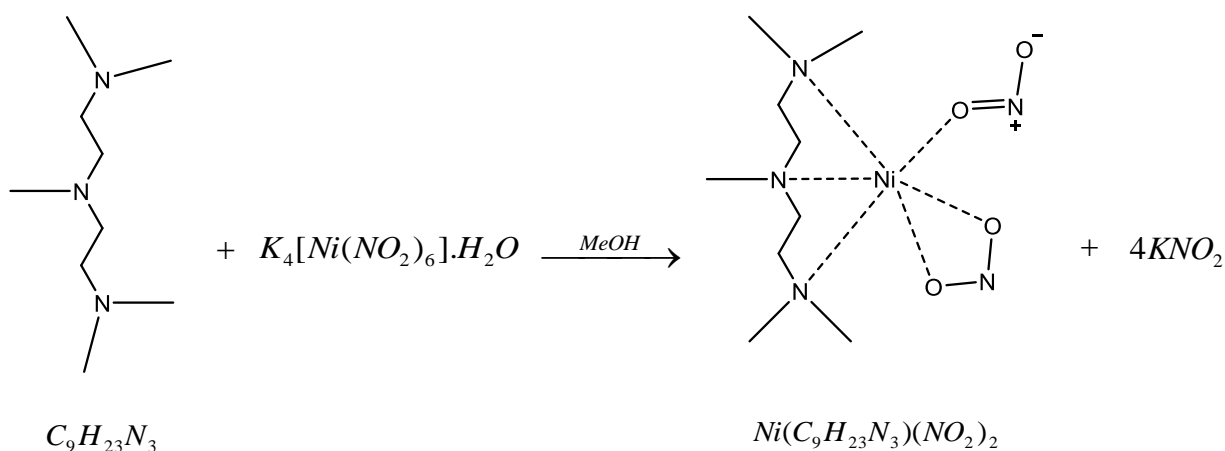
Scheme 9.7: Synthesis of Compound [4]

This compound was synthesised *via* a modified literature procedure.[69] *N,N,N',N'',N''-*pentamethyldiethylenetriamine (0.21 mL, 1 mmol) in methanol (5 mL) and added dropwise to a methanolic suspension of potassium hexanitronickelate(II) monohydrate (0.53, 1 mmol) with vigorous stirring. The initially orange suspension gradually turned to a bright green solution on addition of the amine. After *ca.* 2 h the solvent was removed under vacuum, the resulting green solid taken up in dichloromethane and filtered to remove any inorganic salt impurities. The solvent was again removed under vacuum and the product recrystallised by slow evaporation from a dichloromethane and propan-2-ol mixture.

CHN: calcd (%) for $C_9H_{23}N_5Ni_1O_4$: C 33.36, H 7.16, N 21.62; found (%): C 33.26, H 7.16, N 21.50

FT-IR: v(NO) = 1460, 1381, 733, 704 cm^{-1}

UV/vis: 615, 381 nm

9.2.5. Preparation of Complex [5]: Dinitro-(*N*-isopropyldiethylenetriamine)nickel(II)

$$C_7H_{19}N_3 \qquad\qquad Ni(C_7H_{19}N_3)(NO_2)_2$$
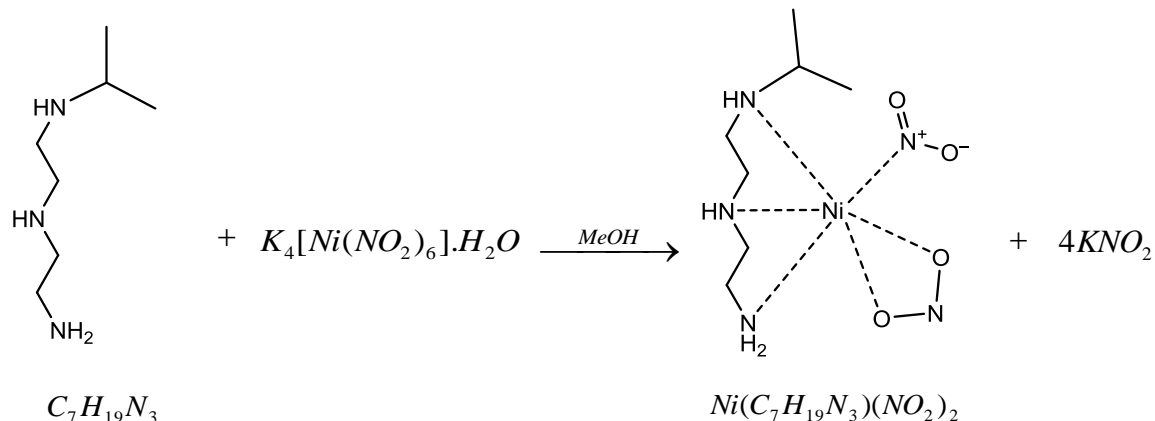
Scheme 9.8: Synthesis of Compound [5]

This compound was synthesised *via* a modified literature procedure.[69] *N*-isopropyldiethylenetriamine (0.17 mL, 1 mmol) in methanol (5 mL) and added dropwise to a methanolic suspension of potassium hexanitronickelate(II) monohydrate (0.53, 1 mmol) with vigorous stirring. The initially orange suspension gradually turned to a purple solution on addition of the amine. After *ca.* 2 h the solvent was removed under vacuum, the resulting purple solid taken up in dichloromethane and filtered to remove any inorganic salt impurities. The solvent was again removed under vacuum and the product recrystallised by slow evaporation from propan-2-ol.

CHN: calcd (%) for $C_7H_{19}N_5Ni_1O_4$: C 29.20, H 6.53, N 23.66; found (%): C 28.41, H 6.47, N 23.66
UV/vis: 558, 364 nm

9.2.6. Preparation of Complex [6]: Dinitro-(2,2'-diamino-*N*-methyldiethylamine) nickel(II)

$C_5H_{15}N_3$ + NiCl₂·6H₂O + 2KNO₂ → Ni(C₅H₁₅N₃)(NO₂)₂ + 2KCl
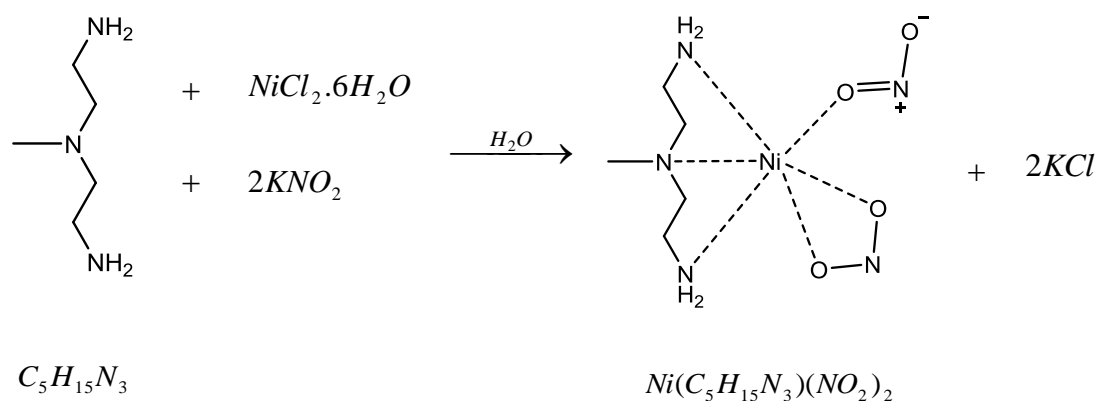
Scheme 9.9: Synthesis of Compound [6]

This compound was synthesised by a modified literature procedure.[136] 2,2'-diamino-*N*-methyldiethylamine (0.13 mL, 1 mmol) was added dropwise to an aqueous solution of nickel chloride hexahydrate (0.24 g, 1 mmol) and potassium nitrite (0.34 g, 4 mmol) with stirring. The initially pale green nickel solution turned blue on addition of the amine. The mixture was stirred for *ca.* 30 min before it was filtered and the remaining blue solution was then allowed to slowly evaporate at room temperature.

CHN: calcd (%) for $C_5H_{19}N_5Ni_1O_4$: C 22.42, H 5.64, N 26.14; found (%): C 20.89, H 6.12, N 23.40

FT-IR: v(NO) = 1594, 1387, 1208, 970 cm^{-1}; v(NH) = 3345 cm^{-1}

UV/vis: 592, 367 nm

9.2.7. Preparation of Complex [7]: Dinitro-(3,3'-diamino-*N*-methyldipropylamine) nickel(II)
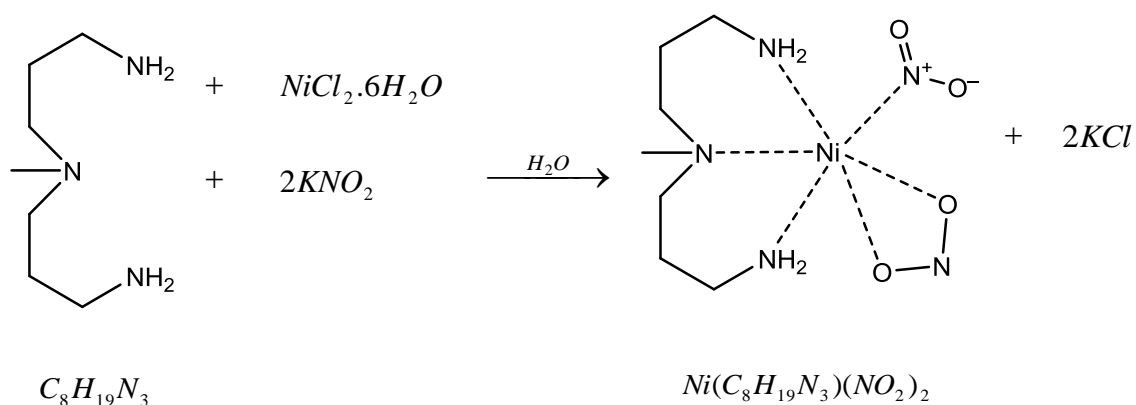
Scheme 9.10: Synthesis of Compound [7]

3,3'-diamino-*N*-methyldipropylamine (0.16 mL, 1 mmol) was added dropwise to an aqueous solution of nickel chloride hexahydrate (0.24 g, 1 mmol) and potassium nitrite (0.34 g, 4 mmol) with stirring. The initially pale green nickel solution turned bright blue on addition of the amine. The mixture was stirred for *ca.* 30 min before it was filtered and the remaining blue solution was then allowed to slowly evaporate at room temperature.[136]

CHN: calcd (%) for $C_9H_{23}N_5Ni_1O_4$: C 28.41, H 6.47, N 23.66; found (%): C 28.50, H 6.54, N 23.54

FT-IR: v(NO) = 1582, 1341, 1200, 1018, 768 cm^{-1}; v(NH) = 3334 cm^{-1}

UV/vis: 562, 361 nm

9.2.8. Preparation of Complex [8]: (*μ*-oxalato)-Di-[nitro-(3,3'-diamino-*N*-methyldipropylamine)nickel(II)]

$$[Ni(C_8H_{19}N_3)(NO_2)]_2(\mu - C_2O_2)$$

$C_8H_{19}N_3$
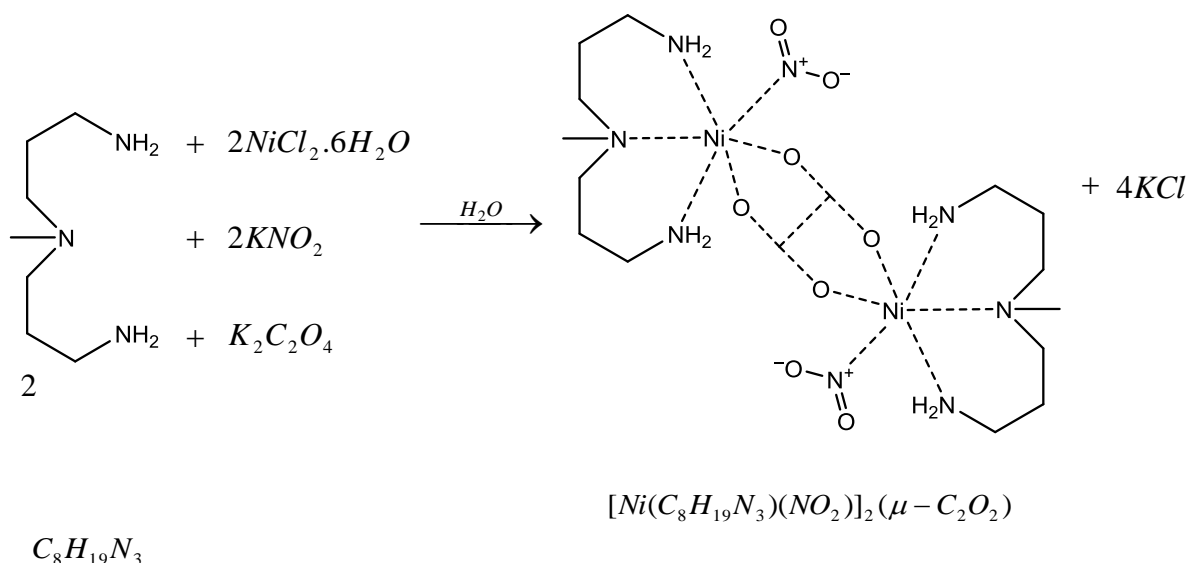
Scheme 9.11: Synthesis of Compound [8]

3,3'-diamino-*N*-methyldipropylamine (0.16 mL, 1 mmol) was added dropwise to an aqueous solution of nickel chloride hexahydrate (0.24 g, 1 mmol), potassium nitrite (0.09 g, 1 mmol) and potassium oxalate (0.09 g, 0.5 mmol) with stirring. The initially pale green nickel solution turned blue-green on addition of the ligands. The mixture was stirred for *ca.* 2 h before it was filtered and the remaining solution allowed to slowly evaporate at room temperature.[139]

CHN: calcd (%) for $C_9H_{23}N_5Ni_1O_4$: C 32.58, H 6.83, N 18.99; found (%): C 32.42, H 6.65, N 18.98

FT-IR: *exo*-nitrito isomer [8a]: v(NO) = 1635, 1360, 1091, 794, 634 cm^{-1}; v(NH) = 3326 cm^{-1}

nitro isomer [8b]: v(NO) = 1648, 1350, 1293, 790, 766 cm^{-1}; v(NH) = 3319 cm^{-1}

UV/vis: 595, 351 nm

9.2.9. Preparation of Complex [9]: Nitro-(*bis*-(2-diphenylphosphinoethyl)-phenylphosphine)nickel(II) tetraphenylborate

All manipulations were carried out under a dry nitrogen atmosphere using Schlenk techniques. All solvents were dried and degassed using standard methods.

bis-(2-diphenylphosphinoethyl)phenylphosphine (1.6 g, 0.3 mmol) in tetrahydrofuran (3 mL) was added to a suspension of potassium hexanitronickelate(II) monohydrate (0.15 g, 0.3 mmol) in methanol (3 mL). The mixture was refluxed for 4 h to produce a red solution. Excess potassium nitrite (0.08 g, 3 mmol) in methanol (5 mL) was added and the mixture stirred for a further 2 h. The solvent was removed under vacuum and the product taken up in dichloromethane and filtered to remove any inorganic salt impurities. The solvent was again removed under vacuum.

$$C_{34}H_{33}P_3 \quad + \quad K_4[Ni(NO_2)_6].H_2O \xrightarrow{THF/MeOH} [Ni(C_{34}H_{33}P_3)(NO_2)]NO_2 \quad + \quad 4KNO_2$$

Counter ion exchange

$$[Ni(C_{34}H_{33}P_3)(NO_2)]NO_2 + NaBPh_4 \xrightarrow{Acetone/H_2O} [Ni(C_{34}H_{33}P_3)(NO_2)]BPh_4 + NaNO_2$$
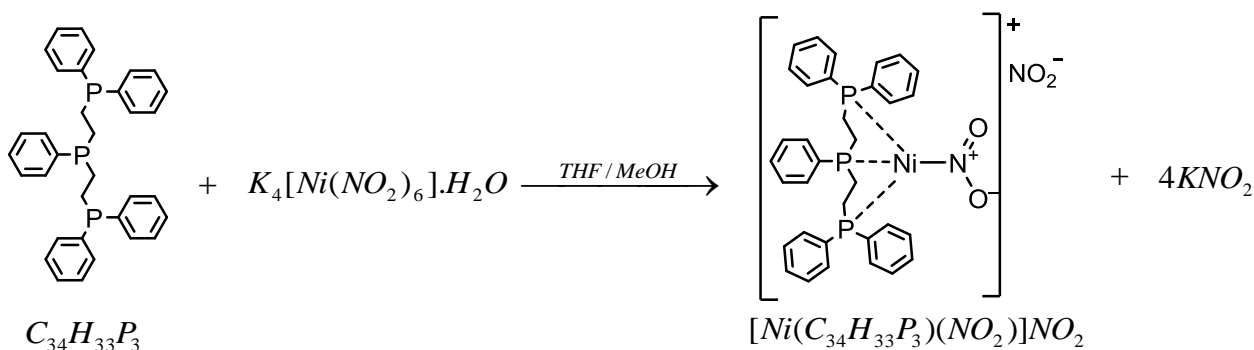
Scheme 9.13: Synthesis of Compound [9]

The product was dissolved in the minimum volume of acetone and sodium tetraphenylborate (0.10 g, 0.3 mmol) in a distilled water : acetone mix (30 : 1) was added dropwise. An orange precipitate formed that was collected by filtration and dried under vacuum.

FT-IR: v(NO) = 1436, 1381, 1102, 733, 705 cm^{-1}

NMR: **^{1}H** (300 MHz, CDCl$_3$): δ_H 1.31 (4H, b, CH$_2$), δ_H 2.98 (4H, b, CH$_2$), δ_H 7.37 − 7.71 (25H, m, C$_6$H$_5$). *Broad spectrum due to coupling with different ^{31}P environments.*

^{31}P (300 MHz, CDCl$_3$): **NO$_2$:** δ_P 33.01 (2P, d, $^2J_{PP}$ = 51.41 Hz), δ_P 42.26 (1P, t, $^2J_{PP}$ = 51.63 Hz); **ONO:** δ_P 47.70 (2P, d, $^2J_{PP}$ = 49.7 Hz), δ_P 109.23 (1P, t, $^2J_{PP}$ = 49.8 Hz). *Two overlapped spectra corresponding to the ^{31}P environments in two nitrite linkage isomer species, as expected at room temperature for [9].*

UV/vis: 321, 403 nm

9.2.10. Preparation of Complex [10]: Nitro-(*bis*-(2-diphenylphosphinoethyl)-phenylphosphine)palladium(II) tetraphenylborate

All manipulations were carried out under a dry nitrogen atmosphere using Schlenk techniques. All solvents were dried and degassed using standard methods before use.

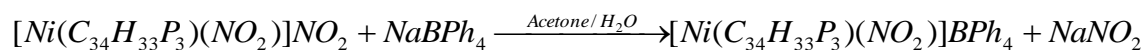*bis*-(2-diphenylphosphinoethyl)phenylphosphine (1.6 g, 0.3 mmol) in tetrahydrofuran (3 mL) was added to a solution of potassium tetranitropalladate(II) (0.11 g, 0.3 mmol) in methanol (3 mL). The mixture was refluxed for 6 h, during which time the yellow solution turned to a cloudy, colourless mixture. An excess of potassium nitrite (0.08 g, 3 mmol) in methanol (5 mL) was added and the mixture was stirred for a further 2 h. The solvent was removed under vacuum, producing a white residue that was taken up in dichloromethane and filtered to remove any inorganic salt impurities. The solvent was then removed under vacuum to yield a yellow solid.

$$C_{34}H_{33}P_3 \qquad\qquad [Pd(C_{34}H_{33}P_3)(NO_2)]NO_2$$

Counter ion exchange

$$[Pd(C_{34}H_{33}P_3)(NO_2)]NO_2 + NaBPh_4 \xrightarrow{\ Acetone/H_2O\ } [Pd(C_{34}H_{33}P_3)(NO_2)]BPh_4 + NaNO_2$$
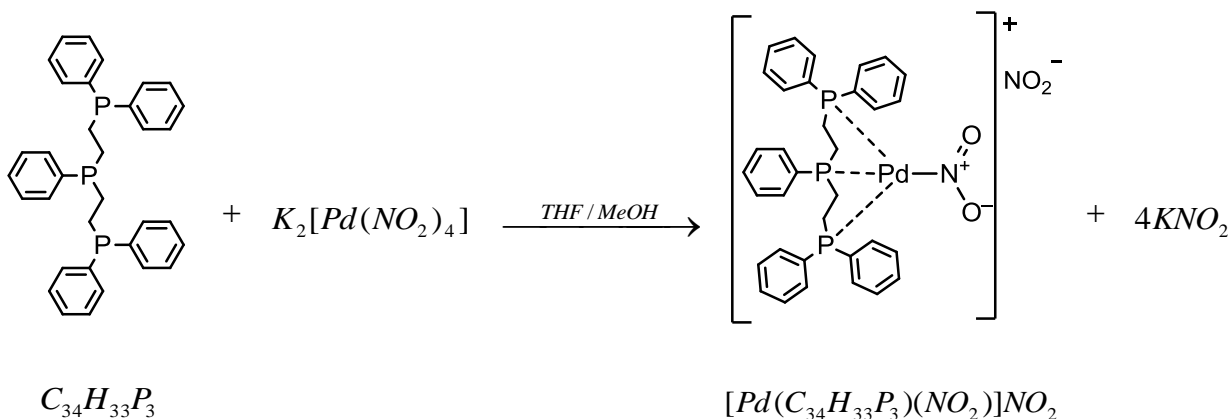
Scheme 9.14: Synthesis of Compound [10]

The yellow product was dissolved in the minimum volume of acetone. Sodium tetraphenylborate (0.10 g, 0.3 mmol) was dissolved in a distilled water : acetone mix (30 : 1) and added dropwise to the solution. The cream precipitate formed was collected by filtration and dried under vacuum.

FT-IR: ν(NO) = 1435, 1380, 1101, 703 cm^{-1}

NMR: **^{1}H** (300 MHz, CDCl$_3$)**:** δ_H 1.87 (8H, b, CH$_2$), δ_H 7.36 – 8.26 (25H, m, C$_6$H$_5$).

Broad spectrum due to coupling with different ^{31}P environments.

^{31}P (300 MHz, CDCl$_3$)**:** δ_P 46.64 (2P, d, ^{2}J$_{pp}$ = 9.90 Hz), δ_P 111.59 (1P, t, ^{2}J$_{pp}$ = 9.95 Hz)
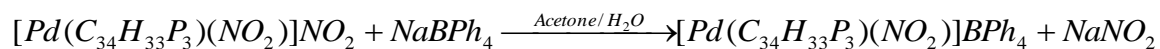
UV/vis: 328 nm

9.2.11. Preparation of Complex [11]: Nitro-(*bis*-(2-diphenylphosphinoethyl)-phenylphosphine)platinum(II) tetraphenylborate

All manipulations were carried out under a dry nitrogen atmosphere using Schlenk techniques. All solvents were dried and degassed using standard methods before use.

bis-(2-diphenylphosphinoethyl)phenylphosphine (1.6 g, 0.3 mmol) in tetrahydrofuran (3 mL) and slowly added to a solution of potassium tetranitroplatinate(II) (0.14 g, 0.3 mmol) in methanol (3 mL). The mixture was refluxed for 24 h, after which the initially homogeneous solution turned to a cloudy, colourless mixture. An excess of potassium nitrite (0.08 g, 3 mmol) in methanol (5 mL) was added to the mixture and stirred for a further 4 h. The solvent was removed under vacuum, producing a white residue that was taken up in dichloromethane and filtered to remove any inorganic salt impurities. The solvent was again removed under vacuum to yield a white solid.

$$C_{34}H_{33}P_3 \qquad\qquad [Pt(C_{34}H_{33}P_3)(NO_2)]NO_2$$

Counter ion exchange

$$[Pt(C_{34}H_{33}P_3)(NO_2)]NO_2 + NaBPh_4 \xrightarrow{Acetone/H_2O} [Pt(C_{34}H_{33}P_3)(NO_2)]BPh_4 + NaNO_2$$
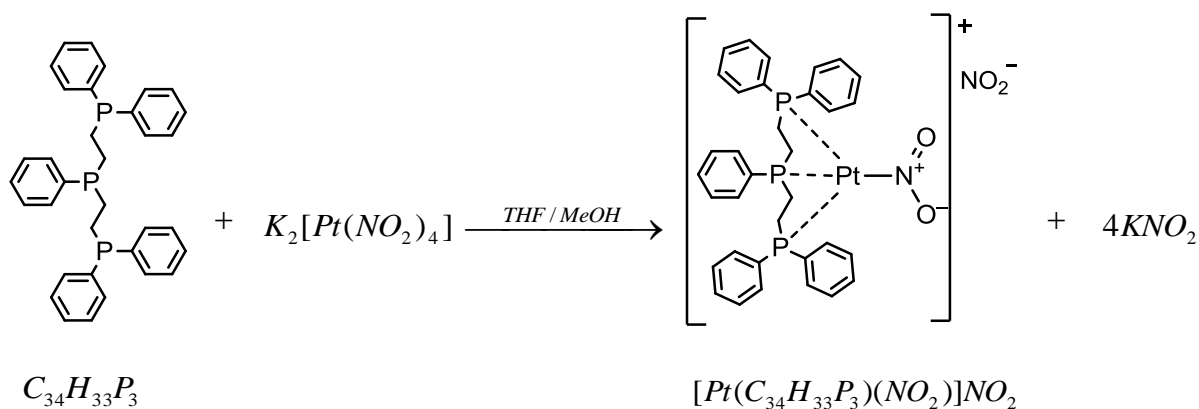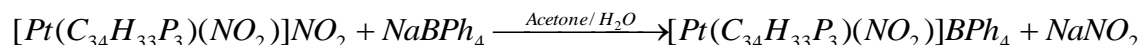
Scheme 9.15: Synthesis of Compound [11]

The product was dissolved in the minimum volume of acetone. Sodium tetraphenylborate (0.10 g, 0.3 mmol) was dissolved in a distilled water : acetone mix (30 : 1) and added dropwise to the solution. The white precipitate formed was collected by filtration and dried under vacuum.

FT-IR: v(NO) = 1436, 1394, 1260, 1102, 704 cm^{-1}

NMR: **^{1}H** (300 MHz, CDCl$_3$)**:** δ_H 1.61 (8H, b, CH$_2$), δ_H 7.36 – 8.40 (25H, m, C$_6$H$_5$).

Broad spectrum due to coupling with different ^{31}P environments.

^{31}P (300 MHz, CDCl$_3$)**:** δ_P 42.32 (2P, d, $^2J_{pp}$ = 2.22 Hz, $^1J_{PtP}$ = 2482 Hz), δ_P 86.17 (1P, t, $^2J_{pp}$ = 2.24 Hz, $^1J_{PtP}$ = 3021 Hz)

UV/vis: 321, 427 nm

9.3.   Spectroscopic Experimental Details

9.3.1.   FT-IR Spectroscopy

IR spectra were obtained on solid state samples using a Perkin Elmer[163] Spectrum 100 FT-IR Spectrometer and data were collected and processed using Perkin Elmer software Spectrum.

9.3.2.   Elemental Analysis

Elemental analyses were performed by Stephen Boyer at London Metropolitan University, using a Thermo Fisher Scientific[164] (formerly Carlo Erba) Flash 2000 Organic Elemental Analyser, operating at 900 ℃, with the oven at 70 ℃ and a helium gas flow of 140 mL min^{-1}.

9.3.3.   NMR Spectroscopy

Solution state ^{1}H and ^{31}P NMR spectra were collected at room temperature using a Bruker[165] UltraShield 300MHz spectrometer. All spectra were collected in deuterated chloroform (CDCl$_3$).

9.3.4.   UV/vis Spectroscopy

For complex [1], a solid state UV/vis spectroscopy was carried out with thanks to Beamline I24 at Diamond Light source, UK,[166] using a custom-made, *in-situ* microspectrophotometer with a 50 μm diameter probe beam. Spectra were collected using mirrored lenses (Bruker) mounted with a deuterium halogen light as the light source (Ocean Optics[167]). A single crystal was cut into a thin plate of dimensions 0.6 x 0.6 x 0.4 mm and an initial orientation chosen to yield the cleanest spectroscopic signal. Absorbance was monitored between 366 – 1100 nm using a Shamrock 303 imaging spectrograph (Andor[168]).

For complexes [2] to [11], solid-state UV/vis spectra were obtained on a powder sample, dispersed evenly between two glass slides. Data were collected using a Perkin Elmer Lambda 35 UV/vis spectrometer, equipped with an integrating sphere. Data collection and processing were conducted using Perkin Elmer software UV WinLab v.1.5.

References

1. M. D. Cohen and G. M. J. Schmidt, *Journal of the Chemical Society (Resumed)*, 1964, 1996-2000.
2. G. M. J. Schmidt, *Journal of the Chemical Society (Resumed)*, 1964, 2014-2021.
3. M. D. Cohen, G. M. J. Schmidt and F. I. Sonntag, *Journal of the Chemical Society (Resumed)*, 1964, 2000-2013.
4. P. Coppens, *Angewandte Chemie International Edition*, 2009, **48**, 4280-4281.
5. U. Hauser, V. Oestreich and H. D. Rohrweck, *Zeitschrift für Physik A Hadrons and Nuclei*, 1977, **280**, 17-25.
6. D. J. Thiel, P. Livins, E. A. Stern and A. Lewis, *Nature*, 1993, **362**, 40-43.
7. R. M. van der Veen, C. J. Milne, A. El Nahhas, F. A. Lima, V.-T. Pham, J. Best, J. A. Weinstein, C. N. Borca, R. Abela, C. Bressler and M. Chergui, *Angewandte Chemie*, 2009, **121**, 2749-2752.
8. D. Schaniel, M. Nicoul and T. Woike, *Physical Chemistry Chemical Physics*, 2010, **12**, 9029-9033.
9. D. Schaniel, N. Mockus, T. Woike, A. Klein, D. Sheptyakov, T. Todorova and B. Delley, *Physical Chemistry Chemical Physics*, 2010, **12**, 6171-6178.
10. S. Techert, F. Schotte and M. Wulff, *Physical Review Letters*, 2001, **86**, 2030.
11. P. Coppens, D. V. Fomitchev, M. D. Carducci and K. Culp, *Dalton Transactions*, 1998, 865-872.
12. A. E. Goeta and J. A. K. Howard, *Chemical Society Reviews*, 2004, **33**, 490-500.
13. W. Clegg, *Dalton Transactions*, 2000, 3223-3232.
14. H. N. Chapman, P. Fromme, A. Barty, T. A. White, R. A. Kirian, A. Aquila, M. S. Hunter, J. Schulz, D. P. DePonte, U. Weierstall, R. B. Doak, F. R. N. C. Maia, A. V. Martin, I. Schlichting, L. Lomb, N. Coppola, R. L. Shoeman, S. W. Epp, R. Hartmann, D. Rolles, A. Rudenko, L. Foucar, N. Kimmel, G. Weidenspointner, P. Holl, M. Liang, M. Barthelmess, C. Caleman, S. Boutet, M. J. Bogan, J. Krzywinski, C. Bostedt, S. Bajt, L. Gumprecht, B. Rudek, B. Erk, C. Schmidt, A. Homke, C. Reich, D. Pietschner, L. Struder, G. Hauser, H. Gorke, J. Ullrich, S. Herrmann, G. Schaller, F. Schopper, H. Soltau, K.-U. Kuhnel, M. Messerschmidt, J. D. Bozek, S. P. Hau-Riege, M. Frank, C. Y. Hampton, R. G. Sierra, D. Starodub, G. J. Williams, J. Hajdu, N. Timneanu, M. M. Seibert, J. Andreasson, A. Rocker, O. Jonsson, M. Svenda, S. Stern, K. Nass, R. Andritschke, C.-D. Schroter, F. Krasniqi, M. Bott, K. E. Schmidt, X. Wang, I. Grotjohann, J. M. Holton, T. R. M. Barends, R. Neutze, S. Marchesini, R. Fromme, S. Schorb, D. Rupp, M. Adolph, T. Gorkhover, I. Andersson, H. Hirsemann, G. Potdevin, H. Graafsma, B. Nilsson and J. C. H. Spence, *Nature*, 2011, **470**, 73-77.
15. A. J. Blake, W. Clegg and J. M. Cole, *Crystal Structure Analysis: Principles and Practice*, Oxford University Press, 2009.
16. R. Kamiński, T. Graber, J. B. Benedict, R. Henning, Y.-S. Chen, S. Scheins, M. Messerschmidt and P. Coppens, *Journal of Synchrotron Radiation*, 2010, **17**, 479-485.
17. Z. Ren, B. Perman, V. Srajer, T. Y. Teng, C. Pradervand, D. Bourgeois, F. Schotte, T. Ursby, O. R. Kort, M. Wulff and K. Moffat, *Biochemistry*, 2001, **40**, 13788-13801.
18. J. R. Dwyer, C. T. Hebeisen, R. Ernstorfer, M. Harb, V. B. Deyirmenjian, R. E. Jordan and R. J. D. Miller, *Philosophical Transactions of the Royal Society A: Mathematical, Physical and Engineering Sciences*, 2006, **364**, 741-778.
19. R. J. D. Miller, R. Ernstorfer, M. Harb, M. Gao, C. T. Hebeisen, H. Jean-Ruel, C. Lu, G. Moriena and G. Sciaini, *Acta Crystallographica Section A*, 2010, **66**, 137-156.
20. J. M. Cole, *Analyst*, 2011, **136**, 448-455.
21. D. Kim Christopher, S. Pillet, G. Wu, K. Fullagar Wilfred and P. Coppens, *Acta Crystallographica Section A*, 2002, **58**, 133-137.

22. A. Makal, E. Trzop, J. Sokolow, J. Kalinowski, J. Benedict and P. Coppens, *Acta Crystallographica Section A*, 2011, **67**, 319-326.
23. V. Enkelmann, G. Wegner, K. Novak and K. B. Wagener, *Journal of the American Chemical Society*, 1993, **115**, 10390-10391.
24. M. F. Mahon, P. R. Raithby and H. A. Sparkes, *CrystEngComm*, 2008, **10**, 573-576.
25. P. Gutlich, Y. Garcia and T. Woike, *Coordination Chemistry Reviews*, 2001, **219-221**, 839-879.
26. S. Decurtins, P. Gütlich, C. P. Köhler, H. Spiering and A. Hauser, *Chemical Physics Letters*, 1984, **105**, 1-4.
27. A. L. Thompson, V. A. Money, A. E. Goeta and J. A. K. Howard, *Comptes Rendus Chimie*, 2005, **8**, 1365-1373.
28. S. Pillet, V. Legrand, H.-P. Weber, M. Souhassou, J.-F. Létard, P. Guionneau and C. Lecomte, *Zeitschrift für Kristallographie*, 2008, **223**, 235-249.
29. M. A. Halcrow, *Coordination Chemistry Reviews*, 2009, **253**, 2493-2514.
30. E. Collet, N. Moisan, C. Balde, R. Bertoni, E. Trzop, C. Laulhe, M. Lorenc, M. Servol, H. Cailleau, A. Tissot, M.-L. Boillot, T. Graber, R. Henning, P. Coppens and M. B.-L. Cointe, *Physical Chemistry Chemical Physics*, 2012.
31. P. Coppens, O. Gerlits, I. I. Vorontsov, A. Y. Kovalevsky, Y.-S. Chen, T. Graber, M. Gembicky and I. V. Novozhilova, *Chemical Communications*, 2004, 2144-2145.
32. S. M. Jörgensen, *Zeitschrift für anorganische Chemie*, 1894, **5**, 147-196.
33. B. Adell, *Zeitschrift für anorganische Chemie*, 1944, **252**, 272-280.
34. M. D. Carducci, M. R. Pressprich and P. Coppens, *Journal of the American Chemical Society*, 1997, **119**, 2669-2678.
35. P. Coppens, I. Novozhilova and A. Kovalevsky, *Chemical reviews*, 2002, **102**, 861-884.
36. M. Warren, S. Brayshaw, A. Johnson, S. Schiffers, P. Raithby, T. Easun, M. George, J. Warren and S. Teat, *Angewandte Chemie*, 2009, **121**, 5821-5824.
37. I. Grenthe and E. Nordin, *Inorganic Chemistry*, 1979, **18**, 1109-1116.
38. I. Grenthe and E. Nordin, *Inorganic Chemistry*, 1979, **18**, 1869-1874.
39. D. V. Fomitchev, K. A. Bagley and P. Coppens, *Journal of the American Chemical Society*, 2000, **122**, 532-533.
40. K. F. Bowes, J. M. Cole, S. L. G. Husheer, P. R. Raithby, T. L. Savarese, H. A. Sparkes, S. J. Teat and J. E. Warren, *Chemical Communications*, 2006, 2448-2450.
41. J. J. Rack, J. R. Winkler and H. B. Gray, *Journal of the American Chemical Society*, 2001, **123**, 2432-2433.
42. P. C. Ford and I. M. Lorkovic, *Chemical Reviews*, 2002, **102**, 993-1018.
43. M. Rüdlinger, J. Schefer, G. Chevrier, N. Furer, H. U. Güdel, S. Haussühl, G. Heger, P. Schweiss, T. Vogt, T. Woike and H. Zöllner, *Zeitschrift für Physik B Condensed Matter*, 1991, **83**, 125-130.
44. H. Zöllner, T. Woike, W. Krasser and S. Haussühl, *Zeitschrift für Kristallographie*, 1989, **188**, 139-153.
45. H. U. Güdel, *Chemical Physics Letters*, 1990, **175**, 262-266.
46. Thomas, C. W. Bauschlicher and M. B. Hall, *The Journal of Physical Chemistry A*, 1997, **101**, 8530-8539.
47. P. Coppens, M. D. Carducci, K. Culp and D. Fomitchev, *Abstracts of Papers of the American Chemical Society*, 1997, **214**, 318-INOR.
48. O. Crichton and A. J. Rest, *Dalton Transactions*, 1977, 986-993.
49. L. X. Chen, M. K. Bowman, Z. Wang, P. A. Montano and J. R. Norris, *The Journal of Physical Chemistry*, 1994, **98**, 9457-9464.
50. D. V. Fomitchev, T. R. Furlani and P. Coppens, *Inorganic Chemistry*, 1998, **37**, 1519-1526.
51. P. S. Schaiquevich, J. A. Güida and P. J. Aymonino, *Inorganica Chimica Acta*, 2000, **303**, 277-281.

52.   B. Cormary, S. Ladeira, K. Jacob, P. G. Lacroix, T. Woike, D. Schaniel and I. Malfant, *Inorganic Chemistry*, 2012, **51**, 7492-7501.
53.   A. Y. Kovalevsky, G. King, K. A. Bagley and P. Coppens, *Chemistry - A European Journal*, 2005, **11**, 7254-7264.
54.   D. A. Johnson and V. C. Dew, *Inorganic Chemistry*, 1979, **18**, 3273-3274.
55.   A. Y. Kovalevsky, K. A. Bagley and P. Coppens, *Journal of the American Chemical Society*, 2002, **124**, 9241-9248.
56.   A. Y. Kovalevsky, K. A. Bagley, J. M. Cole and P. Coppens, *Inorganic Chemistry*, 2002, **42**, 140-147.
57.   S. O. Sylvester, J. M. Cole and P. G. Waddell, *Journal of the American Chemical Society*, 2012, **134**, 11860-11863.
58.   S. O. Sylvester and J. M. Cole, *Journal of Physical Chemistry Letters*, 2013, **4**, 3221-3226.
59.   A. E. Phillips, J. M. Cole, T. d'Almeida and K. S. Low, *Inorganic Chemistry*, 2012, **51**, 1204-1206.
60.   S. O. Sylvester and J. M. Cole, *Advanced Materials*, 2013, **25**, 3388.
61.   T. Chattopadhyay, M. Ghosh, A. Majee, M. Nethaji and D. Das, *Polyhedron*, 2005, **24**, 1677-1681.
62.   A. M. Heyns and D. de Waal, *Spectrochimica Acta Part A: Molecular Spectroscopy*, 1989, **45**, 905-909.
63.   W. M. Phillips, S. Choi and J. A. Larrabee, *Journal of Chemical Education*, 1990, **67**, 267.
64.   M. R. Warren, T. L. Easun, S. K. Brayshaw, R. J. Deeth, M. W. George, A. L. Johnson, S. Schiffers, S. J. Teat, A. J. Warren, J. E. Warren, C. C. Wilson, C. H. Woodall & P. R. Raithby, 2013. *Chemistry-A European Journal,* submitted.
65.   M. R. Warren, S. K. Brayshaw, L. E. Hatcher, A. L. Johnson, S. Schiffers, A. J. Warren, S. J. Teat, J. E. Warren, C. H. Woodall and P. R. Raithby, *Dalton Transactions*, 2012.
66.   S. E. Bajwa, T. E. Storr, L. E. Hatcher, T. J. Williams, C. G. Baumann, A. C. Whitwood, D. R. Allan, S. J. Teat, P. R. Raithby and I. J. S. Fairlamb, *Chemical Science*, 2012, **3**, 1656-1661.
67.   D. M. Goodgame and M. A. Hitchman, *Inorganic Chemistry*, 1964, **3**, 1389-&.
68.   D. M. Goodgame and M. A. Hitchman, *Inorganic Chemistry*, 1966, **5**, 1303-&.
69.   I. R. Laskar, D. Das, G. Mostafa, T. H. Lu, T. C. Keng, J. C. Wang, A. Ghosh and N. R. Chaudhuri, *New Journal of Chemistry*, 2001, **25**, 764-768.
70.   S. Sabbani and S. K. Das, *Inorganic Chemistry Communications*, 2009, **12**, 364-367.
71.   D. Schaniel and T. Woike, *Physical Chemistry Chemical Physics*, 2009, **11**, 4391-4395.
72.   G. Gallé, M. Nicoul, T. Woike, D. Schaniel and E. Freysz, *Chemical Physics Letters*, 2012, **552**, 64-68.
73.   S. L. Michael, C. Mark, E. V. K. Benjamin and K. Munira, *Journal of the American Chemical Society*, 2011, **133**, 5255-5262.
74.   E. M. H. Duke and L. N. Johnson, *Proceedings of the Royal Society A: Mathematical, Physical and Engineering Science*, 2010, **466**, 3421-3452.
75.   J. Drenth, in *Principles of Protein X-Ray Crystallography*, Springer New York, Editon edn., 2007, pp. 241-247.
76.   V. Šrajer, T.-y. Teng, T. Ursby, C. Pradervand, Z. Ren, S.-i. Adachi, W. Schildkamp, D. Bourgeois, M. Wulff and K. Moffat, *Science*, 1996, **274**, 1726-1729.
77.   S. Franzen, B. Bohn, C. Poyart and J. L. Martin, *Biochemistry*, 1995, **34**, 1224-1237.
78.   M. Lim, T. A. Jackson and P. A. Anfinrud, *The Journal of Chemical Physics.*, 1995, **102**, 4355-4366.
79.   V. Šrajer, Z. Ren, T.-Y. Teng, M. Schmidt, T. Ursby, D. Bourgeois, C. Pradervand, W. Schildkamp, M. Wulff and K. Moffat, *Biochemistry*, 2001, **40**, 13802-13815.
80.   S. F. Rice and H. B. Gray, *Journal of the American Chemical Society*, 1983, **105**, 4571-4575.

81. Y. Ozawa, M. R. Pressprich and P. Coppens, *Journal of Applied Crystallography*, 1998, **31**, 128-135.

82. I. Vorontsov, S. Pillet, R. Kaminski, M. Schmokel and P. Coppens, *Journal of Applied Crystallography*, 2010, **43**.

83. V. M. Miskowski, S. F. Rice, H. B. Gray, R. F. Dallinger, S. J. Milder, M. G. Hill, C. L. Exstrom and K. R. Mann, *Inorganic Chemistry*, 1994, **33**, 2799-2807.

84. I. I. Vorontsov and P. Coppens, *Journal of Synchrotron Radiation*, 2005, **12**, 488-493.

85. I. I. Vorontsov, T. Graber, A. Y. Kovalevsky, I. V. Novozhilova, M. Gembicky, Y.-S. Chen and P. Coppens, *Journal of the American Chemical Society*, 2009, **131**, 6566-6573.

86. P. Coppens, S.-L. Zheng, M. Gembicky, M. Messerschmidt and P. M. Dominiak, *CrystEngComm*, 2006, **8**, 735-741.

87. S. L. Zheng, M. Gembicky, M. Messerschmidt, P. M. Dominiak and P. Coppens, *Inorganic chemistry*, 2006, **45**, 9281-9289.

88. P. Coppens, *Journal of Physical Chemistry Letters*, 2011, **2**, 616-621.

89. J. T. Mague, *Inorganica Chimica Acta*, 1995, **229**, 17-25.

90. R. L. Owen, E. Rudiño-Piñera and E. F. Garman, *Proceedings of the National Academy of Sciences of the United States of America*, 2006, **103**, 4912-4917.

91. R. Neutze, R. Wouts, D. van der Spoel, E. Weckert and J. Hajdu, *Nature*, 2000, **406**, 752-757.

92. Linac Coherent Light Source, SLAC National Accelerator Laboratory, Stanford, USA. https://portal.slac.stanford.edu/sites/lcls_public/Pages/Default.aspx. Accessed 19/01/2014.

93. Linac Coherent Light Source, https://slacportal.slac.stanford.edu/sites/lcls_public/Pages/Default.aspx. Accessed 19/01/2014.

94. M. M. Seibert, T. Ekeberg, F. R. N. C. Maia, M. Svenda, J. Andreasson, O. Jonsson, D. Odic, B. Iwan, A. Rocker, D. Westphal, M. Hantke, D. P. DePonte, A. Barty, J. Schulz, L. Gumprecht, N. Coppola, A. Aquila, M. Liang, T. A. White, A. Martin, C. Caleman, S. Stern, C. Abergel, V. Seltzer, J.-M. Claverie, C. Bostedt, J. D. Bozek, S. Boutet, A. A. Miahnahri, M. Messerschmidt, J. Krzywinski, G. Williams, K. O. Hodgson, M. J. Bogan, C. Y. Hampton, R. G. Sierra, D. Starodub, I. Andersson, S. Bajt, M. Barthelmess, J. C. H. Spence, P. Fromme, U. Weierstall, R. Kirian, M. Hunter, R. B. Doak, S. Marchesini, S. P. Hau-Riege, M. Frank, R. L. Shoeman, L. Lomb, S. W. Epp, R. Hartmann, D. Rolles, A. Rudenko, C. Schmidt, L. Foucar, N. Kimmel, P. Holl, B. Rudek, B. Erk, A. Homke, C. Reich, D. Pietschner, G. Weidenspointner, L. Struder, G. Hauser, H. Gorke, J. Ullrich, I. Schlichting, S. Herrmann, G. Schaller, F. Schopper, H. Soltau, K.-U. Kuhnel, R. Andritschke, C.-D. Schroter, F. Krasniqi, M. Bott, S. Schorb, D. Rupp, M. Adolph, T. Gorkhover, H. Hirsemann, G. Potdevin, H. Graafsma, B. Nilsson, H. N. Chapman and J. Hajdu, *Nature*, 2011, **470**, 78-81.

95. J. N. Clark, L. Beitra, G. Xiong, A. Higginbotham, D. M. Fritz, H. T. Lemke, D. Zhu, M. Chollet, G. J. Williams, M. Messerschmidt, B. Abbey, R. J. Harder, A. M. Korsunsky, J. S. Wark and I. K. Robinson, *Science*, 2013, **341**, 56-59.

96. U. Weierstall, J. C. H. Spence and R. B. Doak, *Review of Scientific Instruments*, 2012, **83**, 035108.

97. I. Schlichting and J. Miao, *Current Opinion in Structural Biology*, 2012, **22**, 613-626.

98. Y. Ohashi, *Accounts of Chemical Research*, 1988, **21**, 268-274.

99. M. D. Cohen, *Angewandte Chemie International Edition*, 1975, **14**, 386-393.

100. Y. Ohashi, *Crystallography Reviews*, 2013, **19**, 2-146.

101. A. Natarajan and B. R. Bhogala, in *Supramolecular Photochemistry*, John Wiley & Sons, Inc., Editon edn., 2011, pp. 175-228.

102. D. P. Craig and C. P. Malett, *Chemical Physics*, 1982, **65**, 129-142.

103. D. Schaniel, M. Nicoul and T. Woike, *Physical Chemistry Chemical Physics*, 2010, **12**, 9029-9033.

104. P. Coppens, I. I. Vorontsov and T. Graber, *Acta Crystallographica: Section A*, 2005, **61**, 162-173.
105. W. C. RÖNTGEN, *Science*, 1896, **3**, 227-231.
106. W. Friedrich, P. Knipping and M. Laue, *Sitzungsberichte der Kaiserlichen Akademie der Wissenschaften,* 1912, 303-322.
107. W. H. Miller, *A Treatise on Crystallography*, Deighton, 1839.
108. W. H. Bragg and W. L. Bragg, *Proceedings of the Royal Society of London. Series A*, 1913, **88**, 428-438.
109. W. H. Bragg, *Proceedings of the Royal Society of London. Series A*, 1913, **89**, 246-248.
110. W. L. Bragg, *Proceedings of the Cambridge Philosophical Society*, 1913, **17**, 43-57.
111. W. Clegg, *Crystal Structure Determination*, Oxford University Press, 1998.
112. T. Hahn and I. U. o. Crystallography, *International Tables for Crystallography: Space-Group Symmetry*, D. Reidel Publishing Company, 1987.
113. D. Sayre, *Acta Crystallographica Section A*, 1952, **5**, 60-65.
114. L. Palatinus, *Acta Crystallographica Section A*, 2004, **60**, 604-610.
115. Agilent Technolgies. http://www.chem.agilent.com/. Accessed 19/01/2014.
116. CrysAlis Pro. Data Collection and data reduction GUI. Version 171.35.11.
117. The Advanced Light Source, Berkeley, CA, USA. http://www-als.lbl.gov/index.php/contact/129-1131.html. Accessed 19/01/2014.
118. Bruker AXS X-ray diffraction instruments. http://www.bruker.com/products/x-ray-diffraction-and-elemental-analysis/x-ray-diffraction.html. Accessed 19/01/2014.
119. Oxford Cryosystems. http://www.oxcryo.com/. Accessed 19/01/2014.
120. D. V. Fomitchev, T. R. Furlani and P. Coppens, *Inorganic chemistry*, 1998, **37**, 1519-1526.
121. S. K. Brayshaw, J. W. Knight, P. R. Raithby, T. L. Savarese, S. Schiffers, S. J. Teat, J. E. Warren and M. R. Warren, *Journal of Applied Crystallography*, 2010, **43**, 337-340.
122. Diamond Light Source, http://diamond.ac.uk/Home/.html. Accessed 19/01/2014.
123. M. Gembicky and P. Coppens, *Journal of Synchrotron Radiation*, 2007, **14**, 133-137.
124. I. R. Laskar, A. Ghosh, G. Mostafa, D. Das, A. Mondal and N. Ray Chaudhuri, *Polyhedron*, 2000, **19**, 1015-1020.
125. S. K. Brayshaw, T. L. Easun, M. W. George, A. M. E. Griffin, A. L. Johnson, P. R. Raithby, T. L. Savarese, S. Schiffers, J. E. Warren, M. R. Warren and S. J. Teat, *Dalton Transactions*, 2012, **41**, 90-97.
126. F. Allen, *Acta Crystallographica Section B*, 2002, **58**, 380-388.
127. C. F. Macrae, I. J. Bruno, J. A. Chisholm, P. R. Edgington, P. McCabe, E. Pidcock, L. Rodriguez-Monge, R. Taylor, J. van de Streek and P. A. Wood, *Journal of Applied Crystallography*, 2008, **41**, 466-470.
128. J. J. McKinnon, M. A. Spackman and A. S. Mitchell, *Acta Crystallographica Section B*, 2004, **60**, 627-668.
129. J. J. McKinnon, A. S. Mitchell and M. A. Spackman, *Chemistry – A European Journal*, 1998, **4**, 2136-2141.
130. I. Abdelmoty, V. Buchholz, L. Di, C. Guo, K. Kowitz, V. Enkelmann, G. Wegner and B. M. Foxman, *Crystal Growth & Design*, 2005, **5**, 2210-2217.
131. M. C. Etter, J. C. MacDonald and J. Bernstein, *Acta Crystallographica Section B*, 1990, **46**, 256-262.
132. G. A. Jeffrey, *An Introduction to Hydrogen Bonding*, Oxford University Press, 1997.
133. P. Atkins, P. W. Atkins and D. F. Shriver, *Shriver & Atkins Inorganic chemistry*, W.H. Freeman, 2006.
134. R. G. Pearson, *Journal of Chemical Education*, 1968, **45**, 581.
135. R. G. Pearson, *Journal of Chemical Education*, 1968, **45**, 643.
136. R. Wen, I. Bernal, F. Somoza, W. Li and F. R. Fronczek, *Inorganica Chimica Acta*, 1998, **282**, 96-109.

137. G. M. Sheldrick, *Acta Crystallographica Section A*, 2008, **64**, 112-122.
138. M. A. Spackman and J. J. McKinnon, *CrystEngComm*, 2002, **4**, 378-392.
139. R. Wen, I. Bernal, S. S. Massoud, R. K. Thalji, D. R. Billodeaux and F. R. Fronczek, *Inorganica Chimica Acta*, 1999, **295**, 91-105.
140. M. R. Warren*, Thesis for Doctor of Philosophy,* University of Bath, 2011.
141. J. B. Benedict and P. Coppens, *The Journal of Physical Chemistry A*, 2009, **113**, 3116-3120.
142. W. M. Phillips, S. Choi and J. A. Larrabee, *Journal of Chemical Education*, 1990, **67**, 267-269.
143. V. E. Dulepov and E. V. Boldyreva, *Reaction Kinetics and Catalysis Letters*, 1994, **53**, 289-296.
144. D. Schaniel, T. Woike, C. Merschjann and M. Imlau, *Physical Review B*, 2005, **72**, 195119.
145. N. Feeder and K. Honda, *Molecular Crystals and Liquid Crystals Science and Technology. Section A.*, 1998, **313**, 327 - 334.
146. K. Honda, F. Nakanishi and N. Feeder, *Journal of the American Chemical Society.*, 1999, **121**, 8246-8250.
147. M. Bertmer, R. C. Nieuwendaal, A. B. Barnes and S. E. Hayes, *The Journal of Physical Chemistry B*, 2006, **110**, 6270-6273.
148. D.-K. Cao, T. V. Sreevidya, M. Botoshansky, G. Golden, J. Brown Benedict and M. Kaftory, *The Journal of Physical Chemistry A*, 2010, **114**, 7377-7381.
149. R. More, G. Busse, J. Hallmann, C. Paulmann, M. Scholz and S. Techert, *The Journal of Physical Chemistry C*, 2010, **114**, 4142-4148.
150. M. Avrami, *The Journal of Chemical Physics*, 1939, **7**, 1103-1112.
151. M. Avrami, *The Journal of Chemical Physics*, 1940, **8**, 212-224.
152. M. Avrami, *The Journal of Chemical Physics*, 1941, **9**, 177-184.
153. LOGLOG version 20120413. M. Lutz and M. M. Schreurs, Utrecht University.
154. ANAFCF version 20120413. M. Lutz and M. M. Schreurs, Utrecht University.
155. D. Schaniel, J. Schefer, B. Delley, M. Imlau and T. Woike, *Physical Review B*, 2002, **66**, 085103.
156. Diamond Light Source Beamline I19: Small Molecule Single-Crystal Diffraction. http://diamond.ac.uk/Home/Beamlines/I19.html. Accessed 19/01/2014.
157. M. F. Dumont, O. N. Risset, E. S. Knowles, T. Yamamoto, D. M. Pajerowski, M. W. Meisel and D. R. Talham, *Inorganic Chemistry*, 2013, **52**, 4494-4501.
158. R. K. M. S. Schmøkel, J. B. Benedict and P. Coppens, *Acta Crystallographica Section A*, 2010, **66**, 632-636.
159. A. Makal, J. Benedict, E. Trzop, J. Sokolow, B. Fournier, Y. Chen, J. A. Kalinowski, T. Graber, R. Henning and P. Coppens, *The Journal of Physical Chemistry A*, 2012, **116**, 3359-3365.
160. C. Carbonera, C. J. Sanchez, V. A. Money, J. Elhaik, J. A. K. Howard, M. A. Halcrow and J.-F. Letard, *Dalton Transactions*, 2006, 3058-3066.
161. R. W. Green and B. Bell, *Australian Journal of Chemistry*, 1973, **26**, 1663-1668.
162. R. D. Feltham, G. Elbaze, R. Ortega, C. Eck and J. Dubrawski, *Inorganic Chemistry*, 1985, **24**, 1503-1510.
163. Perkin Elmer. http://www.perkinelmer.co.uk/default.xhtml. Accessed 19/01/2014.
164. ThermoScientific. http://www.thermoscientific.com/. Accessed 19/01/2014
165. Bruker Instruments. http://www.bruker.com/. Accessed 19/01/2014.
166. Beamline I24. http://diamond.ac.uk/mx-home/I24.html. Accessed 1401/2014.
167. Ocean Optics. http://www.oceanoptics.com/. Accessed 19/01/2014.
168. Andor Technology. http://www.andor.com/. Accessed 19/01/2014.

Appendicies

Appendix 1: Complex [1]

Hydrogen Bonding Tables

(i) GS nitro-(η^1-NO$_2$) isomer

Table 3: Hydrogen bonding data for the GS structure of [1]

	d(D-H) / Å	d(H...A) / Å	d(D...A) / Å	<(DHA) / °
N(4)-H(4)...O(2)	0.88(2)	2.45(2)	2.30(1)	121(1)
N(4)-H(4)...O(4) #1	0.88(2)	2.28(2)	3.04(1)	145(2)

Symmetry operations for equivalent atoms: **#1** x+1/2,-y+3/2,-z+2

(ii) 500 nm MS nitrito-(η^1-ONO) isomer

Table 4: Hydrogen bonding table for thhe 500 nm MS structure of [1]

	d(D-H) / Å	d(H...A) / Å	d(D...A) / Å	<(DHA) / °
N(4)-H(4)...O(2A)	0.82(3)	2.28(3)	2.97(1)	142(3)
N(4)-H(4)...O(4) #1	0.82(3)	2.46(3)	3.08(1)	134(2)

Symmetry operations for equivalent atoms: **#1** x+1/2,-y+3/2,-z+2
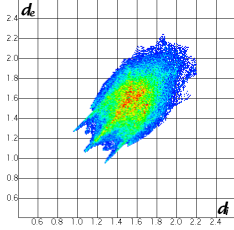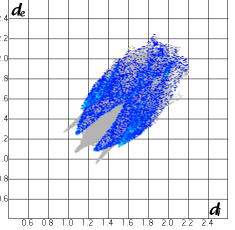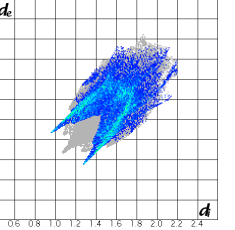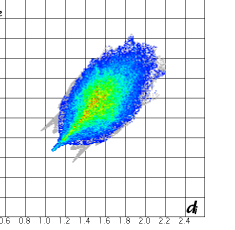
Complete nitro : nitro ratios: thermal studies
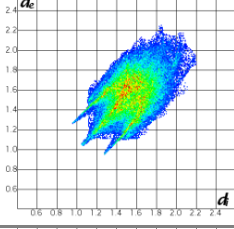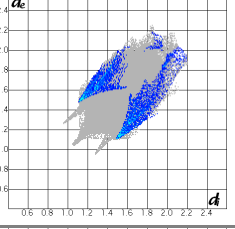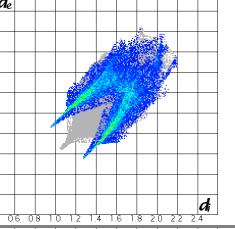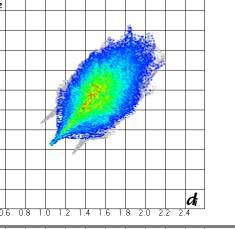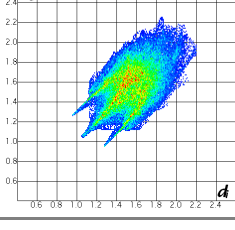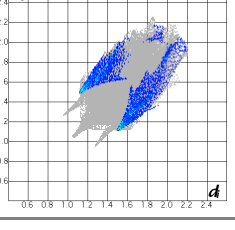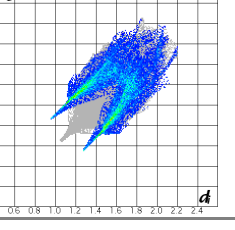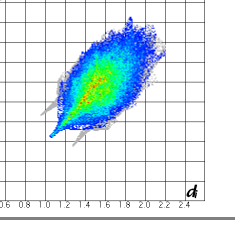
Table 5: Nitro : nitrito occupancies for repeat datasets between 298 and 100 K, in thermal studies with [1]

Temp / K	Nitro-(η^1-NO$_2$) Occupancy			Nitrito-(η^1-ONO) Occupancy		
	Repeat 1	Repeat 2	Repeat 3	Repeat 1	Repeat 2	Repeat 3
100	1.00*	1.00*	1.00*	0.00*	0.00*	0.00*
150	1.00*	1.00*	1.00*	0.00*	0.00*	0.00*
175	0.97(1)	0.98(1)	0.97(1)	0.03(1)	0.02(1)	0.03(1)
200	0.95(1)	0.94(1)	0.95(1)	0.05(1)	0.06(1)	0.05(1)
225	0.94(1)	0.93(1)	0.93(1)	0.06(1)	0.07(1)	0.07(1)
250	0.90(1)	0.90(1)	0.90(1)	0.10(1)	0.10(1)	0.10(1)
275	0.84(1)	0.84(1)	0.85(1)	0.16(1)	0.16(1)	0.15(1)
298	0.82(1)	0.82(1)	0.82(1)	0.18(1)	0.18(1)	0.18(1)

* No esd is reported for full occupancy or zero occupancy as these ratios were not refined

Intermolecular interaction analysis: thermal studies

Table 6: Full Crystal Explorer fingerprint plots for structures obtained during thermal studies with complex [1]

Temp	Experiment	All Contacts	N...H contacts	O…H contacts	H…H contacts
100	Flash cool				
100	Slow cool				
150	VT cool				

175	VT cool				
200	VT cool				
225	VT cool				
250	VT cool				

227

275	VT cool				
298	VT				
350	VT heat				
370	VT heat				

228
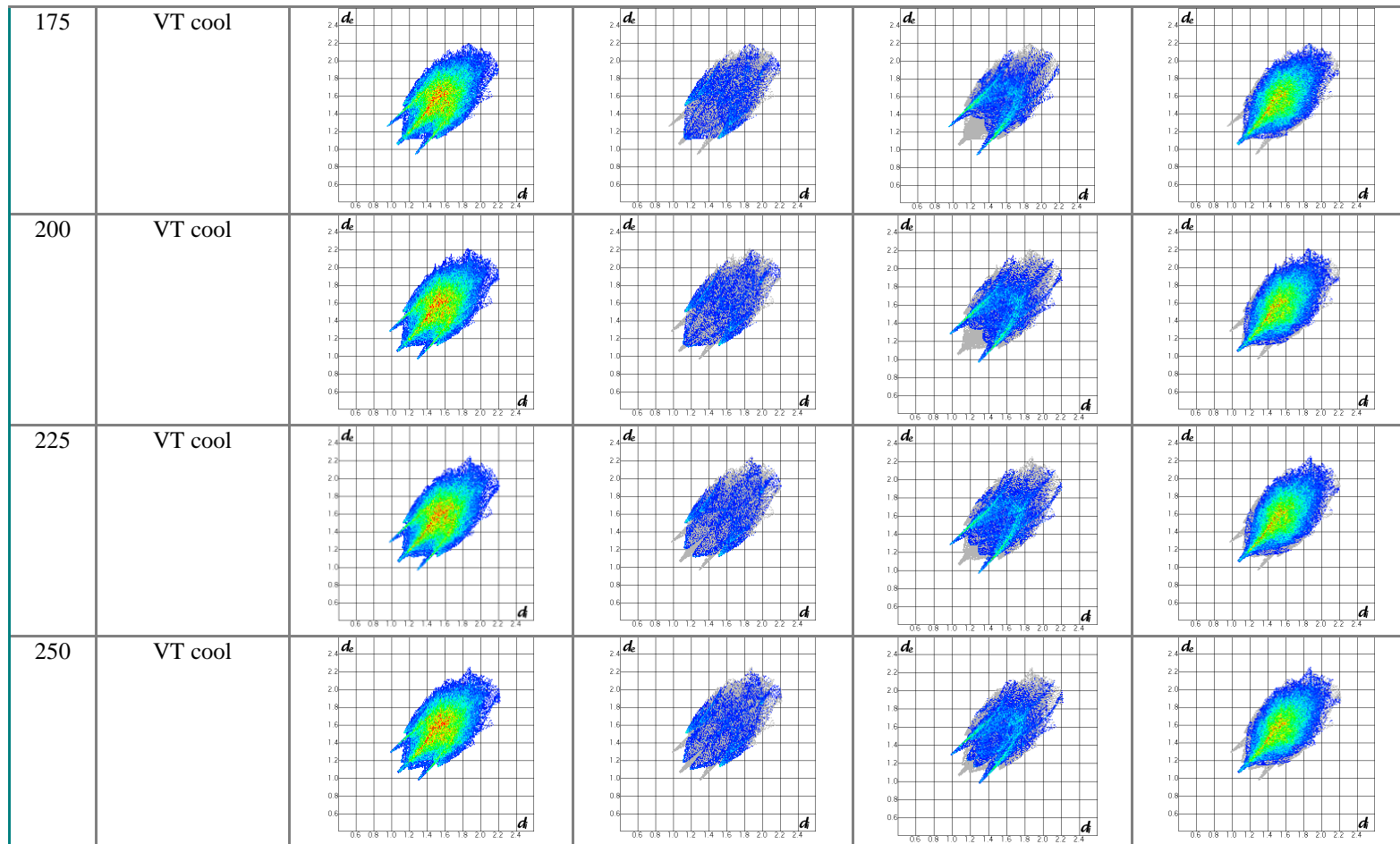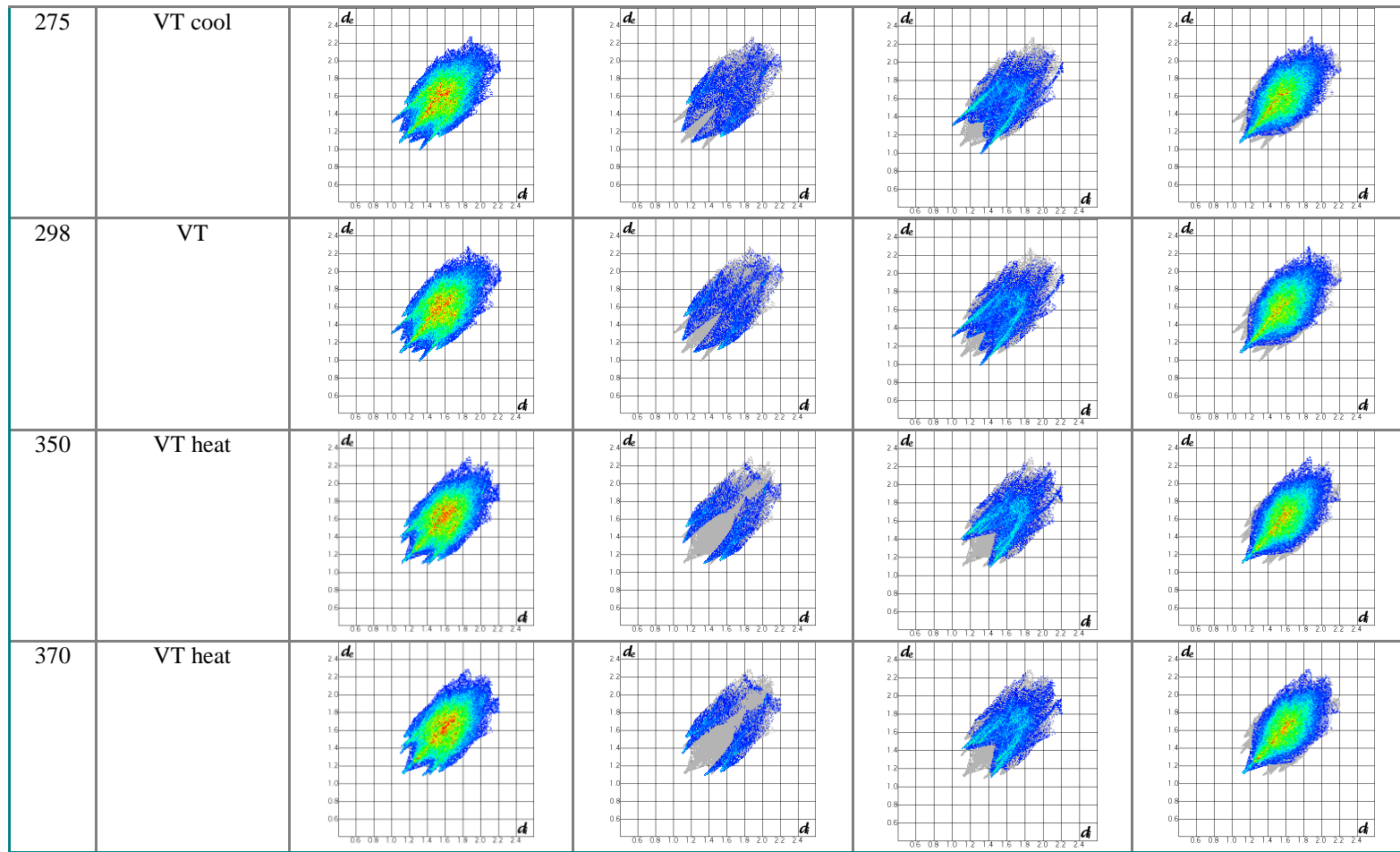
Appendix 2: Complex [2]

Hydrogen Bonding Tables

(i) GS nitro-(η^1-NO$_2$) isomer

Table 7: Hydrogen bonding data for the GS structure of [2]

	(D-H)/ Å	(H...A) / Å	(D...A) / Å	<(DHA) / °
N(3)-H(3)...O(50)	0.88(3)	2.00(3)	2.87(1)	173(3)
O(50)-H(50B)...O(2) #1	0.75(3)	2.15(4)	2.90(1)	171(4)
O(50)-H(50A)...O(1) #2	0.89(5)	2.01(5)	2.88(1)	165(4)

Symmetry operations for equivalent atoms: **#1** = (x, y-1, z)   **#2** = (-x+1/2, y-1/2, -z+3/2)

(ii) 400 nm MS structure

Table 8: Hydrogen bonding data for the MS structure of [2]

	(D-H)/ Å	(H...A) / Å	(D...A) / Å	<(DHA) / °
N(3)-H(3)…O(50)	1.07(6)	1085(6)	2.90(1)	166(4)
O(50)-H(50B)...O(2) #1	– *	– *	2.99(2)	– *
O(50)-H(50A)...O(1) #2	– *	– *	2.79(2)	– *
O(50)-H(50B)...O(2A) #1	– *	– *	2.94(1)	– *
O(50)-H(50A)...O(2B) #2	– *	– *	2.50(2)	– *

Symmetry operations for equivalent atoms: **#1** = (x, y-1, z)   **#2** = (-x+1/2, y-1/2, -z+3/2)

* No D…A distances or DHA angles, involving donor hydrogens were from the solvent water, could be reported for the MS as these hydrogen atoms could not be located due to a reduction in data quality.

Solid State UV/vis Spectrum

Figure 2: Solid state UV/vis spectrum for complex [2], showing the choice of excitation wavelength

Appendix 3: Complex [3]

Hydrogen Bonding Tables

(i) GS nitro-(η^1-NO$_2$) isomer

Table 9: Hydrogen bonding data for the GS structure of [3]

	(D-H)/ Å	(H...A) / Å	(D...A) / Å	<(DHA) / °
N(3)-H(3)...O(50)	0.74(3)	2.13(4)	2.88(1)	178(4)
O(50)-H(50B)...O(2) #1	1.00(1)	1.91(1)	2.90(1)	167(4)
O(50)-H(50A)...O(1) #2	1.00(1)	1.88(1)	2.88(1)	172(4)

Symmetry operations for equivalent atoms: **#1** = (x, y-1, z)   **#2** = (-x+1/2, y-1/2, -z+3/2)

(ii) 365 nm MS structure

Table 10: Hydrogen bonding data for the MS structure of [3]

	(D-H)/ Å	(H...A) / Å	(D...A) / Å	<(DHA) / °
N(3)-H(3)…O(50)	0.93(2)	1.98(2)	2.91(1)	174(2)
O(50)-H(50B)...O(2) #1	– *	– *	2.94(3)	– *
O(50)-H(50A)...O(1) #2	– *	– *	2.76(2)	– *
O(50)-H(50B)…N(1A) #1	– *	– *	3.13(2)	– *
O(50)-H(50A)…O(1A) #2	– *	– *	3.27(2)	– *
O(50)-H(50B)...O(2A) #1	– *	– *	3.04(3)	– *

Symmetry operations for equivalent atoms: **#1** = (x, y-1, z)   **#2** = (-x+1/2, y-1/2, -z+3/2)

* No D…A distances or DHA angles, involving donor hydrogens were from the solvent water, could be reported for the MS as these hydrogen atoms could not be located due to a reduction in data quality.
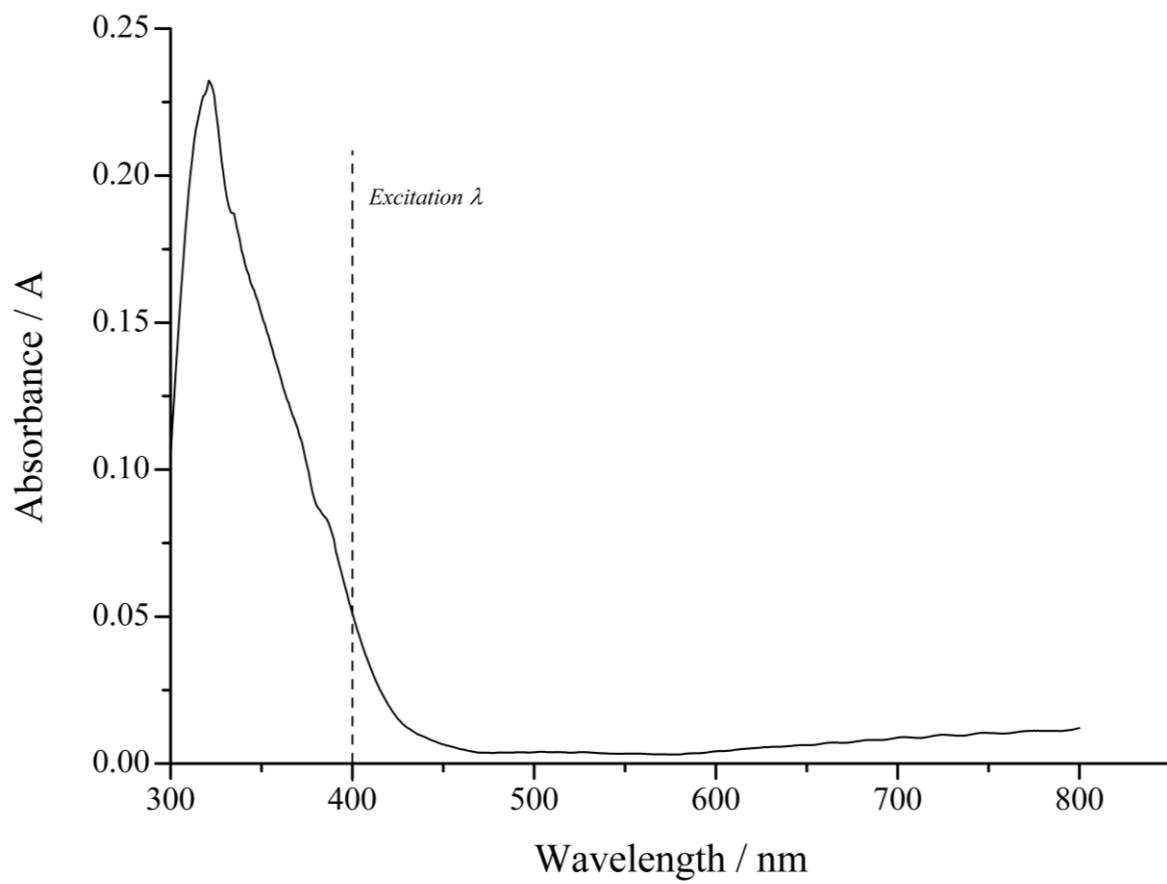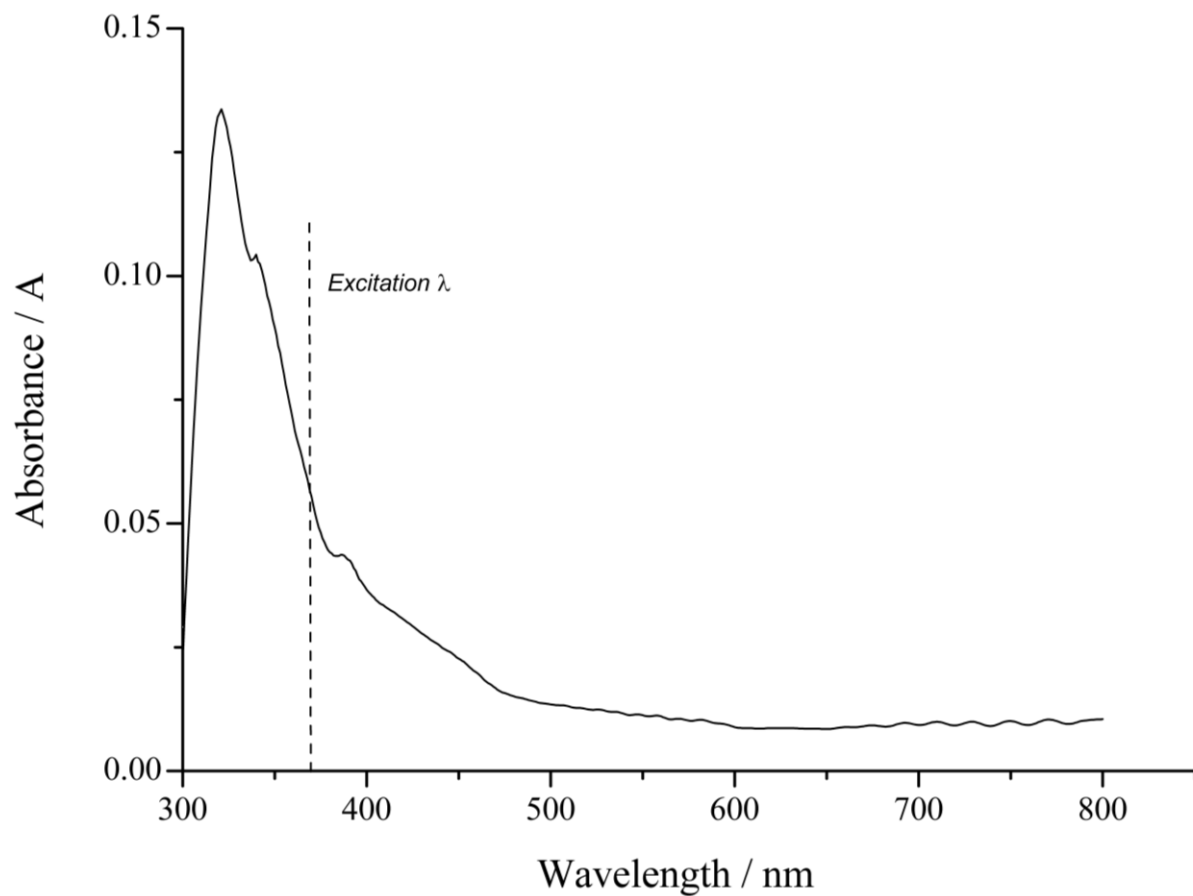
Solid State UV/vis Spectrum

Figure 3: Solid state UV/vis spectrum for complex [3], showing the choice of excitation wavelength
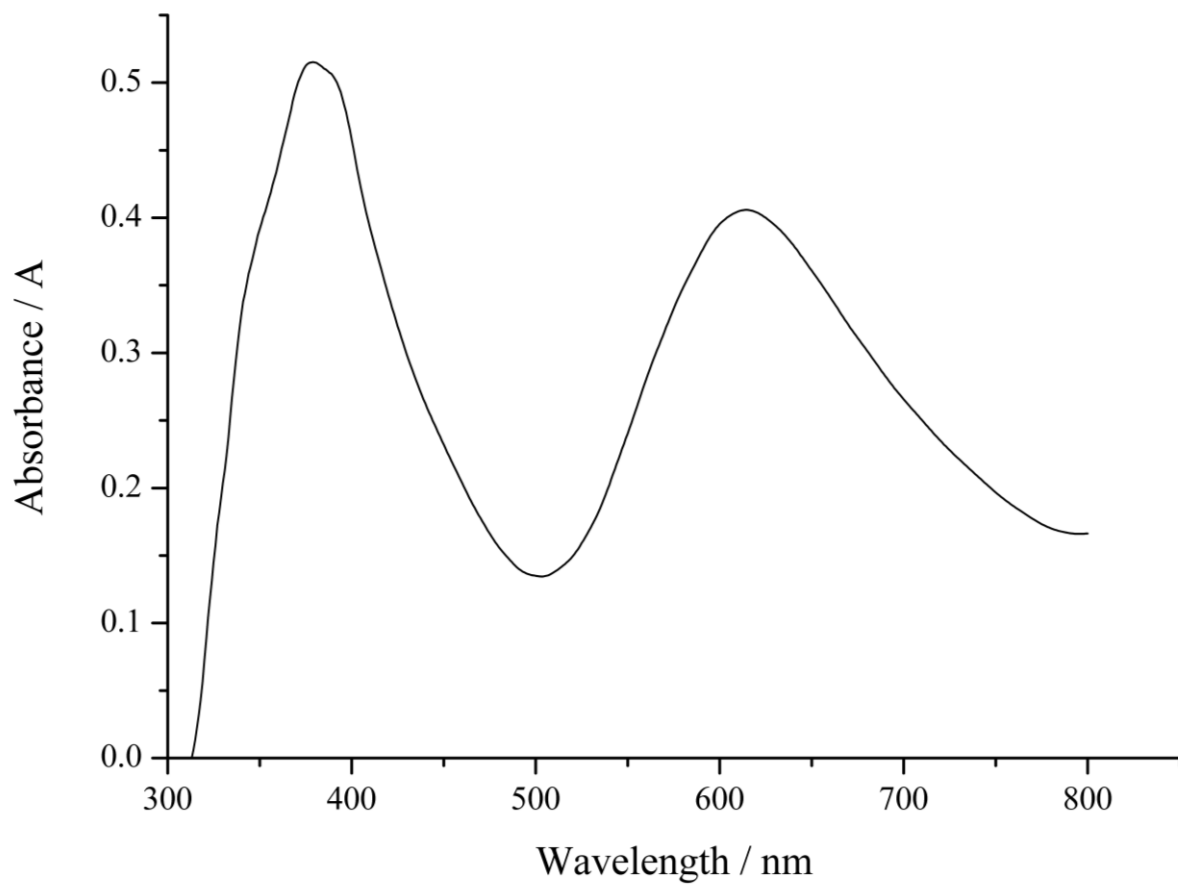
Solid State UV/vis Spectrum

Figure 4: Solid state UV/vis spectrum for complex [4]

Appendix 5: Complex [5]

Hydrogen Bonding Tables

(i) GS nitro-(η^1-NO$_2$) isomer

Table 11: Hydrogen bonding data for the GS structure of [5]

	(D-H) / Å	(H...A) / Å	(D...A) / Å	<(DHA) / °
N(4)-H(4C)...O(3) #1	0.89(3)	2.32(3)	3.09(1)	143(2)
N(3)-H(3C)...O(1)	0.88(3)	2.29(3)	2.94(1)	130(2)
N(5)-H(5B)...O(2)	0.92(3)	2.32(3)	2.99(1)	130(2)
N(5)-H(5C)...O(1) #2	0.86(3)	2.15(3)	2.96(1)	156(3)
N(5)-H(5B)...O(2) #3	0.92(3)	2.64(3)	3.31(1)	130(2)

Symmetry operations for equivalent atoms: **#1** (x, -y+1/2, z+1/2), **#2** (x, y+1, z), **#3** (-x+1, -y, -z+2)

(ii) 400 nm MS structure

Table 2: Hydrogen bonding data for the MS structure of [5]

	(D-H) / Å	(H...A) / Å	(D...A) / Å	<(DHA) / °
N(4)-H(4C)...O(3) #1	0.84(4)	2.33(4)	3.09(1)	150(4)
N(3)-H(3C)...O(1)	0.81(4)	2.45(4)	3.01(1)	127(4)
N(5)-H(5B)...O(2)	0.90(5)	2.18(5)	2.82(1)	128(4)
N(5)-H(5B)...O(2A)	0.90(5)	2.46(5)	3.052(9)	124(4)
N(5)-H(5C)...O(1) #2	0.73(4)	2.14(4)	2.83(1)	158(4)
N(5)-H(5B)...O(2) #3	0.90(5)	2.57(5)	3.32(1)	141(3)
N(5)-H(5B)…N(1A) #3	0.90(5)	2.56(5)	3.27(1)	137(4)

Symmetry operations for equivalent atoms: **#1** (x, -y+1/2, z+1/2), **#2** (x, y+1, z), **#3** (-x+1, -y, -z+2)
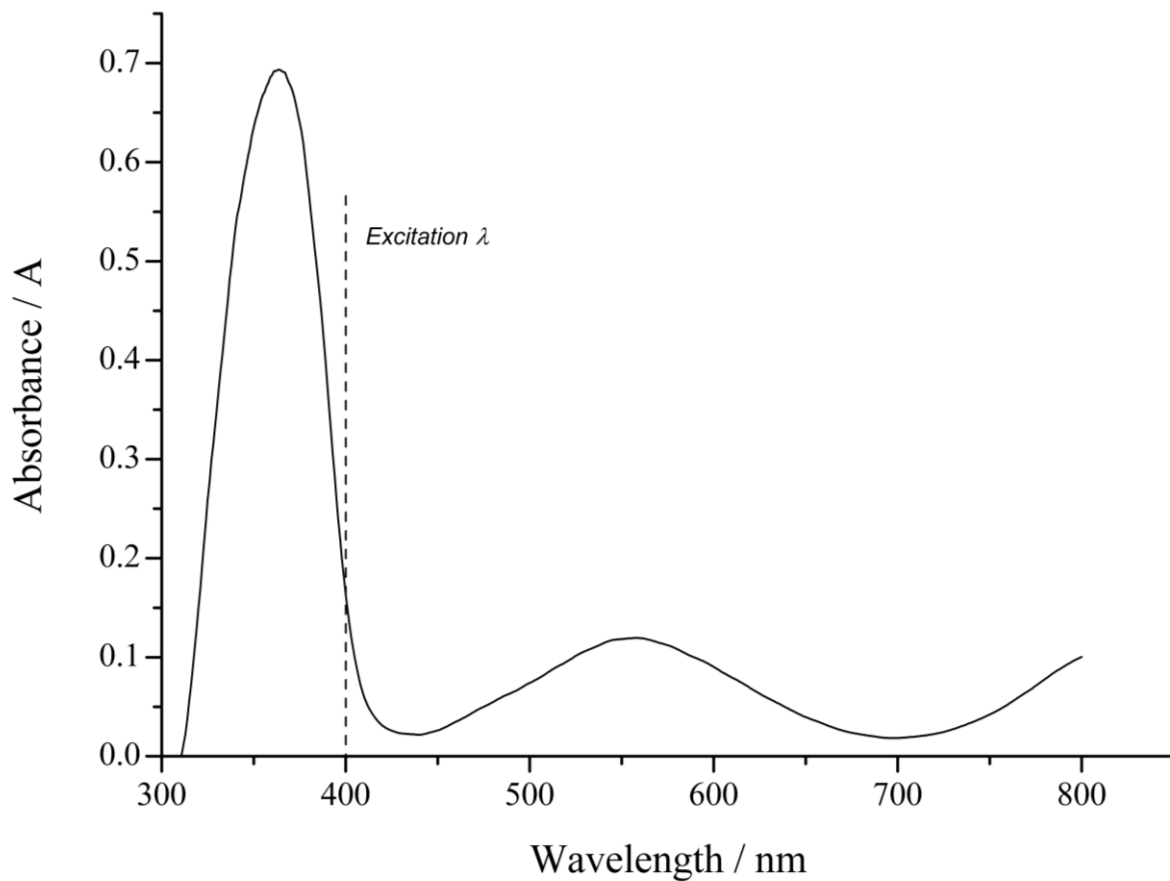
Solid State UV/vis Spectrum

Figure 5: Solid state UV/vis spectrum for complex [5], showing the choice of excitation wavelength

Appendix 6: Complex [6]

Hydrogen Bonding Tables

Table 12: Hydrogen bonding data for the flash cooled structure of [6]

	(D-H) / Å	(H...A) / Å	(D...A) / Å	<(DHA) / °
N(3)-H(3D)...N(1) #1	0.87(2)	2.44(3)	3.279(3)	164(2)
N(5)-H(5D)...O(1) #2	0.76(3)	2.32(3)	3.069(3)	173(3)
N(3)-H(3C)...O(4) #3	0.81(3)	2.32(3)	3.101(2)	163(3)
N(5)-H(5E)...O(4) #4	0.87(2)	2.64(3)	3.261(2)	128.8(19)
N(3)-H(3D)...O(3) #5	0.87(2)	2.70(3)	3.236(2)	120.8(19)

Symmetry operations for equivalent atoms: **#1** = (-x, -y, -z), **#2** = (-x, -y+1, -z), **#3** = (-x+1, -y, -z), **#4** = (x-1, y, z), **#5** = (x, y-1, z)
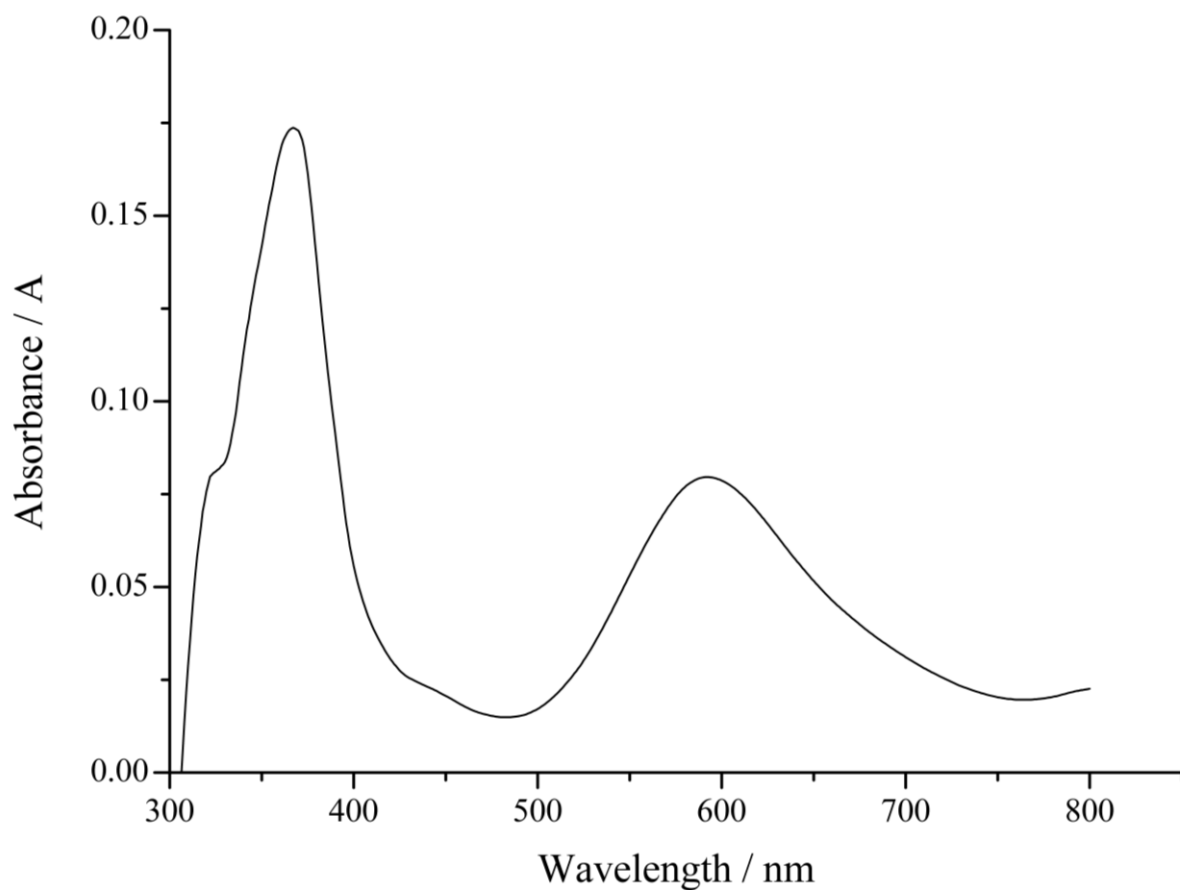
Solid State UV/vis Spectrum

Figure 6: Solid state UV/vis spectrum for complex [6]

Appendix 7: Complex [7]

Hydrogen Bonding Tables

(i) GS nitro-(η^1-NO$_2$) isomer

Table 13: Intermolecular hydrogen bonding data for the slow cooled GS structure of [7] at 100 K

	(D-H) / Å	(H...A) / Å	(D...A) / Å	<(DHA) / °
N(5)-H(5D)...O(11) #1	0.92(2)	2.19(2)	3.06(1)	157(3)
N(5)-H(5C)...O(3) #2	0.92(2)	2.19(2)	3.01(1)	148(3)

Symmetry operations for equivalent atoms: **#1** = x,-y+1/2,z ; **#2** = -x,-y,-z+2

(ii) MS structure

Table 14: Intermolecular hydrogen bonding data for the MS structure of [7] at 100 K

	(D-H) / Å	(H...A) / Å	(D...A) / Å	<(DHA) / °
N(23)-H(23D)…O(2A) #1	0.92(2)	2.56(2)	3.19(1)	126(3)
N(5)-H(5C)...O(22A) #2	0.92(2)	2.65(2)	3.29(1)	127(3)
N(23)-H(23C)...O(11)	0.92(2)	2.28(2)	3.15(1)	159(3)
N(5)-H(5D)...O(12)	0.92(2)	2.13(2)	3.00(1)	157(3)
N(23)-H(23C)...O(12A)	0.92(2)	2.08(2)	2.96(1)	159(3)
N(23)-H(23D)...O(4) #1	0.92(2)	2.22(2)	3.05(1)	150(3)
N(5)-H(5C)...O(23) #2	0.92(2)	2.17(2)	3.01(1)	151(3)

Symmetry operations for equivalent atoms: **#1** = -x, y+1/2, -z; **#2** = -x, y-1/2, -z
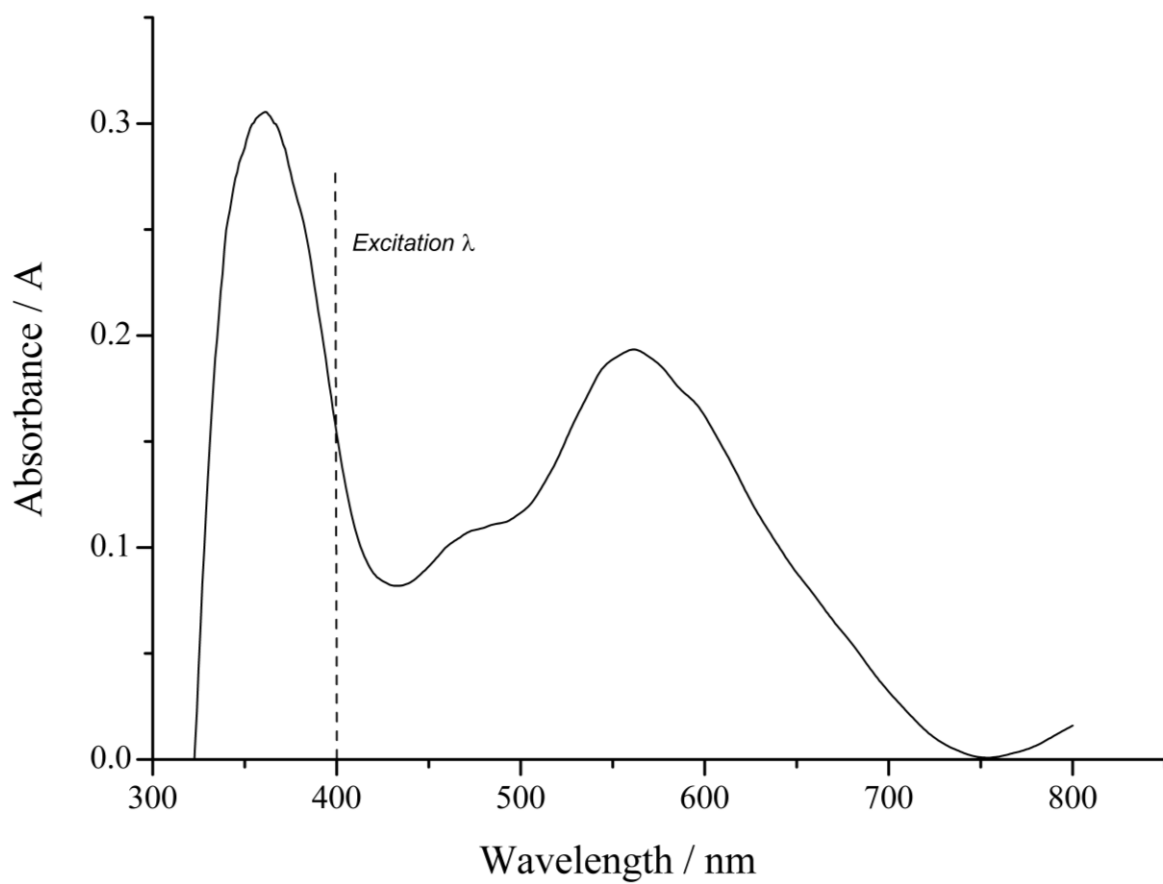
Solid State UV/vis Spectrum

Figure 7: Solid state UV/vis spectrum for complex [7], showing the choice of excitation wavelength

Appendix 8: Complex [8]

Hydrogen Bonding Tables

(i) Complex [8a]

Table 15: Hydrogen bonding data for the flash cooled structure of [8a] at 100 K

	(D-H) / Å	(H...A) / Å	(D...A) / Å	<(DHA) / °
N(2)-H(2C)…O(3) **$1**	0.85(2)	2.60(2)	3.31(1)	141(2)
N(4)-H(4C)...O(1) **$2**	0.87(3)	2.39(3)	3.12(1)	142(2)
N(2)-H(2D)...O(1) **$2**	0.90(3)	2.54(3)	3.29(1)	142(2)
N(4)-H(4C)...O(2) **$2**	0.87(3)	2.70(3)	3.55(1)	164(2)

Symmetry operations for equivalent atoms: **#1** (-x, -y+1, -z+2), **#2** (-x, -y, -z+2)

(ii) Complex [8b]: GS nitro-(η^1-NO$_2$) isomer

Table 16: Hydrogen bonding data for the GS structure of [8a] at 100 K

	(D-H) / Å	(H...A) / Å	(D...A) / Å	<(DHA) / °
O(5)-H(5D)...O(1) **#1**	0.80(2)	2.01(2)	2.80(1)	176(3)
N(3)-H(3D)...O(1) **#2**	0.94(3)	2.32(3)	3.19(1)	154(3)
N(3)-H(3C)...O(2) **#3**	0.83(4)	2.26(4)	3.09(1)	175(4)
N(4)-H(4C)...O(2) **#4**	0.87(4)	2.61(4)	3.33(1)	141(3)
O(5)-H(5D)...Cl(1) **#1**	0.80(2)	2.71(2)	3.50(1)	169(3)
N(3)-H(3D)...Cl(1) **#2**	0.94(3)	2.66(3)	3.45(1)	141(3)
N(3)-H(3C)...Cl(1) **#3**	0.83(4)	2.77(4)	3.53(1)	151(3)
O(5)-H(5C)...O(3)	0.79(2)	2.10(2)	2.87(1)	162(4)
N(4)-H(4D)...O(5)	0.92(3)	2.49(3)	3.36(1)	159(3)
N(4)-H(4C)...O(4) **#5**	0.87(4)	2.61(4)	3.32(1)	139(3)

Symmetry operations for equivalent atoms:
#1 (x+1, y-1, z); **#2** (-x, -y+2, -z); **#3** (x+1, y, z); **#4** (-x,-y+1,-z); **#5** (x-1, y, z)

(iii) Complex [8b]: MS structure

Table 17: Hydrogen bonding data for the MS structure of [8a] at 100 K

	(D-H) / Å	(H...A) / Å	(D...A) / Å	<(DHA) / °
O(5)-H(5D)...O(1) **#1**	0.79(2)	1.85(2)	2.63(1)	169(3)
O(5)-H(5D)...O(1A) **#1**	0.79(2)	2.46(2)	3.24(1)	167(3)
N(3)-H(3D)...O(1) **#2**	0.91(2)	2.37(2)	3.19(1)	152(2)
N(3)-H(3D)...N(1A) **#2**	0.91(2)	2.60(2)	3.25(1)	129(2)
N(3)-H(3C)...O(2) **#3**	0.84(2)	2.30(3)	3.13(1)	175(2)
N(3)-H(3C)...O(2A) **#3**	0.84(2)	2.23(3)	3.06(1)	174(2)
N(3)-H(3C)...N(1A) **#3**	0.84(2)	2.25(2)	2.99(1)	148(2)
N(4)-H(4C)...O(2) **#4**	0.90(2)	2.57(2)	3.28(1)	137(2)
N(4)-H(4C)...O(2) **#4**	0.90(2)	2.51(2)	3.20(1)	134(2)
O(5)-H(5D)...Cl(1) **#1**	0.79(2)	2.57(2)	3.33(1)	164(3)
N(3)-H(3D)...Cl(1) **#2**	0.91(2)	2.69(2)	3.44(1)	141(2)
N(3)-H(3C)...Cl(1) **#3**	0.84(2)	2.86(2)	3.59(1)	147(2)
O(5)-H(5C)...O(3)	0.78(2)	2.14(2)	2.87(1)	155(2)
N(4)-H(4D)...O(5)	0.88(2)	2.53(2)	3.38(3)	162(2)
N(4)-H(4C)...O(4) **#5**	0.90(2)	2.62(2)	3.36(1)	140(2)

Symmetry operations for equivalent atoms:
#1 (x+1, y-1, z); **#2** (-x, -y+2, -z); **#3** (x+1, y, z); **#4** (-x,-y+1,-z); **#5** (x-1, y, z)
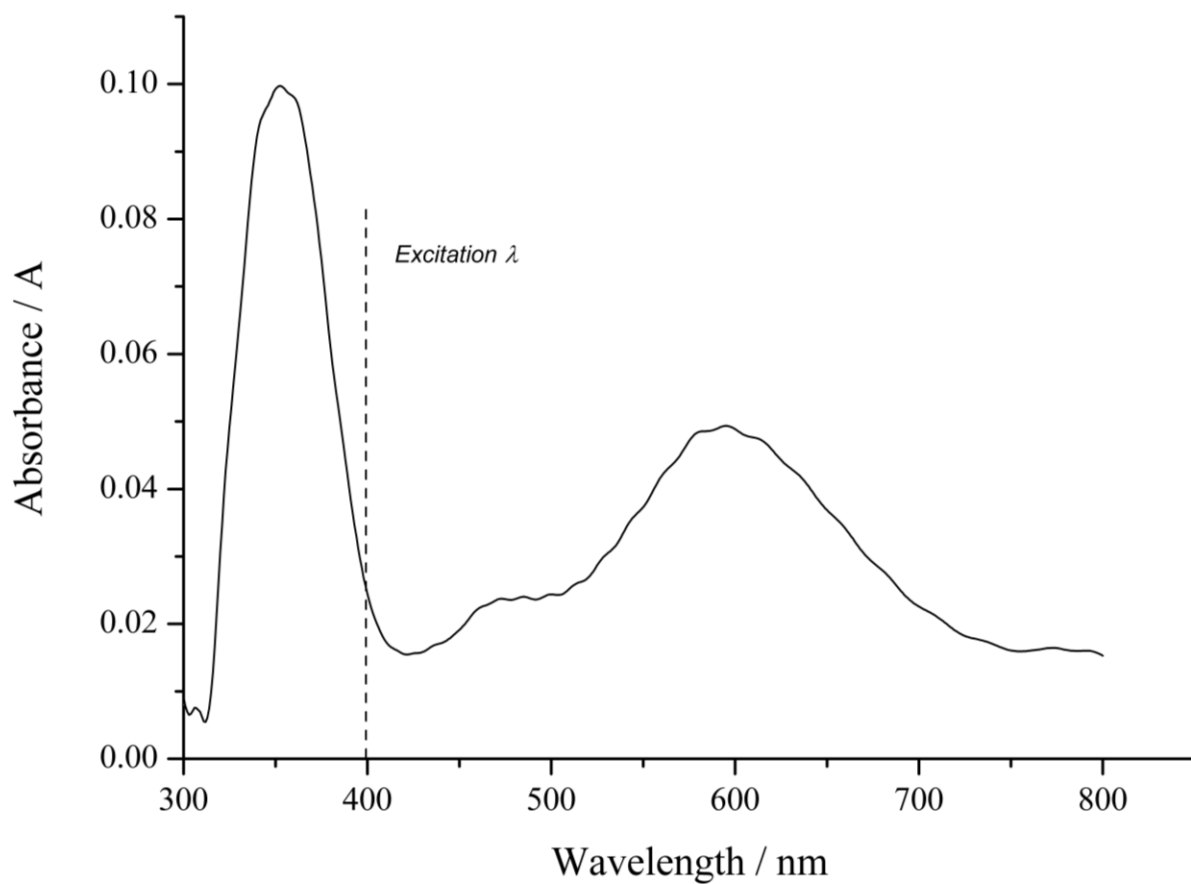
Solid State UV/vis Spectrum

Figure 8: Solid state UV/vis spectrum for complex [8], showing the choice of excitation wavelength

Appendix 9: Complex [9]

Complete nitro : nitro ratios 298 – 225 K: thermal studies

Table 18: Nitro : nitrito occupancies for repeat datasets between 298 and 100 K, in thermal studies with [9]

Temp / K	Nitro-(η^1-NO$_2$) Occupancy			Nitrito-(η^1-ONO) Occupancy		
	Repeat 1	Repeat 2	Repeat 3	Repeat 1	Repeat 2	Repeat 3
100	1.00*	1.00*	1.00*	0.00*	0.00*	0.00*
150	1.00*	1.00*	1.00*	0.00*	0.00*	0.00*
200	1.00*	1.00*	1.00*	0.00*	0.00*	0.00*
225	0.94(1)	0.95(1)	0.95(1)	0.06(1)	0.05(1)	0.05(1)
250	0.92(1)	0.91(1)	0.92(1)	0.08(1)	0.09(1)	0.08(1)
275	0.89(1)	0.89(1)	0.89(1)	0.11(1)	0.11(1)	0.11(1)
298	0.85(1)	0.84(1)	0.84(1)	0.15(1)	0.16(1)	0.16(1)

* No esd is reported for full occupancy or zero occupancy as these ratios were not refined
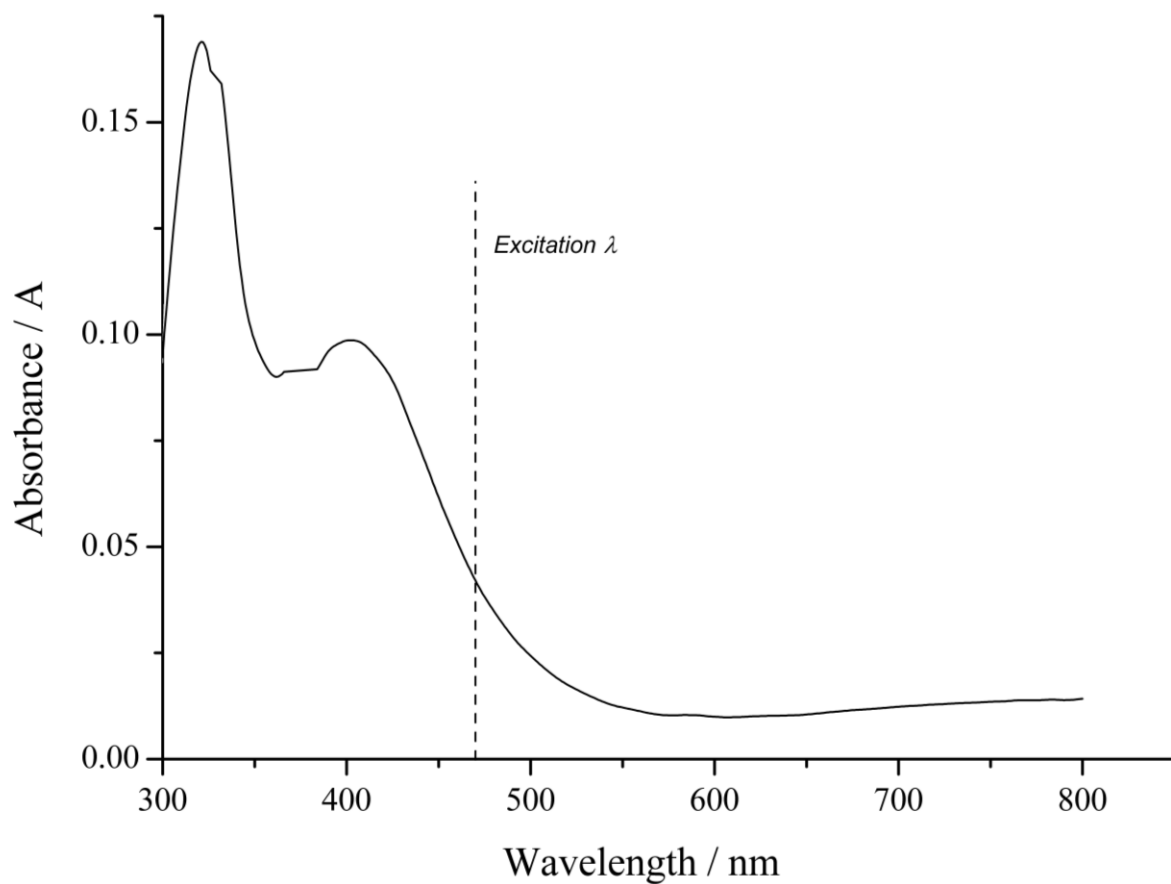
Solid state UV/vis Spectrum

Figure 9: Solid state UV/vis spectrum for [9], showing the choice of excitation wavelength

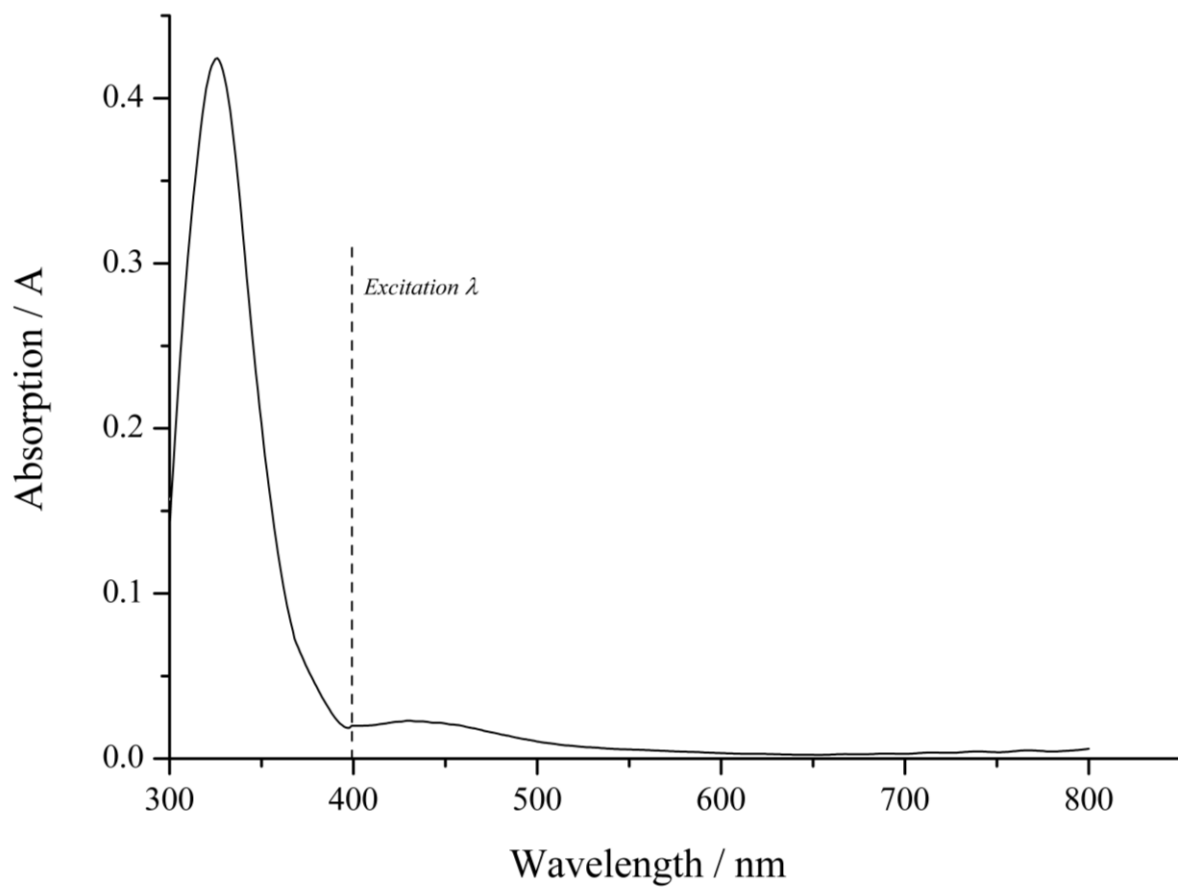# Appendix 10: Complex [10]

Solid State UV/vis Spectrum

Figure 10: Solid state UV/vis spectrum for complex [10], showing the choice of excitation wavelength

Appendix 11: Complex [11]
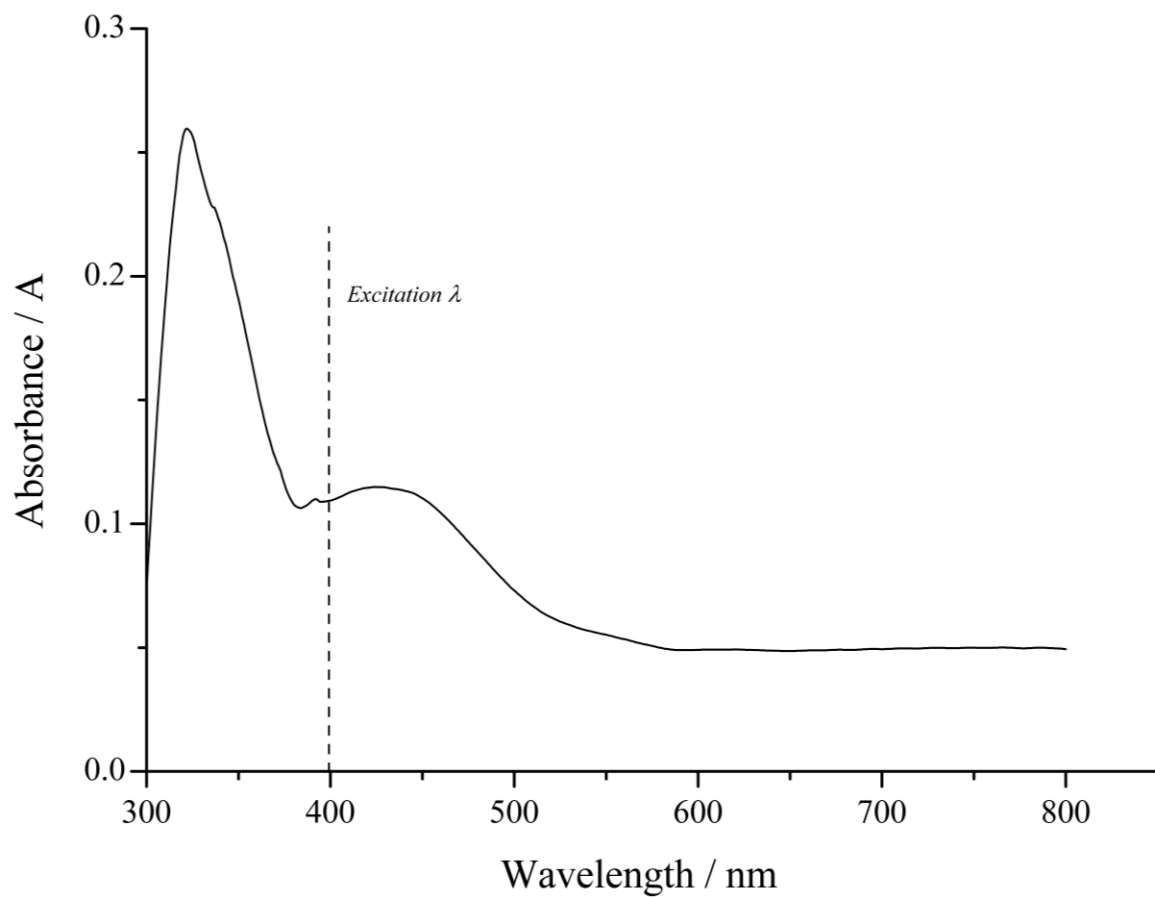
Solid State UV/vis Spectrum

Figure 11: Solid state UV/vis spectrum for complex [11], showing the choice of excitation wavelength

Appendix 12: Photocrystallographic Kinetic Studies

Steady – State Photocrystallographic Kinetic Studies at λ = 500 nm

Table 19: Crystallographically determined nitro : nitrito ratios in steady-state photocrystallographic kinetic studies with complex [1], as a function of total irradiation time at λ = 500 nm

Total Irradiation time / min	Occupancy (esd)	
	Nitro-(η^1-NO$_2$)	Nitrito-(η^1-ONO)
0	1.00*	0.00*
2	0.89(1)	0.11(1)
4	0.84(1)	0.16(1)
8	0.73(1)	0.27(1)
16	0.56(1)	0.44(1)
32	0.32(1)	0.68(1)
64	0.08(1)	0.92(1)
128	0.00*	1.00*

* No esd is reported for full occupancy or zero occupancy as these ratios were not refined

Steady – State Photocrystallographic Kinetic Studies at λ = 400 nm

Table 20: Crystallographically determined nitro : nitrito ratios in steady-state photocrystallographic kinetic studies with complex [1] as a function of irradiation time at λ = 400 nm

Total Irradiation time / min	Occupancy (esd)	
	Nitro-(η^1-NO$_2$)	Nitrito-(η^1-ONO)
0	1.00*	0.00*
2	0.61(1)	0.39(1)
4	0.45(1)	0.55(1)
8	0.30(1)	0.70(1)
16	0.19(1)	0.81(1)
32	0.15(1)	0.85(1)
64	0.15(1)	0.85(1)

* No esd is reported for full occupancy or zero occupancy as these ratios were not refined
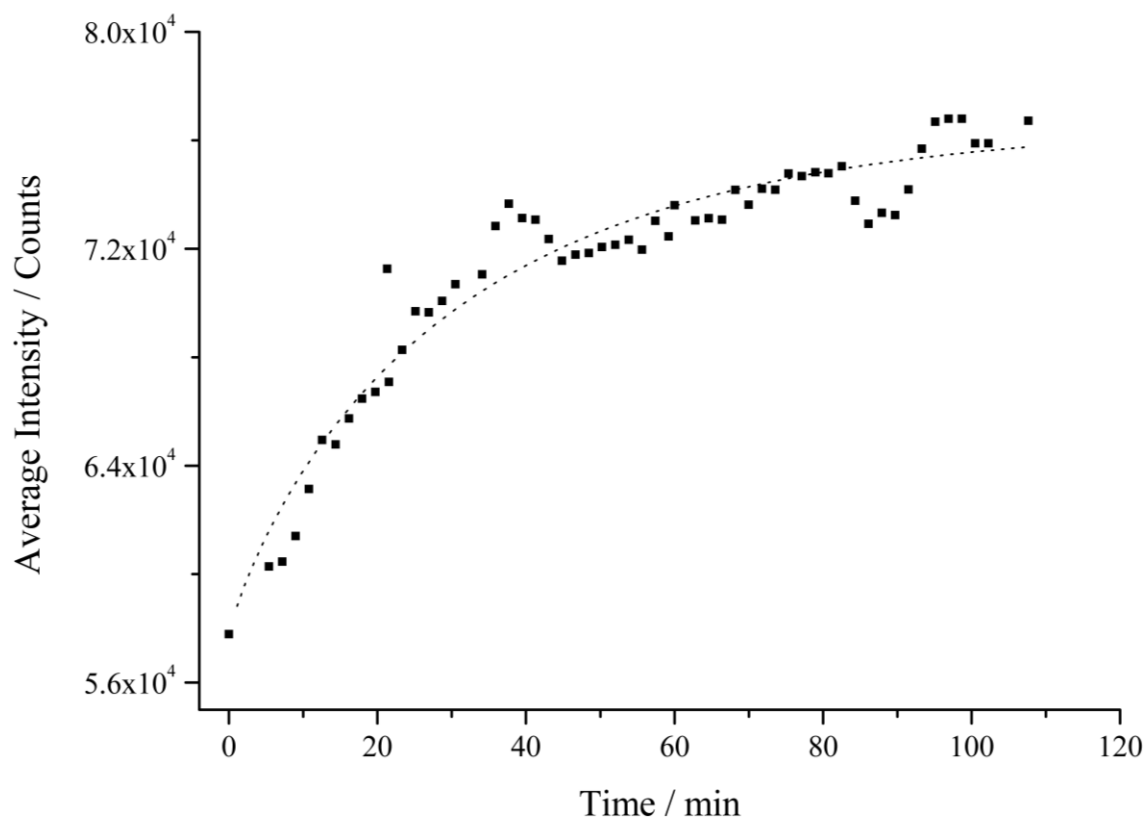
Figure 1: Kinetic plot following the averaged intensity of the (410) reflection with irradiation time in complex [1]. Each data point is averaged over 5 neighbouring intensity readings, and plotted at the centre time. Least squares fitting of $y = 76720 - (76720 - 57787)\exp(kt^n)$: $k = 0.033$ ($\pm$ 0.001) min^{-1}, $n = 0.86$ ($\pm$ 0.05), $R^2 = 0.918$